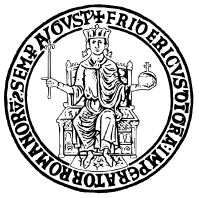

Università degli Studi di Napoli Federico II

SCUOLA POLITECNICA E DELLE SCIENZE DI BASE
Dipartimento di Ingegneria Industriale

Tesi di Laurea Magistrale in Ingegneria Aerospaziale

Numerical and experimental analysis of a wing with distributed electric propulsion

Relatore
Ch.mo Prof. Pierluigi Della Vecchia

Correlatore
Ch.mo Prof. Danilo Ciliberti

Candidato
Vincenzo Orticalco

Anno Accademico 2019-2020

Abstract

Analysis of scenario

Distributed Electric Propulsion (DEP) consists of an array of propellers (powered by electric motors) placed in a generic position, usually in front of the wing leading edge (L.E.), in the spanwise direction. These propellers can improve the aerodynamic characteristics of the wing, for better ground and flight performance. Together with L.E. propellers, a tip-mounted propeller can allow a drag reduction suitable for cruise and climb phases. Nevertheless, the aerodynamic effects of such an array of propellers must be accurately analyzed to see which are pros and cons of this type of technology, through wind tunnel tests benchmarking and numerical analyses.

Statement of the problem

The purpose of the thesis is to analyze the aerodynamic effects generated by changing the positions of an array of three propellers placed in front of the leading edge of a rectangular wing, whose model is under analysis in the wind tunnel subsonic wind tunnel of Dept. of Industrial Engineering of the University of Naples "Federico II". The propellers can be mounted in four different vertical positions and in three different horizontal positions, for a total of twelve combinations. These positions are considered for the clean wing (no flap) and for two flapped configurations (15 and 30 degrees) representative of take-off and landing settings. A tip-mounted propeller, whose effect can be investigated separately and along with the DEP propellers, is also installed. The design of wind-tunnel test bench started from the choice of an airfoil, the GA(W)-1, for which a flap position (gap and overlap) exploration study was performed for choosing the best compromise between takeoff and landing configuration (15 and 30 degrees). The DEP propellers were designed through the conceptual approach for high lift propellers proposed by Patterson (2016), while the tip propeller was designed with the classical method. The radius of the propellers was fixed at the beginning, according to wind

tunnel test section, with the aims to evaluate both L.E. mutual effects and TIP propeller effects. Another driving parameter for the propeller design was the maximum power of the electric motors available.

Adopted methodology

Both L.E. and TIP propellers effects have been investigated with the vortex lattice solver VSPAERO (contained in OpenVSP) and the unstructured cell-centered finite-volume-based solver STAR-CCM+. The analyses performed are time-averaged (RANS) and for this reason the propellers are simulated with a Virtual Disk Model implemented in STAR-CCM+, the Body Force Propeller Method. These analyses constitute a benchmark for the wind tunnel tests which are on-going.

Main results

The effect of DEP is to increase the lift capability of the wing, along with an increase in drag and pitching moment coefficient, that must be carefully evaluated for stability and control. Regarding the clean configuration, for this type of wing the presence of DEP propellers leads to a deterioration of the aerodynamic performance, generating a stall anticipation and, in general, there is no gain in term of maximum lift coefficient. Moreover, the efficiency of the wing is decreased significantly. On the other hand, the flapped configurations benefit from the presence of DEP propellers. With a flap deflection of 15 degrees there is a gain in the maximum lift coefficient for all the combinations of positions, except for one of them (corresponding to the higher vertical and maximum forward position). The gain in lift coefficient becomes more significant with a flap deflection of 30 degrees. The best position in term of maximum lift coefficient is the closest to the wing leading edge (20% of wing chord) regarding the horizontal position, both for clean and flapped configuration. Considering the vertical position, the clean configuration reaches the highest lift coefficient when the propellers are in the neutral position, aligned to the wing chord, while for the flapped configurations seems to be better to place the propellers slightly below the wing chord (5% of the wing chord). The tip propeller has the effect to reduce the induced drag if the rotation sense is opposite to the wing-tip vortices (in-board up). The wing induced drag factor becomes even higher than one and the wing efficiency is increased. This induced drag reduction can be exploited to increase the performance in cruise and climb phases.

Contents

List of Figures

List of Tables

Nomenclature

Abbreviations

DP	Distributed Propulsion
DEP	Distributed Electric Propulsion
LEAPTech	Leading Edge Asynchronous Propeller Technology
HEIST	Hybrid Electric Integrated Systems Testbed
RANS	Reynolds-averaged Navier–Stokes equations

Symbols

δ_f	Flap deflection angle
ρ_∞	Free-stream density
C_{D_i}	Induced drag coefficient
C_D	Drag coefficient (3D)
C_d	Drag coefficient (2D)
C_{L_α}	Lift curve slope (3D)
$C_{L_{MAX}}$	Maximum lift coefficient (3D)
C_L	Lift coefficient (3D)
C_l	Lift coefficient (2D)
C_M	Pitching moment coefficient (3D)

C_m	Pitching moment coefficient (2D)
C_P	Power coefficient: $2\pi C_Q$
C_Q	Torque coefficient: $\frac{Q}{\rho_\infty n^2 D^5}$
C_T	Thrust coefficient: $\frac{T}{\rho_\infty n^2 D^4}$
D	Propeller diameter
J	Propeller advance ratio: $\frac{V_\infty}{nD}$
n	Revolutions per second
P	Propeller power
p_∞	Free-stream static pressure
Q	Propeller torque
RPM	Revolutions per minute
T	Propeller thrust
V_∞	Free-stream velocity

Chapter 1

Introduction

Among the several challenges in aircraft design, improvements in aerodynamics are undoubtedly very impactful on the whole aircraft performance. During the last decade, Distributed Propulsion has been one of the most investigated technology: a simple definition of DP can be described as a propulsion system where the vehicle thrust is produced from an array of propulsors located across the air vehicle [1]. An interesting type of DP, which is currently being studied across various research and industry organizations, is a system where electrical energy sources are connected, via transmission lines, to multiple electric motor-driven propulsors. This system is called Distributed Electric Propulsion and has the potential to introduce substantial improvements in future air-vehicle performance, efficiency, and robustness. DEP can be employed to provide both the required thrust for flight and additional advantages associated with synergistic propulsion-airframe integration. Many studies have shown significant benefits of synergistic airframe-propulsion design [2, 3, 4, 5, 6, 7], to reduce aircraft fuel burn and noise and to achieve shorter takeoffs and landings. The aircraft concepts in these studies achieve this synergy through distributed propulsion, which Kim defines as “the spanwise distribution of the propulsive thrust stream such that overall vehicle benefits in terms of aerodynamic, propulsive, structural, and/or other efficiencies are mutually maximized to enhance the vehicle mission" [8]. As explained by Patterson [9], DEP can bring to an increase of cruise efficiency of small aircrafts through different types of mechanisms and herein the attention is focused on two of these ones, that are

- increasing the dynamic pressure over the wing above freestream during approach to allow for increased design wing loading ("high-lift propeller"),

- installing propellers at the wingtips to reduce induced drag ("tip propeller").

1.1 High-lift propeller

The first mechanism leverages the fact that the distributed propellers upstream of the wing increase the flow velocity aft of themselves. In this way the wing sections in the propeller slipstreams experience an increase in flow velocity such that their lift increases, making the wing more effective at low speeds. The LEAPTech (Leading Edge Asynchronous Propeller Technology) Experiment was one of the earliest experiments regarding the investigation of this effect. The test apparatus was named Hybrid Electric Integrated Systems Testbed (HEIST), shown in Figure 1.1. The aerodynamic system

Figure 1.1: HEIST at NASA Armstrong (NASA photo) [10]

analysed was a wing designed for a four-place general aviation aircraft with high wing loading to reduce cruise drag and improve ride quality. Takeoff and landing performance were maintained by distributing eighteen small propellers across the leading edge of the wing that blow the wing and increase the dynamic pressure during takeoff and landing [10]. Some steady-state RANS simulations were performed with several turbulence models using the unstructured cell-centered finite-volume-based solver STAR- CCM+. The comparison between numerical and low-speed experimental results has shown a difference of about 10%: considering that the propellers were modeled by prescribing

uniform volume force distributions over cylindrical virtual disks, the results were in excellent agreement (Figure 1.2). Moreover, another computational study related to this experimental apparatus showed that there is large benefit in lift coefficient, over the entire range of angle of attack studied, by using co-rotating propellers that all spin counter to the wingtip vortex, instead of counter-rotating propellers, and this benefit is quantified from a maximum lift coefficient amplified by a factor of 2.4 respect to the unblown condition [11].

An interesting development of the LEAPTech Experiment is the NASA SCEPTOR Distributed Electric Propulsion Flight Demonstrator, which is based on a Tecnam P2006T aircraft fuselage and reconfigured with a much smaller wing than the baseline aircraft. The smaller wing is achievable for this design due to the high lift provided by twelve small electric propellers along the leading edge of the wing during the take-off and landing phases of flight [12].

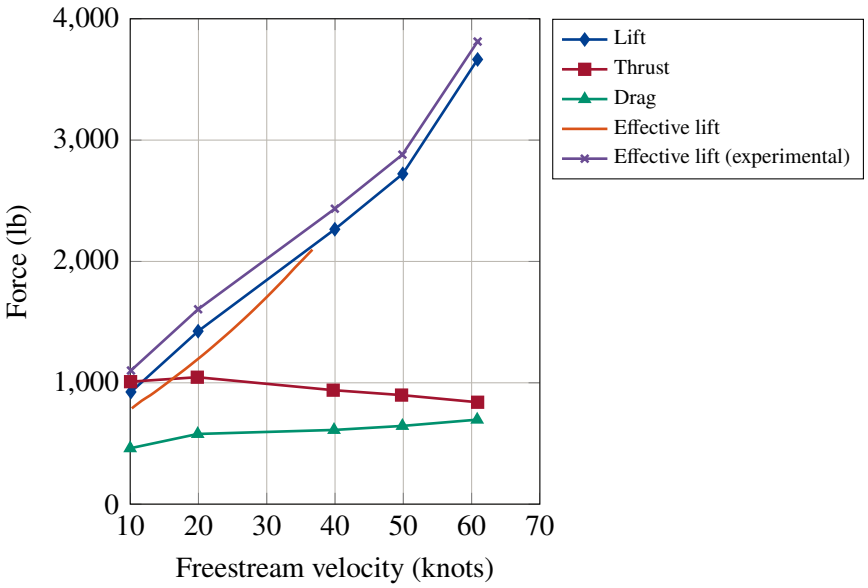

Figure 1.2: Comparison of STAR-CCM+ results with low-speed experimental results. "Effective lift" includes the vertical component of the propeller thrust. The experimental results curve shown is an average of quadratic fits to data from two runs in opposite directions (Reproduced from [10])

Della Vecchia et alii [13] investigated another interesting effect related to the number of distributed propellers along the spanwise direction. With a certain number of propellers, for each angle of attack a higher lift coefficient can be reached, and even a higher lift curve slope. Moreover, for high lift coefficient distributed propulsion also

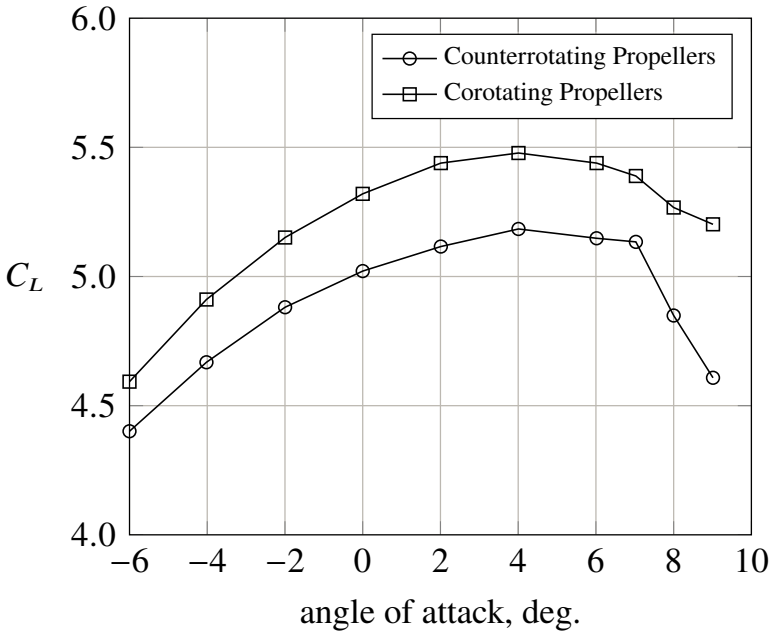

Figure 1.3: The comparison of lift coefficient between propeller spin direction approaches for the blown, high-lift wing (40° flap) at 73 mph - $M = 0.096$ - $Re = 1 \cdot 10^6$ - $h = 2300\,ft$ - $T = 60\,F$ - 300.6 hp (16.7 $hp/prop$, 6147 RPM) (Reproduced from [11])

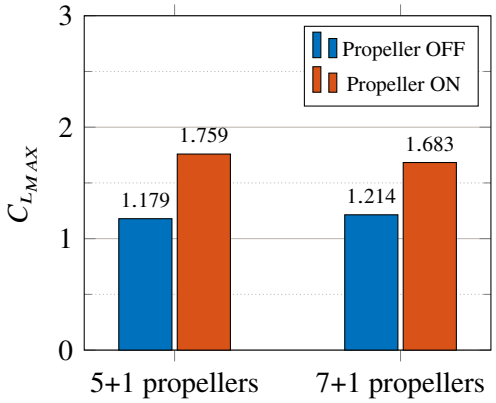

(a) Variation of $C_{L_{MAX}}$ for $\delta_f = 0°$ with propeller on and off

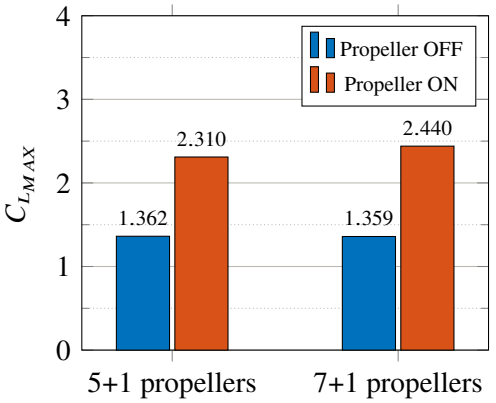

(b) Variation of $C_{L_{MAX}}$ for $\delta_f = 20°$ with propeller on and off

Figure 1.4: Effect of the number of propellers on $C_{L_{MAX}}$ for clean and flapped configurations [13]

positively affects aerodynamic drag. As shown in Figure 1.4, if the flap is not deflected the $C_{L_{MAX}}$ is higher in case of 5+1 propellers, while with a flap deflection of twenty degrees the higher $C_{L_{MAX}}$ is reached with 7+1 propellers.

1.2 Tip propeller

Regarding the second mechanism, it can be simple to understand the effect of a propeller installed at a wing-tip looking at the Figures 1.5a and 1.5b. The axial induction of the propeller (the actuator disk) has an upwash effect, reducing the induced angle due to the downwash of the wing (so the induced drag). If the propeller rotates in an opposite direction respect to the wingtip vortices, the tangential induction due to the disk has likewise an upwash effect, with a further reduction of the induced angle.

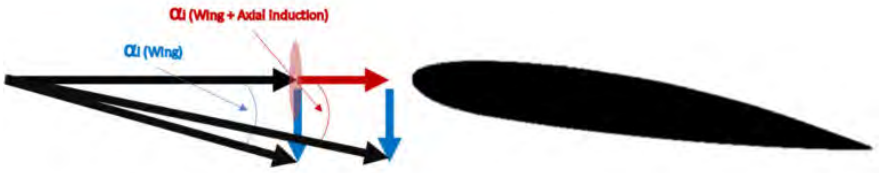

(a) Induced angles due to wing and actuator disk

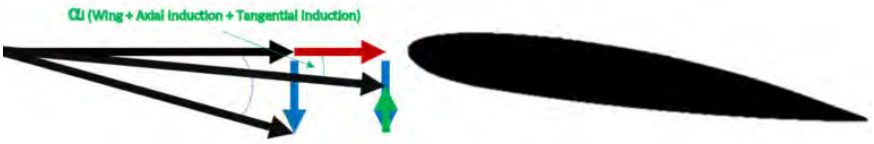

(b) Induced angles due to wing and rotating disk

Figure 1.5: Schematization of the interaction between a propeller and a wing [14]

In this way, by placing the propellers in front of the wings at the tips, the rotation of the propellers can be used to counteract the effects of the wingtip vortices to effectively push these vortices farther outboard, which can reduce the induced drag of the configuration, also increasing the $C_{L_{MAX}}$ and the effective aspect ratio (if the propeller rotates in the same direction of the wingtip vortices, the effect is reverse and there are no benefits). This is shown by Snyder and Zumwalt [15] through an experimental program testing a wing with propellers mounted at the wingtips. An interesting aspect is that the efficiency of the propeller is a limitation because, with an efficiency of 80%, about 80% of the energy provides axial acceleration of the air and only about 20% is available to produce

rotation with which to supplement or to counteract the trailing vortex. Earlier tests of an impeller (shaped something like an orange juice extractor) had shown that the device does produce thrust, but the propulsive efficiency peaks at less than 50%, so there is more energy to counteract the trailing vortices. The differences between propeller and impeller are shown in Figure 1.6. In Figure 1.7 are illustrated the effect of the spanwise position of the propeller on the wing performance and in Figure 1.8 there is a generalization of these results based on the parameters $\Delta C_{D_i}/C_L^2$ and Hd/b, where H is the difference between rotor speed and windmilling speed, d is the propeller diameter and b the wing span.

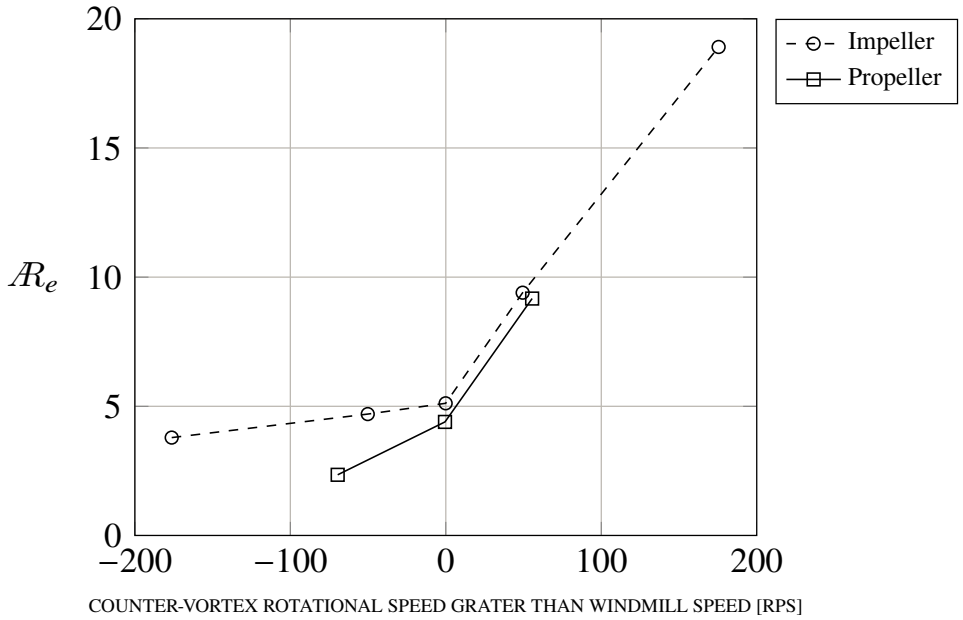

Figure 1.6: Variation of effective aspect ratio caused by rotor speed - $\mathcal{AR} = 8$ - $Re = 6.7 \cdot 10^5$ - Baseline $\mathcal{AR}_e = 6.45$ - $\delta_f = 0°$ (Reproduced from [15])

Tests conducted on a wing-body configuration of $\mathcal{AR} = 6.10$ with a wing-tip pusher propeller [16] have shown that a drag reduction of about 20 drag counts for the counter-rotating wing-tip pusher propeller is achieved, in the range of low value of lift coefficient (Figure 1.9).

Sinnige et al. [17] showed that wingtip-mounted propellers installed in a tractor configuration can decrease wing induced drag by attenuating the wingtip vortex by the propeller slipstream. The experimental tests were conducted on a half wing with a wingtip-mounted propeller and compared to a conventional configuration (Figure

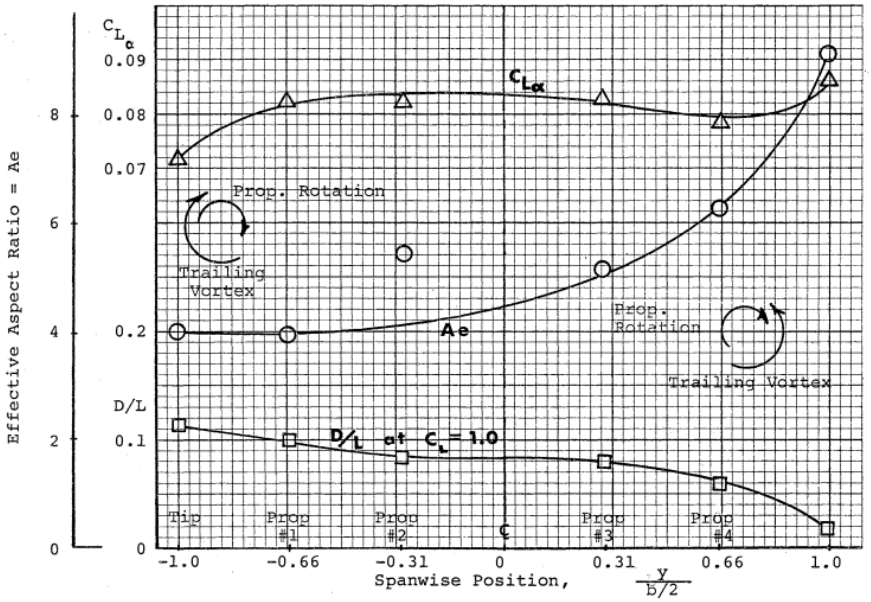

Figure 1.7: Four blade Tip-Propeller effects on a $\mathcal{AR} = 8$ wing - $Re = 6.7 \cdot 10^5$ - $T_c = 0.42$ or 0.6 [15]

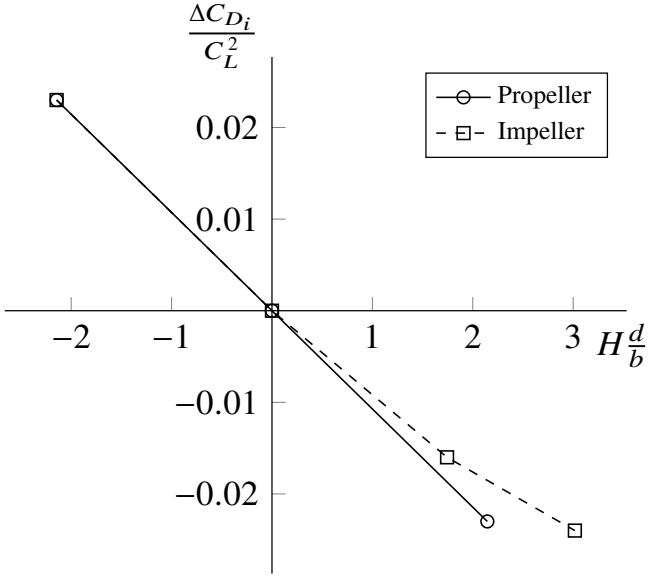

Figure 1.8: Effect of propeller speed and size on induced drag coefficient (Reproduced from [15])

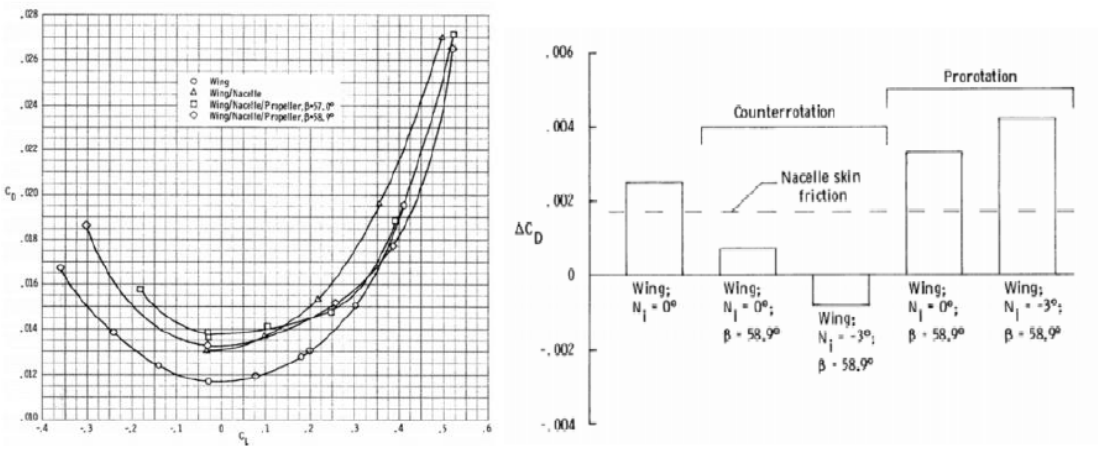

Figure 1.9: Left: Vortex-propeller interaction on drag coefficient versus lift coefficient for 0° incidence Right: drag difference respect to the isolated wing for counter-rotating and pro-rotating wing-tip pusher propeller - $M = 0.7$ - $Re = 3.82 \cdot 10^6$ [16]

1.10). The results shown a drag reduction increasing the thrust setting level and the lift coefficient, leading to a drag reduction of about 30 up to 60 drag counts in a typical C_T range of cruise lift coefficient condition of general aviation small regional aircraft (Figure 1.11).

Numerical analyses conducted by Della Vecchia et al. [13] showed that, for a given propeller, there is a drag reduction which increases if the thrust level increases but decreases if the diameter of the propeller decreases. This behaviour is due to the variation of RPM, which must increase, decreasing the diameter, to provide the same level of thrust. Basically, the higher is the diameter of the propeller, or the higher is the thrust provided by the propeller, the lower is the induced drag. However, very large propellers diameters will not lead to a further drag reduction, or even affect negatively the drag, while for too short propellers diameters there is additional drag induced by the presence of the active propeller (Figure 1.12).

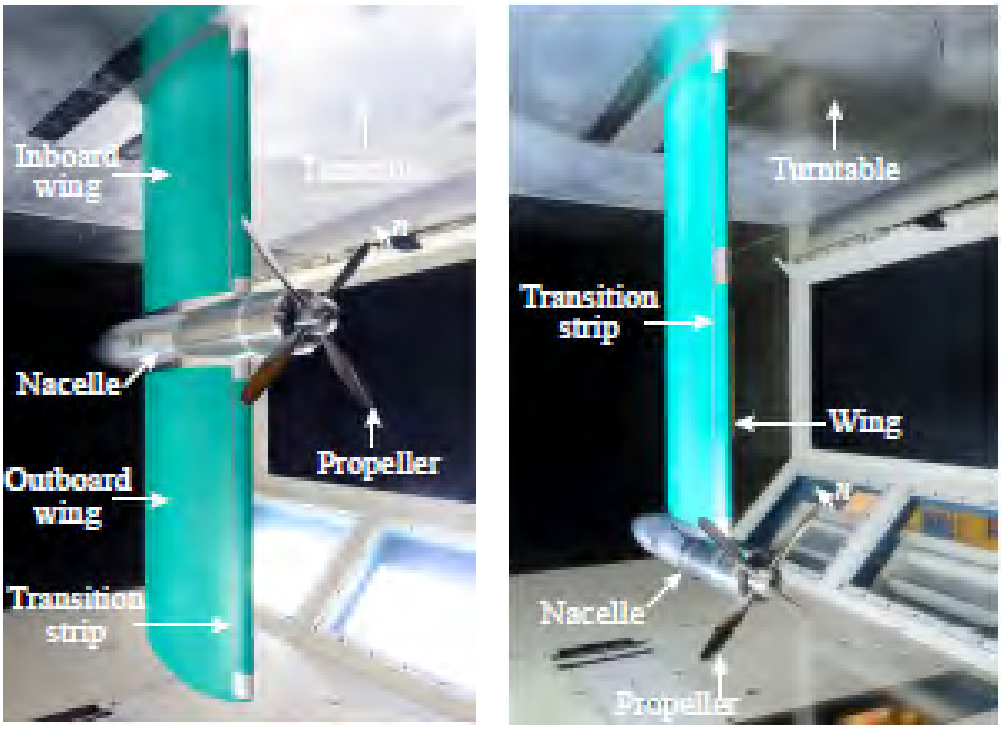

(a) Conventional configuration **(b)** Wingtip-mounted configuration

Figure 1.10: Model II (modular cambered wing) installed in the wind tunnel for the tests presented in [17]

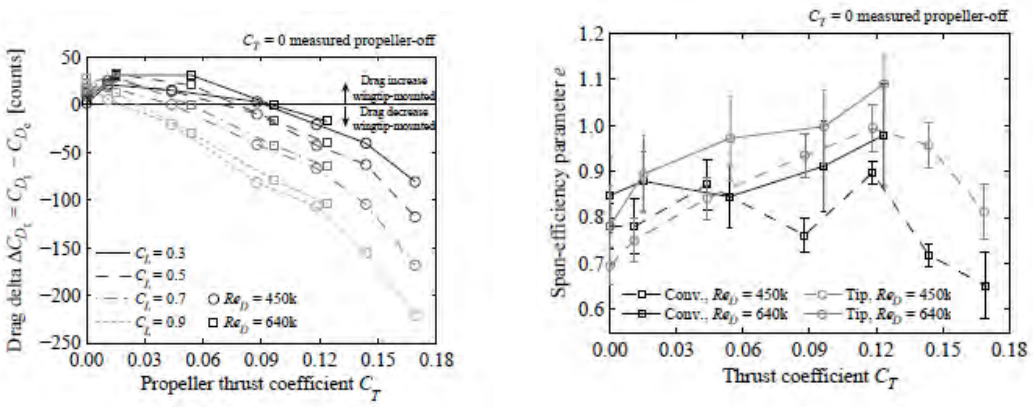

(a) Drag benefit of wingtip-mounted configuration compared to conventional configuration

(b) Effect of propeller thrust setting on the lift-curve slope of the wing with nacelle for the conventional and wingtip-mounted configurations

Figure 1.11: Some experimental results from [17]

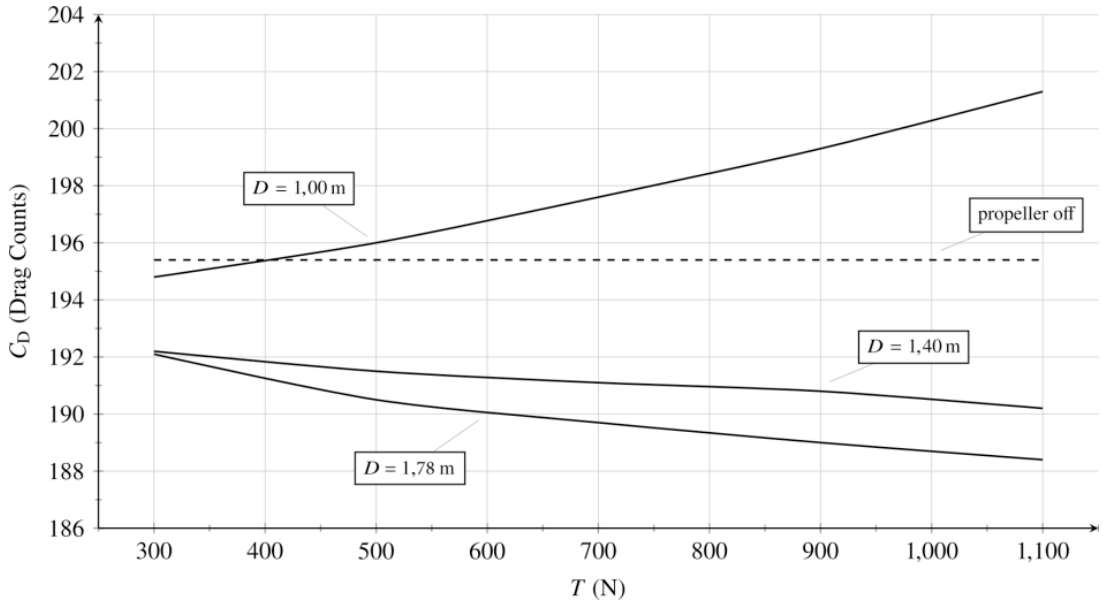

Figure 1.12: Effect on C_D of wing-tip propeller, variating diameter D and thrust T, for a cruise condition $C_L = 0.4$ [13]

Chapter 2

Methodologies

In this chapter, an overview on the methodologies and tools to study the propellers and their interaction with a wing is provided. A brief summary of the classical theories of the propellers is presented at first (references from [18]), then the Patterson's approach to the design of "high-lift propellers" is reminded. Finally, the tools used for the analysis presented hereinafter are described.

2.1 Propeller analysis and design

2.1.1 Theoretical background

Momentum theory

Momentum theory, first introduced by Rankine (1865), is based on the idea of the actuator disk, i.e. the propeller is seen as a surface of discontinuity or as an infinitely thin disk. The hypotheses of the theory are

- one dimensional flow,
- stationary flow,
- incompressible flow,
- non-dissipative flow,
- radial and tangential components of velocity introduced by the disk are neglected,

- the propeller has an infinite number of blades,

- the variation of the area of the section of the streamtube is small.

In these hypotheses, the disk is a surface of discontinuity only for the pressure, while the velocity is continuous across the disk; moreover, the static pressure in the section infinitely far upstream is equal to the static pressure in the section infinitely far downstream because there is no swirl (the tangential component of the velocity is neglected, see Fig. 2.1 and for more details see [18]).

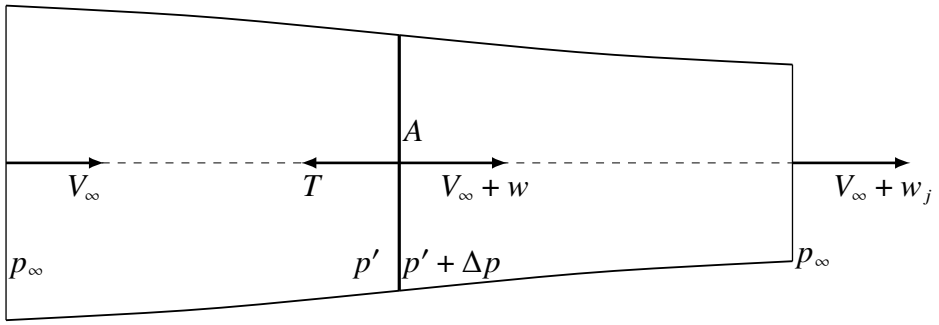

Figure 2.1: Streamtube according to momentum theory

The thrust generated by the actuator disk is expressed as Eq. 2.1, where Δp is the pressure jump across the disk, A is the disk area, w is the axial induction on the disk and w_j is the axial induction infinitely far downstream.

$$T = \Delta p A = \rho_\infty (V_\infty + w) w_j A \tag{2.1}$$

The most important result of this theory is that $w_j = 2w$, i.e. to produce thrust the propeller must increase the velocity of the flow. Introducing the axial induction factor, $a = w/V_\infty$, the thrust is expressed as Eq. 2.2.

$$T = 2\rho_\infty A V_\infty^2 (1 + a) a \tag{2.2}$$

The disk must be powered in a certain way to increase the kinetic energy of the fluid which flows across it and the power supplied is related to the variation of kinetic energy experienced by the flow. The expression of the power can be written as in Eq. 2.3,

where $\dot{m}$ is the mass flow rate, which is constant in every section of the streamtube.

$$P = \dot{m}\left[\frac{1}{2}(V_\infty + w_j)^2 - \frac{1}{2}V_\infty^2\right] = TV_\infty(1+a) \tag{2.3}$$

The expression of the efficiency of the system is presented in Eq. 2.4.

$$\eta = \frac{TV_\infty}{P} = \frac{1}{1+a} \tag{2.4}$$

The only information which the momentum theory gives about the propeller geometry is that the propeller with the highest efficiency is the propeller with the largest area: indeed, for $a \to 0$, $\eta \to 1$ and, to keep the thrust constant, A must tend to infinity.

The simple momentum theory introduced above assumes that the axial induction is constant along the radial direction. Assuming instead that the axial induction is a function of the radial coordinate, $a = a(r)$, it is possible to re-formulate the momentum theory with a differential approach considering two concentric streamtubes at two different radial coordinates, r and $r + dr$ (Fig. 2.2). The fundamental hypothesis is

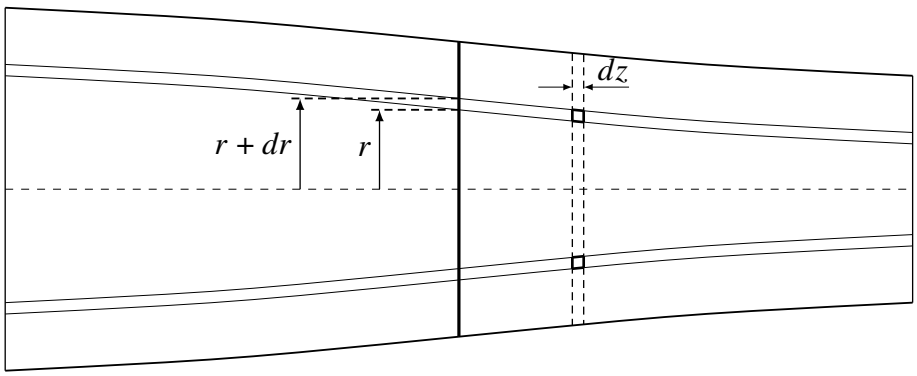

Figure 2.2: Scheme of two concentric streamtubes

that there is no interaction between the several streamtubes. From Eq. 2.2 and 2.3, considering that the area of the anulus identified by the two streamtubes on the disk is $dA = 2\pi r dr$, the contributions of the anulus to thrust and power are expressed as Eq. 2.5 and 2.6.

$$dT = \Delta p\, dA = 4\pi\rho_\infty V_\infty^2 \left[1 + a(r)\right] a(r) r dr \tag{2.5}$$

$$dP = dTV_\infty \left[1 + a(r)\right] = 4\pi\rho_\infty V_\infty^3 \left[1 + a(r)\right]^2 a(r) r dr \tag{2.6}$$

To optimise the propeller, the power must be minimized for a fixed thrust. This

is a constrained minimization problem: the result is that the optimum propeller is characterized by a constant axial induction along the radial direction, $a(r) = const$. A propeller of a fixed diameter D, which must produce a certain thrust T, has the maximum efficiency if the disk loading dT/dA is uniformly distributed on the disk area (Eq. 2.7).

$$\frac{dT}{dA} = \frac{1}{2\pi r}\frac{dT}{dr} = \rho_\infty V_\infty (1+a)a = const \tag{2.7}$$

The theory can be complicated introducing the tangential velocity v neglected so far, still neglecting the radial component of the velocity. Considering a control volume of height dz downstream of the disk (represented with bold lines in Fig. 2.2), delimited by the two streamtubes mentioned above, the only contribution to the momentum equation applyed to this control volume comes from the tangential velocity, which, for a fixed radial coordinate, is constant moving along the axis of the streamtubes. Upstream of the disk there is no tangential velocity, so the latter is non-continuous across the disk. The momentum discontinuity across the disk results in the presence of a torque, expressed as Eq. 2.8, where $\omega = v/r$ is the angular velocity induced by the disk, Ω is the angular velocity of the blades and $a' = \omega/(2\Omega)$ is the tangential induction factor. The main assumption in this case is that $\omega \ll \Omega$.

$$dQ = d\dot{m}\,\omega r^2 = 4\pi\rho_\infty V_\infty\,\Omega(1+a)a'r^3 dr \tag{2.8}$$

If the two induction factors a and a' are considered constant along the radial direction and the tangential induction is such small that the static pressure in the section infinitely far downstream can be still considered equal to p_∞, a similar process like above can lead to the equations of thrust and power. In these hypotheses, the mathematical expression of the thrust is not modified, while in the expression of the power there is a further contribution (Eq. 2.9), and the power can be even written as Eq. 2.10.

$$\begin{aligned} P = \dot{m}\left[\frac{1}{2}(V_\infty + w_j)^2 - \frac{1}{2}V_\infty^2\right] + \int_0^R \frac{1}{2}(\omega r)^2 d\dot{m} = \\ = TV_\infty(1+a) + \dot{m}\frac{D^2}{4}\Omega^2(a')^2 \end{aligned} \tag{2.9}$$

$$P = \int_0^R \Omega\, dQ = \dot{m}\frac{D^2}{4}\Omega^2(a')^2 \tag{2.10}$$

Combining Eq. 2.9 and 2.10, the propeller efficiency can be expressed as Eq. 2.11, where η_1 is the expression of the efficiency obtained from the simple momentum theory (Eq. 2.4), while η_2 is the further loss introduced by the tangential induction.

$$\eta = \frac{1}{1+a}(1-a') = \eta_1 \eta_2 \tag{2.11}$$

Also in this case through a differential approach the variation of a and a' with the radial coordinate can be considered, obtaining the following expressions of thrust (unchanged), torque and power.

$$dT = 4\pi\rho_\infty V_\infty^2 [1+a(r)]\, a(r) r dr \tag{2.12}$$

$$dQ = 4\pi\rho_\infty V_\infty \Omega [1+a(r)]\, a'(r) r^3 dr \tag{2.13}$$

$$dP = dT\, V_\infty [1+a(r)] + \frac{1}{2}(\omega r)^2 d\dot{m} = \Omega\, dQ \tag{2.14}$$

From Eq. 2.14, a relation between a and a' can be derived (Eq. 2.15), where $\chi = (\Omega r / V_\infty)$.

$$\frac{(1+a)a}{\chi^2} = a'(1-a') \tag{2.15}$$

Again, a constrained minimization problem must be resolved, obtaining the relation in Eq. 2.16.

$$\frac{1+a}{\chi^2(1-2a)} + \frac{a'}{1+2a} = const \tag{2.16}$$

So there is a different optimum condition but, even then, the axial induction can be considered almost constant along the radial direction, except for the sections near hub and tip.

Blade element theory

The blade element theory sees the propeller from a completely different perspective respect to the momentum theory, because it considers the propeller geometry, namely the radial chord distribution $c(r)$ and the pitch angle distribution $\theta(r)$, to obtain the propeller performance, which are $C_T(J)$, $C_P(J)$ and $\eta(J)$, where $J = V_\infty/(nD)$ is the advance ratio (Fig. 2.4). The propeller blade is divided into segments, the blade elements, and it is assumed that each blade element works in a two-dimensional flow field and there is no interference among the several blades. The propeller thus is not seen as a surface of discontinuity, but each blade is viewed as a rotating, twisted wing.

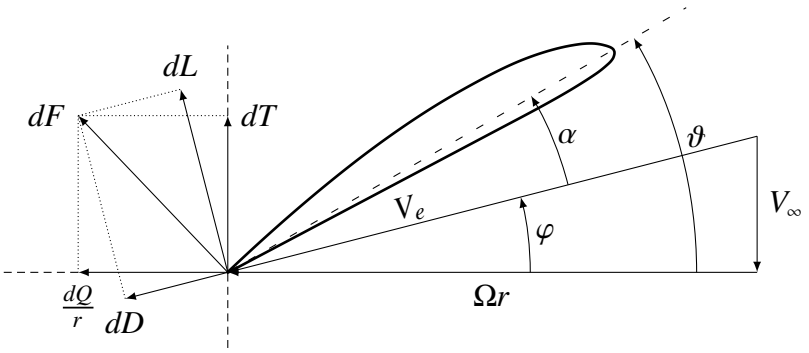

Figure 2.3: Aerodynamic forces on a blade element according to blade element theory

At a certain radial station, considering a section of the blade in a plane perpendicular to the plane of the propeller, which identifies a blade element (see Fig. 2.3), if the inflow angle φ is known, together with the pitch angle θ, the section angle of attack α can be calculated and, if the airfoil aerodynamic characteristics are known, the C_l and C_d of the section can simply be used to calculate the contribution to thrust and torque, whose expressions can be written as in Eq. 2.17 and 2.18. The total force on the blade is the sum of the forces over each blade element.

$$dT = dLcos\varphi - dDsin\varphi \tag{2.17}$$

$$\frac{dQ}{r} = dLsin\varphi + dDcos\varphi \tag{2.18}$$

Vortex theory for propellers

The blade element theory seems to be almost in contrast with the momentum theory, because it doesn't include the presence of the axial induction, for example. However, introducing the vortex model of the actuator disk it is possible to merge the two theories formulating the blade element momentum theory, which is a very powerful tool for propeller analysis and design. The vortex model of the actuator disk (first developed by Betz) is introduced to model the flow field generated by the propeller with a vortex system characterized by an infinite number of bound vortex lines, whose intensity is $\gamma(r)$, placed in the radial direction on the disk surface (each bound vortex line "simulates" the presence of a blade as a lifting line, like in the Prandtl's lifting line theory). The total circulation on the disk at a certain radial station is $\Gamma(r) = 2\pi\gamma(r)r$ and if $\Gamma(r)$ varies along the radial direction of a quantity equal to $d\Gamma$, a cylindrical vortex sheet

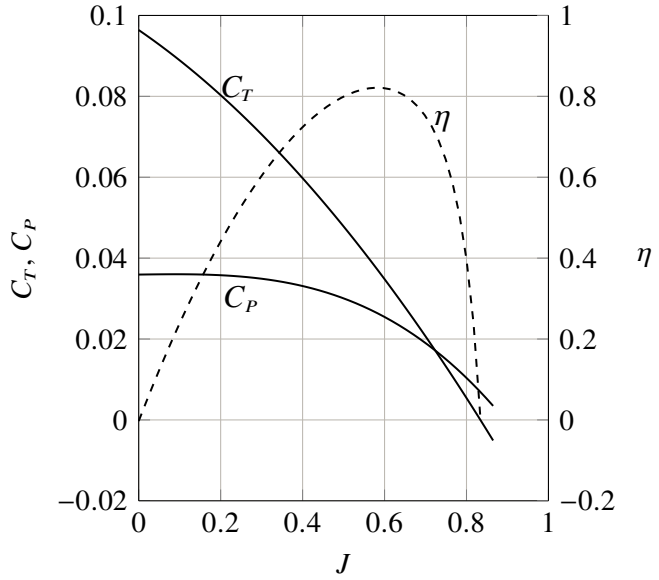

Figure 2.4: Propeller performance from [19]

with the same intensity detaches from that radial station. This cylindrical vortex sheet consists of an infinite number of free, trailing vortices detaching from the disk and going infinitely far downstream. For small values of the axial induction (low disk loading), these trailing vortices, assuming that there is no mutual interaction between the vortex elements, have the shape of a cylindrical helix with constant pitch. In this way the propeller wake contraction is neglected, and the wake consists of a cylinder starting from the disk surface and going infinitely far downstream. For small values of the advance ratio J ($\varphi \approx 0$), the total circulation in the optimum condition is constant along the radial direction because the disk loading is constant (see Eq. 2.7). In this latter scenario, represented in Fig. 2.5 with only three bound vortices for the sake of simplicity, the vortex system described above consists only in a cylindrical vortex sheet detaching from the edge of the disk, composed of free, trailing vortices of intensity $\gamma = \Gamma/(2\pi R)$. Moreover, a vortex line of intensity equal to Γ detaches from the center of the disk. The flow field induced by the general vortex system so far described can be considered equivalent to the flow field generated by a system of vortex lines parallel to the disk axis, which induce a rotational velocity, superimposed on a system of concentric ring vortices placed along the wake, which induce an axial velocity (and, of course, the bound vortex lines on the disk): it can be seen that the induced flow field is consistent with the

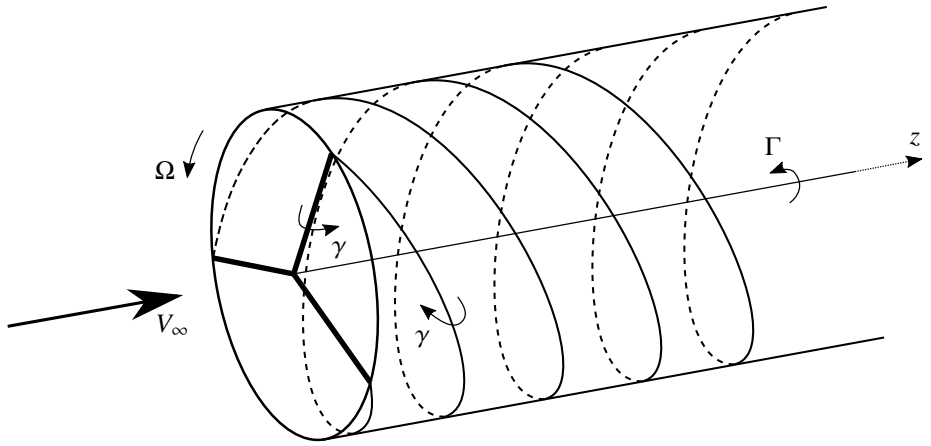

Figure 2.5: Scheme of the vortex system of the actuator disk

momentum theory. The optimum propeller according to the vortex model of the actuator disk is the propeller whose trailing vortex system generates as few losses as possible in producing a specified thrust (Minimum Induced Loss - MIL). In this condition, the vortex sheets shedding from the blades move downstream as rigid "screw" surfaces. At this point, after the description of the propeller wake through a vortex system and the similarity with Prandtl's lifting line theory, the apparent disparity between the blade element theory and the momentum theories can be overcome.

Blade element momentum theory

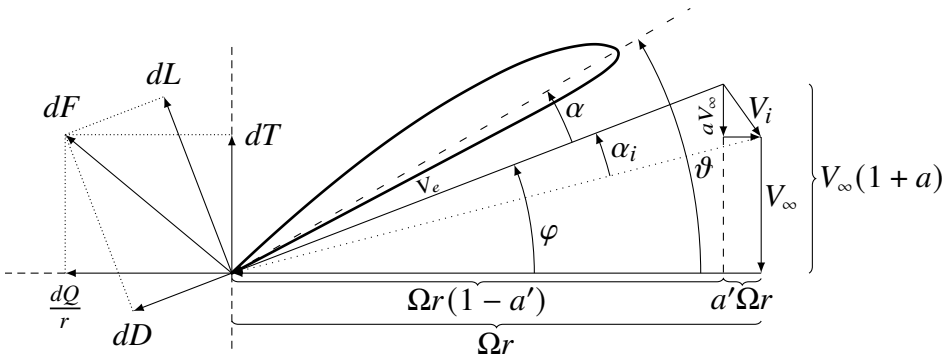

Figure 2.6: Aerodynamic forces on a blade element according to the blade element momentum theory

The blade element momentum theory can be formulated introducing the axial and tangential inductions in the blade element theory. Fig. 2.6 represents the relative

velocities on the blade element: V_i is the total induced velocity which introduces the induced angle α_i, which modifies the inflow angle φ seen in Fig. 2.3. The blade element sees a relative velocity expressed as Eq. 2.19.

$$V_e = \sqrt{V_\infty^2(1+a)^2 + \Omega^2 r^2(1-a')^2} \tag{2.19}$$

The differential expressions of thrust and torque for the single blade element are presented in Eq. 2.20 and 2.21, where N is the number of blades and c is the chord length.

$$dT = N\frac{1}{2}\rho_\infty V_e^2 c(C_l cos\varphi - C_d sin\varphi)dr = N\frac{1}{2}\rho_\infty V_e^2 c\lambda_1 dr \tag{2.20}$$

$$dQ = N\frac{1}{2}\rho_\infty V_e^2 c(C_l sin\varphi + C_d cos\varphi)rdr = N\frac{1}{2}\rho_\infty V_e^2 c\lambda_2 rdr \tag{2.21}$$

Equating Eq. 2.20 and Eq. 2.12 for the thrust while Eq. 2.21 and 2.13 for torque, a system of two equations whose unknowns are a and a' is obtained (Eq. 2.22 and 2.23, where $\sigma = Nc/(2\pi r)$ is the so-called blade solidity).

$$\frac{a}{1+a} = \frac{\sigma\lambda_1}{2\,[1 - cos(2\varphi)]} \tag{2.22}$$

$$\frac{a'}{1-a'} = \frac{\sigma\lambda_2}{2sin(2\varphi)} \tag{2.23}$$

It is noteworthy that V_e is a function of a and a', and it can be expressed as a function of a and φ or a' and φ, where appropriate, to derive useful expressions to determine the propeller performance.

The vortex model of the actuator disk assumes an infinite number of blades, which leads to a nonzero disk loading at the tip. In reality, the value of the disk loading (or circulation) at the tip is zero because of the finite number of blades and there is also a contribution of radial velocity no longer negligible. The effect of the finite number of blades is called tip loss, because this leads to a reduction of the thrust contribution of the tip regions. To take account of this effect, Goldstein proposed his well-known mathematical formulation for the optimum propeller [20], while Prandtl proposed a more pratical solution to simply quantify the tip loss (for low values of the advance ratio, $J \rightarrow 0$), introducing the tip loss factor which nullifies the circulation at blade tip (Eq.

2.24, where $\lambda \approx \tan\varphi$, R the propeller radius).

$$F(r) = \frac{2}{\pi} cos^{-1}\left\{\exp\left[\frac{N}{2\lambda}\left(\frac{r-R}{R}\right)\right]\right\} \tag{2.24}$$

The tip loss factor is introduced in the expressions of thrust and torque of momentum theory (Eq. 2.25 and Eq. 2.26).

$$dT = 4\pi\rho_\infty V_\infty^2 \left[1 + a(r)\right] a(r) r F(r) dr \tag{2.25}$$

$$dQ = 4\pi\rho_\infty V_\infty \Omega \left[1 + a(r)\right] a'(r) r^3 F(r) dr \tag{2.26}$$

It is also possible to take account of the effect of propeller hub of radius, r_h: the blade sections near the hub don't give any contribution to the overall thrust and torque and for this reason it may be appropriate to integrate between r_h and R. Moreover, the hub generates a drag force which reduces the overall thrust.

2.1.2 High-lift propeller conceptual design

Patterson [9] proposed a new conceptual design method for high lift propellers. The effect of a propeller slipstream on a wing can be modeled from the effects of airfoils placed in non-uniform parallel velocity streams. A velocity profile like the one presented in Fig. 2.7 is a Joukowsky velocity profile, which is described by Eq. 2.27, where a defines the maximum velocity, d defines a characteristic width of the velocity increase and z_c specifies the height relative to the airfoil chord line where the maximum velocity occurs.

$$V(z) = V_\infty \left(1 + a e^{-(z-z_c)^2/d^2}\right) \tag{2.27}$$

Chow et al. [21] introduced the "non-uniformity parameter", a/d^2, to indicate how far a particular profile deviates from a uniform value. They also defined an "adjusted lift coefficient" expressed as Eq. 2.28, which decreases increasing the non-uniformity parameter (Fig. 2.8a).

$$\bar{C}_L = C_L \frac{V_\infty^2}{V_{max}^2} = \frac{C_L}{(1+a)^2} \tag{2.28}$$

From Fig. 2.8b it is possible to see that

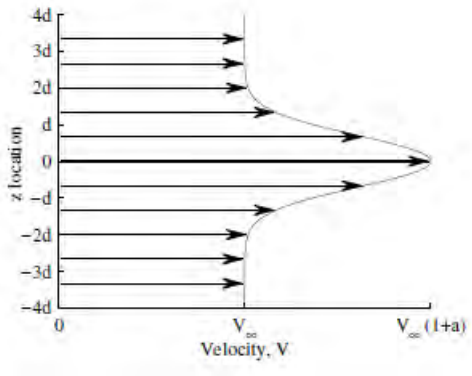

Figure 2.7: Generic Joukowski velocity profile with $z_c = 0$ [9]

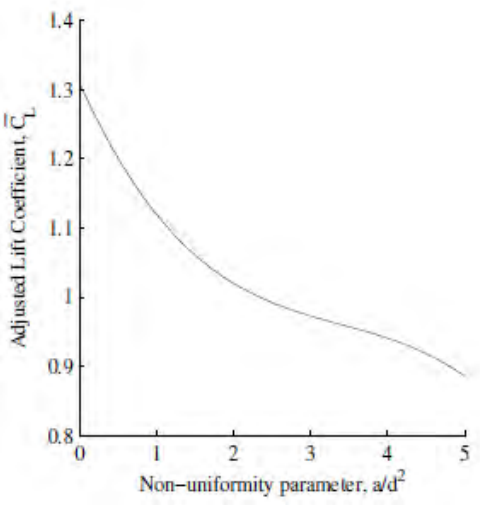

(a) Maximum adjusted lift coefficient (reproduced from Reference [21] in [9]

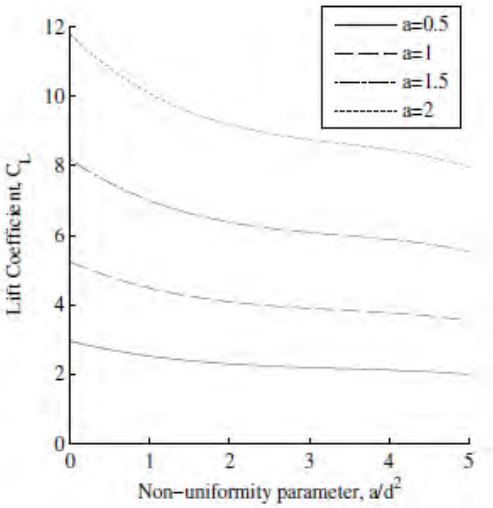

(b) Maximum lift coefficient for four velocity profiles with differing maximum velocities

Figure 2.8: Empirically determined maximum lift coefficient as a function of the non-uniformity in the upstream velocity profile based on Reference [21] (from [9])

- the higher the non-uniformity, the lower the airfoil lift coefficient,

- the higher the maximum velocity in the slipstream, the higher the airfoil lift coefficient,

- the higher the maximum velocity in the slipstream, the higher the impact of non-uniformity.

These observations imply that a well-designed high-lift propeller should produce a highly-uniform slipstream with a high maximum velocity. The high-lift propeller design method proposed by Patterson is based on this last statement and it is derived modifying the well-known blade element momentum theory (BEMT): the objective of the design is not to have the "minimum induced loss" in producing a specified thrust, but it is to provide a near-uniform axial velocity increase aft of the propeller (Fig. 2.9). The result of these new design approach is a blade with increased chord lengths and twists near the root and decreased chord lengths and twists near the middle of the blade (Fig. 2.10).

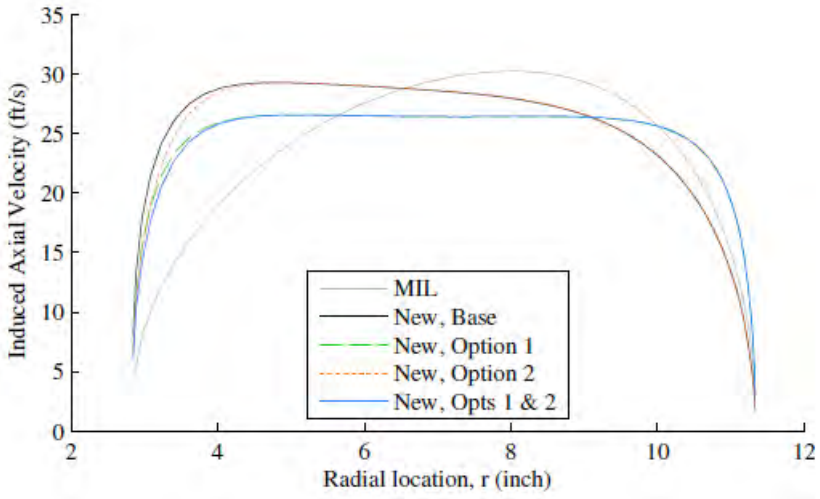

Figure 2.9: Predicted induced axial velocity distributions for five propellers designed to produce the same average induced axial velocity [9]

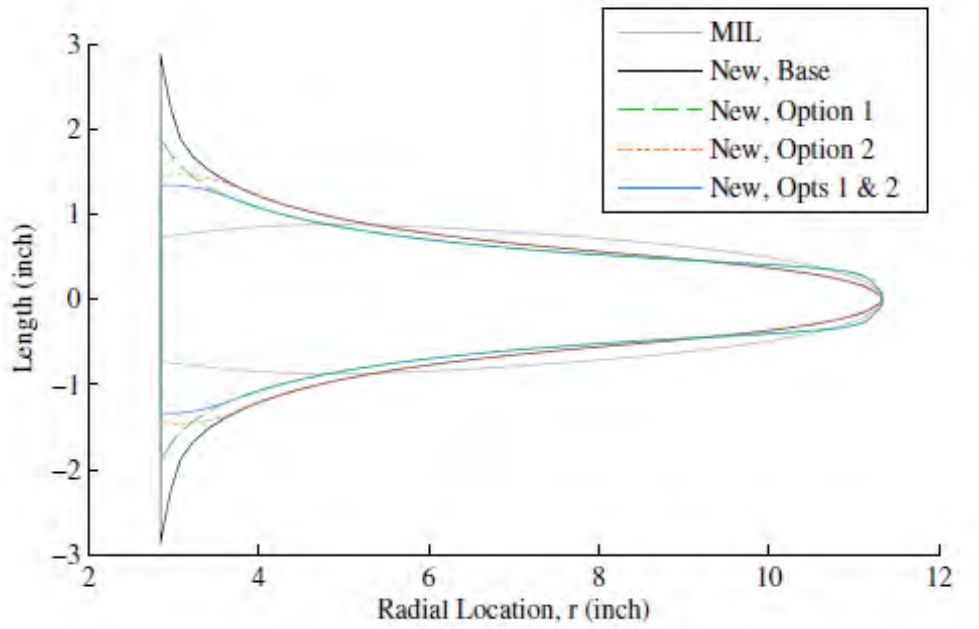

(a) Comparison of the chord lengths of the final blade designs for five propellers designed to produce the same average induced axial velocity [9]

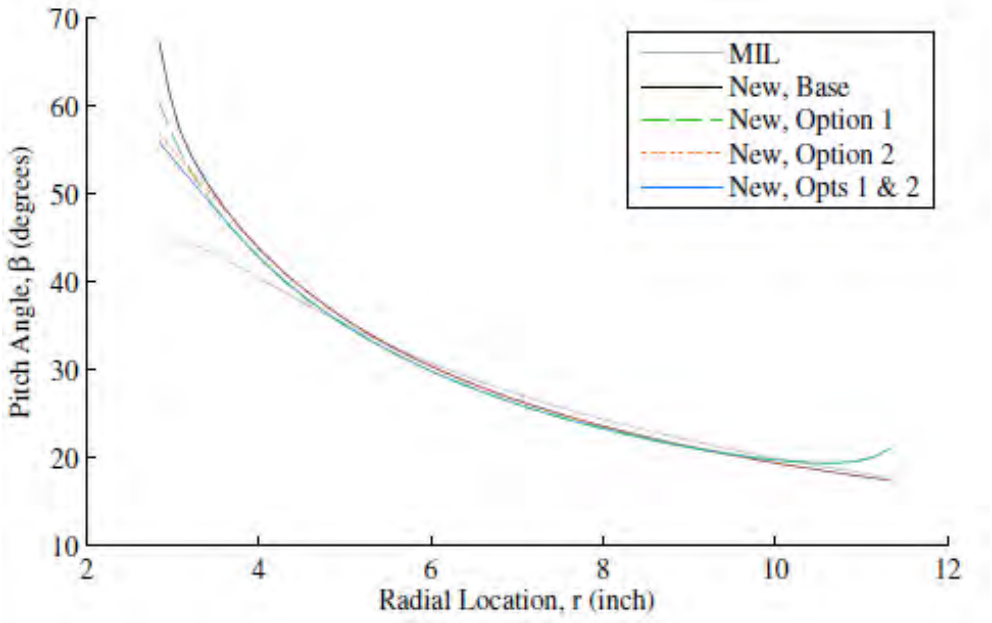

(b) Comparison of the twist distributions for the final blade designs for five propellers designed to produce the same average induced axial velocity [9]

Figure 2.10: Blades characteristics of the high-lift propeller designed with Patterson's method

2.2 Propeller wing aerodynamic interference

2.2.1 Wing effect on the propeller

The effect of the wing loading on the inflow field of a tractor propeller is similar to the impact of an incidence angle α_p on an uninstalled propeller [22], as represents Fig. 2.11, where $\Psi = 0°$ and $\Psi = 180°$ the position of the blade in the upper and lower position, while $\Psi = 90°$ and $\Psi = 270°$ refer to respectively the down-going and the up-going blade position. In this condition, the blade elements of the up-going blade experience a reduction of the angle of attack and dynamic pressure, which results in a load decrease; the down-going blade experience, instead, a load increase (see Fig. 2.12).

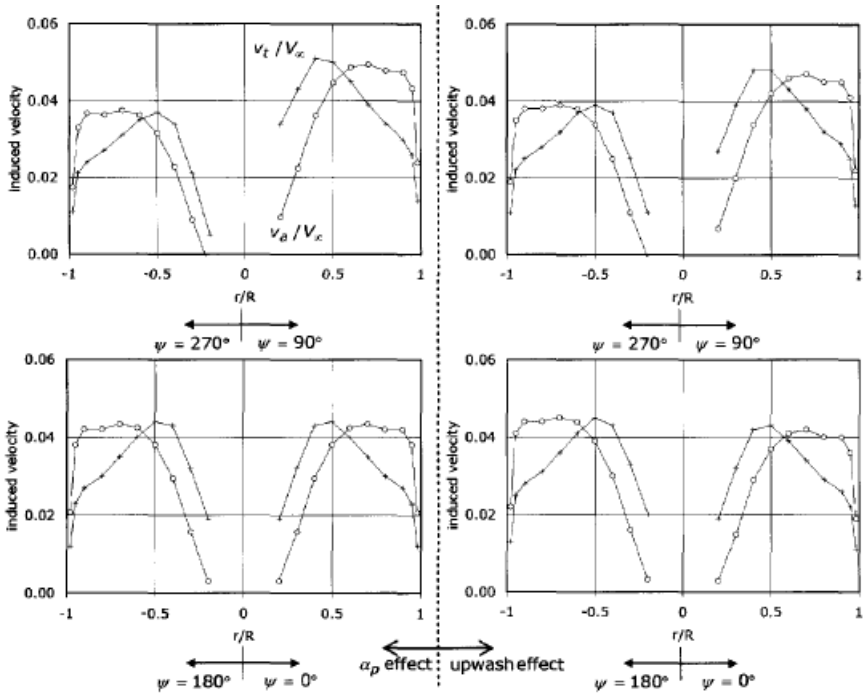

Figure 2.11: Local induced velocity in the propeller (survey) plane of a typical tractor propeller wing configuration. Left: uninstalled propeller at $\alpha_p = 1.5°$; Right: propeller in the upwash field of the wing at the same average effective propeller angle of attack (results obtained by performing a 2-dimensional panel code on a NACA64_2A015 airfoil with the propeller plane at $1R$ in front of the wing) [22]

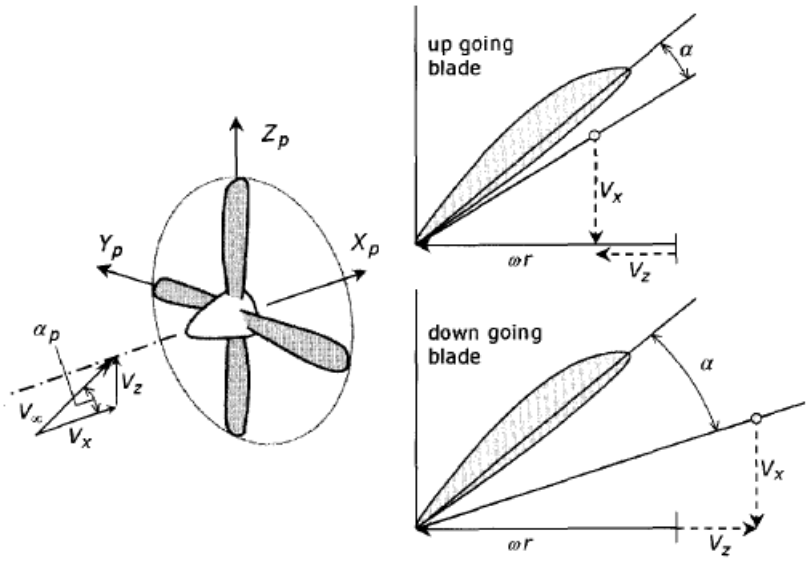

Figure 2.12: Blade angle of attack variation due to propeller pitch angle. For positive angles of attack, α_p, the down-going blade experiences a higher loading that the up-going blade [22]

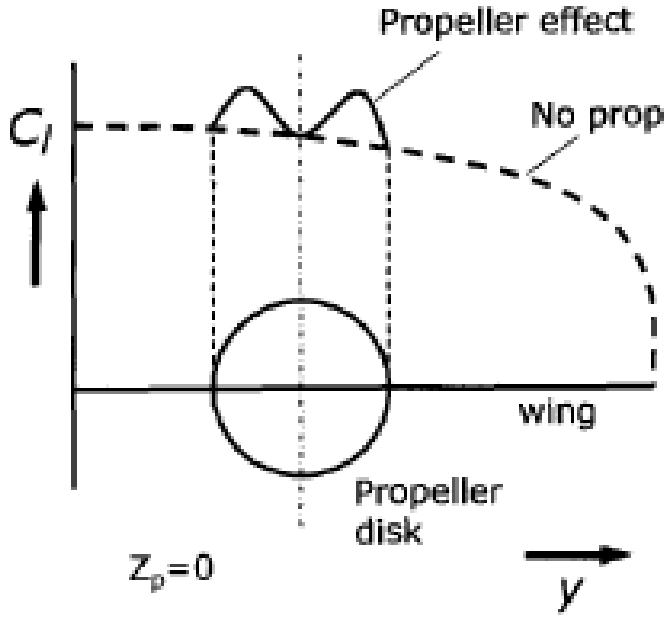

Figure 2.13: Change in local wing lift coefficient due to the axial velocity increase in the slipstream [22]

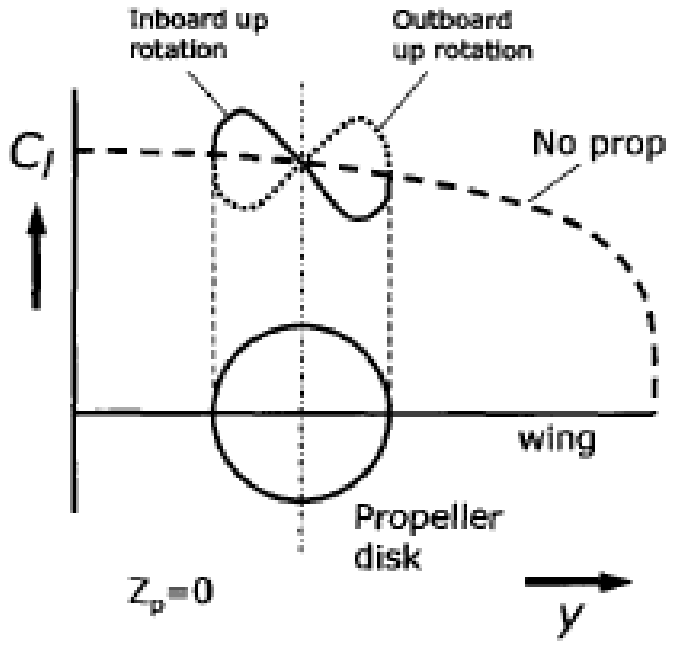

Figure 2.14: Change in local wing lift coefficient due to the swirl velocity increase in the slipstream [22]

2.2.2 Propeller slipstream effects on the wing

The slipstream of a propeller consists of a swirl and an axial velocity component as well as a pressure jump and when it impacts a portion of the wing surface, the wing coefficients (based on the undisturbed flow conditions) and the lift distribution are strongly modified. The axial velocity of the propeller has the effect to increase the dynamic pressure on the part of the wing invested by the propeller slipstream, increasing the local lift and drag coefficient. If the effect of wing upwash on the propeller is neglected, the axial velocity distribution is symmetrical with respect to the propeller thrust axis and the effect on the wing load is equal for both the inboard and outboard side of the nacelle, as represented in Fig. 2.13. The effect of the swirl velocity component is instead anti-symmetrical, because the up-going blade generates an increase in angle of attack on the wing while, conversely, the down-going blade causes a reduction of the angle of attack on the wing, with the resultant wing load represented in Fig. 2.14. The combined effect of axial and swirl velocity component on the wing load is represented in Fig. 2.15, and it is clearly understandable that the rotation direction of the propeller dominates the shape of the wing lift distribution. It is interesting to note that both

experimental and numerical studies have shown that wing reduces significantly the rotation of the slipstream (swirl recovery). The propeller position with respect to the wing is another important parameter which strongly affects the aerodynamic interaction. As can be seen from Fig. 2.16, wing can experience an angle of attack increase or decrease depending on a low or high propeller position. Moreover, also propeller thrust is influenced by the type of configuration (a high propeller position leads to a reduced thrust, while with a low propeller position the thrust is increased).

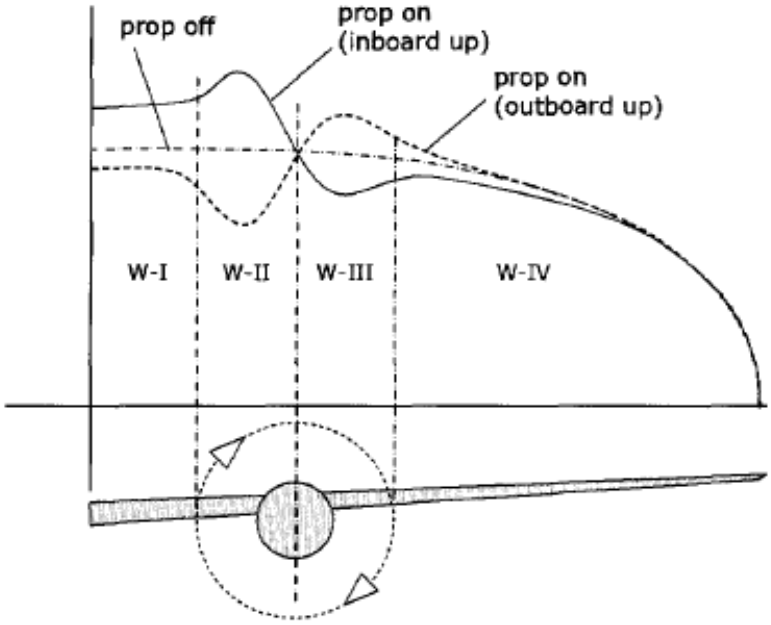

Figure 2.15: Lift distributions in wing regions affected by the combined effect of the axial and the tangential velocity component in the slipstream [22]

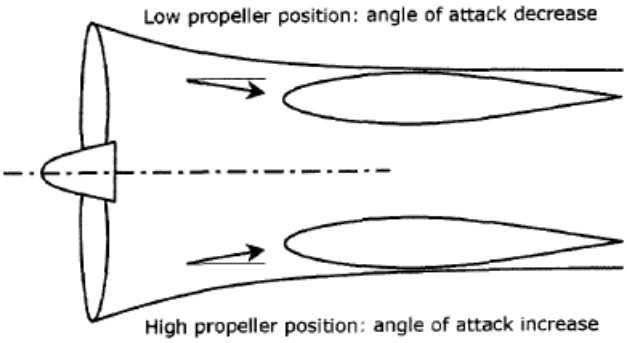

Figure 2.16: Local wing angle of attack effect for a high and low propeller position [22]

2.2.3 Numerical methods for propeller-wing configurations

Vortex Lattice Methods

Vortex Lattice Methods (VLM's) represent a powerful tool in conceptual airplane design because of their reduced computational time. A VLM is a combination between the approximate lifting line (and surface) theory and the Vortex Lumped Method, therefore its application is limited to linearized inviscid flows, based on a Neumann problem for Laplace equation, and to conditions in which there is neither separated flow nor normal shockwaves (inviscid sub- and supersonic flow fields) [23]. The lifting surfaces are modeled as infinitely thin sheets: a wing can be approximated through its planform (but, more efficiently, also through its mean surface). The chosen simplified geometry is then divided into a lattice of quadrilateral panels, and a horseshoe vortex is put on each panel. The bound vortex of the horseshoe vortex (whose intensity is unknown) is put on the 1/4 chord element line of each panel, while the trailing vortices are disposed parallel to the direction of the free stream, or parallel to the wing stream-wise axis. The boundary condition is imposed on the control point placed at 3/4 chord point of each panel: this is an arbitrary imposition based on the Vortex Lumped Method (strictly valid for 2-dimensional flow fields), without a rigorous theoretical foundation. Then the method involves the calculation of the velocities induced by each vortex on the vortex point (1/4 chord point), to determine the downwash on the bound vortex, and on the control point of each panel, where only the normal component of the induced velocity is important. In this way the construction of the influence matrices is performed and the unknown intensities of the bound vortices can be computed. The velocity induced by $2N$ horseshoe vortices at the control point m is expressed as Eq. 2.29, where $C_{m,n}$ is the influece matrix [22].

$$V_m = \sum_{n=1}^{2N} V_{m,n} = \sum_{n=1}^{2N} C_{m,n}\,\Gamma_n \tag{2.29}$$

The Kutta–Joukowski theorem is used to calculate the aerodynamic force acting on the 1/4 chord point. This force is perpendicular to the effective velocity in that point, which is a composition between the free stream velocity and the downwash induced by each vortex. The total aerodynamic force acting on the overall surface is the sum of the forces acting on each panel. To model the propeller effect in a VLM, an additional velocity vector, $\underline{V}_p$, induced by the slipstream, must be considered on the control point.

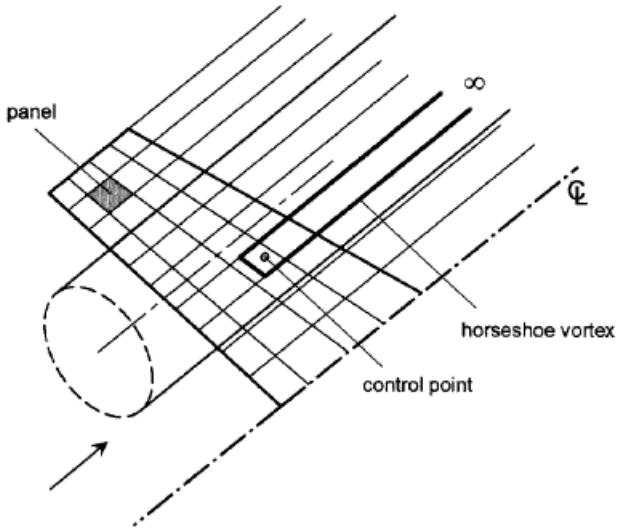

Figure 2.17: VLM-layout representing the lifting wing behind a propeller. The horseshoe vortex of one panel only was sketched [22]

The single interaction mode (SIM) considers only the propeller effect on the wing, while the fully interaction mode (FIM) includes the wing effect on the propeller as well. Including the propeller slipstream effect, the total inflow velocity vector is composed by the contribution of the free stream, the induced velocity and the additional velocity, Eq. 2.30.

$$\underline{V}_{tot} = \underline{V}_{\infty} + \underline{V}_{m} + \underline{V}_{p} \tag{2.30}$$

The velocity contribution of the propeller slipstream must be also considered on the lattice elements outside the slipstream tube since the local flow angles outside the slipstream are changed by the contraction of the slipstream tube [22]. A schematic representation of the geometry and the location of the horseshoe vortices is depicted in Fig. 2.17. Some analysis presented later in this thesis are performed with VSPAERO, a vortex lattice analysis solver included in the open source software OpenVSP.

Panel Methods

VLM's don't include the thickness effect, using a planar representation of the original geometry. To overcome this limitation, a panel method can be used. With a panel method, the analysed surface is covered with a singularity distribution: for example, source elements can be used to simulate the effect of thickness, while doublets or

vortices can be used for lifting problems. Different approaches can be followed to model the propeller effect (SMI or FMI, time averaged or unsteady analysis). The application of a panel method is limited to an inviscid, irrotational flow, with some exceptions. Indeed, wakes modeled as infinitesimally thin vortex sheets and compressibility effects excluding shocks can be taken into account.

2.3 Virtual Disk Models in STAR-CCM+

The unstructured cell-centered finite-volume-based solver STAR- CCM+ provides some tools to model the effect of a propeller in a steady RANS simulation. These models are based on the blade element momentum theory and they are called Virtual Disk Models, because the real geometry of the propeller is not inserted in the fluid domain: instead the propeller is modeled as a thin disk. There are two Virtual Disk Models of interest:

- the Body Force Propeller Method (BFPM),
- the Blade Element Method (BEM).

2.3.1 Body Force Propeller Method

The Body Force Propeller Method [24] simulates the effects of a marine propeller. However, this model can be also used for a propeller with aeronautics applications. This method has been implemented to model the flow field interaction of the hull of a ship and the propeller, with a fully interaction mode. In this way, a propeller-wing interaction can be simulated to capture the main effects on the aerodynamic coefficients. The firs step of the method is to define a virtual disk, specifying its position, the direction of the thrust and the rotation direction. Then, a table containing the propeller performance curve as thrust coefficient, torque coefficient and efficiency for different values of J is provided to the solver that, according to the specified operating point (basically thrust or rotational speed), calculates the axial and tangential forces of the modeled propeller and its effect on the flow, using the Goldstein optimum theory. To determine the advance ratio J, the method requires the setting of the inflow specification of the virtual disk. Among the several option, the inflow velocity plane can be chosen: this plane is located upstream of the virtual disk and is always oriented respect to the direction of the virtual disk normal. The velocity components and the density of the fluid approaching the virtual disk are

volume-averaged over the inflow velocity plane. The averaged velocity components are then projected onto the normal plane of the virtual disk to yield one average velocity vector value. Moreover, in the application of this method, some meshing requirements in the region interested by the disk must be observed.

2.3.2 Blade Element Method

The Blade Element Method [24] is primarily designed to analyze the complex flow field that is associated with helicopter rotors. The blade element method models the spinning rotor as a distribution of momentum sources. The strength of the source terms and their variations are interactively determined from the rotor geometry and the local velocity field. The number and the geometry of the blades in terms of chord and twist variation along the rotor radius are specified. The blade geometry is not explicitly resolved. The influence of the blade geometry on the flow field is described by the aerodynamic behavior of the blade in terms of lift and drag coefficients that are obtained for the corresponding two-dimensional cross-section of the blade. The aerodynamic characteristic of a blade can vary along the radius for an unlimited number of airfoil cross-sections.

2.4 Wind tunnel tests

The wind tunnel tests are of course another possible method to apply for analysing a complex phenomenon like the propeller-wing interaction. Generally, an experimental program starts from the design and the production of the test model, a process that involves the expertise of different professionals. Several instruments are needed to keep track of the variables of interest during the tests. Among others:

- balances to measure forces and moments;
- temperature sensors;
- inclinometers to measure the angle of attack;
- RPM counters (if rotating elements are present);
- pressure transducers;

- acquisition system and control units.

In some cases particular techniques such as Particle Image Velocimetry (PIV) or flow visualization can be used to capture some effects in detail.

This thesis is based on an experimental program that will be done at the University of Naples "Federico II". At time of this writing, the model is under analysis in the wind tunnel of Dept. of Industrial Engineering. Some details of the test model and the results of the numerical analyses performed in preparation of the experimental tests are presented in the following chapter.

Chapter 3

Numerical Analyses

The purpose of this thesis is to perform some preliminary numerical analysis of the test model designed for the PROSIB (PROpulsione e Sistemi IBridi per velivoli ad ala fissa e rotante) research project, which consists of some wind tunnel tests that will be done at the University of Naples "Federico II" (UNINA), to investigate the aerodynamic effects of DEP. In this chapter, a description of the model and its design is made, then the results of the numerical analyses are presented.

3.1 The test model

The test model is a simple rectangular wing (which will be realized in outsourcing with CNC milling in Al 2024-O) with a single slotted flap and the aim of the tests is to determine the aerodynamic effects of distributed electric propulsion on this type of wing. In particular, there are three "high lift propellers" designed with the Patterson's method, described in chapter 1, positioned in front of the wing, in correspondence of the zone covered by the flap. These three propellers can be mounted in three different positions along the chordwise direction, X, and in four different positions along the direction perpendicular to the wing planform, Z (see Tab. 3.6 and 3.7). Moreover, there is a tip-mounted tractor propeller designed with the classical method of the minimum induced loss. The scheme of the installed wing model is presented in Fig. 3.1. The wing geometry is defined in Tab. 3.1.

The subsonic wind tunnel of the Department of Industrial Engineering of the University of Naples "Federico II" is a closed circuit, closed test section tunnel, whose characteristics are reported in Tab. 3.2. For the forces measurements, an external strain

gauge balance is used, whose characteristics are presented in Tab. 3.3. It comprises five load cells (Fig. 3.3a), the values of which will be combined to provide moment and force components (lift and drag). The model is held on the balance and an electric motor, installed above the balance system (Fig. 3.3b, is used to control the wing angle of attack.

Three lines of pressure taps for about 100 channels is provided. Spanwise locations of these lines are shown in Fig. 3.1 as dotted lines in the top view, while the positions of the several pressure taps on a section of the main component are represented in Fig. 3.2. The pressure taps are connected by small tubes to a miniaturized electronic pressure measurement system (Scanivalve ZOC33, Libery Lake, Washington State) with a full-scale range of 25.4 cm (10 $in.$) of H_2O (about 2.5 KPa) and an accuracy of ±0.15% (±3.75 Pa).

Wing span, b_w	2.8 m
Root chord, c_r	0.4 m
Taper ratio, λ_w	1
Mean aerodynamic chord, $\bar{c}$	0.4 m
Wing area, S_w	1.12 m^2
Aspect ratio, $\mathcal{AR}$	7
Flap chord ratio, c_f/c	0.3
Inner flap position, y_{in}	0.2 m
Outer flap position, y_{out}	1.1 m

Table 3.1: Geometrical characteristics of the analysed wing model

The wing airfoil is the NASA/LANGLEY LS(1)-0417 (GA(W)-1), also considered by NASA for the development of a low drag airfoil for the X-57 cruise conditions with high maximum lift coefficient [25]. A CFD analysis with STAR-CCM+ on the airfoil with a single slotted flap was performed at UNINA, with a mesh convergence study based on the Grid Sensitivity Index (GCI) method (see Fig. 3.4). The fine mesh was composed of 320 thousands of polygonal cells, Fig. 3.5. A flap position exploration study (in terms of gap and overlap, Fig. 3.6) was performed to design the best flap position, chosen as a compromise between performance at takeoff (15°) and landing (30°), Fig. 3.7. The values of gap and overlap for each flap deflection are presented in Tab. 3.4. The results for different flap deflections are presented in Fig. 3.8.

After the airfoil study, the first predictions on the wing lift curve were performed with a semi-empirical approach, Fig. 3.9. The design of the wing model was performed

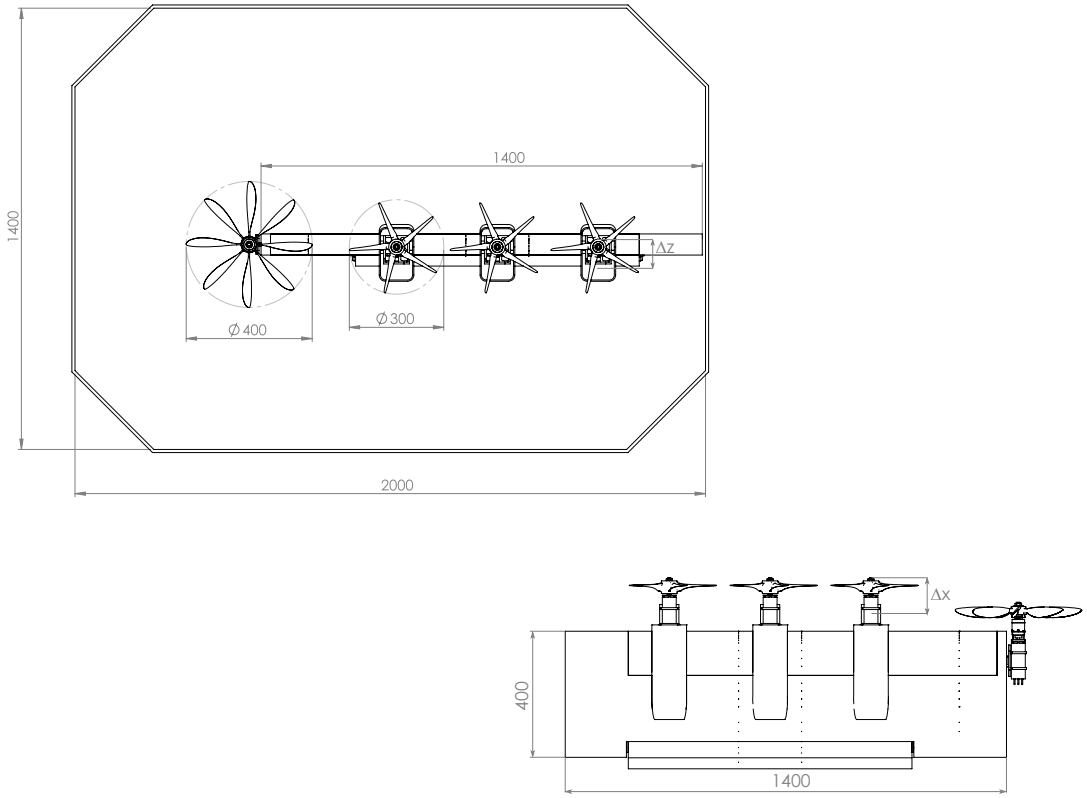

Figure 3.1: Drawing of the installed wing semi-model

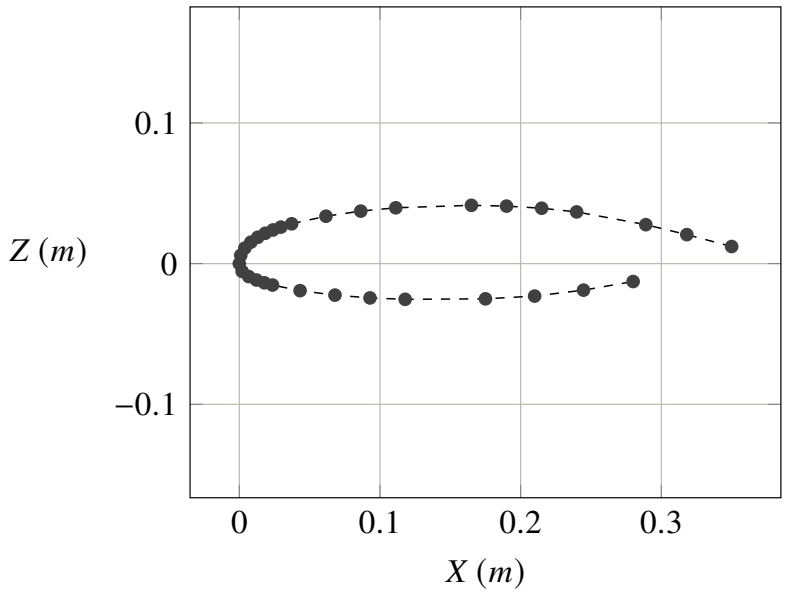

Figure 3.2: Positions of pressure taps on a section of the main component of the wing model (other five pressure taps will be provided on the flap)

Item	Value
Tunnel type	closed circuit - closed test section
Test section	$2.0\,m \times 1.4\,m \times 4.0\,m$ (width × height × depth)
Test section frontal area	$3.68\,m^2$
Max power	$150\,kW$
Max flow speed	$45\,m/s$
Turbulence intensity	0.1%
Temperature range	$10 - 50°C$
Reynolds number	0.5 – 2.0 million (according to model size)
Dynamic pressure range	$15 - 1200\,Pa$
Max stagnation pressure	$104700\,Pa$ (ambient + dynamic)

Table 3.2: Wind tunnel characteristics

Component	Range		Accuracy
	Min	Max	
Normal force (Lift)	$-80\ Kgf$	$100\ Kgf$	$0.030\ Kgf$
Horizontal force (Drag)	$-12\ Kgf$	$12\ Kgf$	$0.005\ Kgf$
Pitching moment	$-15\ Kgf \cdot m$	$15\ Kgf \cdot m$	$0.010\ Kgf \cdot m$
Bending moment	$-40\ Kgf \cdot m$	$60\ Kgf \cdot m$	$0.030\ Kgf \cdot m$
Yawing moment	$-8\ Kgf \cdot m$	$8\ Kgf \cdot m$	$0.06\ Kgf \cdot m$

Table 3.3: Wind tunnel balance characteristics

δ_f	Gap	Overlap
15°	0.79 %	−11.7 %
30°	1.89 %	−5.6 %

Table 3.4: Flap position assignment - Values of gap and overlap

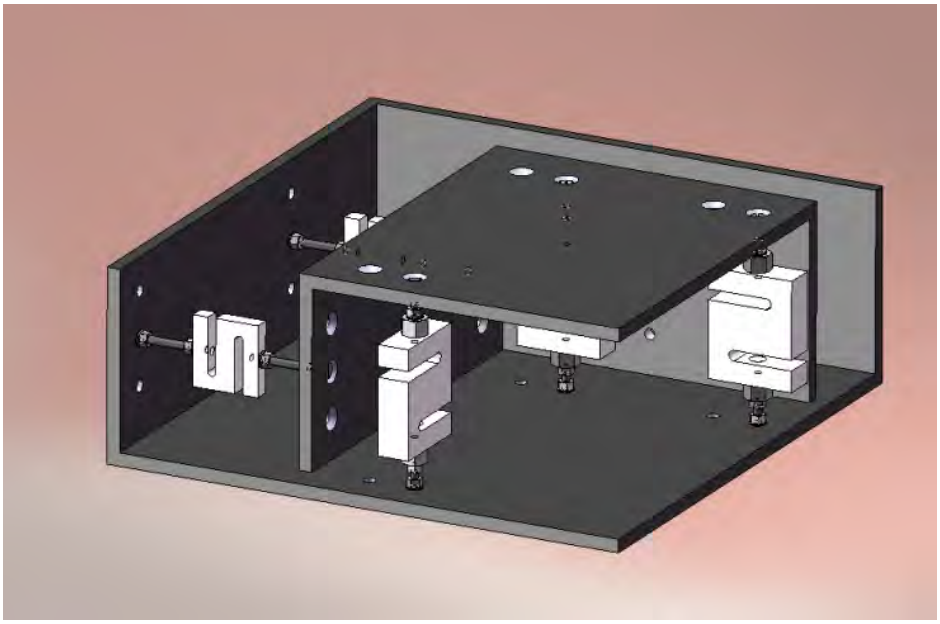

(a) The wind tunnel balance

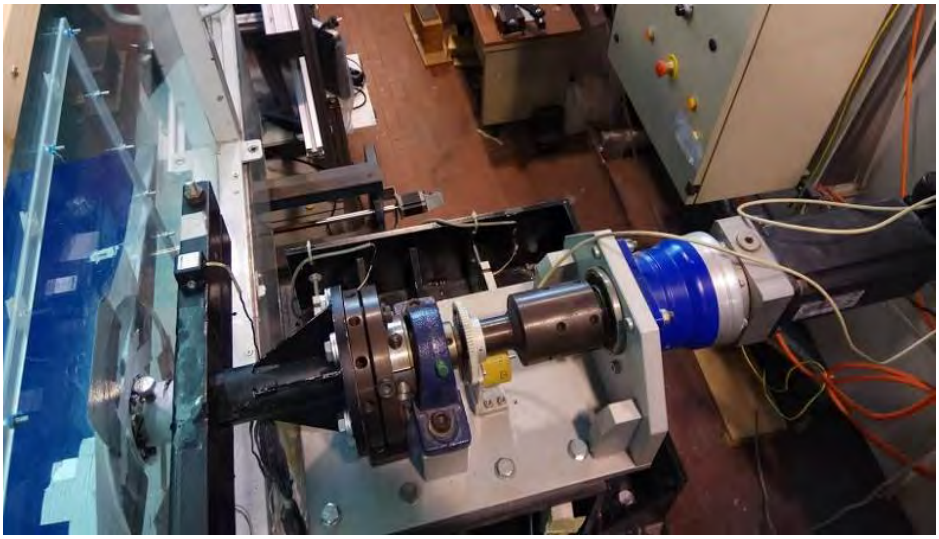

(b) The electric motor above the wind tunnel balance

Figure 3.3: The wind tunnel balance for the measurements

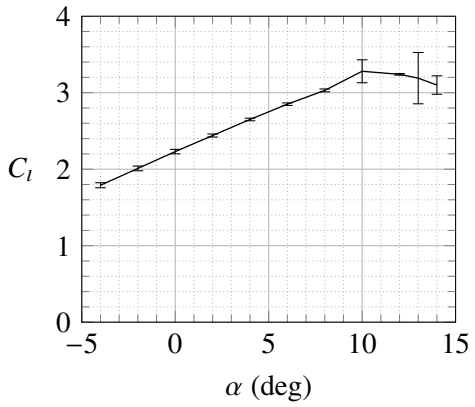

(a) Lift coefficient

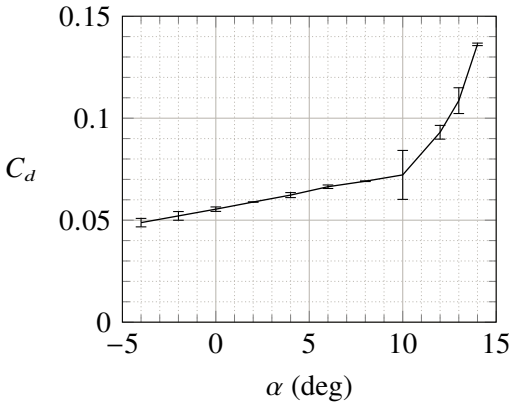

(b) Drag coefficient

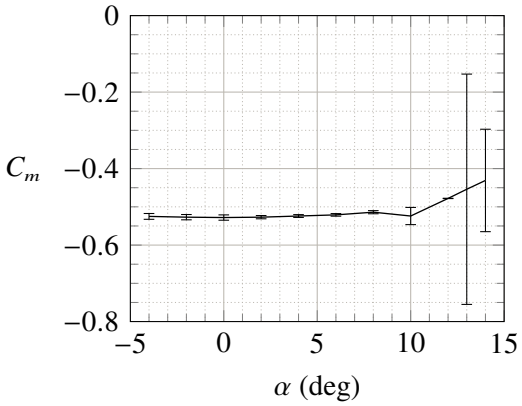

(c) Pitching moment coefficient

Figure 3.4: Fine grid solution of airfoil mesh convergence study with GCI error bar - $\delta_f = 35°$ - $Re_\infty = 5.3 \cdot 10^5$ - STAR-CCM+

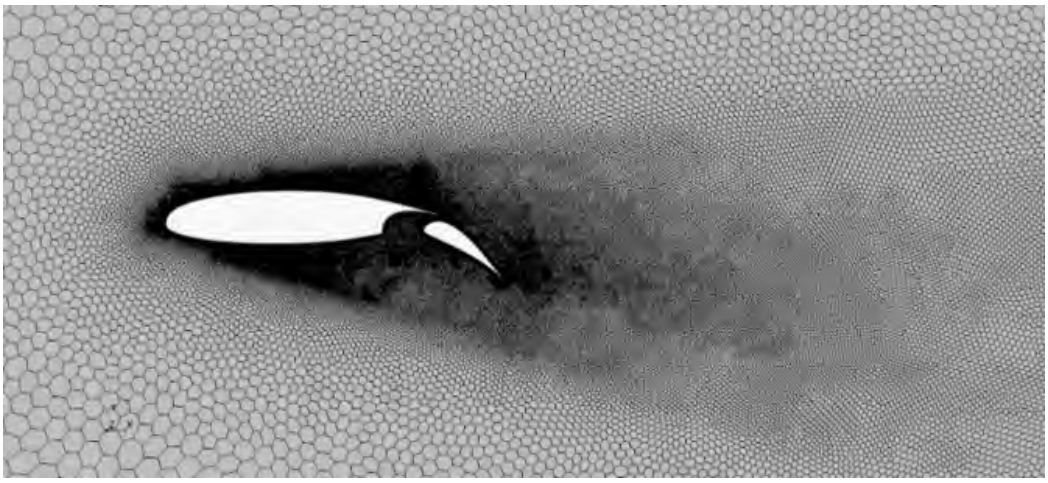

Figure 3.5: Fine mesh for flapped GA(W)-1 airfoil CFD analysis - STAR-CCM+

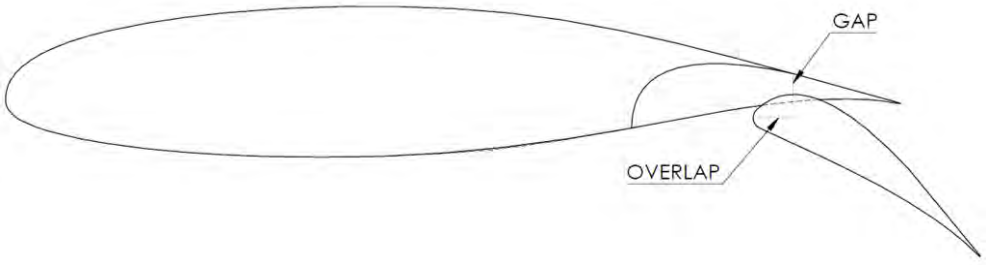

Figure 3.6: Representation of gap and overlap for the GA(W)-1 airfoil

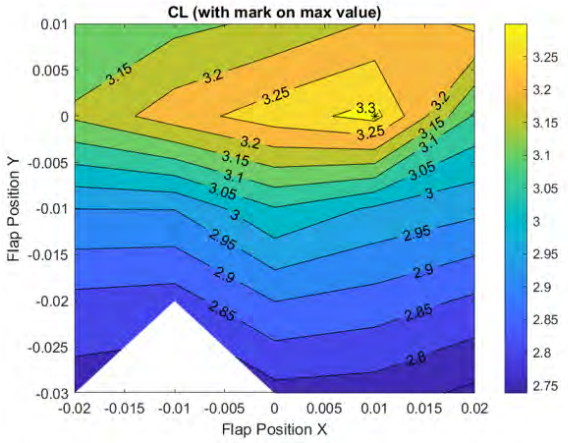

(a) Lift coefficient

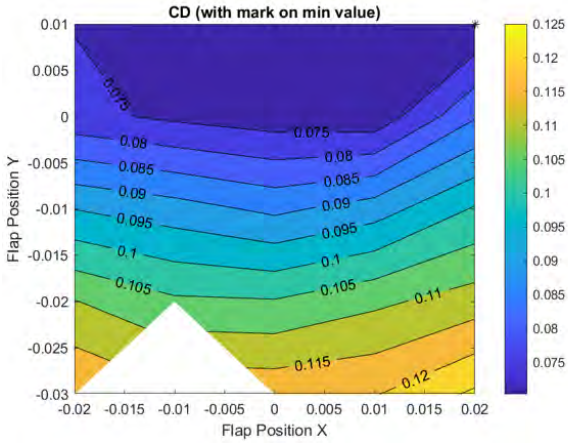

(b) Drag coefficient

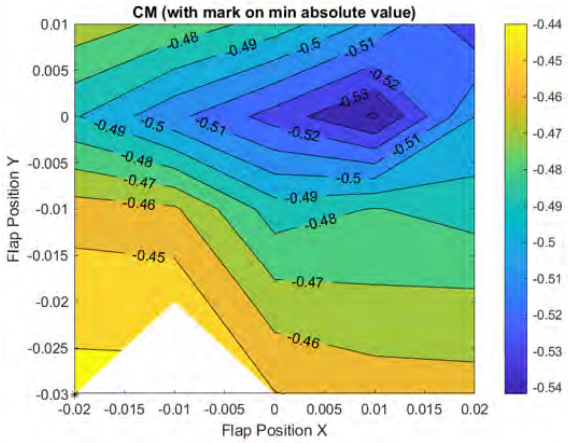

(c) Pitching moment coefficient

Figure 3.7: Results of the flap position exploration study - $Re_\infty = 5.3 \cdot 10^5$ - STAR-CCM+

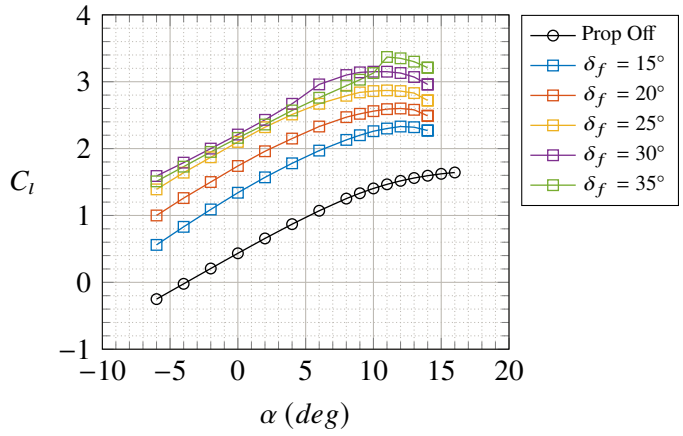

(a) Lift coefficient

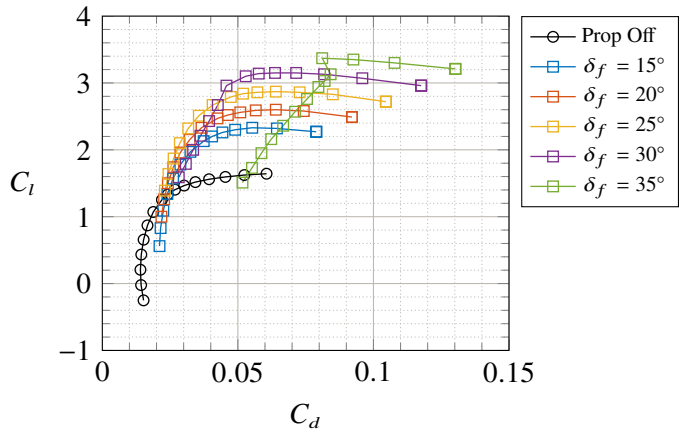

(b) Drag coefficient

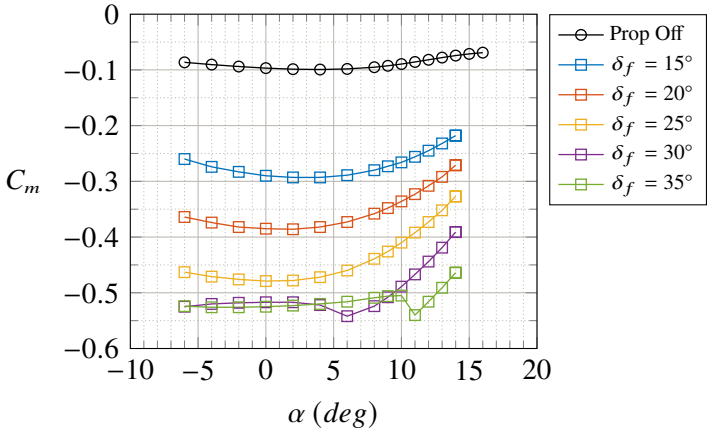

(c) Pitching moment coefficient

Figure 3.8: GA(W)-1 airfoil CFD analysis for different flap deflections - $Re_\infty = 5.3 \cdot 10^5$ - STAR-CCM+

with a CAD software. Some details of the drawing are represented in Fig 3.10. The

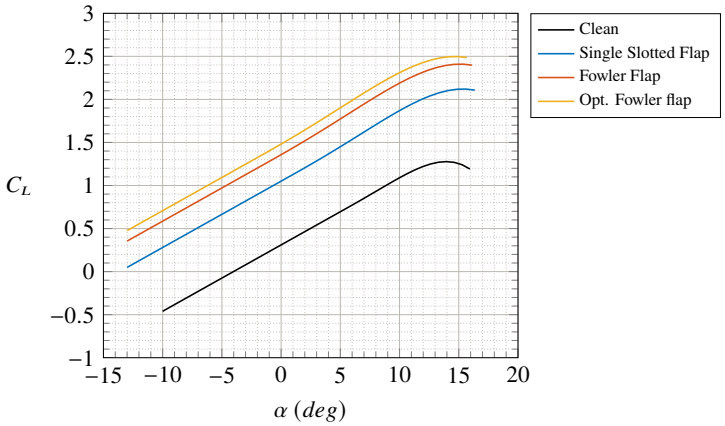

Figure 3.9: Wing lift curves with semi-empirical approach for a flap deflection of 35° - $Re_\infty = 5.3 \cdot 10^5$

design of DEP propellers, as mentioned above, was performed following the design approach for "high lift propellers" proposed by Patterson [9]. One of the most important parameters to achieve significant blowing effects is the diameter to chord ratio, D/c, which should be of unit order. However, such a value is difficult to reach for these tests and it was fixed to 0.75. These type of propellers are expected to operate in takeoff, landing and/or climb conditions, with an operating point corresponding to an advance ratio $J < 1$. Fig. 3.14a represents the CAD model of the DEP propeller.

	$Y\ (m)$	$\eta = 2Y/b$
Dep 1 Y-Position	0.330	0.236
Dep 2 Y-Position	0.650	0.464
Dep 3 Y-Position	0.970	0.693

Table 3.5: Y-Position of the DEP propellers - Each propeller is fixed along the spanwise direction

DEP Position	$X\ (m)$	$\Delta X/\bar{c}$
First X-Position, xA	$-0.2\,\bar{c}$	−0.10
Second X-Position, xC	$-0.3\,\bar{c}$	0
Third X-Position, xF	$-0.4\,\bar{c}$	0.10

Table 3.6: X-Positions of the DEP propellers - The reference position for the quantity $\Delta X/\bar{c}$ is the Second X-Position

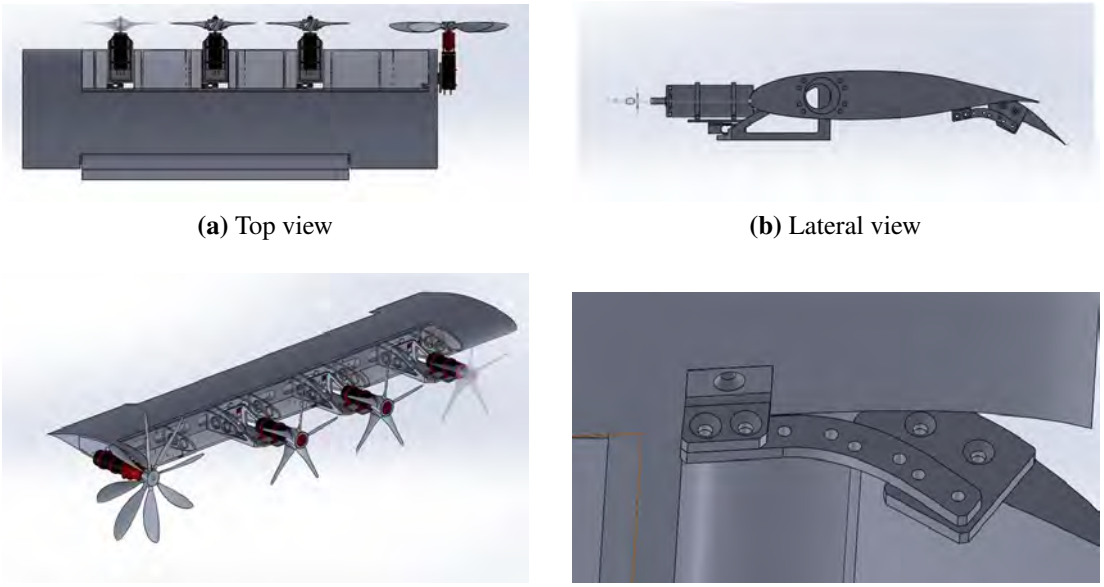

(a) Top view

(b) Lateral view

(c) Isometric view

(d) Detail of the flap connection

Figure 3.10: CAD drawing of the wing model

DEP Position	$Z\ (m)$	$\Delta Z/\bar{c}$
First Z-Position, zU	$0.05\,\bar{c}$	0.05
Second Z-Position, zC	0	0
Third Z-Position, zD	$-0.05\,\bar{c}$	−0.05
Fourth Z-Position, zDD	$-0.1\,\bar{c}$	−0.10

Table 3.7: Z-Positions of the DEP propellers

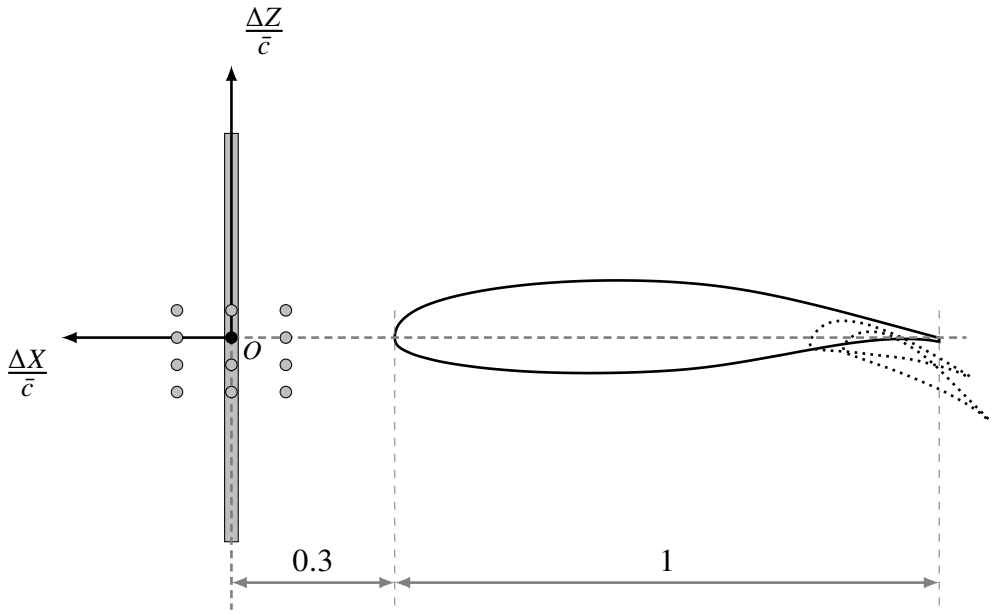

Figure 3.11: Sketch of dimensionless disks positions with respect to the wing leading edge

Regarding the tip propeller, it has been designed with the classical method, with a diameter to chord ratio equal to 1, considering as reference the thrust coefficient of typical propellers for 10 pax, 19 pax and 40 pax aircraft. In this case, the operating point corresponds to an advance ratio $J > 1$, given that the tip propeller is expected to work in cruise and in climb. The CAD model of the tip propeller is presented in FIg. 3.14b. The propeller performance calculated in XROTOR are presented in Fig. 3.12a and 3.12b. The propellers will be powered by the electric motor Lehner 2280/40 LK (Fig. 3.14c), which is an air-cooled, inrunner motor, whose data are represented in Fig. 3.16, with the DEP propeller operating at $20\,m/s$. Each motor will work providing the maximum torque at 8000 RPM and a couple of motors will be powered by a single power supply (Aim TTi QPX1200S by THURLBY THANDAR INSTRUMENTS, Fig. 3.13). The DEP propellers will be directly connected to the electric motors, while the TIP propeller, working at a lower value of RPM, will need a gear box (4:1), Fig. 3.14d. Each motor will be linked to the wing structure through two axial load cells, one measuring the force component parallel to the propeller plane and another measuring the force component perpendicular to the propeller plane. Fig. 3.15 represents the structure supporting the motors, with the several holes corresponding to the different positions in which the DEP propelles will be mounted in turn.

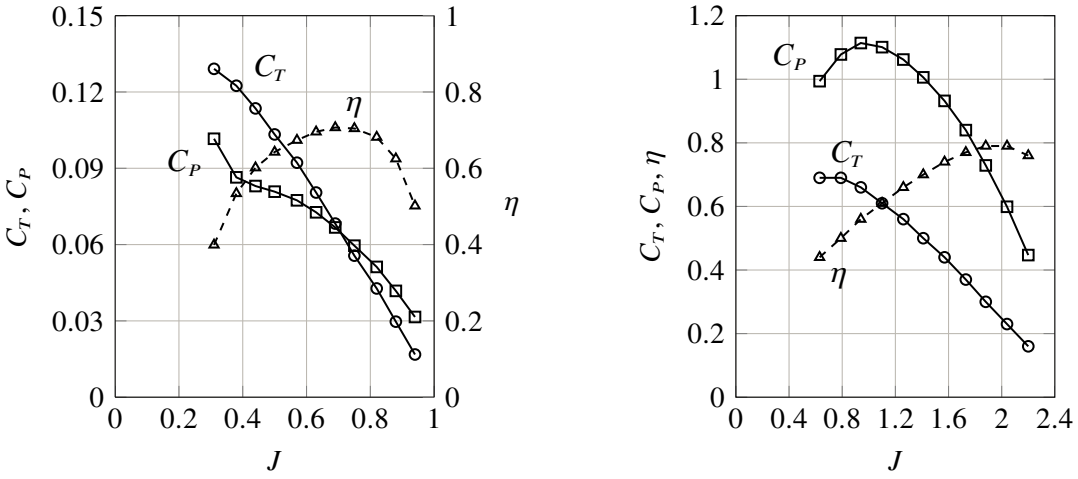

(a) DEP propeller **(b)** TIP propeller

Figure 3.12: Characteristic curves of the propellers (XROTOR)

Figure 3.13: Power supply Aim TTi QPX1200S

(a) DEP propeller CAD model

(b) Tip propeller CAD model

(c) Electric motor Lehner 2280/40 LK

(d) Electric motor Lehner 2280/40 LK with Neugart PLE 40 gear box (4:1)

Figure 3.14: Propellers CAD model with motors

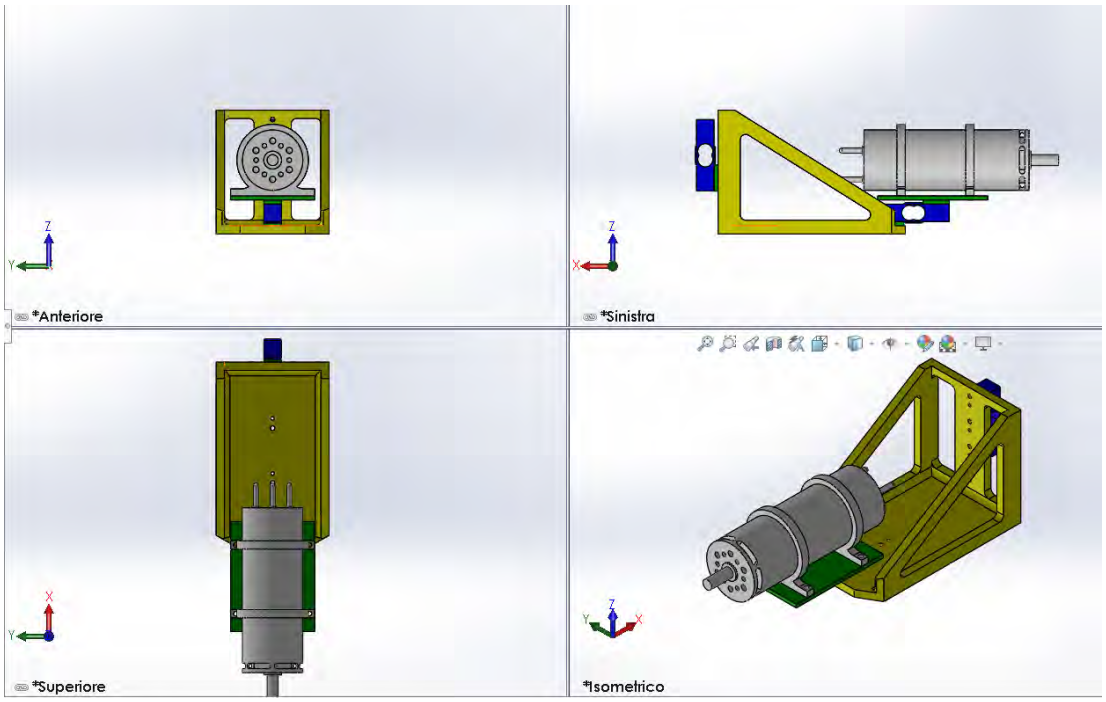

(a) Engine frame representation

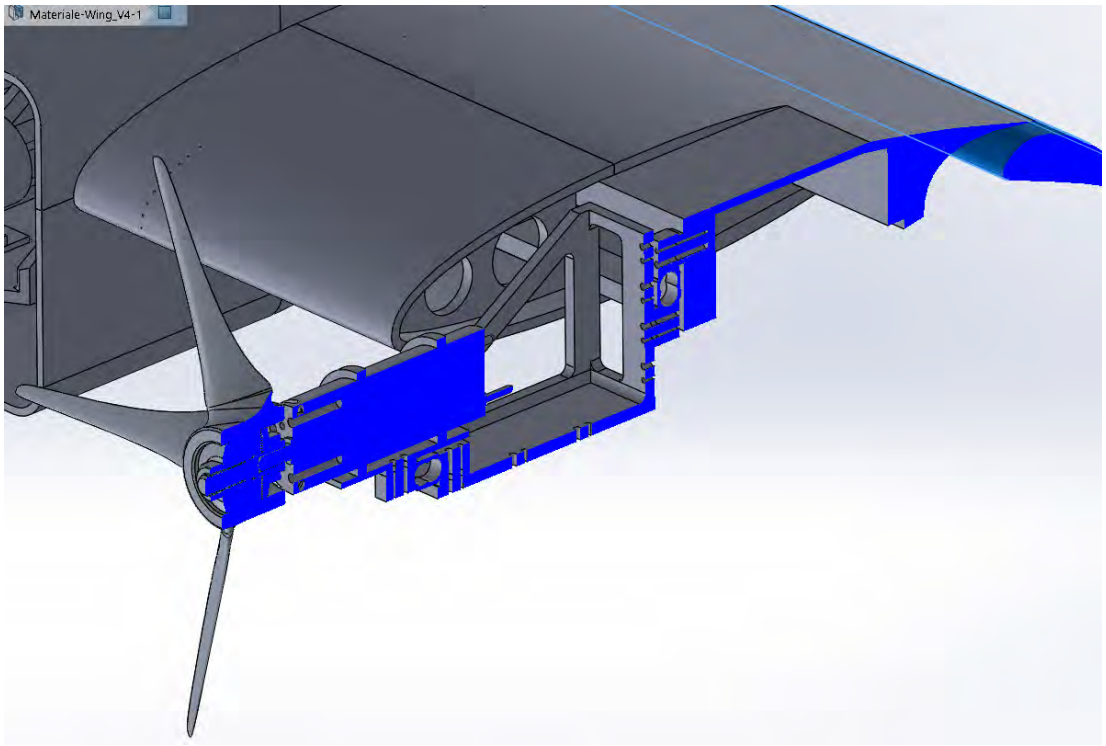

(b) Engine mount on wing section

Figure 3.15: Details of the engine mount

Fig. 3.17 represents the scheme of data acquisition and control for one motor. The light blue block named ESC represents the control unit with which is possible to set the motor RPM. As explained before, each motor will be linked to two load cells; a temperature sensor will be provided to keep track of the temperature of the motors, along with an RPM counter to measure the propellers RPM. Each signal coming from the sensors will be sent to the hardware of the acquisition system, which consists of the multi-function I/O device USB-6343 by National Instruments.

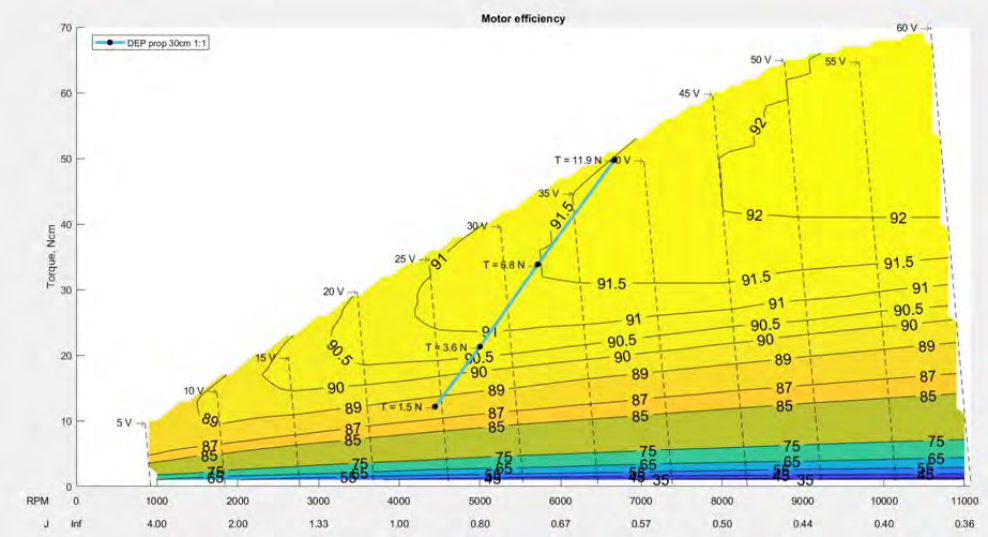

Figure 3.16: Lehner 2280/40 LK motor map

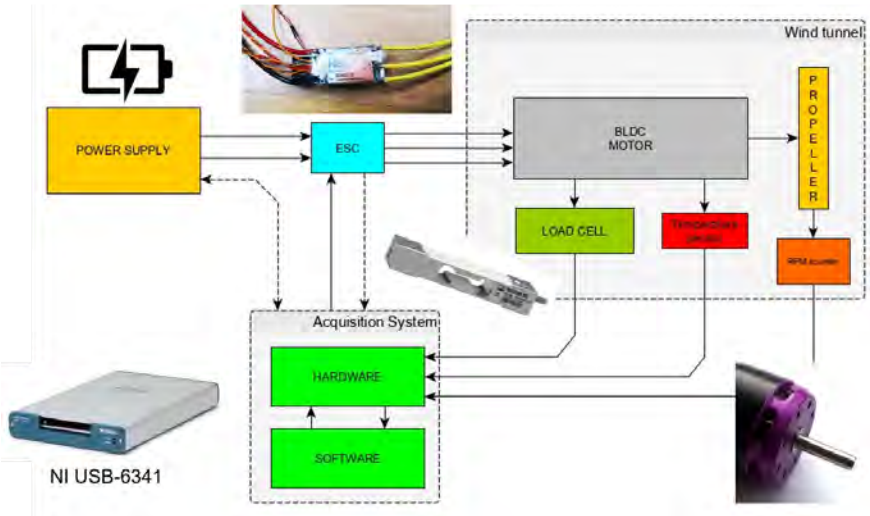

Figure 3.17: Data acquisition and control scheme

3.2 Vortex Lattice analysis

In this section, the results of the analysis based on a VLM performed with the software VSPAERO are presented. The vortex lattice is obtained from the geometry created in OpenVSP, presented in Fig.3.18. The reference conditions for all the simulations are presented in Tab. 3.8.

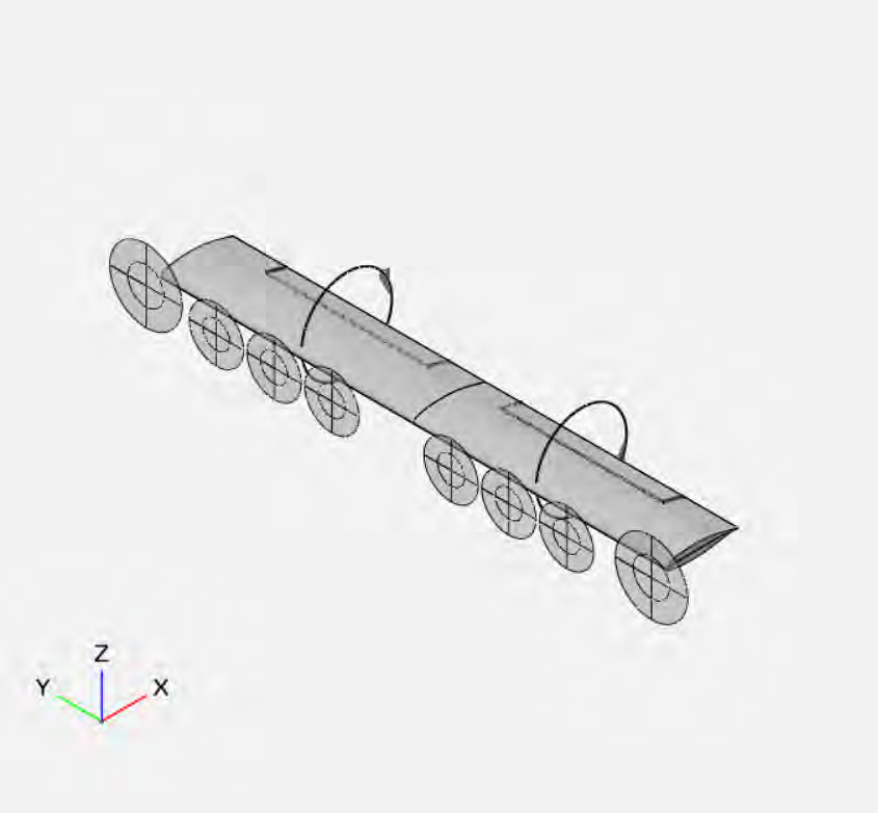

Figure 3.18: The model created in OpenVSP

Mach Number, M_∞	0.059
Reynolds Number, Re_∞	$5.48 \cdot 10^5$
Free stream velocity, V_∞	$20\,m/s$

Table 3.8: Reference conditions for the analysis

3.2.1 Selection of the number of panels

A wing analysed with a VLM needs a small number of panels to determine the aerodynamic coefficients and the load distribution with a certain accuracy; tipically 25 panels in the chordwise direction and 15 panels in the spanwise direction give satisfactory results. However, in this case, because of the effect of the propellers, it could require a larger number of panels. To select a reasonable number of panels, some analysis varying the number of the tessellation parameters in OpenVSP were performed. The software gives the possibility to change the tessellation both in the spanwise and in the chordwise direction. With Num_W is indicated the number of tessellated curves in the chordwise direction, with Num_U in the spanwise one. In Fig. 3.19 is represented how the value of the lift coefficient C_L at $\alpha = 0°$ varies in percentage changing the values of Num_U and Num_W, respect to the value obtained with the max values of Num_U and Num_W. The values of the contour lines in Fig. 3.19 are calucated as Eq. 3.1, where $C_L^{i,j}$ is the generic value of the lift coefficient computed with a certain couple (Num_U, Num_W) and C_L^{max} is the value computed with the max values chosen for Num_U and Num_W. It is possible to see that very low values (about 15-20) of the spanwise tessellation are needed to stay within a difference of about 5% respect to larger values of Num_U, while the chordwise tessellation must be higher (about 40) to stay in the limit of 5% of the result variaiton. The same process has been done for drag and pitching moment coefficient (see Fig. 3.20 and 3.21). Introducing the effect of the propellers, it can be seen from Fig. 3.22, 3.24 and 3.23 that at least 24 tessellated curves in the spanwise direction are needed to obtain adequate results. The computational time is another important parameter to take in account, because it would make no sense to increase a lot the time needed for the analysis, since the VLM is a tool used to obtain preliminary results in a fast manner. Moreover, it is clearly understandable that the computed values don't change significantly increasing the parameters Num_U and Num_W besides 40-50. For the analysis presented later, Num_W = 117 and Num_U = 112 have been chosen.

$$\Delta_{C_L,\%} = \left| \frac{C_L^{i,j} - C_L^{max}}{C_L^{max}} \right| \quad \Delta_{C_D,\%} = \left| \frac{C_D^{i,j} - C_D^{max}}{C_D^{max}} \right| \quad \Delta_{C_M,\%} = \left| \frac{C_M^{i,j} - C_M^{max}}{C_M^{max}} \right| \tag{3.1}$$

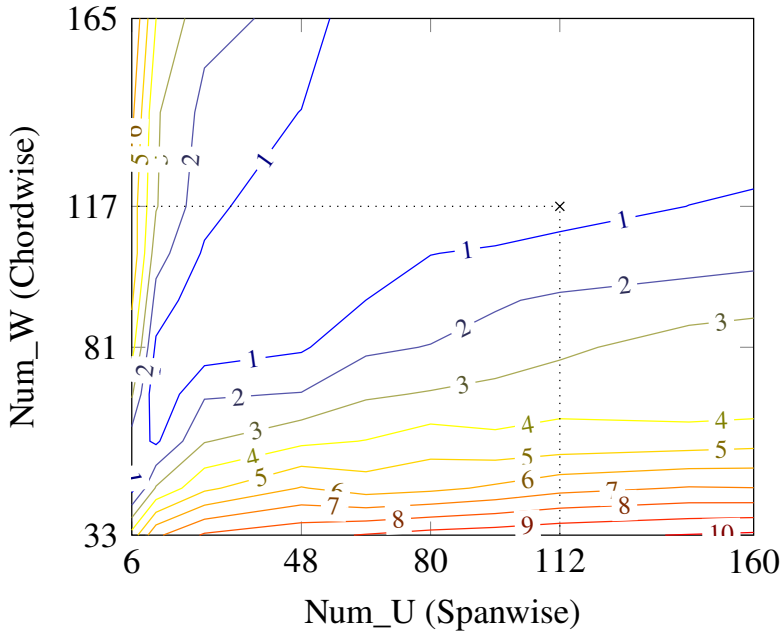

Figure 3.19: Percentage variation of the value of the lift coefficient at $\alpha = 0°$ for the isolated wing without flap and Prop off

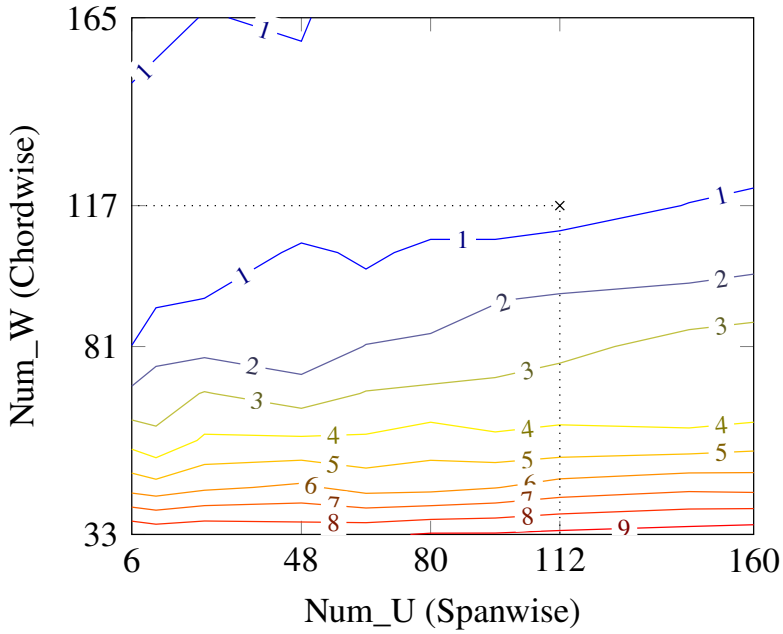

Figure 3.20: Percentage variation of the value of the drag coefficient at $\alpha = 0°$ for the isolated wing without flap and Prop off

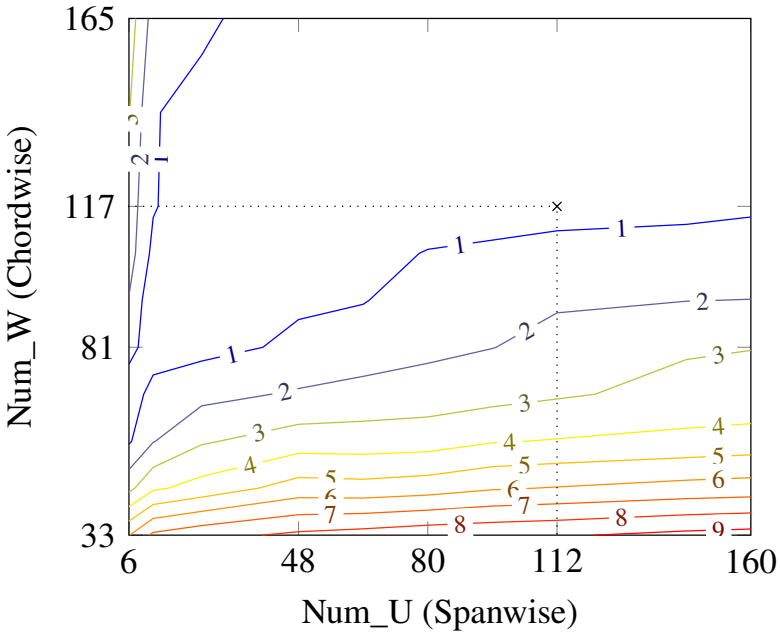

Figure 3.21: Percentage variation of the value of the pitching moment coefficient at $\alpha = 0°$ for the isolated wing without flap and Prop off

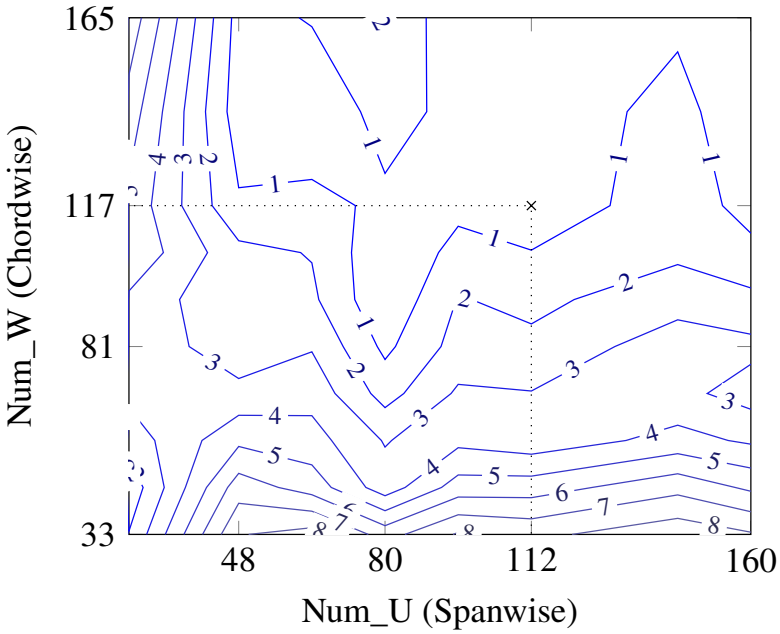

Figure 3.22: Percentage variation of the value of the lift coefficient at $\alpha = 0°$ for the isolated wing without flap and propellers on

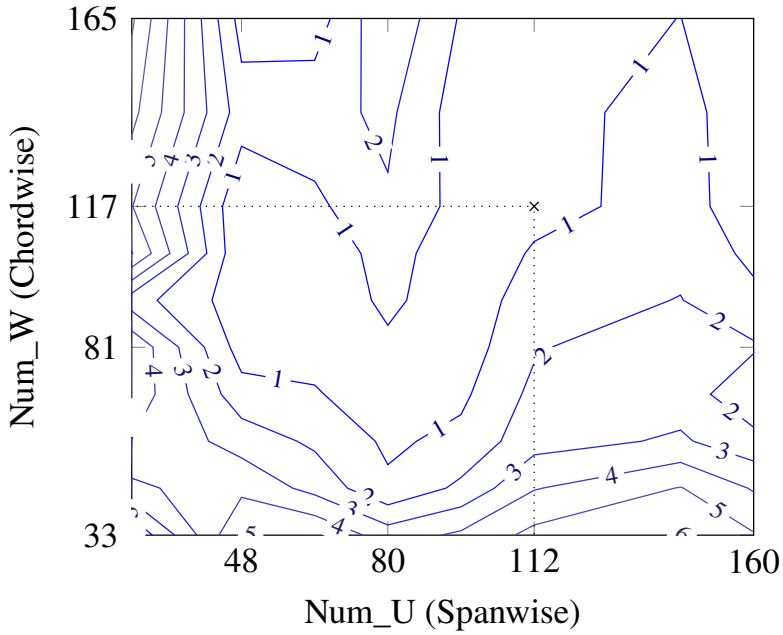

Figure 3.23: Percentage variation of the value of the drag coefficient at $\alpha = 0°$ for the isolated wing without flap and propellers on

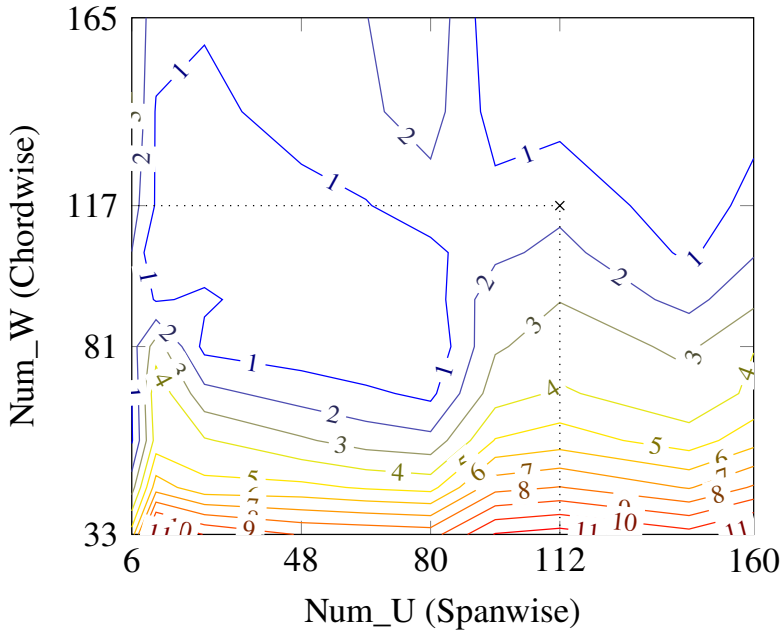

Figure 3.24: Percentage variation of the value of the pitching moment coefficient at $\alpha = 0°$ for the isolated wing without flap and propellers on

3.2.2 Wing analysis with VLM

The analysis presented in this section were performed calling in batch mode OpenVSP and VSPAero through a MATLAB code written at the University of Naples "Federico II". In this way it was possible to do a series of analyses for different DEP propellers positions and different flap deflections. The results presented in Fig. 3.25 show an unremarkable difference between the wing lift curves calculated by varying the DEP propellers position. However, the method allows to see the increase in lift coefficient due to propellers blowing, which results in a higher pitching moment coefficient, Fig. 3.27. Regarding the drag coefficient, from Fig. 3.26 it is clear that the method provides far-fetched results because the drag coefficient with DEP propellers enabled actually is lower than the one without propulsive effects. For this reason, it is useless to present the results of drag coefficient for other wing configurations.

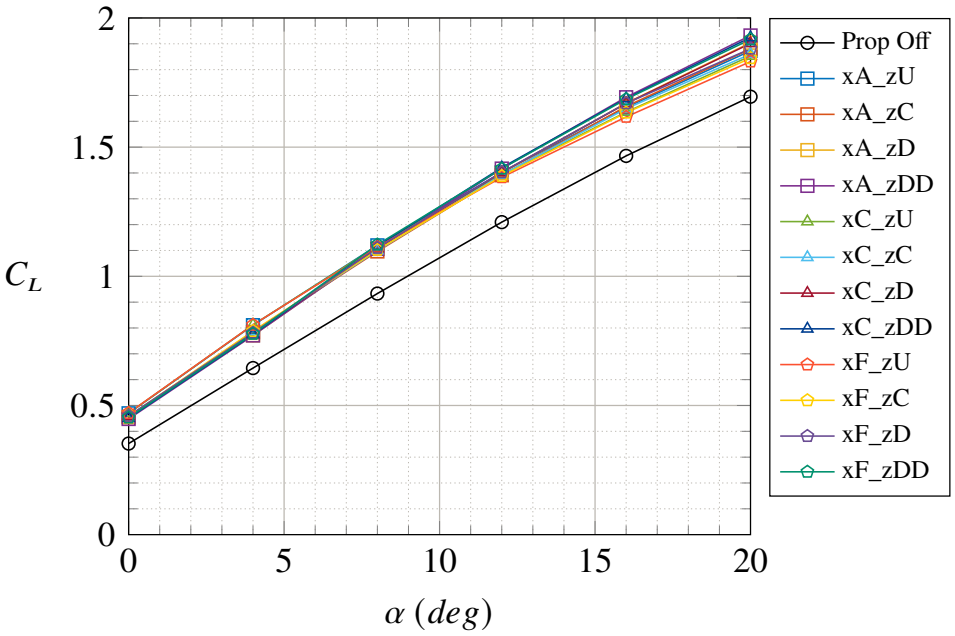

Figure 3.25: Wing lift curves by varying the position of DEP propellers - No flap - $V_\infty = 20\ m/s$ - $Re_\infty = 5.48 \cdot 10^5$ - $RPM_{DEP} = 7000$ - (VSPAERO)

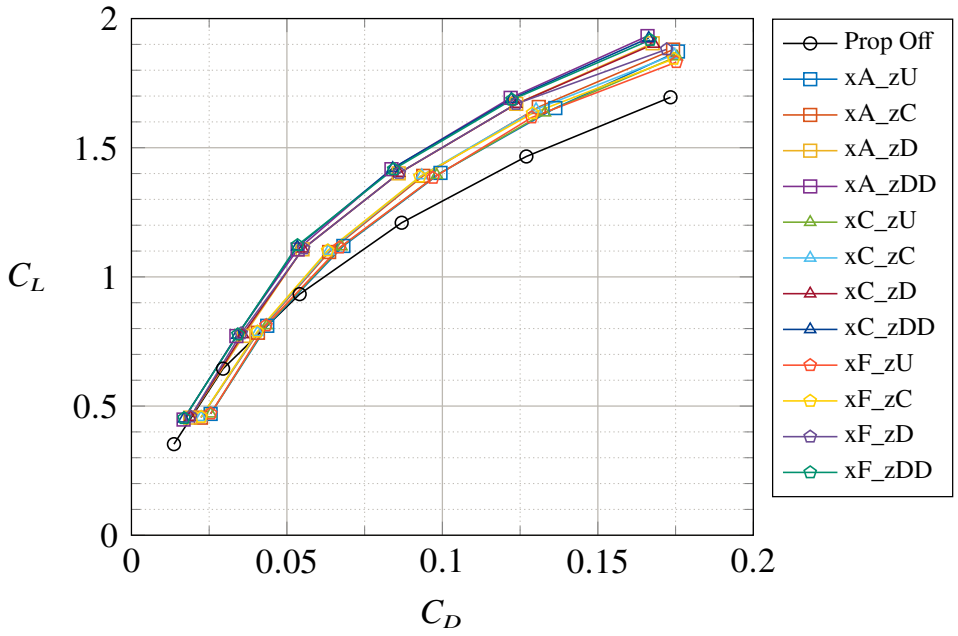

Figure 3.26: Wing drag polars by varying the position of DEP propellers - No flap - $V_\infty = 20\ m/s$ - $Re_\infty = 5.48 \cdot 10^5$ - $RPM_{DEP} = 7000$ - (VSPAERO)

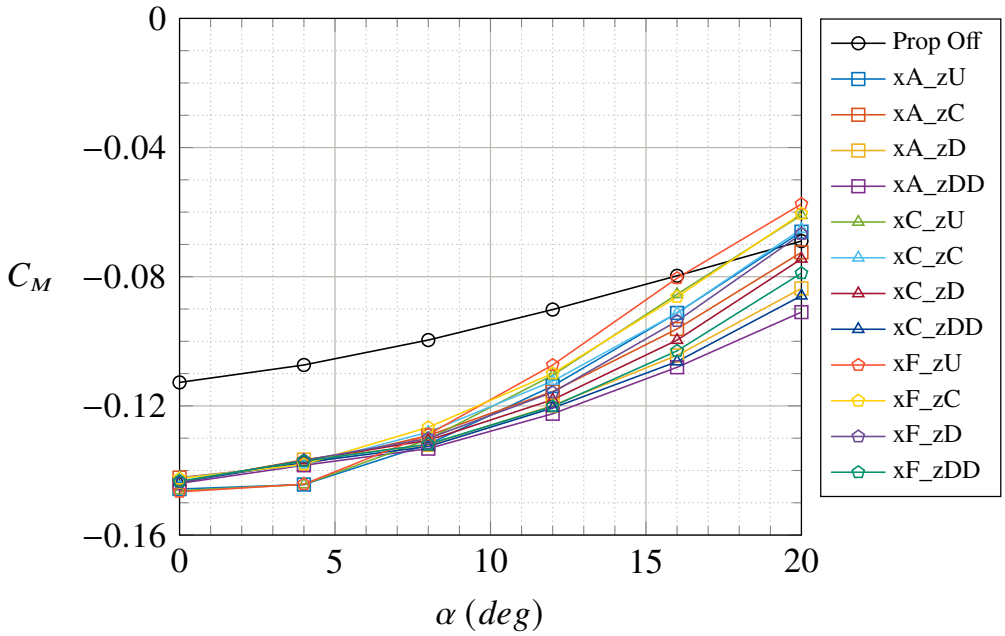

Figure 3.27: Wing pitching moment coefficient by varying the position of DEP propellers - No flap - $V_\infty = 20\ m/s$ - $Re_\infty = 5.48 \cdot 10^5$ - $RPM_{DEP} = 7000$ - (VSPAERO)

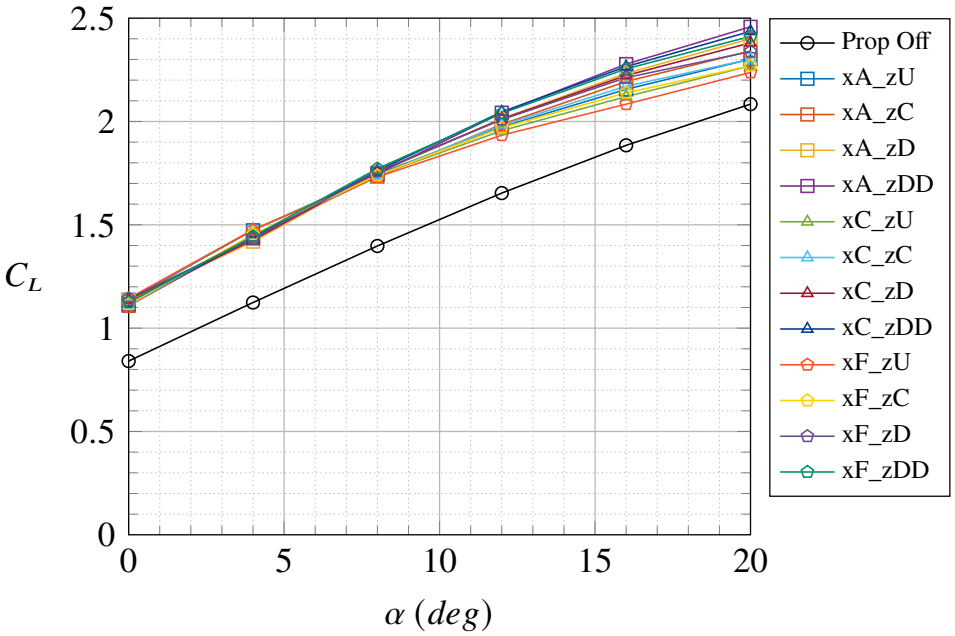

Figure 3.28: Wing lift curves by varying the position of DEP propellers - $\delta_f = 15° - V_\infty = 20\ m/s$ - $Re_\infty = 5.48 \cdot 10^5$ - $RPM_{DEP} = 7000$ - (VSPAERO)

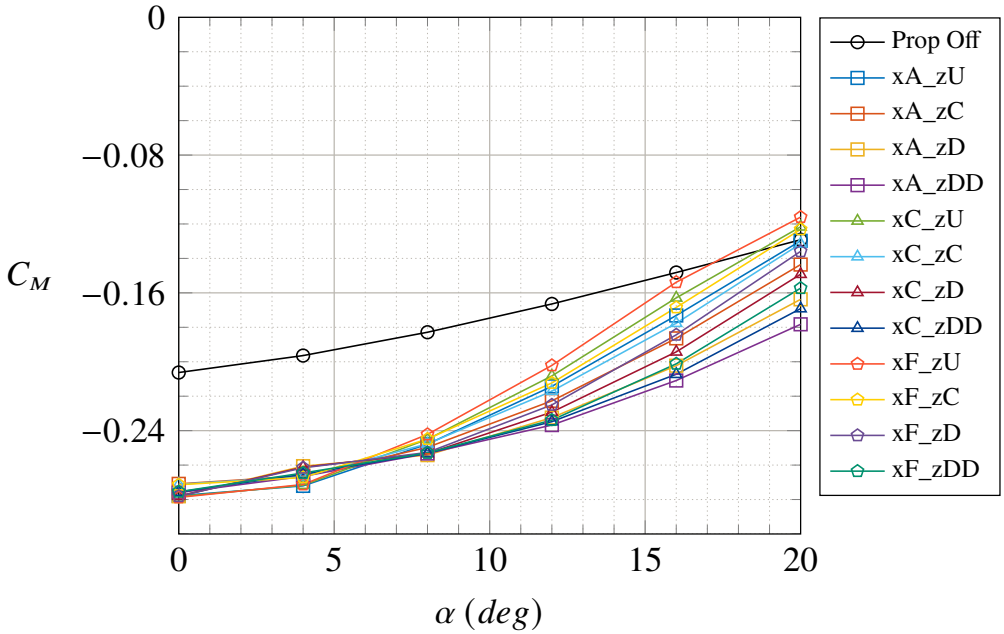

Figure 3.29: Wing pitching moment coefficient by varying the position of DEP propellers - $\delta_f = 15° - V_\infty = 20\ m/s$ - $Re_\infty = 5.48 \cdot 10^5$ - $RPM_{DEP} = 7000$ - (VSPAERO)

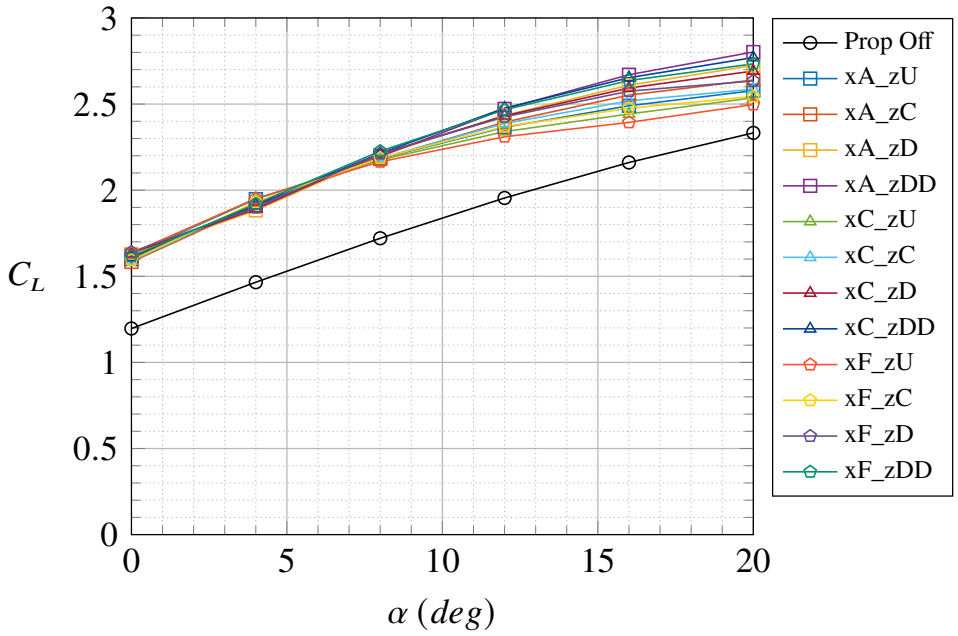

Figure 3.30: Wing lift curves by varying the position of DEP propellers - $\delta_f = 30°$ - $V_\infty = 20\ m/s$ - $Re_\infty = 5.48 \cdot 10^5$ - $RPM_{DEP} = 7000$ - (VSPAERO)

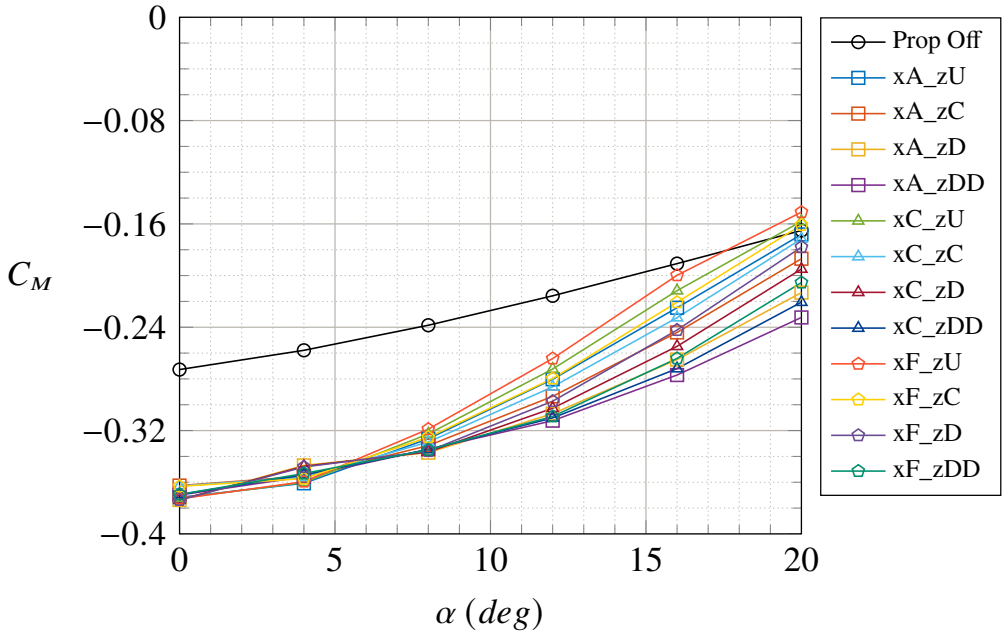

Figure 3.31: Wing pitching moment coefficient by varying the position of DEP propellers - $\delta_f = 30°$ - $V_\infty = 20\ m/s$ - $Re_\infty = 5.48 \cdot 10^5$ - $RPM_{DEP} = 7000$ - (VSPAERO)

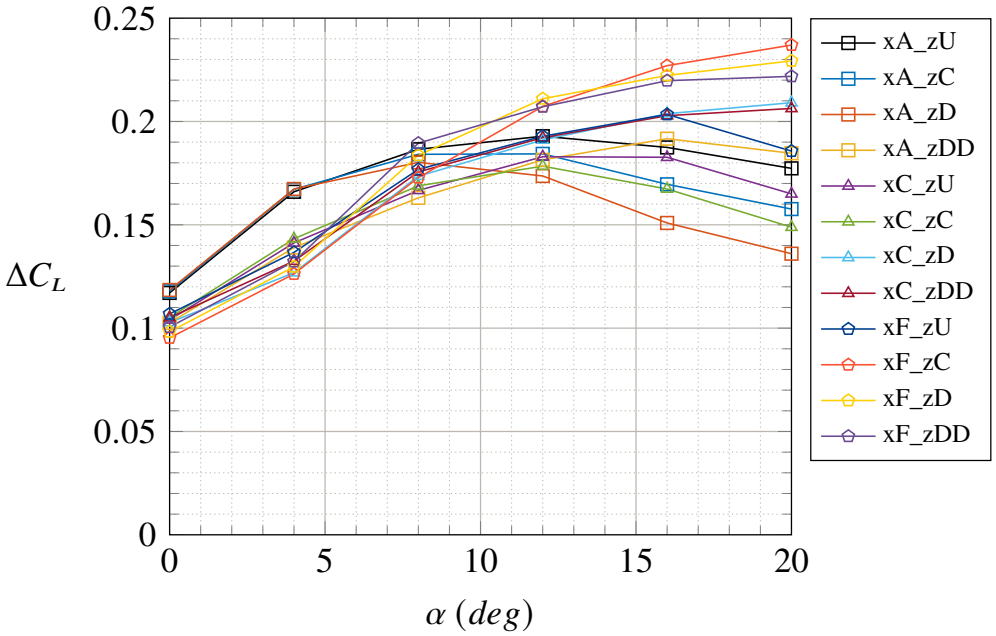

Figure 3.32: Increase of lift coefficient due to DEP propellers blowing - No flap - $V_\infty = 20\ m/s$ - $Re_\infty = 5.48 \cdot 10^5$ - $RPM_{DEP} = 7000$ - (VSPAERO)

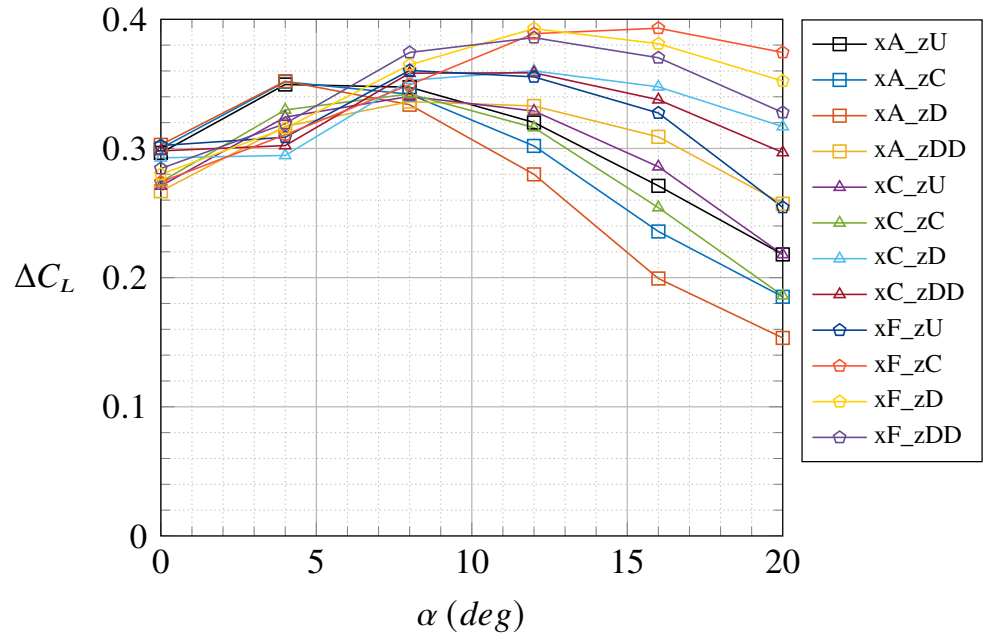

Figure 3.33: Increase of lift coefficient due to DEP propellers blowing - $\delta_f = 15°$ - $V_\infty = 20\ m/s$ - $Re_\infty = 5.48 \cdot 10^5$ - $RPM_{DEP} = 7000$ - (VSPAERO)

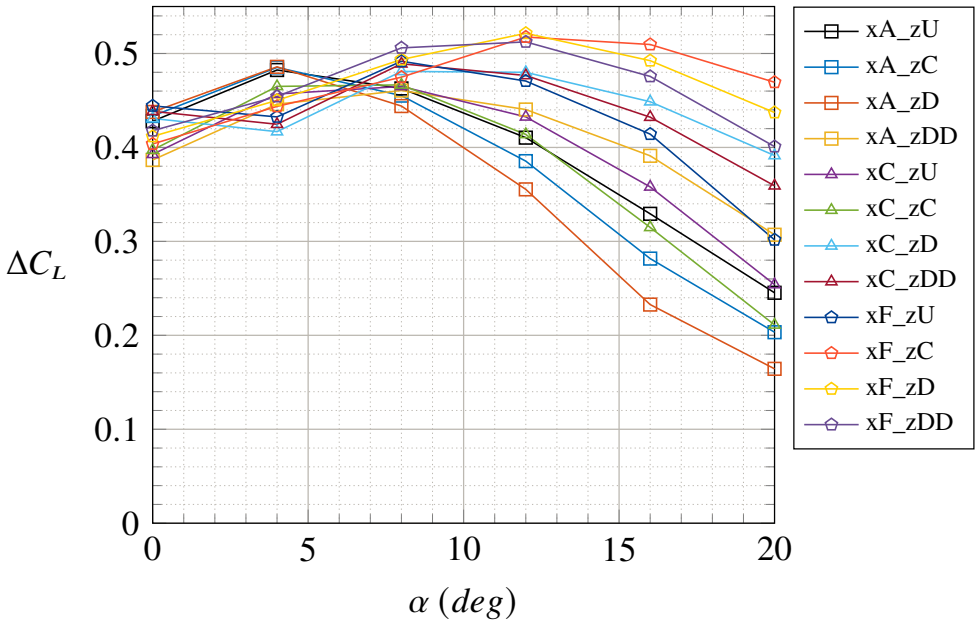

Figure 3.34: Increase of lift coefficient due to DEP propellers blowing - $\delta_f = 30°$ - $V_\infty = 20\ m/s$ - $Re_\infty = 5.48 \cdot 10^5$ - $RPM_{DEP} = 7000$ - (VSPAERO)

3.3 CFD analysis

In this section, the results of the CFD RANS analyses are presented. The software used was the well known STAR-CCM+, which includes the Virtual Disk Models briefly described in the previous chapter. The effect of the propellers was simulated with the Body Force Propeller Method (for both tip and DEP propellers), giving as input the propeller performances, represented in Fig. 3.12a and 3.12b. The adopted turbulence model was the Spalart-Allmaras one. A y+ wall distance of unitary order was setted.

3.3.1 Estimation of discretization error

The study of the discretization error was performed using the Grid Convergence Index (GCI) method [26], based on the Richardson extrapolation. The method prescribes several steps, starting from the definition of a representative mesh size, which is espressed as Eq. 3.2, where ΔV_i is the volume of the i^{th} cell and N is the total number of cells used for the computations.

$$h = \left[\frac{1}{N} \sum_{i=1}^{N} (\Delta V_i) \right]^{\frac{1}{3}} \tag{3.2}$$

Then, three significantly different sets of grids must be selected, to determine the values of key variables, such as the aerodynamic coefficients. The grid refinement factor, $r = h_{coarse}/h_{fine}$, should be greater than 1.3, which is a value based on experience. If the coarser mesh is indicated with the index 3, the medium one with 2 and the finest one with 1, it is $h_1 < h_2 < h_3$ and $r_{21} = h_2/h_1$, $r_{32} = h_3/h_2$. At this point it is possible to calculate, with an iterative procedure, the apparent order of convergence of the method, using the expression in Eq. 3.3, where $\varepsilon_{32} = \phi_3 - \phi_2$ and $\varepsilon_{21} = \phi_2 - \phi_1$, with ϕ_k denoting the value of a key variable obtained on the k^{th} grid.

$$p = \frac{1}{ln\,(r_{21})} \left| \left| \frac{\varepsilon_{32}}{\varepsilon_{21}} \right| + q(p) \right| \tag{3.3}$$

$$q(p) = ln \left(\frac{r_{21}^p - s}{r_{32}^p - s} \right) \tag{3.4}$$

$$s = 1 \cdot sign \left(\frac{\varepsilon_{32}}{\varepsilon_{21}} \right) \tag{3.5}$$

(a) Coarse

(b) Medium

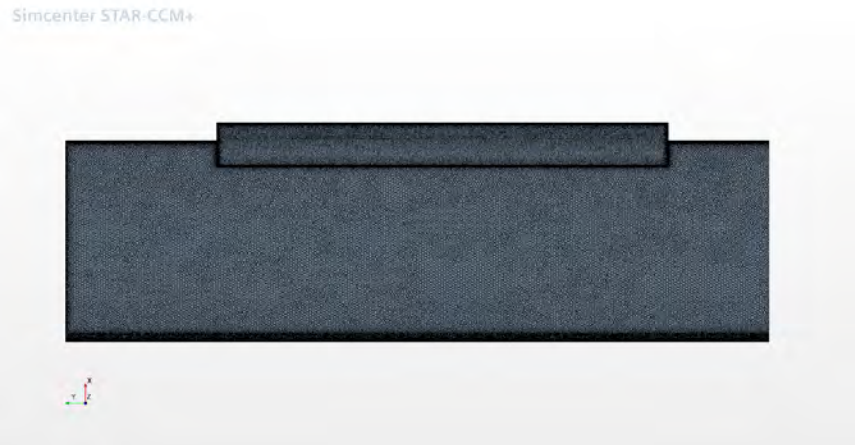

(c) Fine

Figure 3.35: The three meshes used for the estimation of discretization error - STAR-CCM+

Finally, the extrapolated values of the key variables can be calculated as Eq. 3.6, which provides a useful estimation of the numerically converged solution. Eq. 3.7 represents the approximate relative error and Eq. 3.8 the extrapolated relative error, while the fine-grid convergence index is expressed as Eq. 3.9. The GCI provides an estimate of the amount of discretization error in the finest grid solution relative to the converged numerical solution (as the exact solution is unknown). The number 1.25 in Eq. 3.9 is a safety factor and represents a 95% confidence bound on the estimated relative error, i.e. the converged numerical solution lies in the interval $\left[\phi_1\left(1 - GCI^{21}_{fine}\right), \phi_1\left(1 + GCI^{21}_{fine}\right)\right]$ with a 95% confidence level [27].

$$\phi^{21}_{ext} = \frac{r^p_{21}\phi_1 - \phi_2}{r^p_{21} - 1} \tag{3.6}$$

$$e^{21}_a = \left|\frac{\phi_1 - \phi_2}{\phi_1}\right| \tag{3.7}$$

$$e^{21}_{ext} = \left|\frac{\phi^{12}_{ext} - \phi_2}{\phi^{12}_{ext}}\right| \tag{3.8}$$

$$GCI^{21}_{fine} = \frac{1.25e^{21}_a}{r^p_{21} - 1} \tag{3.9}$$

The analysis presented in this thesis were performed with STAR-CCM+, and the meshing operations as well. The procedure of estimation of discretization error presented above was applied using three different meshes, whose characteristics are presented in Tab. 3.9. It goes without saying that Mesh 1 is the finest mesh, while Mesh 3 is the coarser one. The configuration analysed consisted of the wing with 30 degrees of flap and with DEP and TIP propellers enabled, because it was considered the most challenging one. The Virtual Disk Model used to simulate the effect of the propellers was the Body Force Propeller Method and, in particular, the disks meshing refinement required by the method was kept constant for the three meshes. The results of the application of the GCI method are presented in Tab. 3.10, for $\alpha = 0°$. Other two similar tables were obtained for $\alpha = 8°$ and $\alpha = 12°$, and the several solutions for the aerodynamic coefficients of interest are representend in Fig. 3.36, 3.37 and 3.38. Fig. 3.39, 3.40 and 3.41 represent the variation of the values of the aerodynamic coefficients by varying the number of cells. Finally, the fine-grid solutions with discretization error bars are shown in Fig. 3.42, 3.43 and 3.44. From these results, the fine-grid (Mesh 1) was considered suitable

to perform the analysis presented hereinafter.

	Mesh 1	Mesh 2	Mesh 3
$N_i/10^6$	8.26	3.67	1.67
$h_i\ (m)$	0.135	0.177	0.230
Base size (m)	0.130	0.280	0.559

Table 3.9: Characteristic of the meshes chosen for the GCI method

	$\phi = C_L$	$\phi = C_D$	$\phi = C_M$
$N_1,\ N_2,\ N_3\ (/10^6)$	8.26, 3.67, 1.67	8.26, 3.67, 1.67	8.26, 3.67, 1.67
r_{21}	1.31	1.31	1.31
r_{32}	1.30	1.30	1.30
ϕ_1	1.6866	0.1963	−0.5043
ϕ_2	1.7078	0.2003	−0.5116
ϕ_3	1.6954	0.2000	−0.5071
p	1.9525	8.5855	1.7342
ϕ_{ext}^{21}	1.6564	0.1959	−0.4923
e_a^{21}	1.25%	2.06%	1.43%
e_{ext}^{21}	1.83%	0.22%	2.45%
GCI_{fine}^{21}	2.24%	0.28%	2.99%

Table 3.10: Values calculated applying the GCI method - $\alpha = 0°$ - $V_\infty = 20\ m/s$ - $Re_\infty = 5.48 \cdot 10^5$ - $RPM_{DEP} = 7000$ - $RPM_{TIP} = 2000$ - $X_{DEP} = X_{TIP} = -0.04\ m$ - $Z_{DEP} = Z_{TIP} = 0\ m$

	C_L	C_D	C_M
GCI_{max}	2.24%	5.51%	2.99%
p_{avg}	4.8307	4.0303	3.6938

Table 3.11: Maximum GCI and average order of convergence on the fine-grid for the aerodynamic coefficients

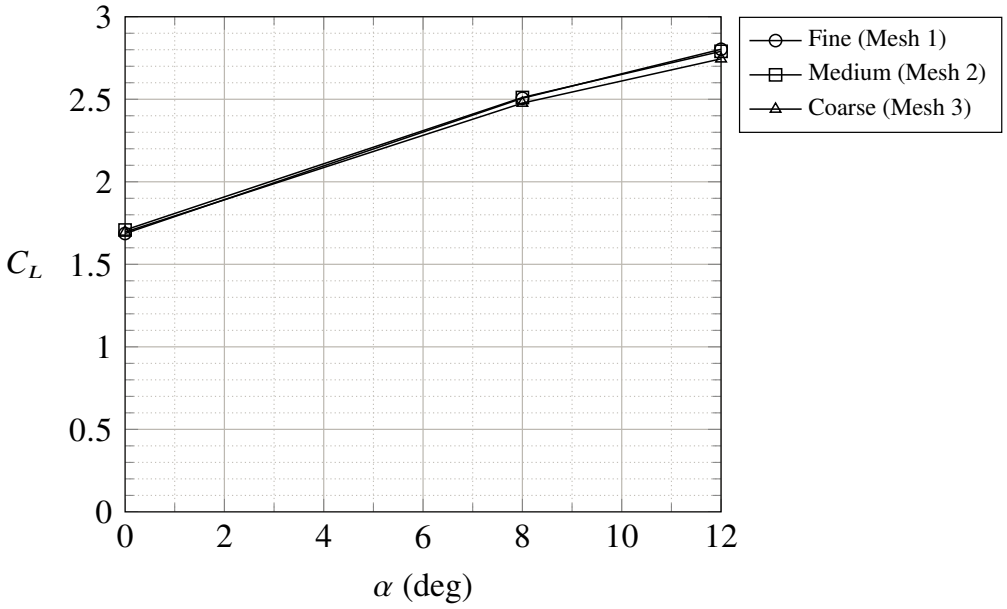

Figure 3.36: Lift curves calculated with the three meshes - $V_\infty = 20\ m/s$ - $Re_\infty = 5.48 \cdot 10^5$ - $RPM_{DEP} = 7000$ - $RPM_{TIP} = 2000$ - $X_{DEP} = X_{TIP} = -0.04\ m$ - $Z_{DEP} = Z_{TIP} = 0\ m$

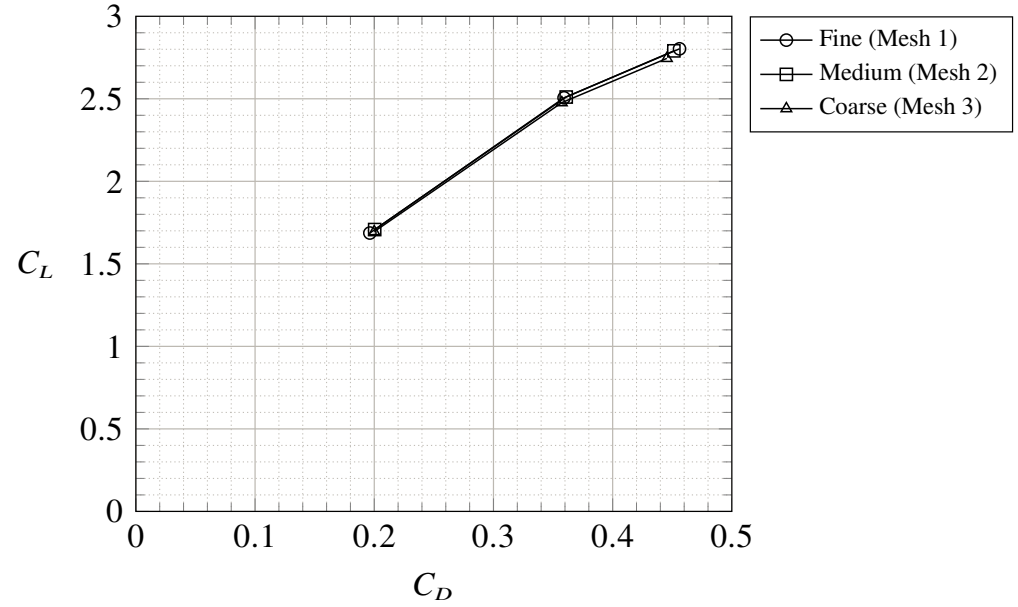

Figure 3.37: Drag polars calculated with the three meshes - $V_\infty = 20\ m/s$ - $Re_\infty = 5.48 \cdot 10^5$ - $RPM_{DEP} = 7000$ - $RPM_{TIP} = 2000$ - $X_{DEP} = X_{TIP} = -0.04\ m$ - $Z_{DEP} = Z_{TIP} = 0\ m$

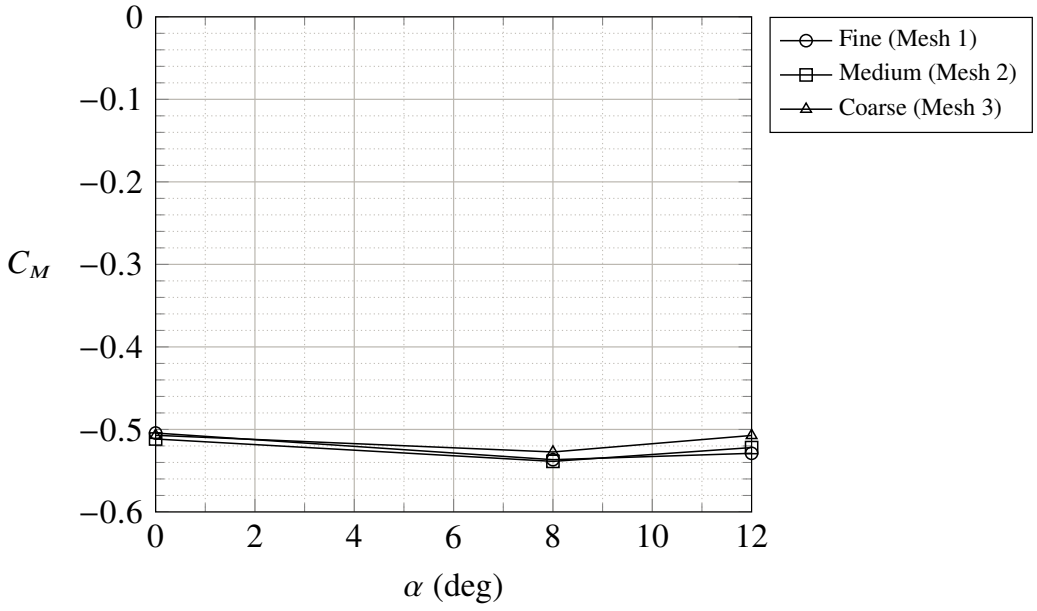

Figure 3.38: Pitching moment coefficients calculated with the three meshes - $V_\infty = 20\ m/s$ - $Re_\infty = 5.48 \cdot 10^5$ - $RPM_{DEP} = 7000$ - $RPM_{TIP} = 2000$ - $X_{DEP} = X_{TIP} = -0.04\ m$ - $Z_{DEP} = Z_{TIP} = 0\ m$

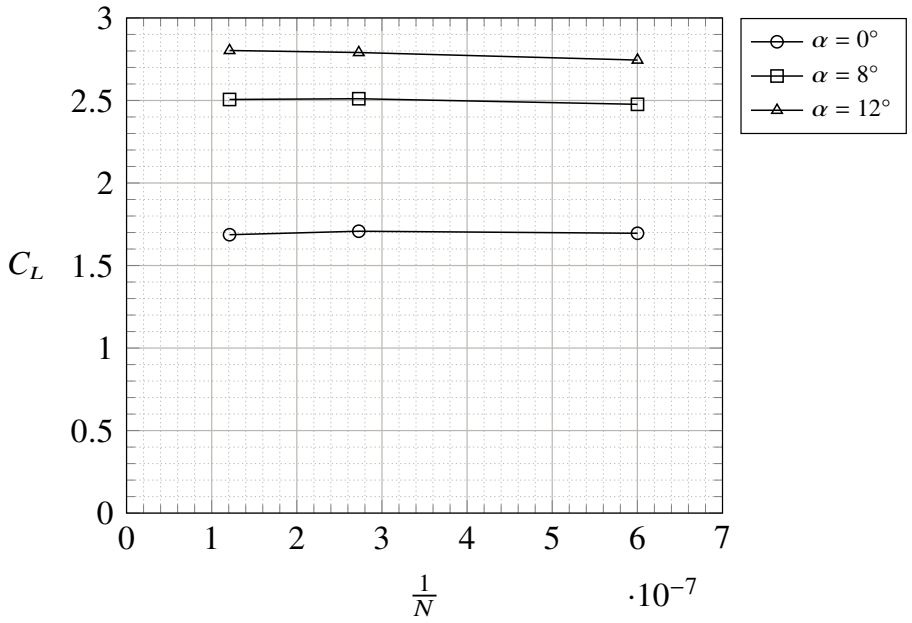

Figure 3.39: Variation of lift coefficient for different angles of attack, varying the number of cells N - $V_\infty = 20\ m/s$ - $Re_\infty = 5.48 \cdot 10^5$ - $RPM_{DEP} = 7000$ - $RPM_{TIP} = 2000$ - $X_{DEP} = X_{TIP} = -0.04\ m$ - $Z_{DEP} = Z_{TIP} = 0\ m$

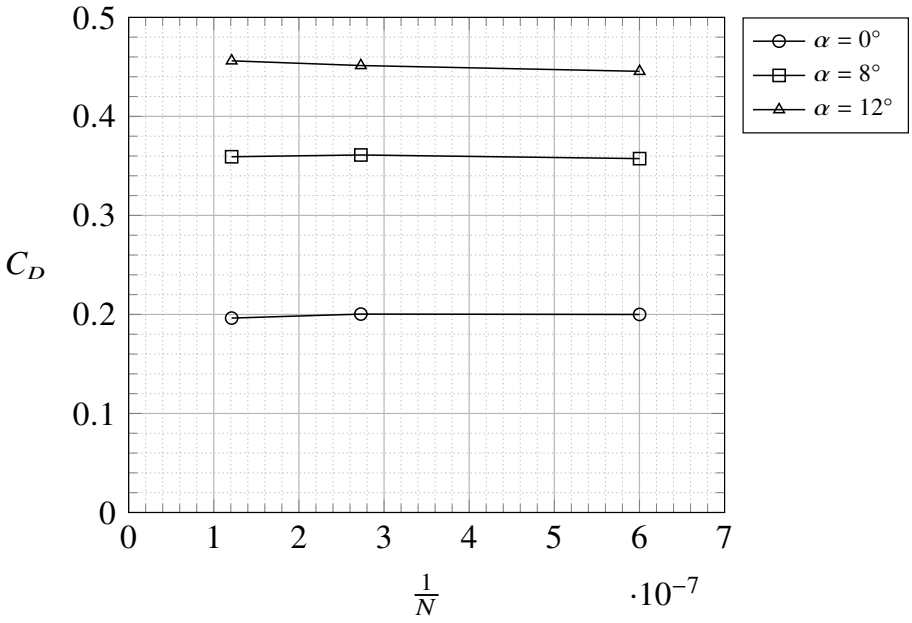

Figure 3.40: Variation of drag coefficient for different angles of attack, varying the number of cells N - $V_\infty = 20\ m/s$ - $Re_\infty = 5.48 \cdot 10^5$ - $RPM_{DEP} = 7000$ - $RPM_{TIP} = 2000$ - $X_{DEP} = X_{TIP} = -0.04\ m$ - $Z_{DEP} = Z_{TIP} = 0\ m$

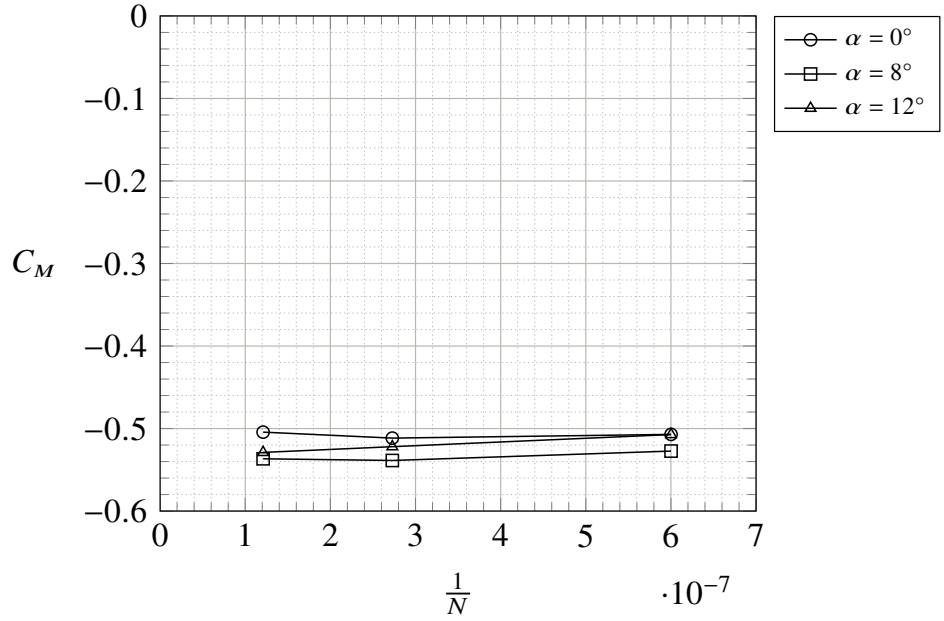

Figure 3.41: Variation of pitching moment coefficient for different angles of attack, varying the number of cells N - $V_\infty = 20\ m/s$ - $Re_\infty = 5.48 \cdot 10^5$ - $RPM_{DEP} = 7000$ - $RPM_{TIP} = 2000$ - $X_{DEP} = X_{TIP} = -0.04\ m$ - $Z_{DEP} = Z_{TIP} = 0\ m$

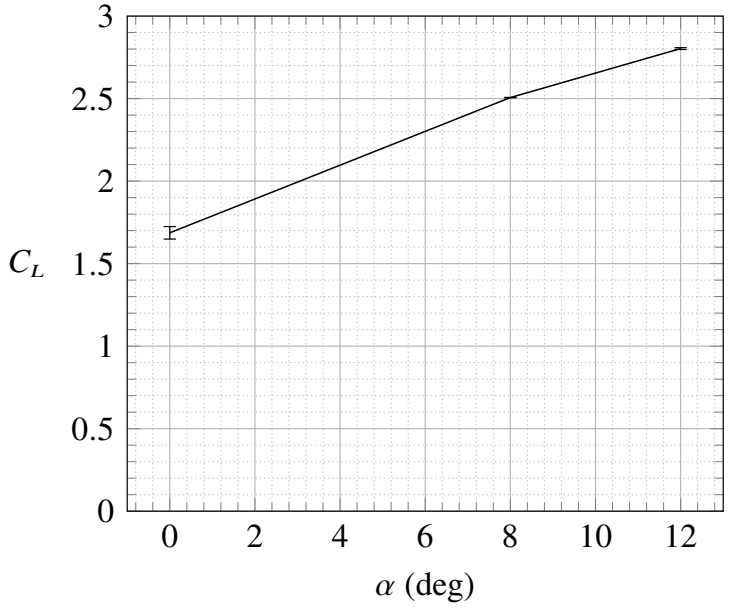

Figure 3.42: Fine-grid (Mesh 1) solution for lift coefficient with discretization error bars computed usign Eq. 3.9

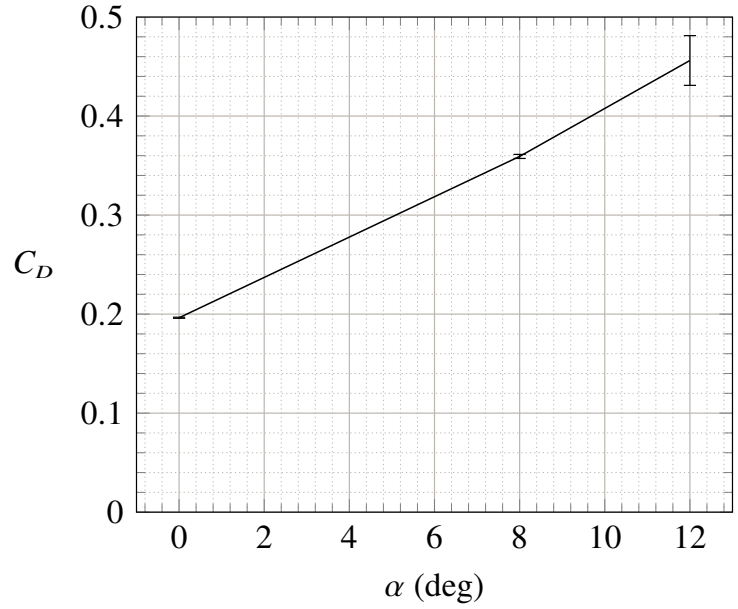

Figure 3.43: Fine-grid (Mesh 1) solution for drag coefficient with discretization error bars computed usign Eq. 3.9

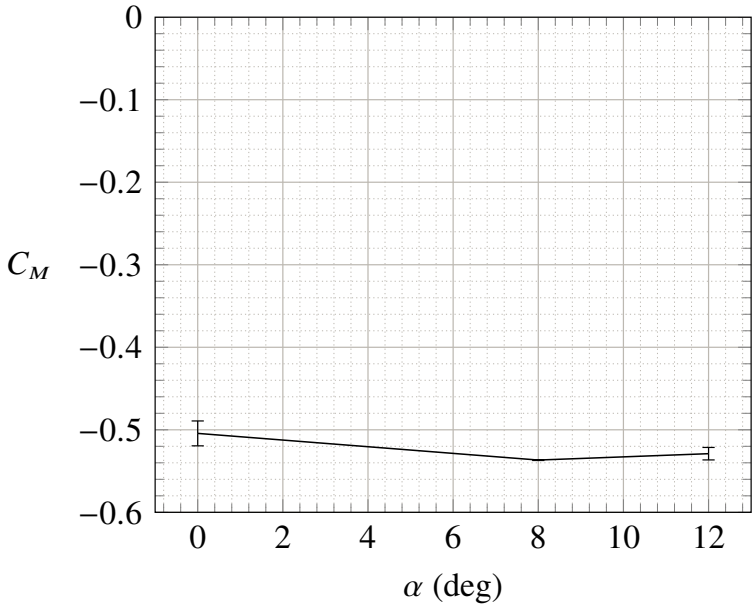

Figure 3.44: Fine-grid (Mesh 1) solution for pitching moment coefficient with discretization error bars computed usign Eq. 3.9

3.3.2 DEP effects on clean configuration

In this section, the CFD analyses of the wing in clean configuration, performed with STAR-CCM+, are presented. In particular, the effect of DEP propellers are underlined, showing the differences with respect to the case without propellers. The several positions of DEP propellers considered for the analyses are those of Tab. 3.6 and 3.7, sketched in Fig. 3.45. The spanwise position of each propeller is fixed, Tab. 3.5. The lift curves

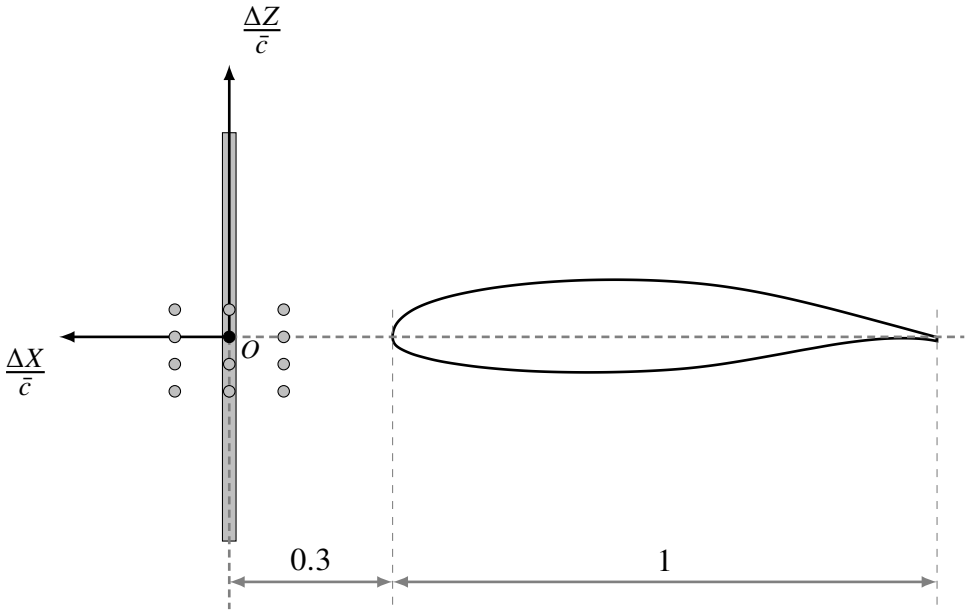

Figure 3.45: Sketch of dimensionless disks positions with respect to the wing leading edge

of each case are represented in Fig. 3.46, where, from a global point of view, the position indicated with xA_zC is the better at stall, reaching the higher maximum lift coefficient. The worst behaviour at stall is given by the xF_zU position. Nevertheless, the performance at stall for the wing in clean configuration gets undoubtedly worse with the DEP propellers enabled, compared to the case without propulsive effect. The drag polars for all cases are presented in Fig. 3.47, from which it can be seen that the highest drag coefficient for each lift coefficient is obtained for the case xA_zDD. In general, the blowing action of the propellers clearly generates a drag rise (mainly pressure drag), along with an increase of the pitching moment, Fig. 3.48. This is due to the accelerated slipstream which causes a greater expansion of the flow on the wing leading edge. It can be interesting to see how the aerodynamic performance of the wing varies by changing the Z-Position of the DEP propellers, fixed an X-Position (and vice versa). The effect

of the Z-Position, fixed an X-Position, can be different depending on the distance of the DEP propellers from the wing leading edge. For instance, looking at Fig. 3.50, the best behaviour at stall with xA fixed is given from the zC position, while to the zU position corresponds a stall anticipation. Fig. 3.51 represents the lift curves for the xC position fixed. In this case, the zC and zD cases seems to be almost similiar, while the upper position zU corresponds to the lowest maximum lift coefficient and the lowest position zDD exhibits a stall delay with respect to the other Z-Positions. Fixing the xF position, zD and zDD positions show a comparable behaviour, while moving up the DEP propellers generates a deterioration of stall performance. Regarding the linear zone of the lift curves, for a fixed X-Position, a higher lift coefficient can be reached moving from the lowest zDD to the upper zU positions. A global point of view of the different stall conditions driven by the several Z-positions of DEP propellers, for a fixed X-Position, is given by Fig. 3.80, 3.81 and 3.82, which represent the magnitude of the X-Component of wall shear stress on the upper wing, along with the Q-Criterion isosurfaces. The blue zones give an idea of the wing portions affected by separated flow, because the magnitude of the X-Component of wall shear stress becomes negative (reverse flow). Regarding the drag coefficient, fixed the X-Positions xA and xC, there is an increment moving the propellers down from zU to zDD, Fig. 3.57 and 3.58. For the xF position, the difference is less remarkable.

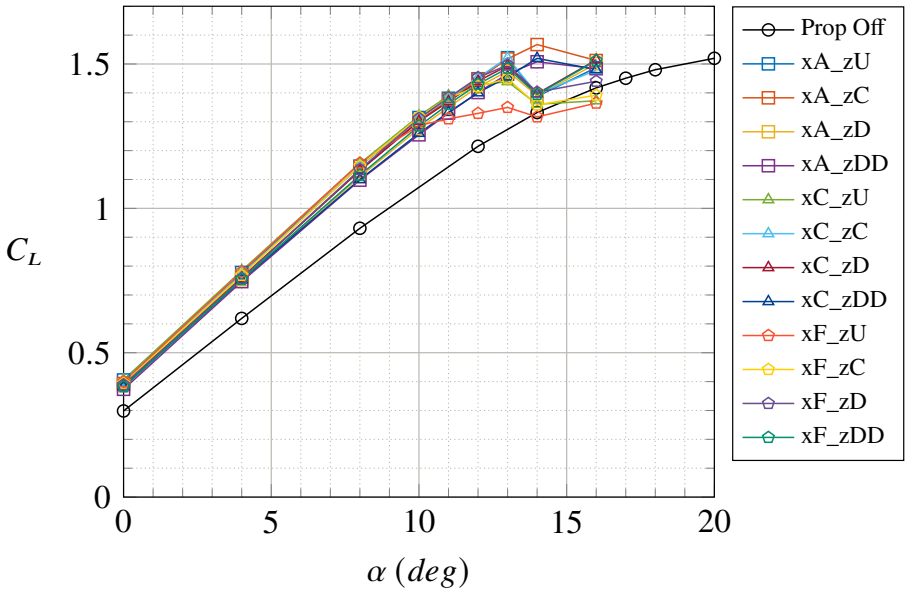

Figure 3.46: Wing lift curves by varying the position of DEP propellers - No flap - $V_\infty = 20\ m/s$ - $Re_\infty = 5.48 \cdot 10^5$ - $RPM_{DEP} = 7000$ (In-Board Up) - STAR-CCM+

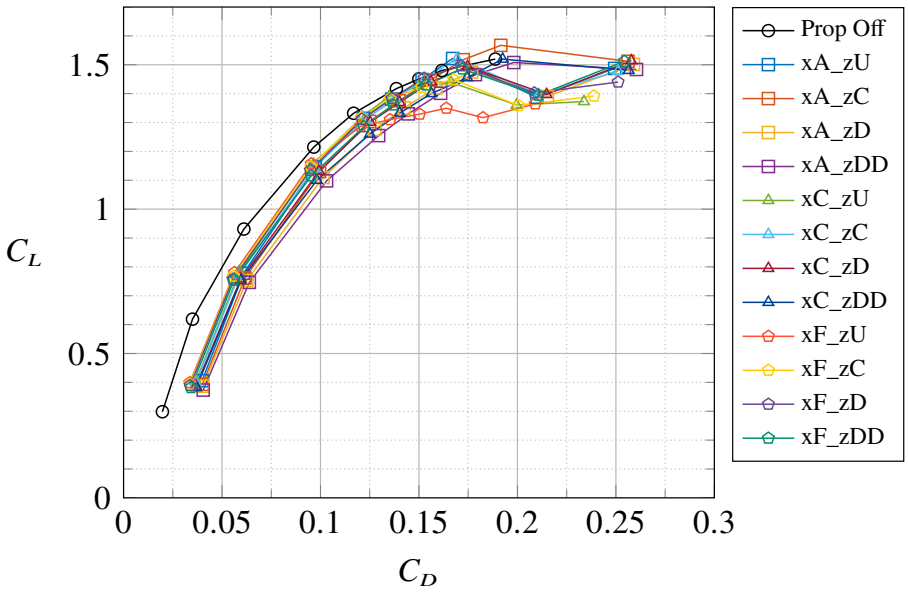

Figure 3.47: Wing drag polars by varying the position of DEP propellers - No flap - $V_\infty = 20\ m/s$ - $Re_\infty = 5.48 \cdot 10^5$ - $RPM_{DEP} = 7000$ (In-Board Up) - STAR-CCM+

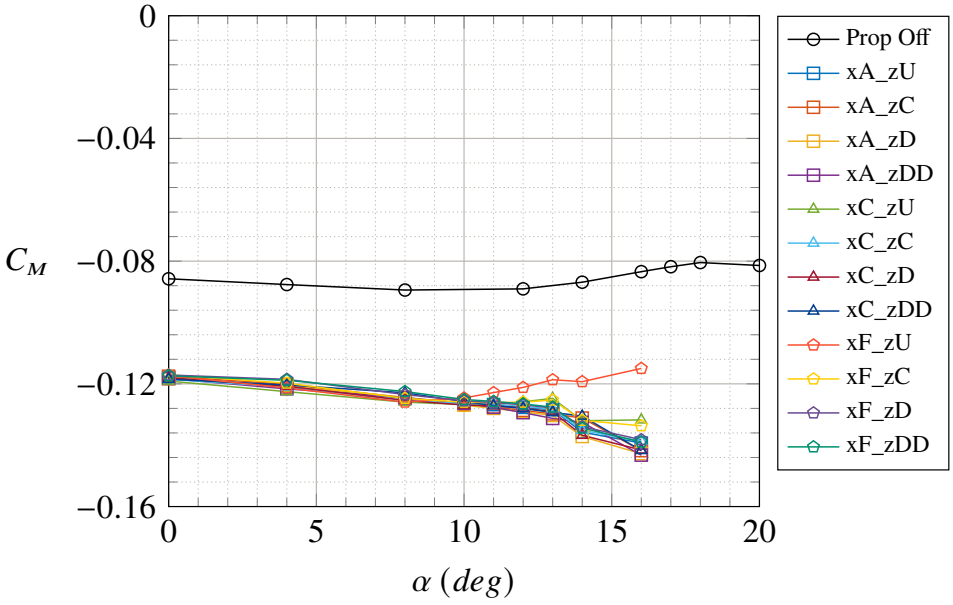

Figure 3.48: Wing pitching moment coefficient by varying the position of DEP propellers - No flap - $V_\infty = 20\ m/s$ - $Re_\infty = 5.48 \cdot 10^5$ - $RPM_{DEP} = 7000$ (In-Board Up) - STAR-CCM+

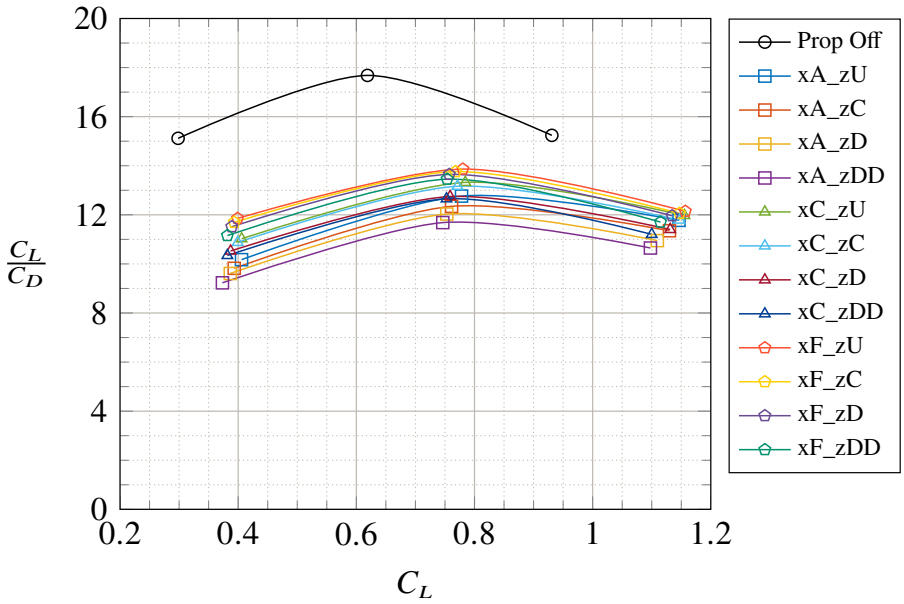

Figure 3.49: Wing efficiency by varying the position of DEP propellers - No flap - $V_\infty = 20\ m/s$ - $Re_\infty = 5.48 \cdot 10^5$ - $RPM_{DEP} = 7000$ (In-Board Up) - STAR-CCM+

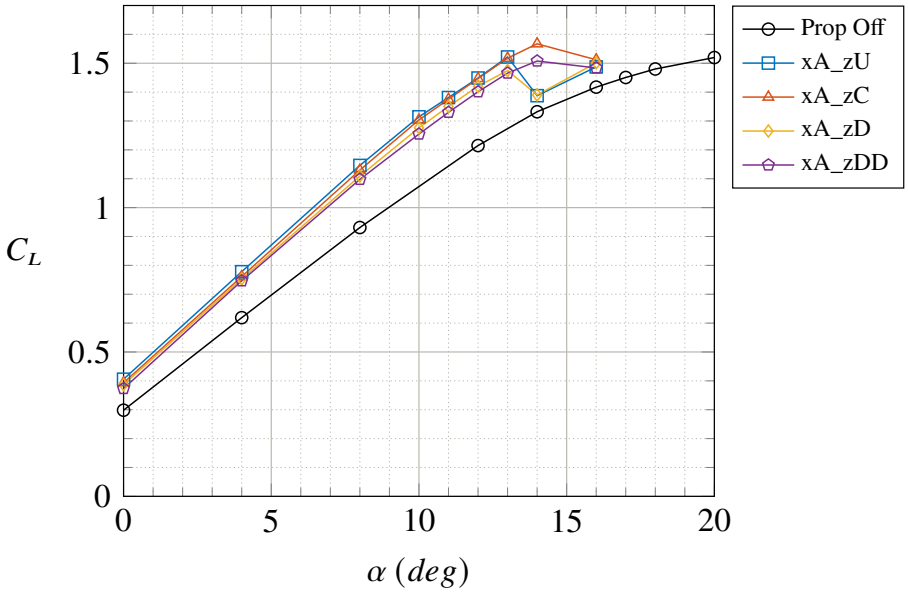

Figure 3.50: Wing lift curves by varying the Z-Position of DEP propellers with xA fixed - No flap - $V_\infty = 20\ m/s$ - $Re_\infty = 5.48 \cdot 10^5$ - $RPM_{DEP} = 7000$ (In-Board Up) - STAR-CCM+

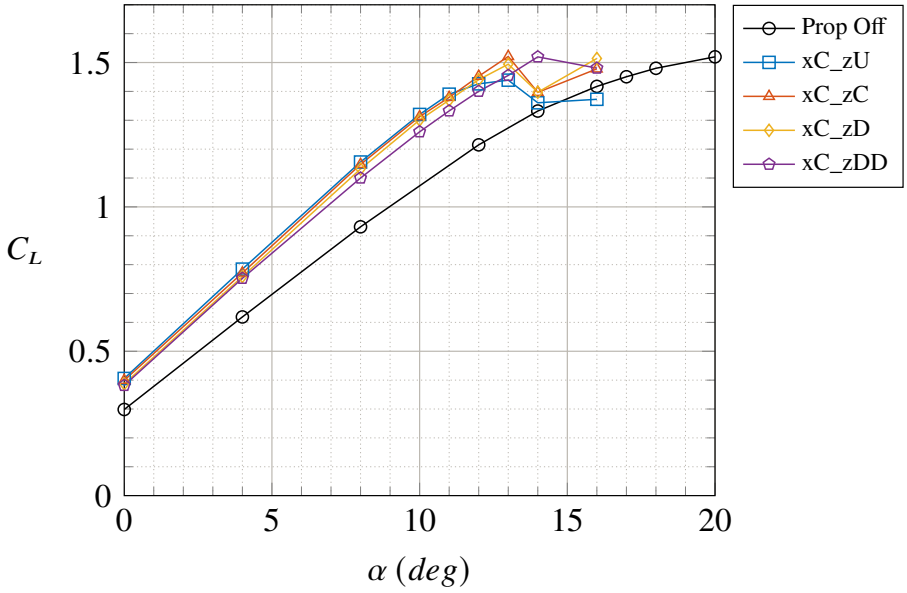

Figure 3.51: Wing lift curves by varying the Z-Position of DEP propellers with xC fixed - No flap - $V_\infty = 20\ m/s$ - $Re_\infty = 5.48 \cdot 10^5$ - $RPM_{DEP} = 7000$ (In-Board Up) - STAR-CCM+

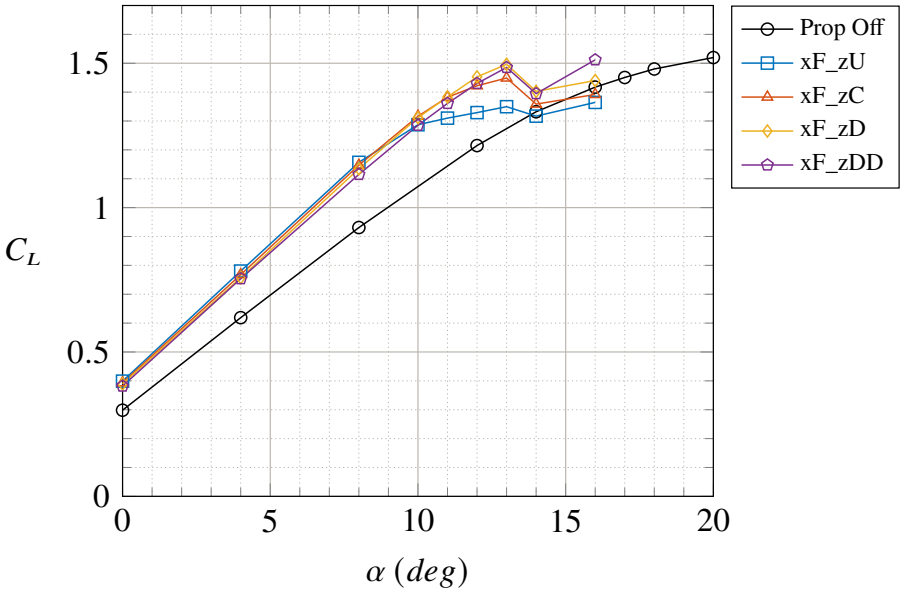

Figure 3.52: Wing lift curves by varying the Z-Position of DEP propellers with xF fixed - No flap - $V_\infty = 20\ m/s$ - $Re_\infty = 5.48 \cdot 10^5$ - $RPM_{DEP} = 7000$ (In-Board Up) - STAR-CCM+

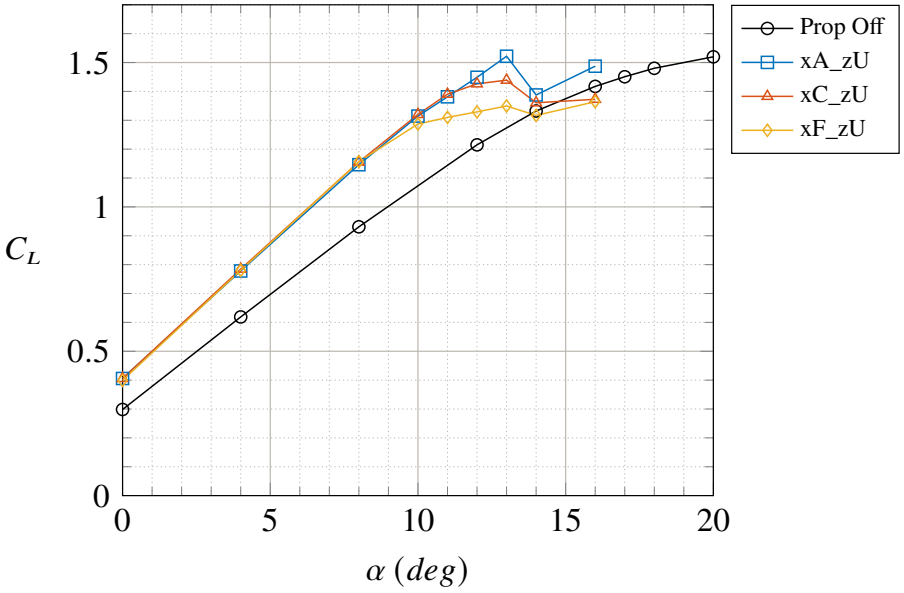

Figure 3.53: Wing lift curves by varying the X-Position of DEP propellers with zU fixed - No flap - $V_\infty = 20\ m/s$ - $Re_\infty = 5.48 \cdot 10^5$ - $RPM_{DEP} = 7000$ (In-Board Up) - STAR-CCM+

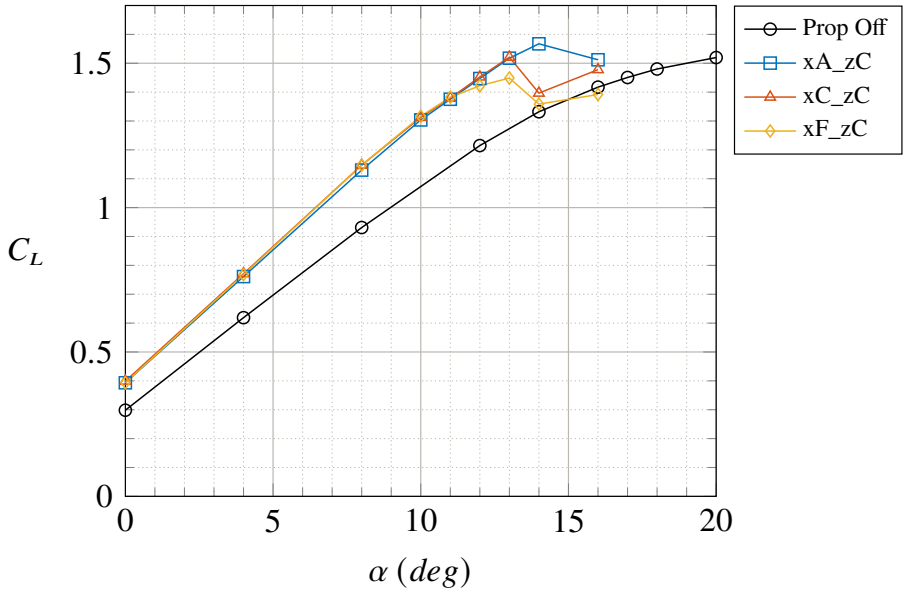

Figure 3.54: Wing lift curves by varying the X-Position of DEP propellers with zC fixed - No flap - $V_\infty = 20\ m/s$ - $Re_\infty = 5.48 \cdot 10^5$ - $RPM_{DEP} = 7000$ (In-Board Up) - STAR-CCM+

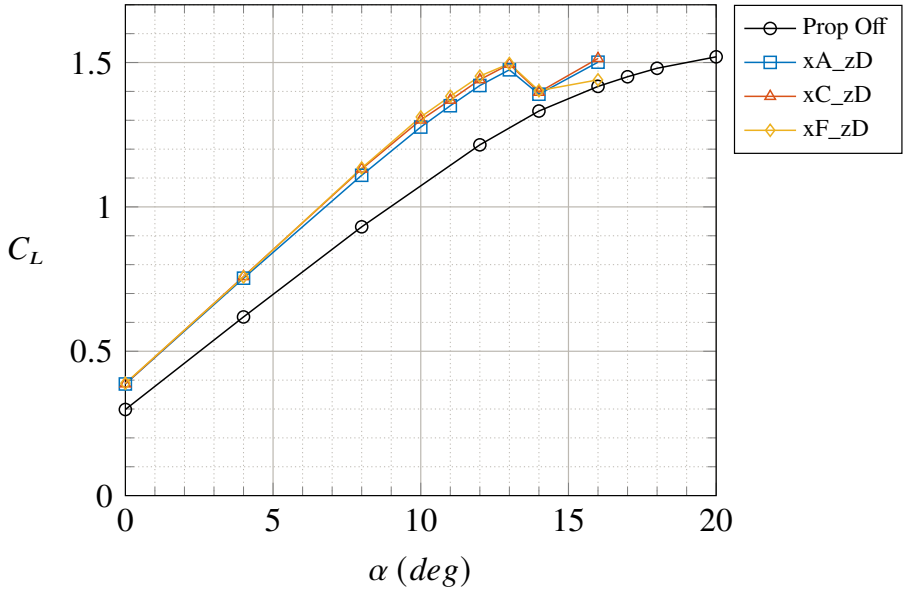

Figure 3.55: Wing lift curves by varying the X-Position of DEP propellers with zD fixed - No flap - $V_\infty = 20\ m/s$ - $Re_\infty = 5.48 \cdot 10^5$ - $RPM_{DEP} = 7000$ (In-Board Up) - STAR-CCM+

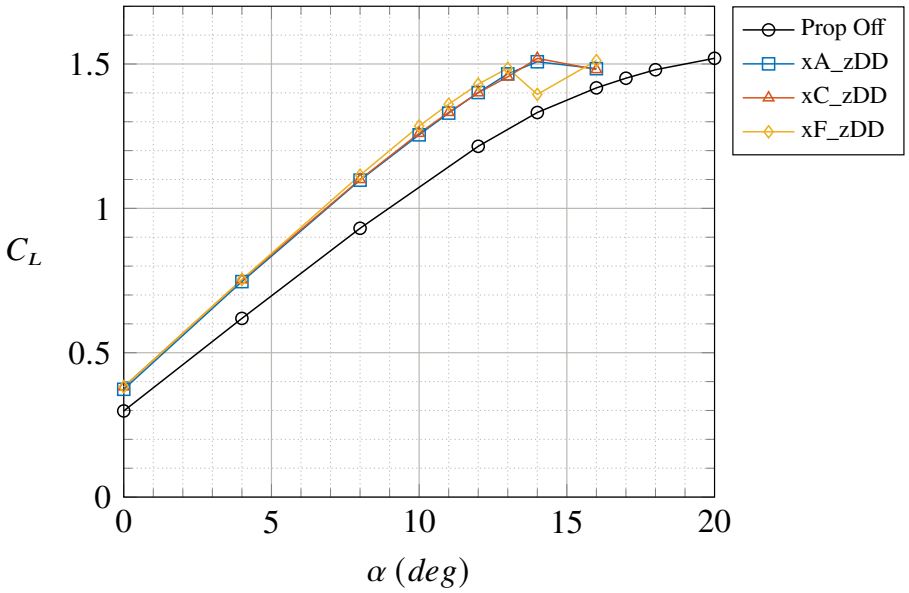

Figure 3.56: Wing lift curves by varying the X-Position of DEP propellers with zDD fixed - No flap - $V_\infty = 20\ m/s$ - $Re_\infty = 5.48 \cdot 10^5$ - $RPM_{DEP} = 7000$ (In-Board Up) - STAR-CCM+

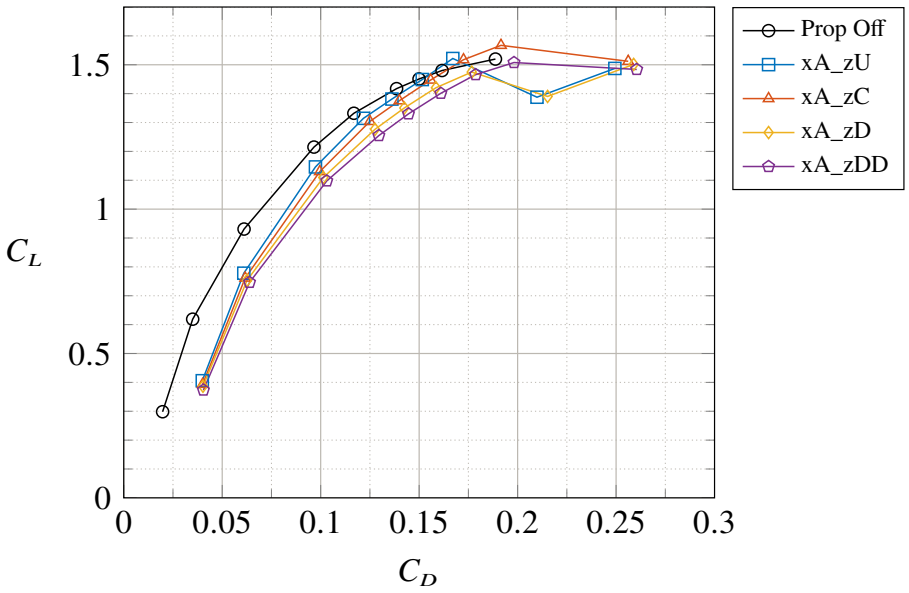

Figure 3.57: Wing drag polars by varying the Z-Position of DEP propellers with xA fixed - No flap - $V_\infty = 20\ m/s$ - $Re_\infty = 5.48 \cdot 10^5$ - $RPM_{DEP} = 7000$ (In-Board Up) - STAR-CCM+

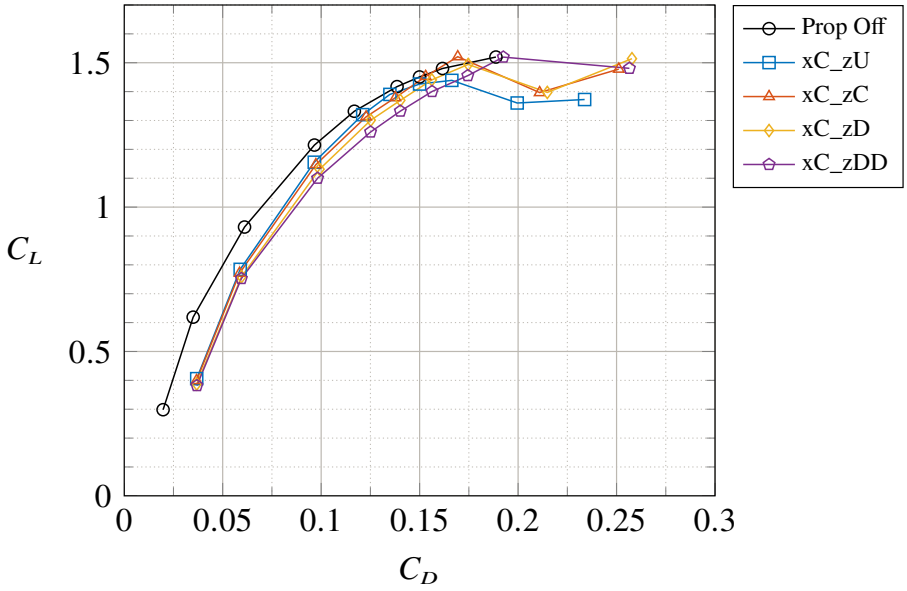

Figure 3.58: Wing drag polars by varying the Z-Position of DEP propellers with xC fixed - No flap - $V_\infty = 20\ m/s$ - $Re_\infty = 5.48 \cdot 10^5$ - $RPM_{DEP} = 7000$ (In-Board Up) - STAR-CCM+

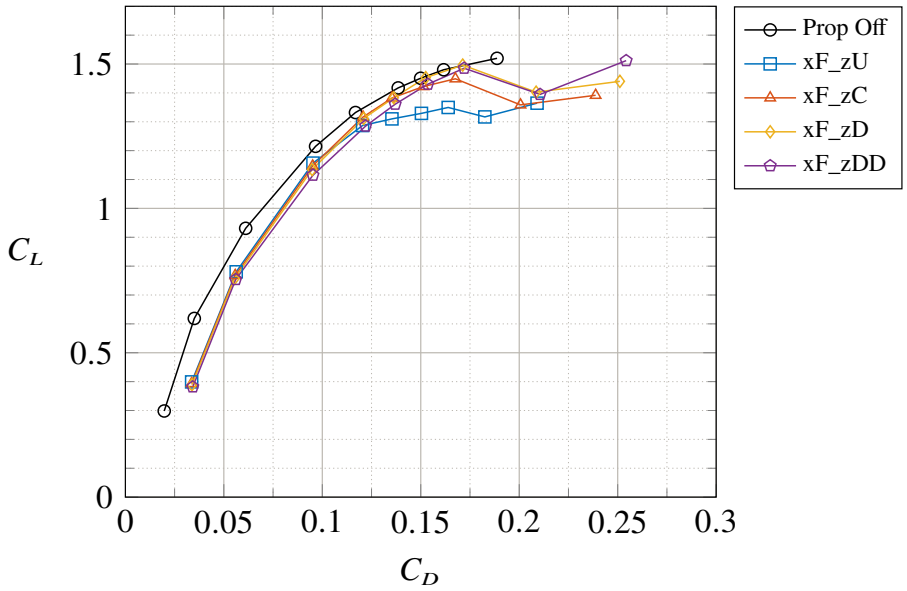

Figure 3.59: Wing drag polars by varying the Z-Position of DEP propellers with xF fixed - No flap - $V_\infty = 20\ m/s$ - $Re_\infty = 5.48 \cdot 10^5$ - $RPM_{DEP} = 7000$ (In-Board Up) - STAR-CCM+

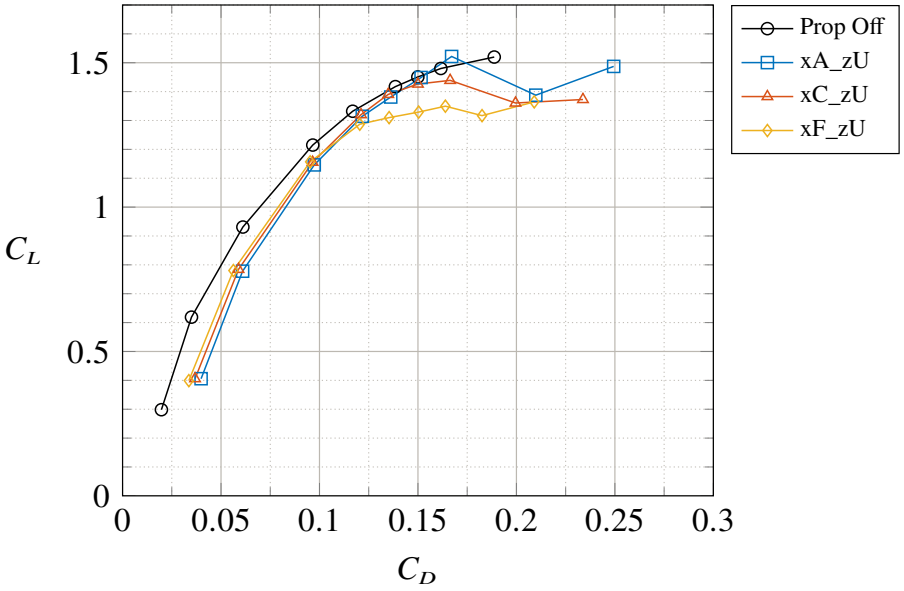

Figure 3.60: Wing drag polars by varying the X-Position of DEP propellers with zU fixed - No flap - $V_\infty = 20\ m/s$ - $Re_\infty = 5.48 \cdot 10^5$ - $RPM_{DEP} = 7000$ (In-Board Up) - STAR-CCM+

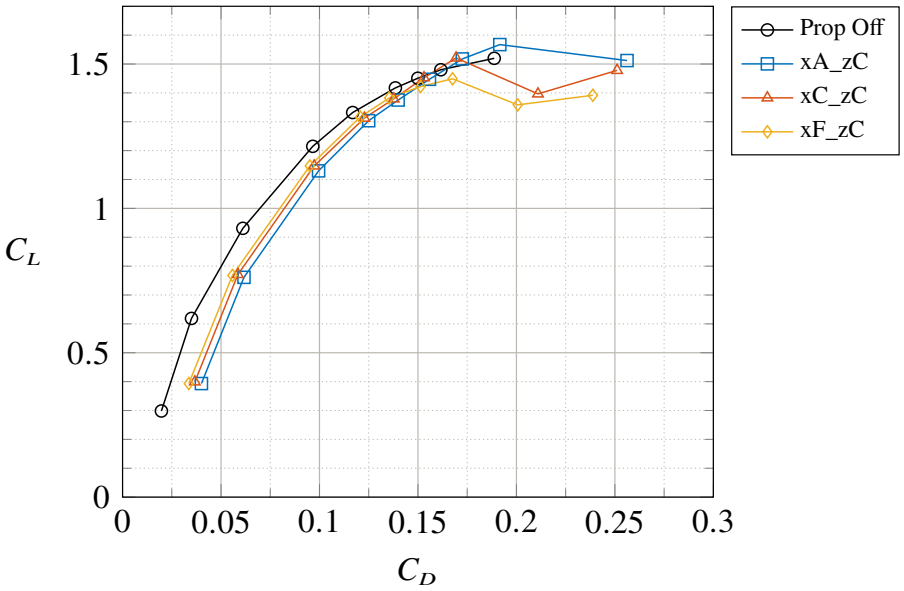

Figure 3.61: Wing drag polars by varying the X-Position of DEP propellers with zC fixed - No flap - $V_\infty = 20\ m/s$ - $Re_\infty = 5.48 \cdot 10^5$ - $RPM_{DEP} = 7000$ (In-Board Up) - STAR-CCM+

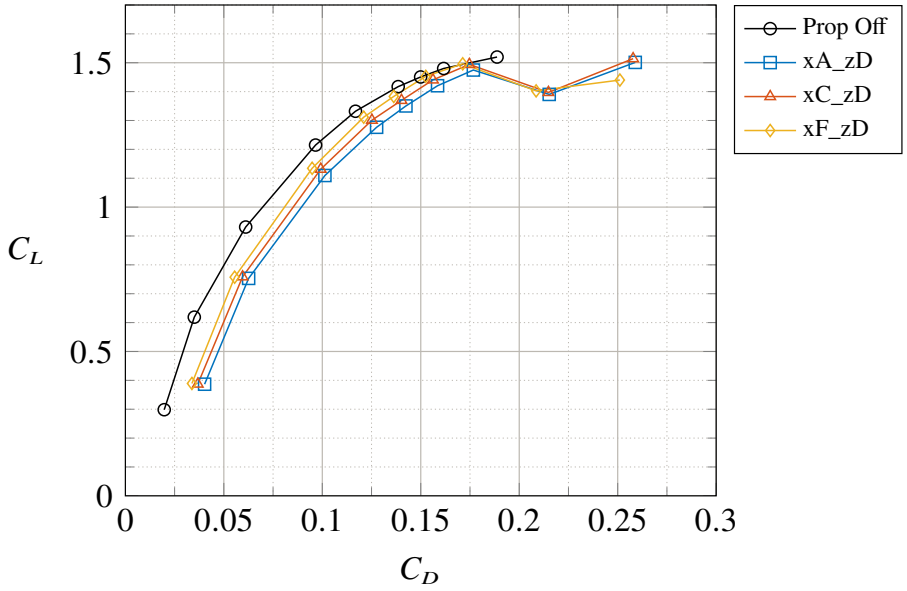

Figure 3.62: Wing drag polars by varying the X-Position of DEP propellers with zD fixed - No flap - $V_\infty = 20\ m/s$ - $Re_\infty = 5.48 \cdot 10^5$ - $RPM_{DEP} = 7000$ (In-Board Up) - STAR-CCM+

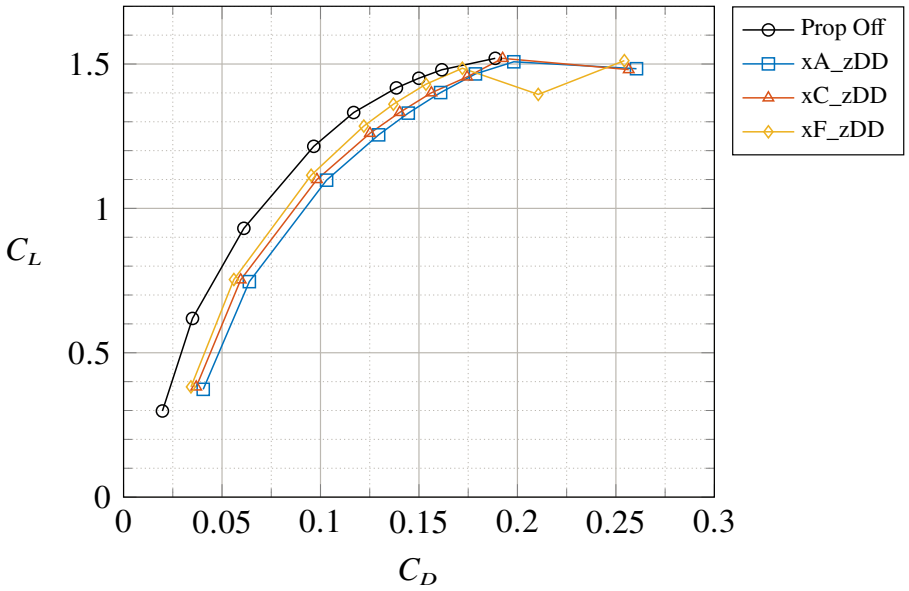

Figure 3.63: Wing drag polars by varying the X-Position of DEP propellers with zDD fixed - No flap - $V_\infty = 20\ m/s$ - $Re_\infty = 5.48 \cdot 10^5$ - $RPM_{DEP} = 7000$ (In-Board Up) - STAR-CCM+

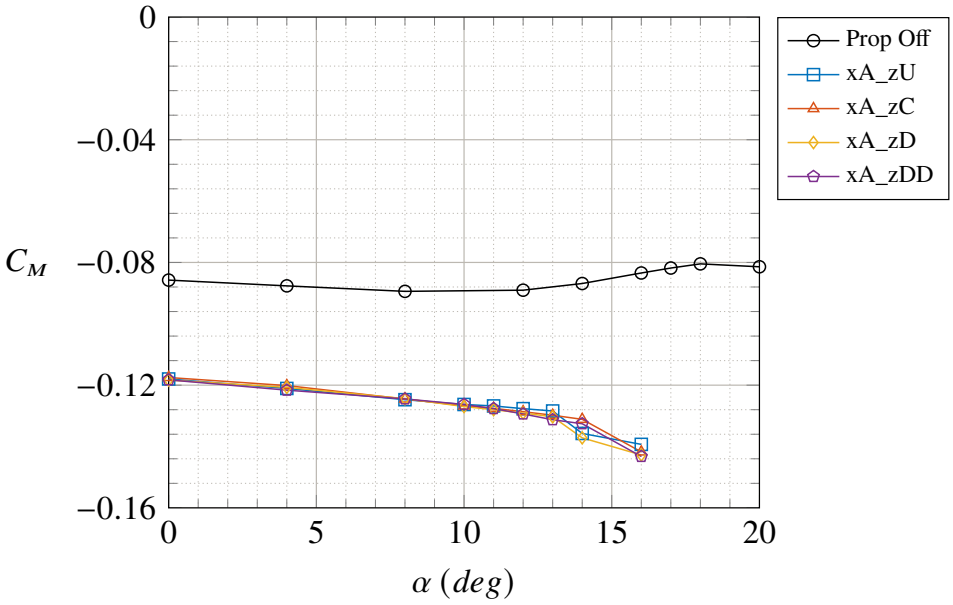

Figure 3.64: Wing pitching moment coefficient by varying the Z-Position of DEP propellers with xA fixed - No flap - $V_\infty = 20\ m/s$ - $Re_\infty = 5.48 \cdot 10^5$ - $RPM_{DEP} = 7000$ (In-Board Up) - STAR-CCM+

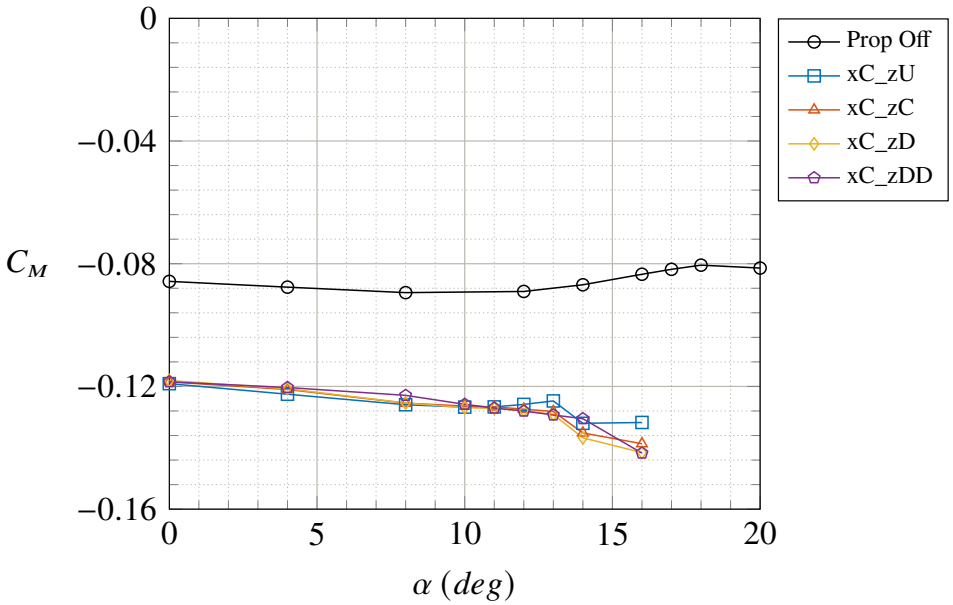

Figure 3.65: Wing pitching moment coefficient by varying the Z-Position of DEP propellers with xC fixed - No flap - $V_\infty = 20\ m/s$ - $Re_\infty = 5.48 \cdot 10^5$ - $RPM_{DEP} = 7000$ (In-Board Up) - STAR-CCM+

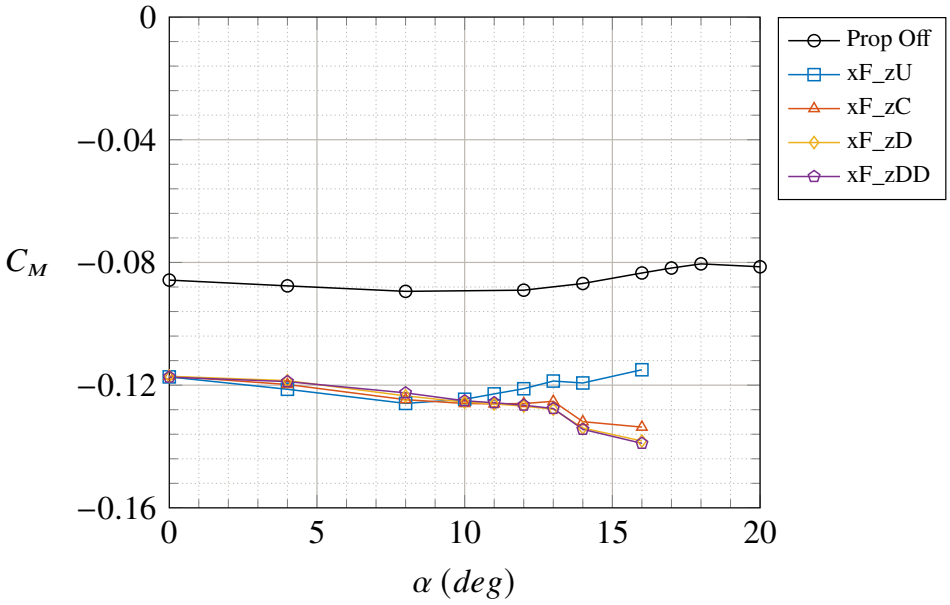

Figure 3.66: Wing pitching moment coefficient by varying the Z-Position of DEP propellers with xF fixed - No flap - $V_\infty = 20\ m/s$ - $Re_\infty = 5.48 \cdot 10^5$ - $RPM_{DEP} = 7000$ (In-Board Up) - STAR-CCM+

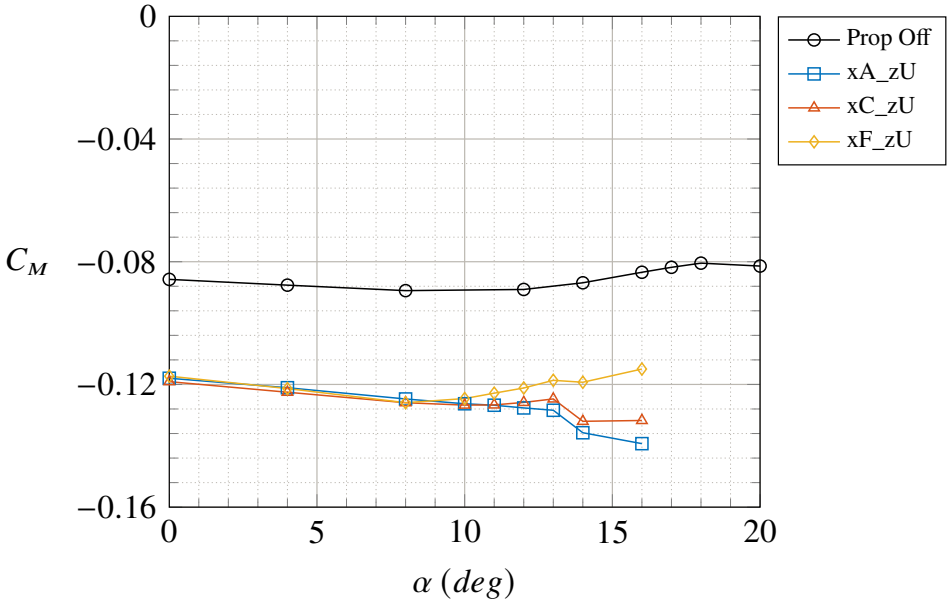

Figure 3.67: Wing pitching moment coefficient by varying the X-Position of DEP propellers with zU fixed - No flap - $V_\infty = 20\ m/s$ - $Re_\infty = 5.48 \cdot 10^5$ - $RPM_{DEP} = 7000$ (In-Board Up) - STAR-CCM+

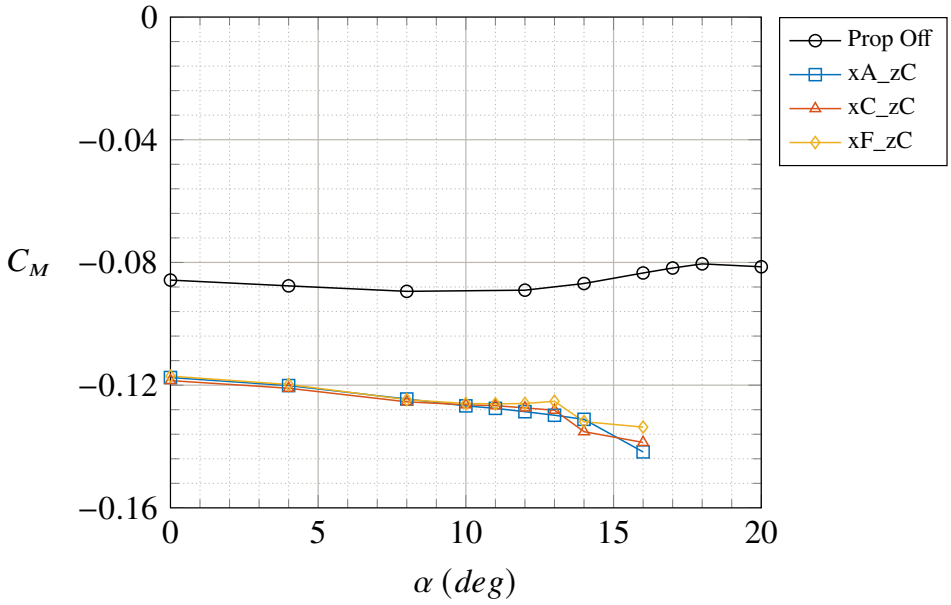

Figure 3.68: Wing pitching moment coefficient by varying the X-Position of DEP propellers with zC fixed - No flap - $V_\infty = 20\ m/s$ - $Re_\infty = 5.48 \cdot 10^5$ - $RPM_{DEP} = 7000$ (In-Board Up) - STAR-CCM+

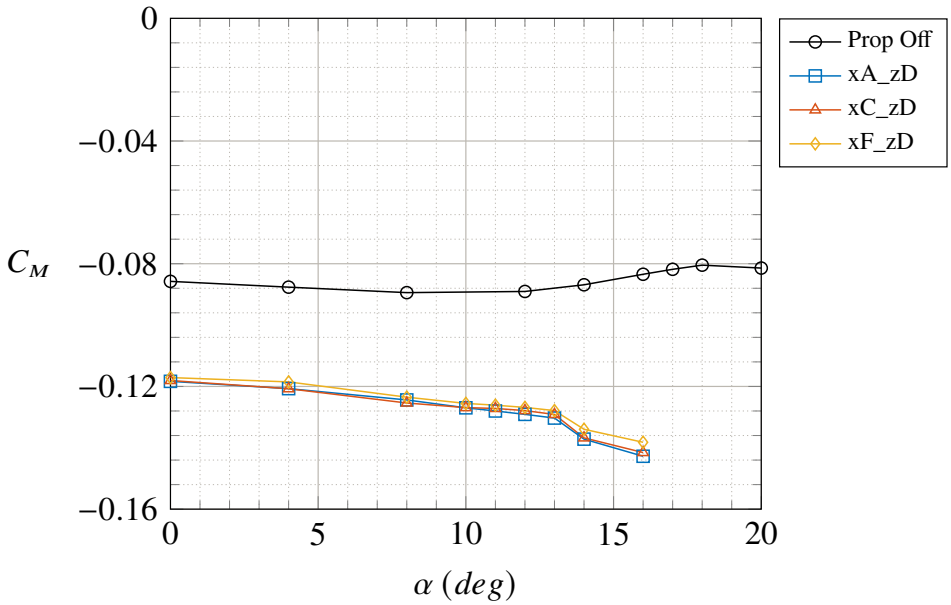

Figure 3.69: Wing pitching moment coefficient by varying the X-Position of DEP propellers with zD fixed - No flap - $V_\infty = 20\ m/s$ - $Re_\infty = 5.48 \cdot 10^5$ - $RPM_{DEP} = 7000$ (In-Board Up) - STAR-CCM+

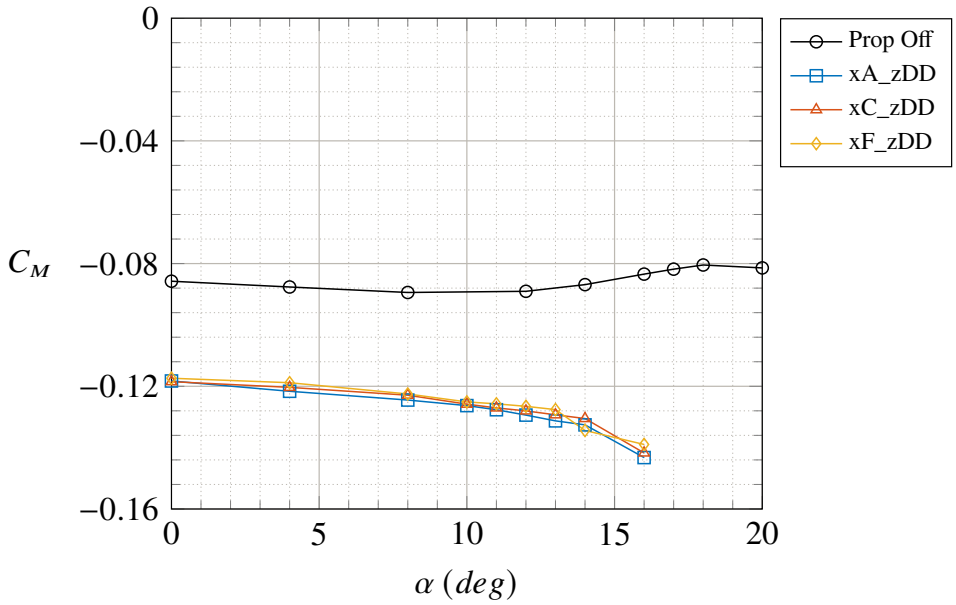

Figure 3.70: Wing pitching moment coefficient by varying the X-Position of DEP propellers with zDD fixed - No flap - $V_\infty = 20\ m/s$ - $Re_\infty = 5.48 \cdot 10^5$ - $RPM_{DEP} = 7000$ (In-Board Up) - STAR-CCM+

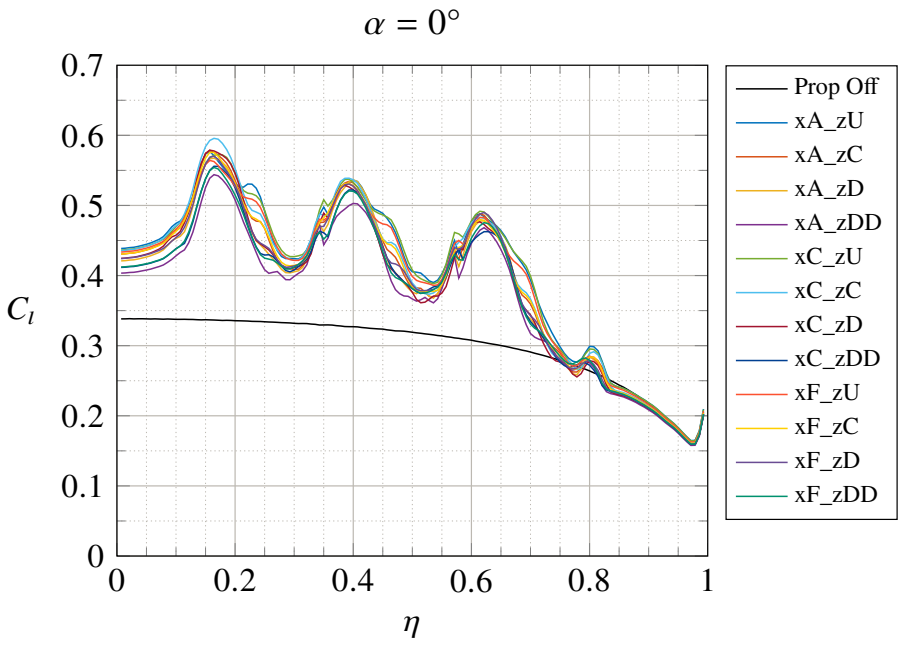

Figure 3.71: Wing load distribution by varying the position of DEP propellers - No flap - $V_\infty = 20\ m/s$ - $Re_\infty = 5.48 \cdot 10^5$ - $RPM_{DEP} = 7000$ (In-Board Up) - STAR-CCM+

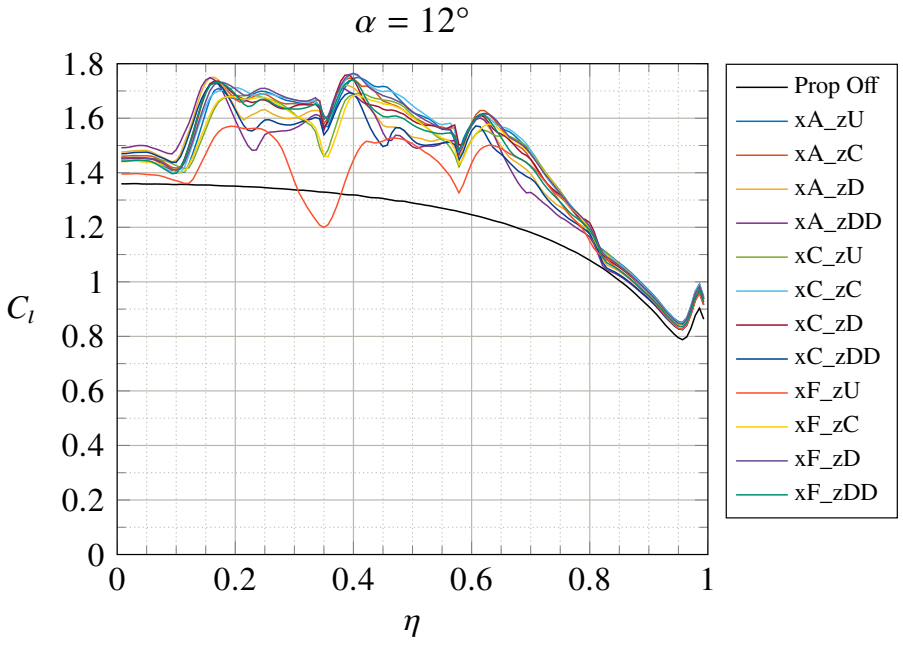

Figure 3.72: Wing load distribution by varying the position of DEP propellers - No flap - $V_\infty = 20\ m/s$ - $Re_\infty = 5.48 \cdot 10^5$ - $RPM_{DEP} = 7000$ (In-Board Up) - STAR-CCM+

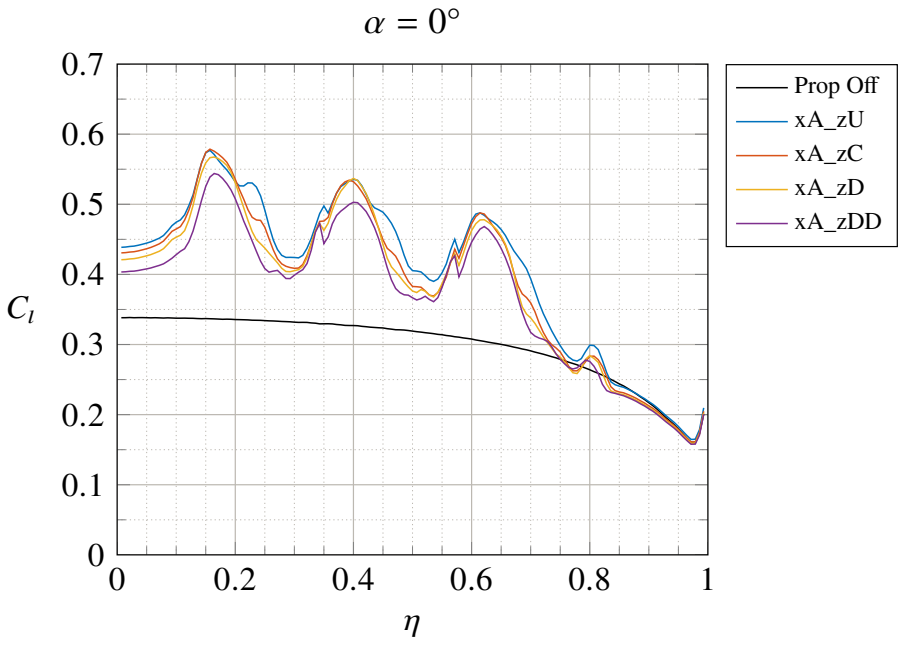

Figure 3.73: Wing load distribution by varying the Z-Position of DEP propellers with xA fixed - No flap - $V_\infty = 20\ m/s$ - $Re_\infty = 5.48 \cdot 10^5$ - $RPM_{DEP} = 7000$ (In-Board Up) - STAR-CCM+

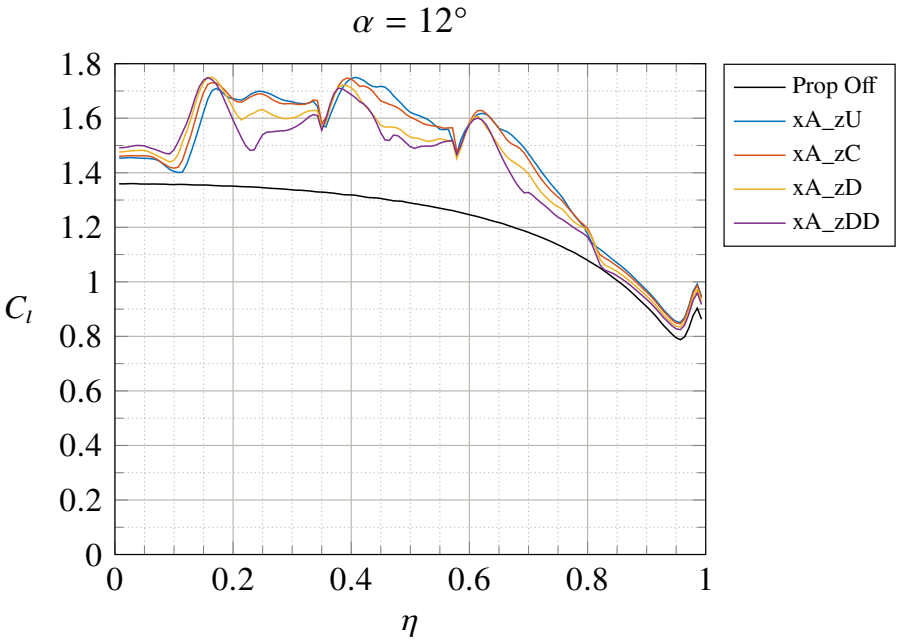

Figure 3.74: Wing load distribution by varying the Z-Position of DEP propellers with xA fixed - No flap - $V_\infty = 20\ m/s$ - $Re_\infty = 5.48 \cdot 10^5$ - $RPM_{DEP} = 7000$ (In-Board Up) - STAR-CCM+

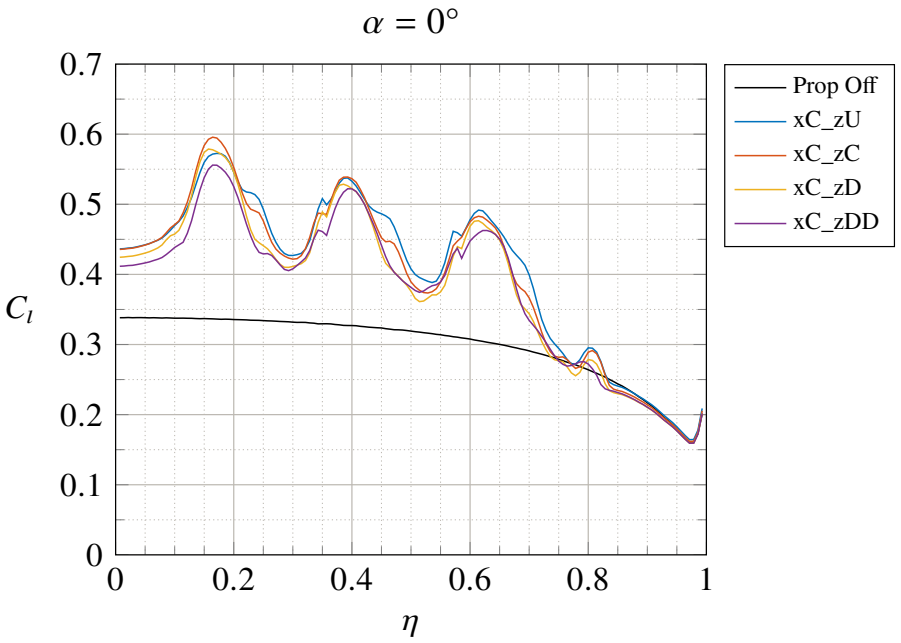

Figure 3.75: Wing load distribution by varying the Z-Position of DEP propellers with xC fixed - No flap - $V_\infty = 20\ m/s$ - $Re_\infty = 5.48 \cdot 10^5$ - $RPM_{DEP} = 7000$ (In-Board Up) - STAR-CCM+

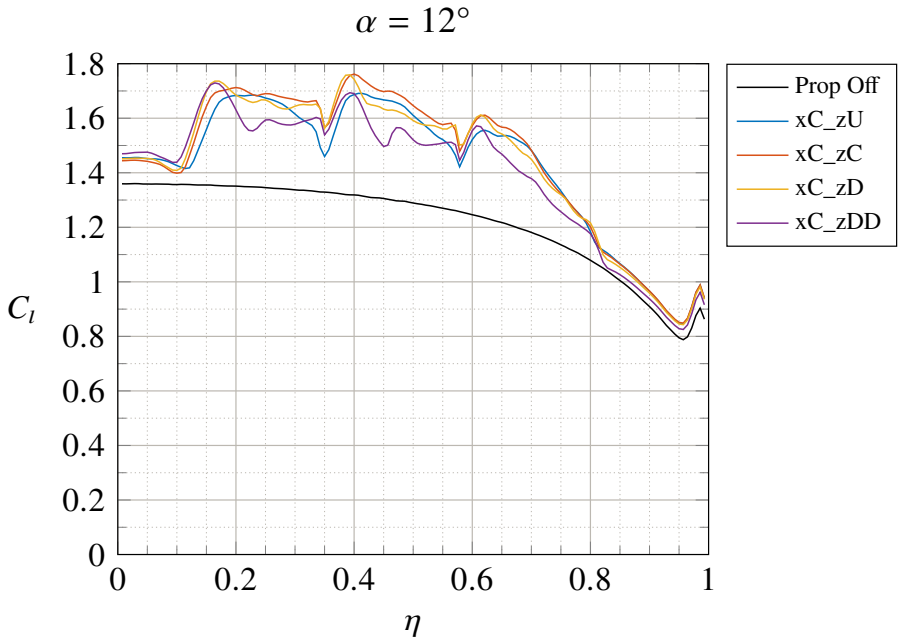

Figure 3.76: Wing load distribution by varying the Z-Position of DEP propellers with xC fixed - No flap - $V_\infty = 20\ m/s$ - $Re_\infty = 5.48 \cdot 10^5$ - $RPM_{DEP} = 7000$ (In-Board Up) - STAR-CCM+

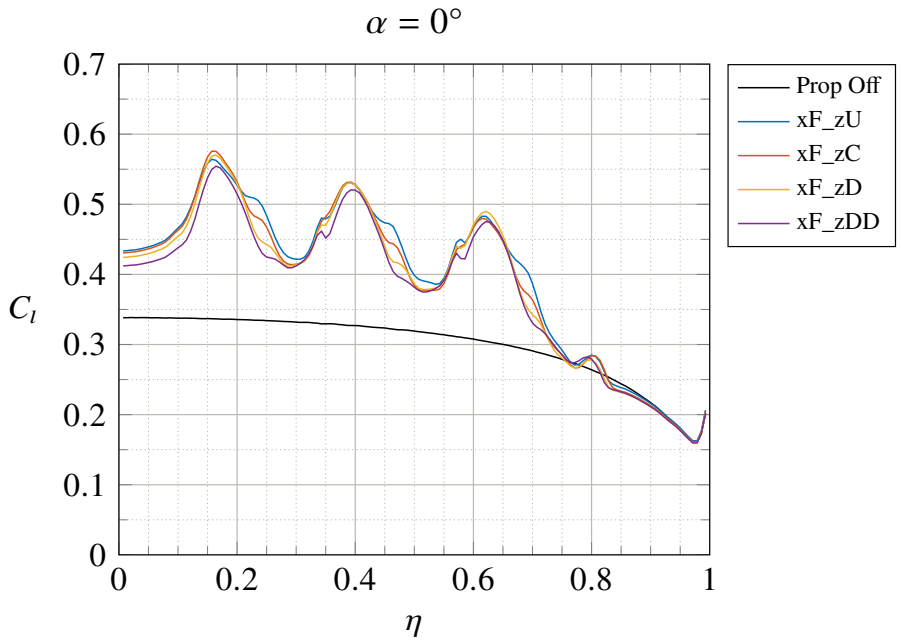

Figure 3.77: Wing load distribution by varying the Z-Position of DEP propellers with xF fixed - No flap - $V_\infty = 20\ m/s$ - $Re_\infty = 5.48 \cdot 10^5$ - $RPM_{DEP} = 7000$ (In-Board Up) - STAR-CCM+

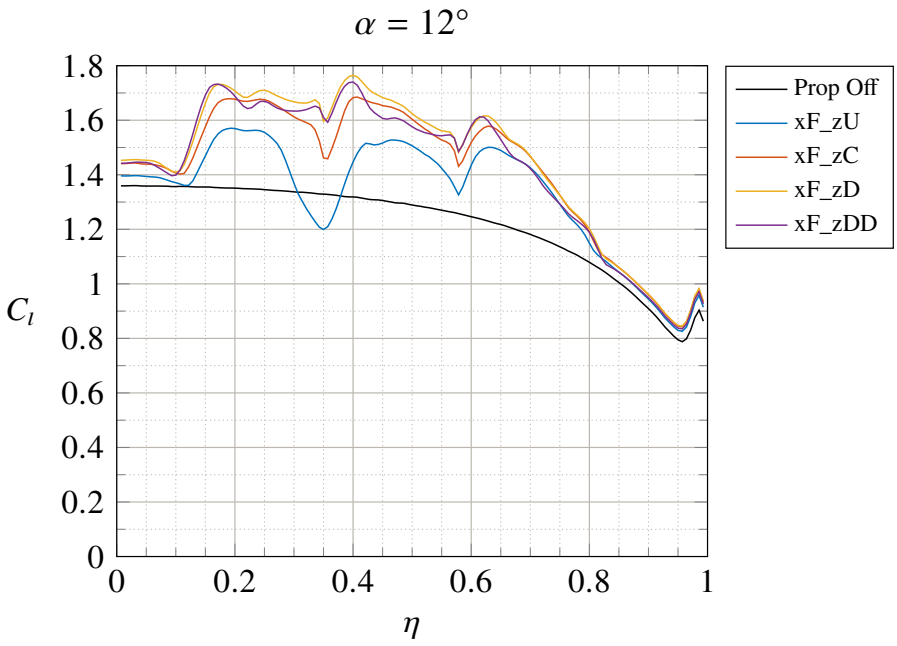

Figure 3.78: Wing load distribution by varying the Z-Position of DEP propellers with xF fixed - No flap - $V_\infty = 20\ m/s$ - $Re_\infty = 5.48 \cdot 10^5$ - $RPM_{DEP} = 7000$ (In-Board Up) - STAR-CCM+

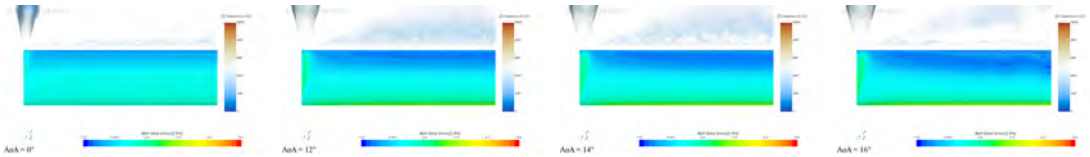

(a) $\alpha = 0°$ - Prop Off **(b)** $\alpha = 12°$ - Prop Off **(c)** $\alpha = 14°$ - Prop Off **(d)** $\alpha = 16°$ - Prop Off

Figure 3.79: Contours of the X-Component of wall shear stress and Q-Criterion isosurfaces for the prop off condition - No flap - $V_\infty = 20\ m/s$ - $Re_\infty = 5.48 \cdot 10^5$ - STAR-CCM+

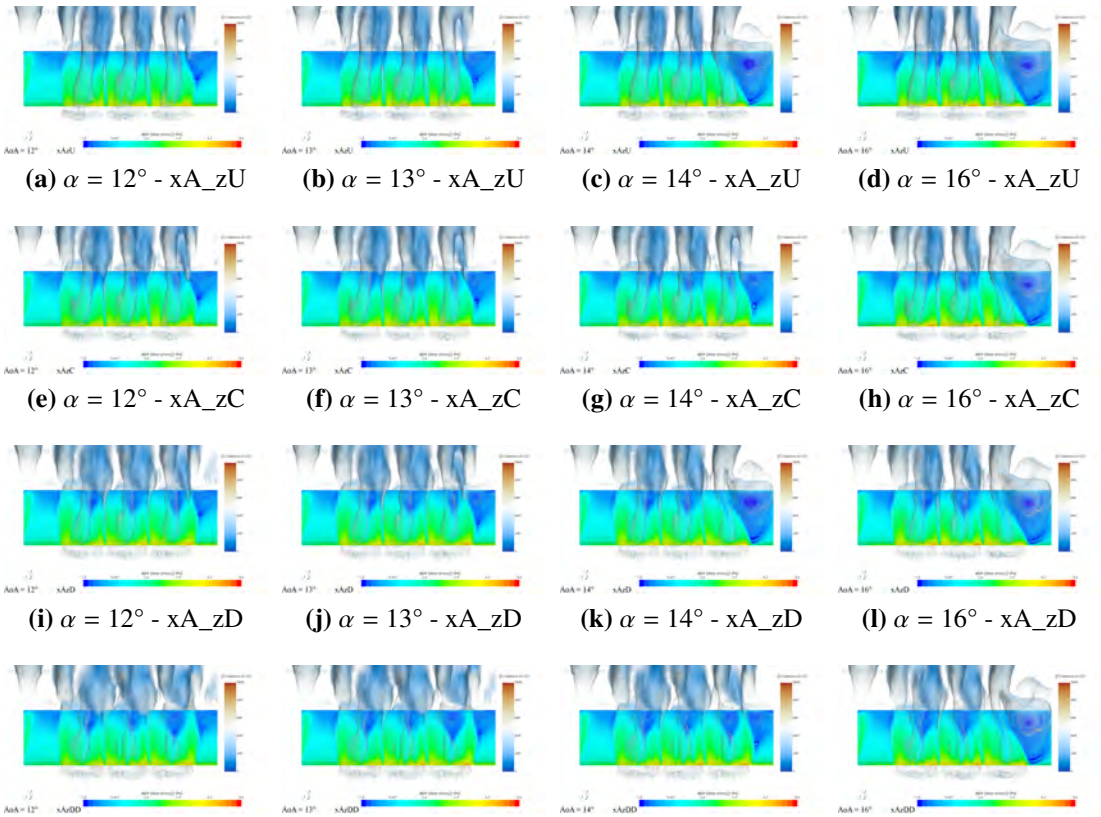

(a) α = 12° - xA_zU **(b)** α = 13° - xA_zU **(c)** α = 14° - xA_zU **(d)** α = 16° - xA_zU

(e) α = 12° - xA_zC **(f)** α = 13° - xA_zC **(g)** α = 14° - xA_zC **(h)** α = 16° - xA_zC

(i) α = 12° - xA_zD **(j)** α = 13° - xA_zD **(k)** α = 14° - xA_zD **(l)** α = 16° - xA_zD

(m) α = 12° - xA_zDD **(n)** α = 13° - xA_zDD **(o)** α = 14° - xA_zDD **(p)** α = 16° - xA_zDD

Figure 3.80: Contours of the X-Component of wall shear stress and Q-Criterion isosurfaces for xA position fixed and varying the Z-Position of DEP propellers - No flap - V_∞ = 20 m/s - $Re_\infty = 5.48 \cdot 10^5$ - RPM_{DEP} = 7000 (In-Board Up) - STAR-CCM+

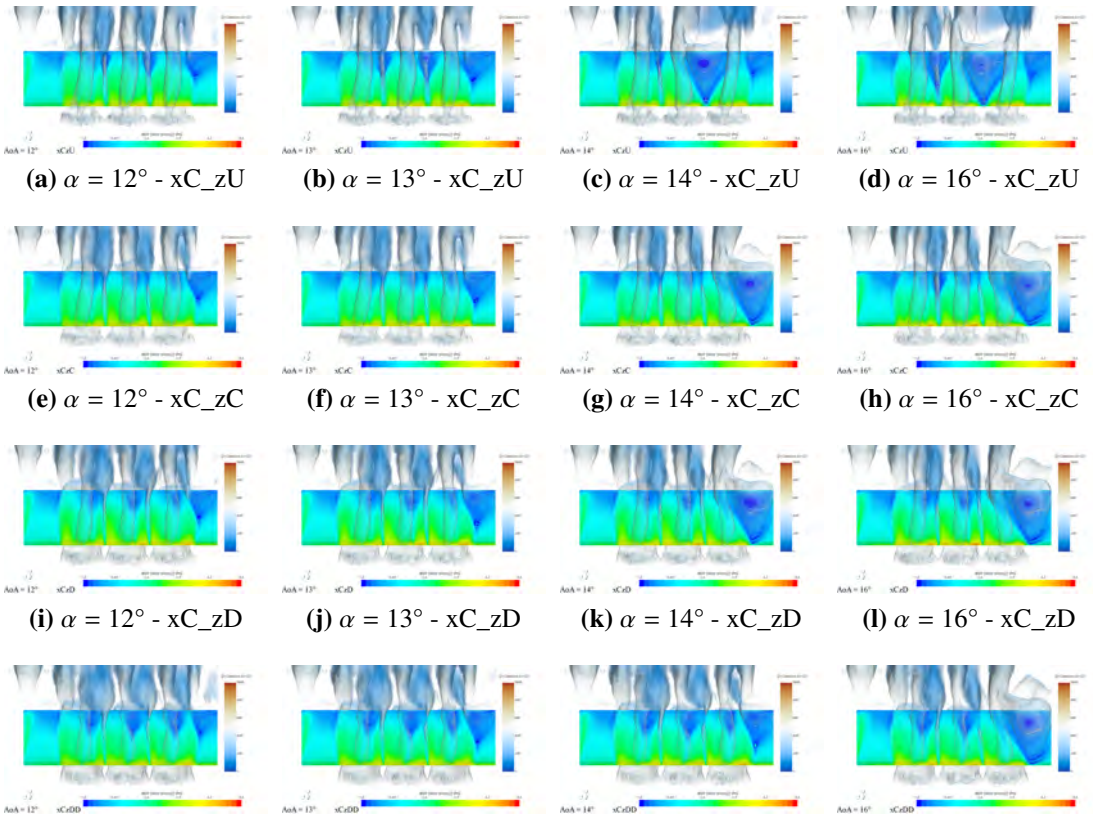

(a) α = 12° - xC_zU **(b)** α = 13° - xC_zU **(c)** α = 14° - xC_zU **(d)** α = 16° - xC_zU

(e) α = 12° - xC_zC **(f)** α = 13° - xC_zC **(g)** α = 14° - xC_zC **(h)** α = 16° - xC_zC

(i) α = 12° - xC_zD **(j)** α = 13° - xC_zD **(k)** α = 14° - xC_zD **(l)** α = 16° - xC_zD

(m) α = 12° - xC_zDD **(n)** α = 13° - xC_zDD **(o)** α = 14° - xC_zDD **(p)** α = 16° - xC_zDD

Figure 3.81: Contours of the X-Component of wall shear stress and Q-Criterion isosurfaces for xC position fixed and varying the Z-Position of DEP propellers - No flap - V_∞ = 20 m/s - $Re_\infty = 5.48 \cdot 10^5$ - RPM_{DEP} = 7000 (In-Board Up) - STAR-CCM+

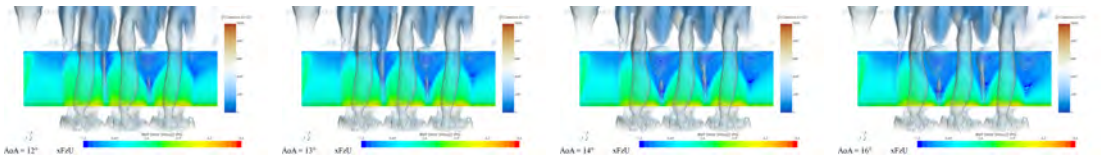

(a) α = 12° - xF_zU **(b)** α = 13° - xF_zU **(c)** α = 14° - xF_zU **(d)** α = 16° - xF_zU

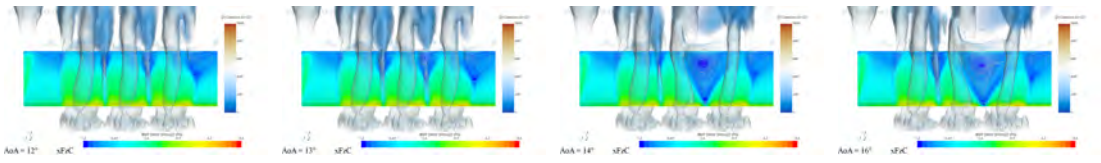

(e) α = 12° - xF_zC **(f)** α = 13° - xF_zC **(g)** α = 14° - xF_zC **(h)** α = 16° - xF_zC

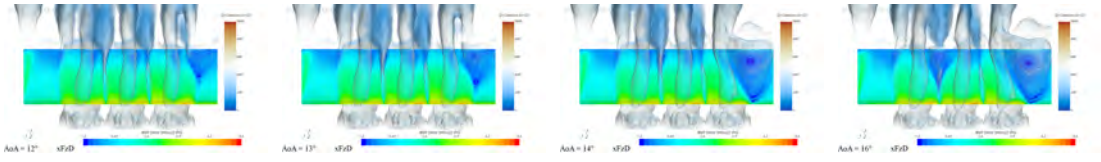

(i) α = 12° - xF_zD **(j)** α = 13° - xF_zD **(k)** α = 14° - xF_zD **(l)** α = 16° - xF_zD

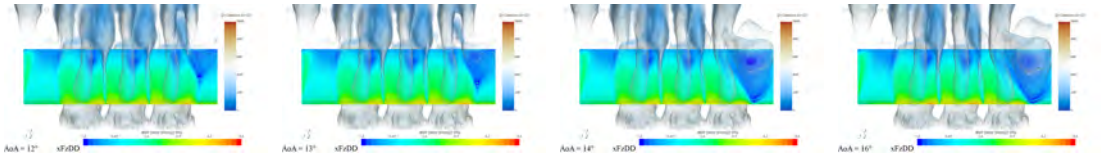

(m) α = 12° - xF_zDD **(n)** α = 13° - xF_zDD **(o)** α = 14° - xF_zDD **(p)** α = 16° - xF_zDD

Figure 3.82: Contours of the X-Component of wall shear stress and Q-Criterion isosurfaces for xF position fixed and varying the Z-Position of DEP propellers - No flap - V_∞ = 20 m/s - $Re_\infty = 5.48 \cdot 10^5$ - RPM_{DEP} = 7000 (In-Board Up) - STAR-CCM+

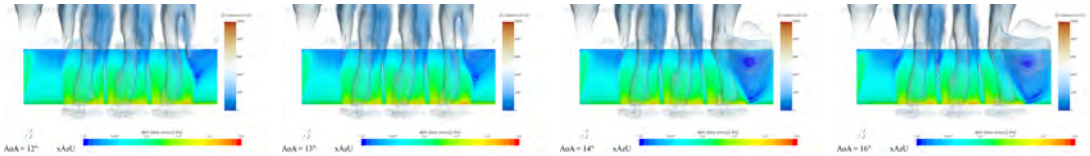

(a) $\alpha = 12°$ - xA_zU **(b)** $\alpha = 13°$ - xA_zU **(c)** $\alpha = 14°$ - xA_zU **(d)** $\alpha = 16°$ - xA_zU

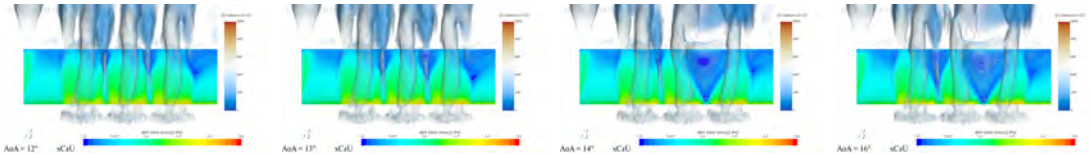

(e) $\alpha = 12°$ - xC_zU **(f)** $\alpha = 13°$ - xC_zU **(g)** $\alpha = 14°$ - xC_zU **(h)** $\alpha = 16°$ - xC_zU

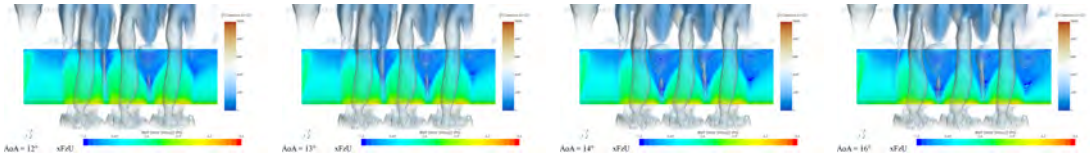

(i) $\alpha = 12°$ - xF_zU **(j)** $\alpha = 13°$ - xF_zU **(k)** $\alpha = 14°$ - xF_zU **(l)** $\alpha = 16°$ - xF_zU

Figure 3.83: Contours of the X-Component of wall shear stress and Q-Criterion isosurfaces for zU position fixed and varying the X-Position of DEP propellers - No flap - $V_\infty = 20\ m/s$ - $Re_\infty = 5.48 \cdot 10^5$ - $RPM_{DEP} = 7000$ (In-Board Up) - STAR-CCM+

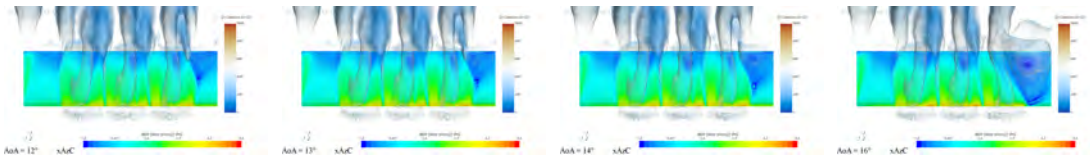

(a) $\alpha = 12°$ - xA_zC **(b)** $\alpha = 13°$ - xA_zC **(c)** $\alpha = 14°$ - xA_zC **(d)** $\alpha = 16°$ - xA_zC

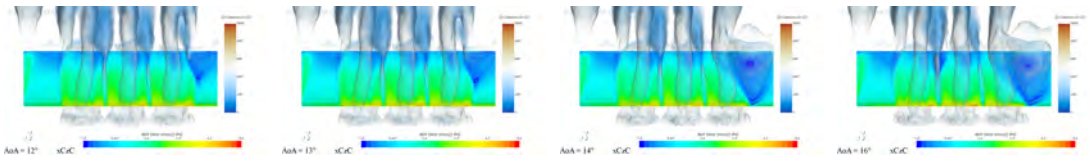

(e) $\alpha = 12°$ - xC_zC **(f)** $\alpha = 13°$ - xC_zC **(g)** $\alpha = 14°$ - xC_zC **(h)** $\alpha = 16°$ - xC_zC

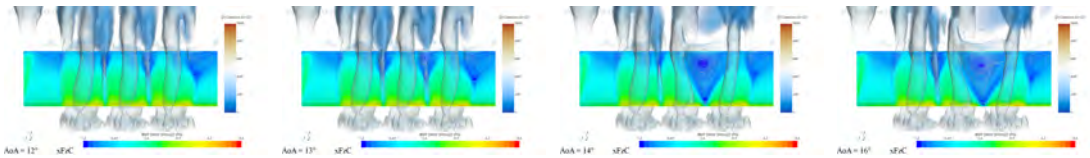

(i) $\alpha = 12°$ - xF_zC **(j)** $\alpha = 13°$ - xF_zC **(k)** $\alpha = 14°$ - xF_zC **(l)** $\alpha = 16°$ - xF_zC

Figure 3.84: Contours of the X-Component of wall shear stress and Q-Criterion isosurfaces for zC position fixed and varying the X-Position of DEP propellers - No flap - $V_\infty = 20\ m/s$ - $Re_\infty = 5.48 \cdot 10^5$ - $RPM_{DEP} = 7000$ (In-Board Up) - STAR-CCM+

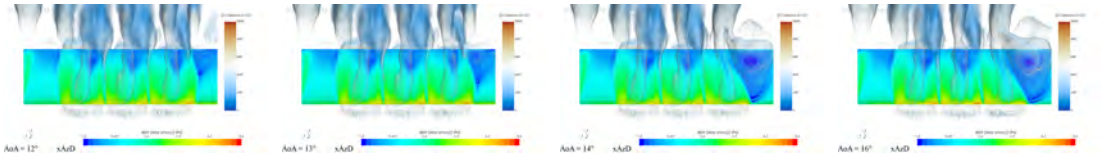

(a) $\alpha = 12°$ - xA_zD **(b)** $\alpha = 13°$ - xA_zD **(c)** $\alpha = 14°$ - xA_zD **(d)** $\alpha = 16°$ - xA_zD

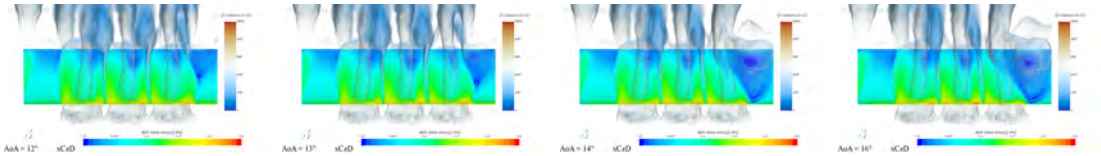

(e) $\alpha = 12°$ - xC_zD **(f)** $\alpha = 13°$ - xC_zD **(g)** $\alpha = 14°$ - xC_zD **(h)** $\alpha = 16°$ - xC_zD

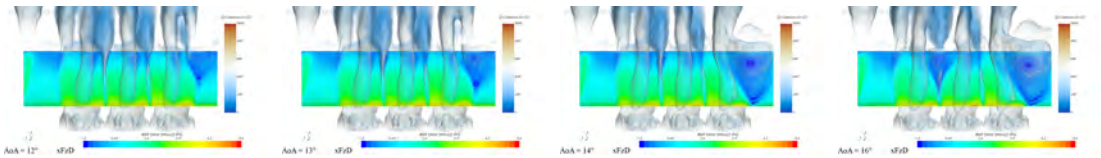

(i) $\alpha = 12°$ - xF_zD **(j)** $\alpha = 13°$ - xF_zD **(k)** $\alpha = 14°$ - xF_zD **(l)** $\alpha = 16°$ - xF_zD

Figure 3.85: Contours of the X-Component of wall shear stress and Q-Criterion isosurfaces for zD position fixed and varying the X-Position of DEP propellers - No flap - $V_\infty = 20\ m/s$ - $Re_\infty = 5.48 \cdot 10^5$ - $RPM_{DEP} = 7000$ (In-Board Up) - STAR-CCM+

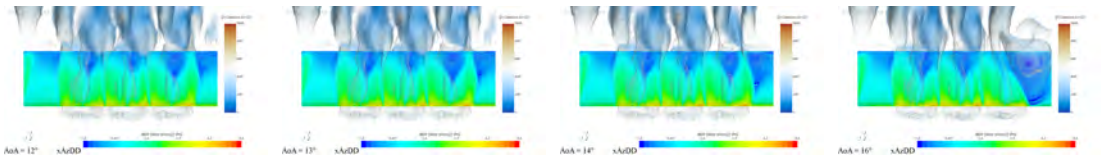

(a) $\alpha = 12°$ - xA_zDD **(b)** $\alpha = 13°$ - xA_zDD **(c)** $\alpha = 14°$ - xA_zDD **(d)** $\alpha = 16°$ - xA_zDD

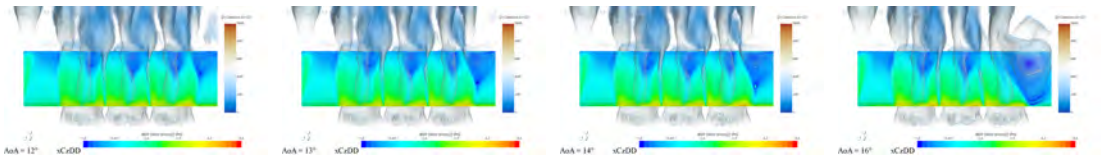

(e) $\alpha = 12°$ - xC_zDD **(f)** $\alpha = 13°$ - xC_zDD **(g)** $\alpha = 14°$ - xC_zDD **(h)** $\alpha = 16°$ - xC_zDD

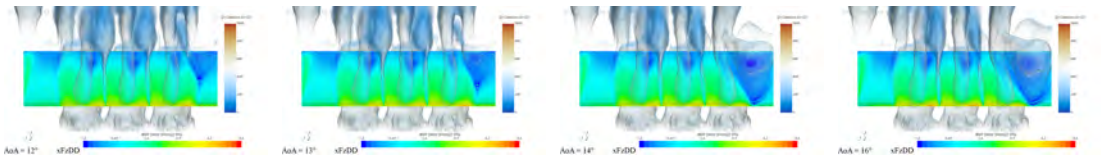

(i) $\alpha = 12°$ - xF_zDD **(j)** $\alpha = 13°$ - xF_zDD **(k)** $\alpha = 14°$ - xF_zDD **(l)** $\alpha = 16°$ - xF_zDD

Figure 3.86: Contours of the X-Component of wall shear stress and Q-Criterion isosurfaces for zDD position fixed and varying the X-Position of DEP propellers - No flap - $V_\infty = 20\ m/s$ - $Re_\infty = 5.48 \cdot 10^5$ - $RPM_{DEP} = 7000$ (In-Board Up) - STAR-CCM+

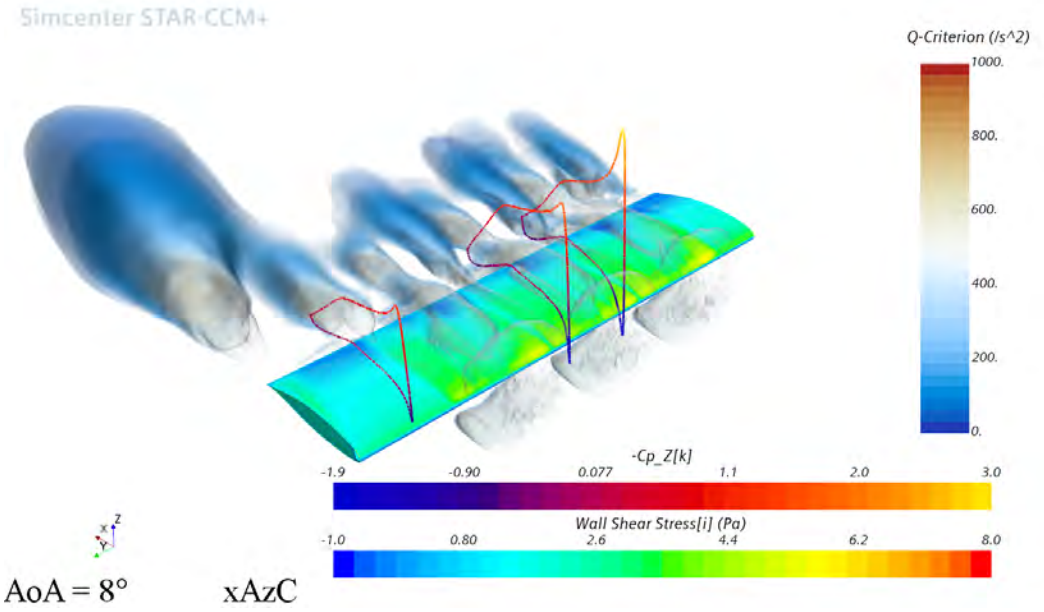

(a) $\alpha = 8°$ - xA_zC

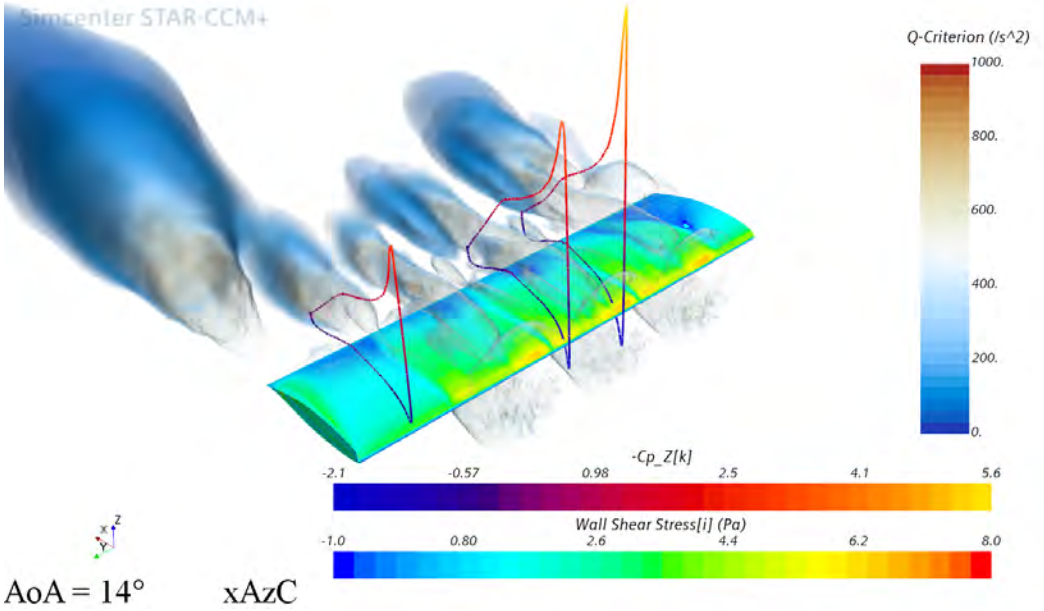

(b) $\alpha = 14°$ - xA_zC

Figure 3.87: 3D view of pressure coefficient distribution on three different sections (0.65 m, 0.75 m, 1.25 m) - No flap - $V_\infty = 20\ m/s$ - $Re_\infty = 5.48 \cdot 10^5$ - $RPM_{DEP} = 7000$ (In-Board Up) - STAR-CCM+

Some parameters of interest have been extracted from the results of the analyses. A simple linear regression was applied to the first three angles considered in the simulations, i.e. 0, 4 and 8 degrees, for lift, drag and pitching moment coefficient (see Fig. 3.88). In this way, a contour plot of lift curve slopes for the different cases was generated, Fig. 3.94. Generally speaking, moving up and forward the DEP propellers generates an increase in lift curve slope. Moreover, the value of the drag coefficient at $\alpha = 0°$, which reduces moving the propellers far from the wing leading edge, is represented in Fig. 3.89.

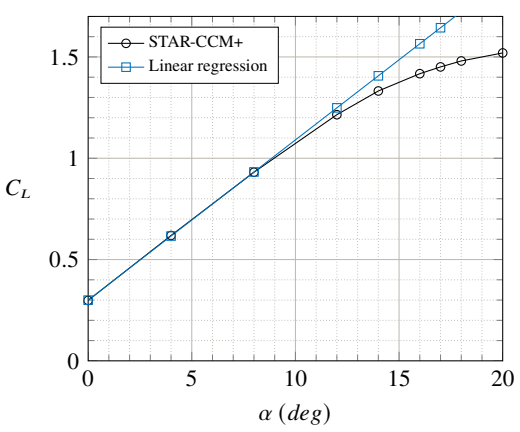

(a) C_L vs α

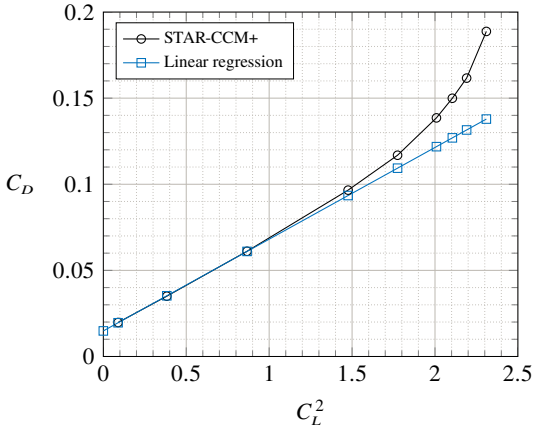

(b) C_D vs C_L^2

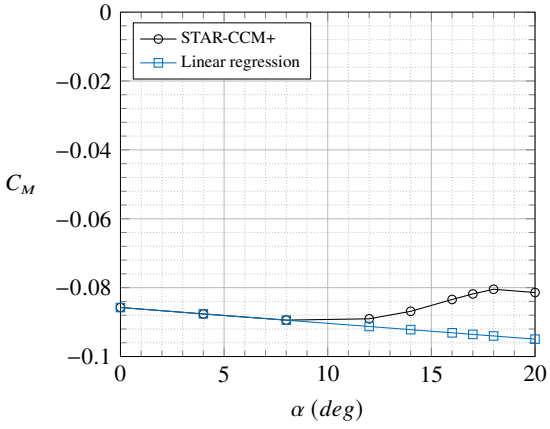

(c) C_M vs α

Figure 3.88: Examples of linear regression - Prop Off - No flap - $V_\infty = 20\ m/s$ - $Re_\infty = 5.48 \cdot 10^5$ - (STAR-CCM+)

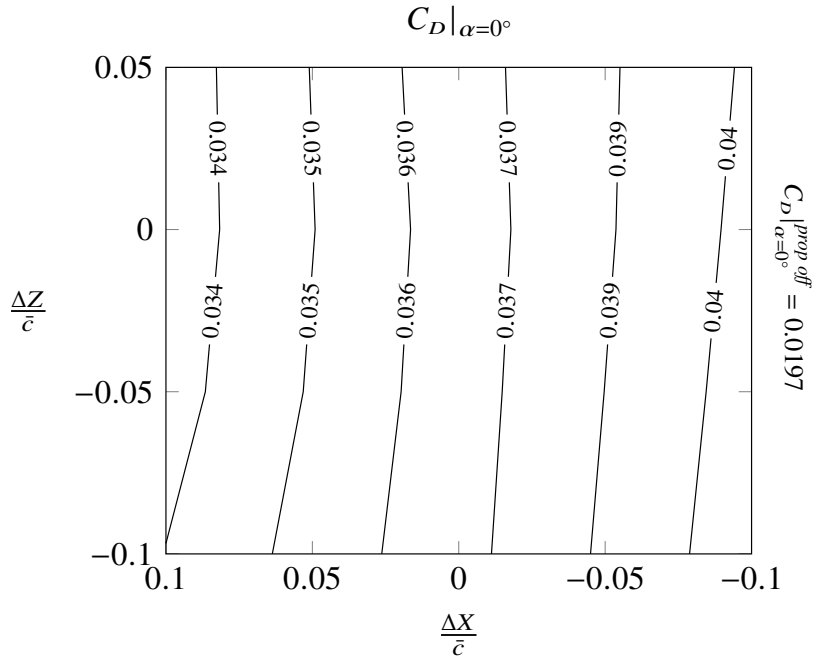

Figure 3.89: Values of $C_D|_{\alpha=0°}$ of wing by varying the position of DEP propellers - No flap - $V_\infty = 20\ m/s$ - $Re_\infty = 5.48 \cdot 10^5$ - $RPM_{DEP} = 7000$ (In-Board Up) - STAR-CCM+

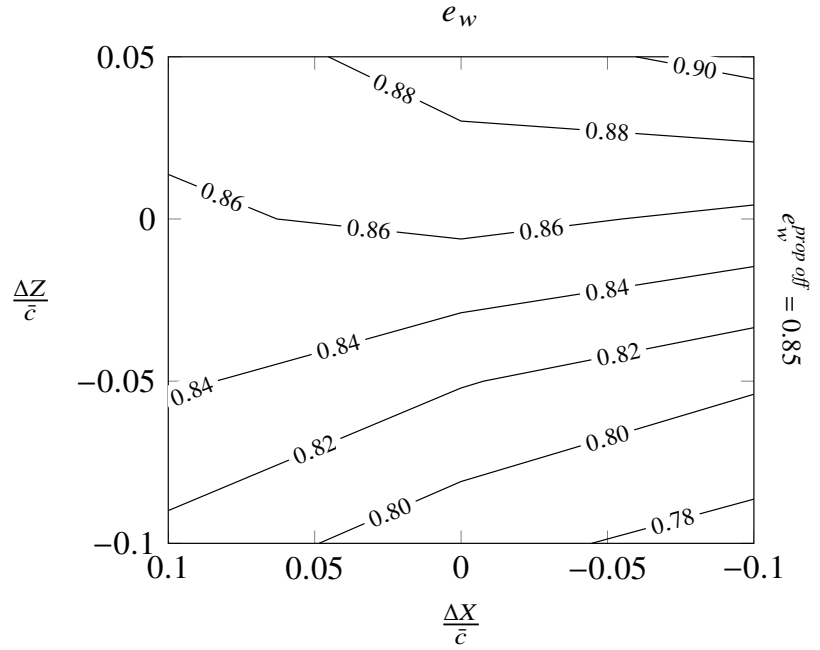

Figure 3.90: Values of the induced drag factor of wing by varying the position of DEP propellers - No flap - $V_\infty = 20\ m/s$ - $Re_\infty = 5.48 \cdot 10^5$ - $RPM_{DEP} = 7000$ (In-Board Up) - STAR-CCM+

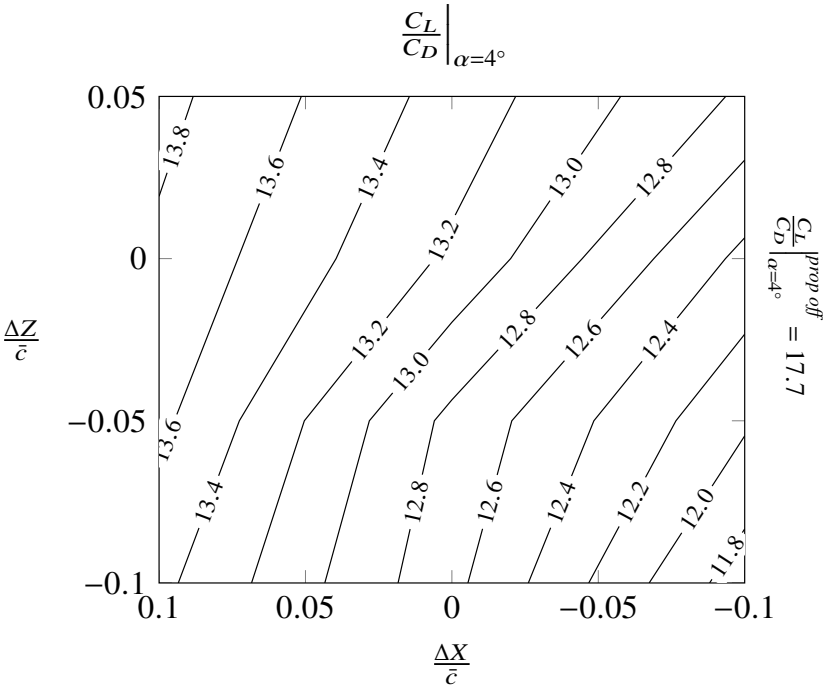

Figure 3.91: Wing efficiency at $\alpha = 4°$ by varying the position of DEP propellers - No flap - $V_\infty = 20\ m/s$ - $Re_\infty = 5.48 \cdot 10^5$ - $RPM_{DEP} = 7000$ (In-Board Up) - STAR-CCM+

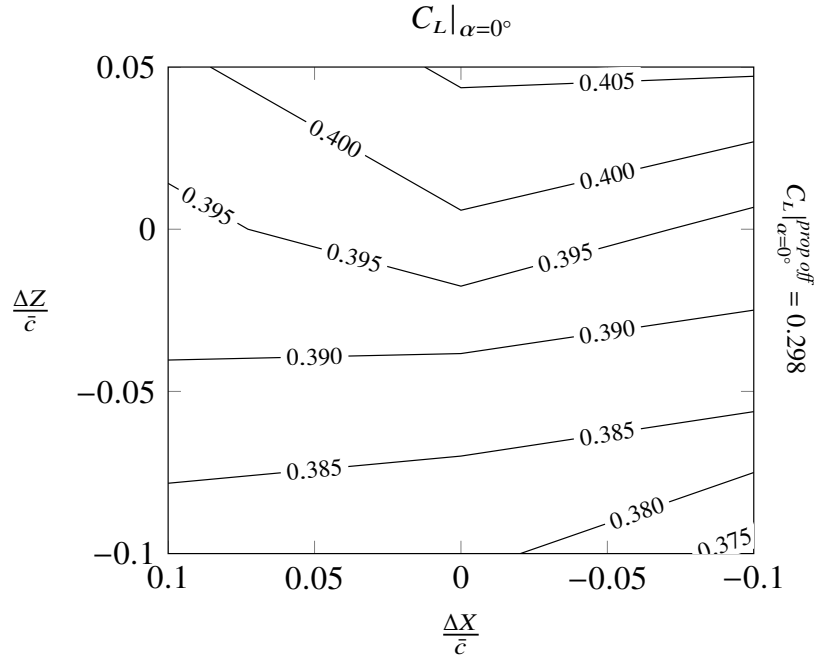

Figure 3.92: Values of $C_L|_{\alpha=0^\circ}$ of wing by varying the position of DEP propellers - No flap - $V_\infty = 20\ m/s$ - $Re_\infty = 5.48 \cdot 10^5$ - $RPM_{DEP} = 7000$ (In-Board Up) - STAR-CCM+

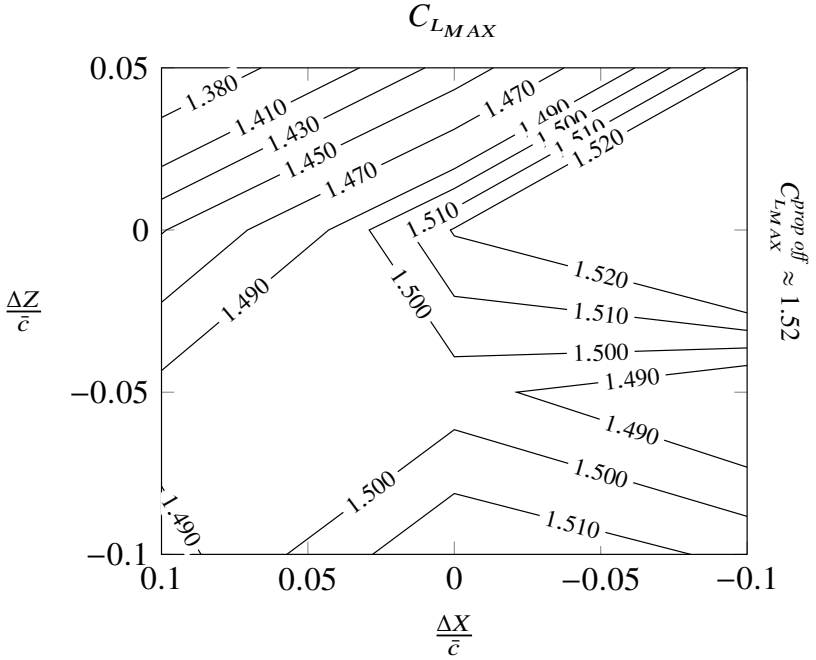

Figure 3.93: Values of $C_{L_{MAX}}$ (corresponding to different angles of attack) of wing by varying the position of DEP propellers - No flap - $V_\infty = 20\ m/s$ - $Re_\infty = 5.48 \cdot 10^5$ - $RPM_{DEP} = 7000$ (In-Board Up) - STAR-CCM+

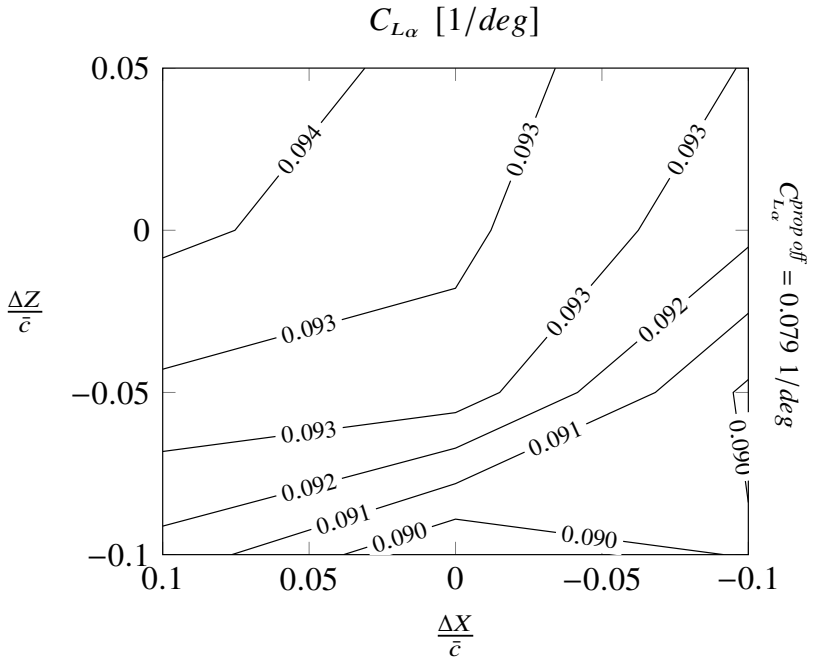

Figure 3.94: Lift curve slope of wing by varying the position of DEP propellers - No flap - $V_\infty = 20\ m/s$ - $Re_\infty = 5.48 \cdot 10^5$ - $RPM_{DEP} = 7000$ (In-Board Up) - STAR-CCM+

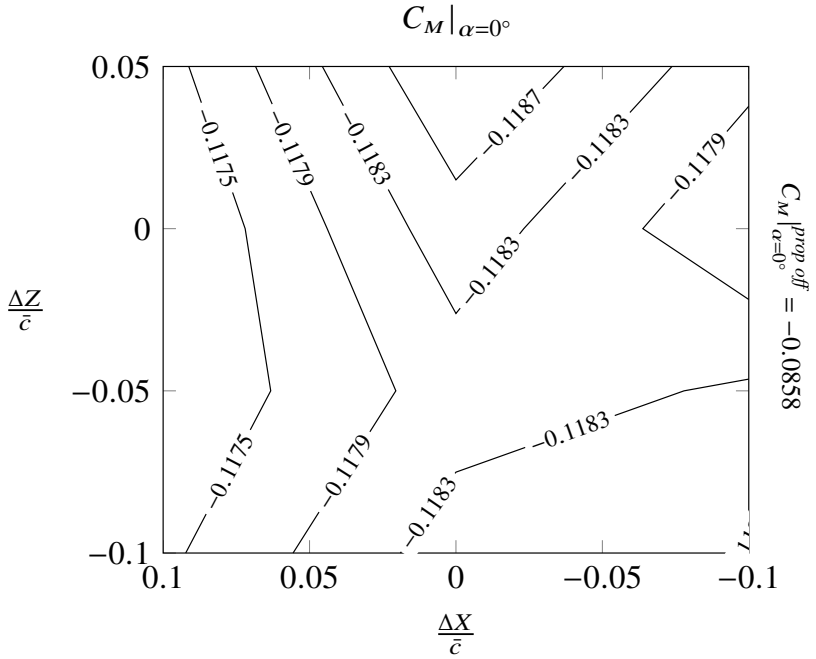

Figure 3.95: Values of $C_M|_{\alpha=0°}$ of wing by varying the position of DEP propellers - No flap - $V_\infty = 20\ m/s$ - $Re_\infty = 5.48 \cdot 10^5$ - $RPM_{DEP} = 7000$ (In-Board Up) - STAR-CCM+

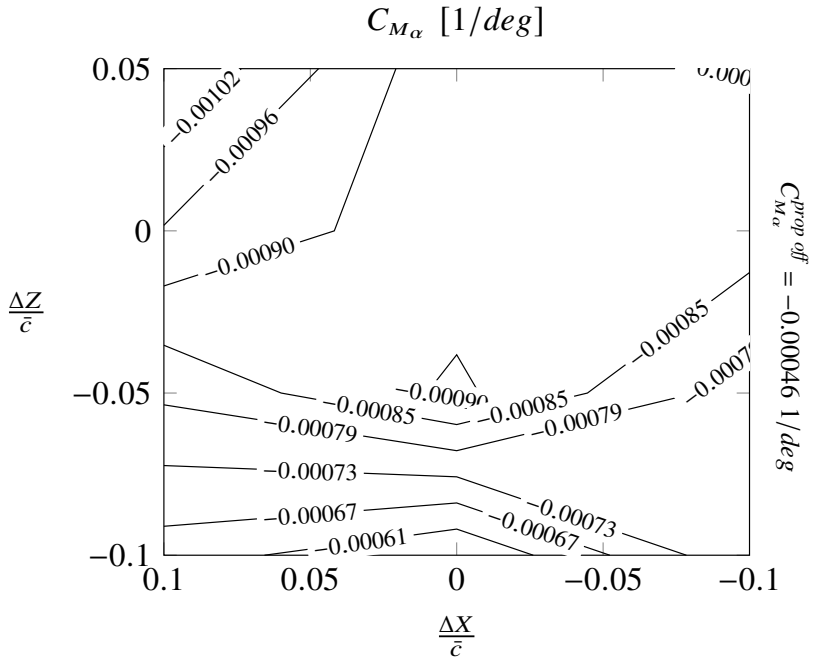

Figure 3.96: Pitching moment curve slope of wing by varying the position of DEP propellers - No flap - $V_\infty = 20\ m/s$ - $Re_\infty = 5.48 \cdot 10^5$ - $RPM_{DEP} = 7000$ (In-Board Up) - STAR-CCM+

3.3.3 DEP effects on flapped configuration (15 deg)

The same analyses presented in the previous section were performed for the flapped configuration with 15 degrees of deflection (Fig. 3.97). Fig. 3.98 represents the several lift curves for each position. The flapped configuration is more "sensitive" to a change in DEP propellers position, respect to the clean configuration. In this case, the highest maximum lift coefficient is reached with the xA_zD position, while a ruinous stall behaviour is obtained with the xF_zU position. Fixing an X-Position of DEP propellers, the upper position zU always leads to the lowest maximum lift coefficient and to an anticipated stall, while for low values of the angle of attack this position leads to higher lift coefficient (Fig. 3.101, 3.102, 3.103). In general, the zD position seems to be the better choice in this configuration. The differences between the lift curves, by varying the X-Position for a fixed Z-Position, become less remarkable moving down the DEP propellers from the zU position.

Fixing an X-Position, the drag coefficient increases moving the DEP propellers from the zU to the zDD position, while, just like for the clean wing, distancing the propellers from the wing leading edge generates a drag reduction.

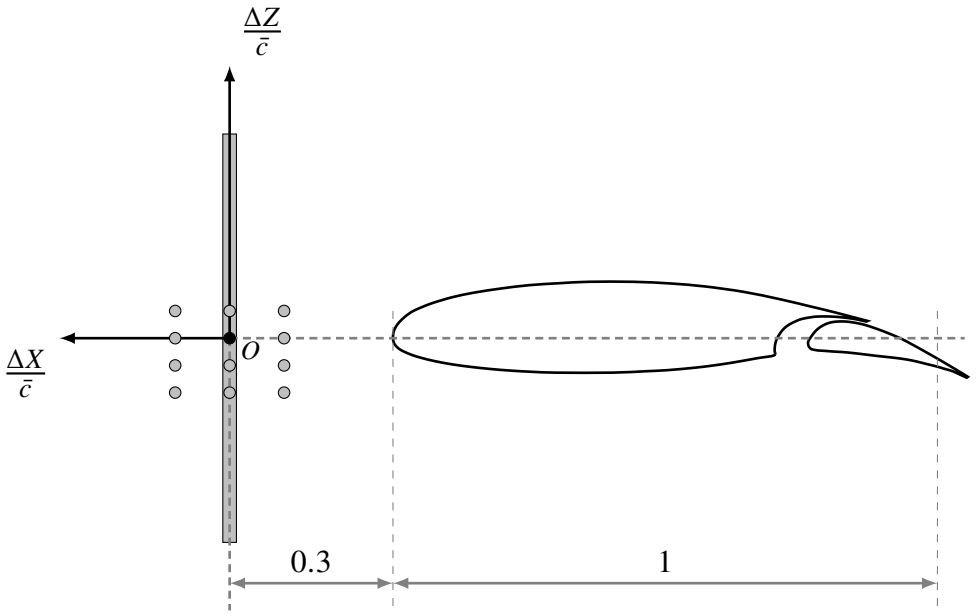

Figure 3.97: Sketch of dimensionless disks positions with respect to the wing leading edge

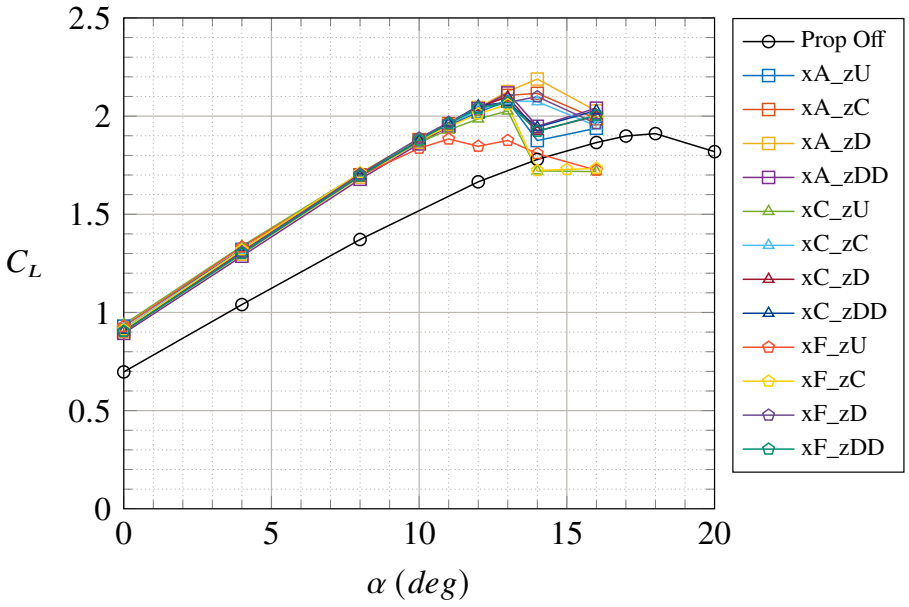

Figure 3.98: Wing lift curves by varying the position of DEP propellers - $\delta_f = 15°$ - $V_\infty = 20\ m/s$ - $Re_\infty = 5.48 \cdot 10^5$ - $RPM_{DEP} = 7000$ (In-Board Up) - STAR-CCM+

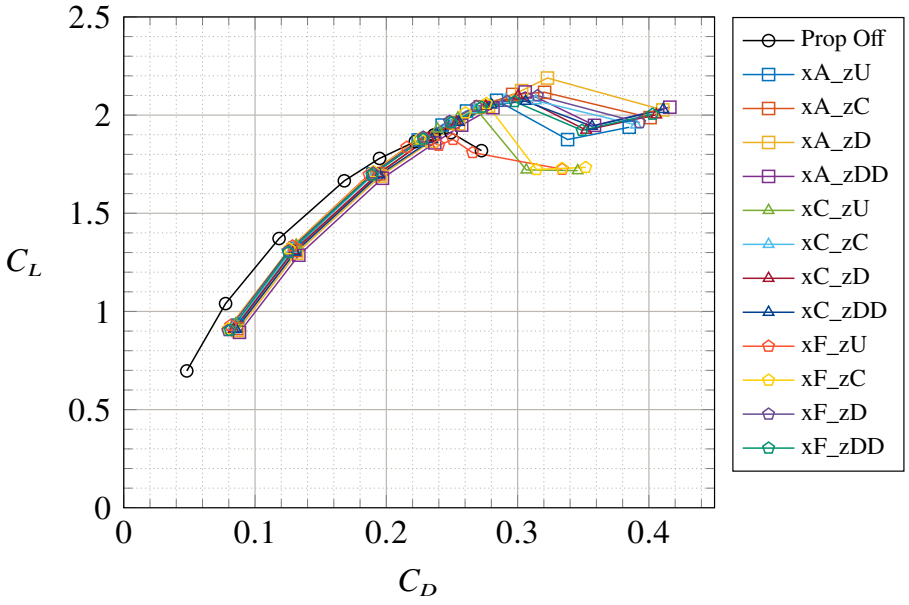

Figure 3.99: Wing drag polars by varying the position of DEP propellers - $\delta_f = 15°$ - $V_\infty = 20\ m/s$ - $Re_\infty = 5.48 \cdot 10^5$ - $RPM_{DEP} = 7000$ (In-Board Up) - STAR-CCM+

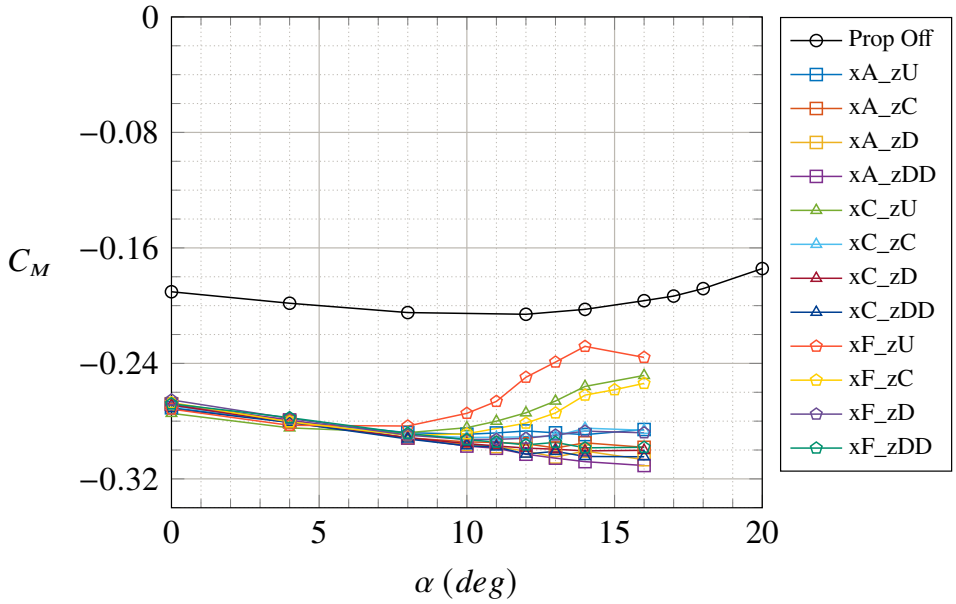

Figure 3.100: Wing pitching moment coefficient by varying the position of DEP propellers - $\delta_f = 15°$ - $V_\infty = 20\ m/s$ - $Re_\infty = 5.48 \cdot 10^5$ - $RPM_{DEP} = 7000$ (In-Board Up) - STAR-CCM+

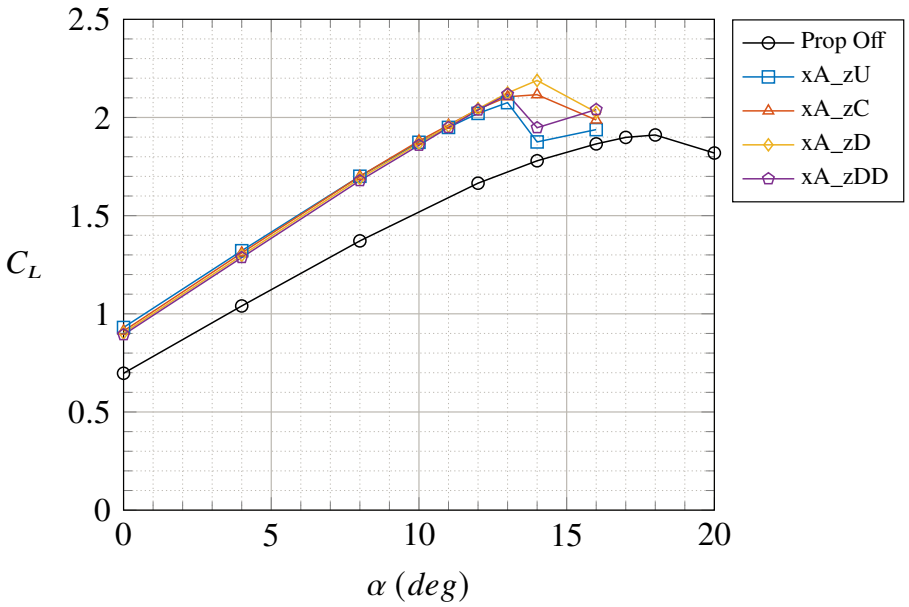

Figure 3.101: Wing lift curves by varying the Z-Position of DEP propellers with xA fixed - $\delta_f = 15°$ - $V_\infty = 20\ m/s$ - $Re_\infty = 5.48 \cdot 10^5$ - $RPM_{DEP} = 7000$ (In-Board Up) - STAR-CCM+

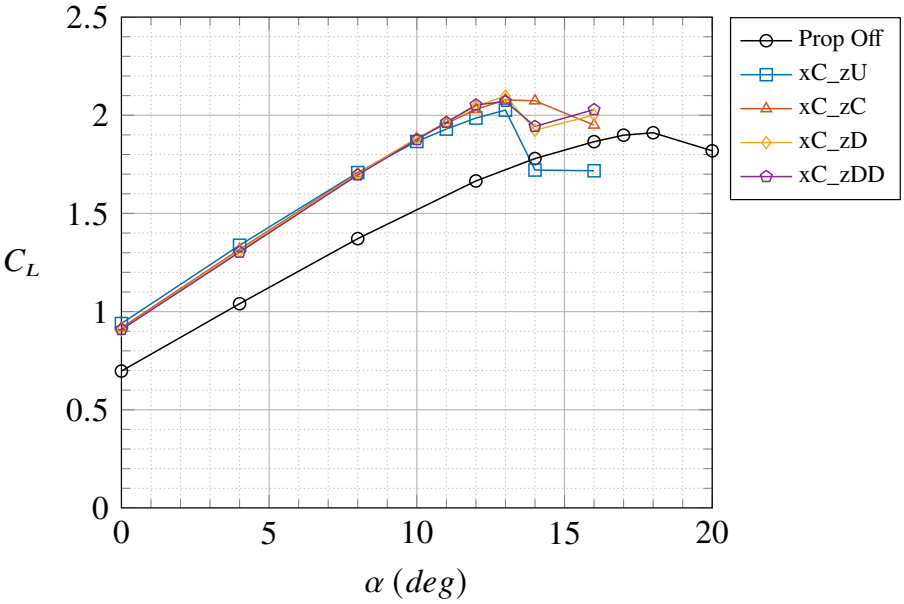

Figure 3.102: Wing lift curves by varying the Z-Position of DEP propellers with xC fixed - $\delta_f = 15°$ - $V_\infty = 20\ m/s$ - $Re_\infty = 5.48 \cdot 10^5$ - $RPM_{DEP} = 7000$ (In-Board Up) - STAR-CCM+

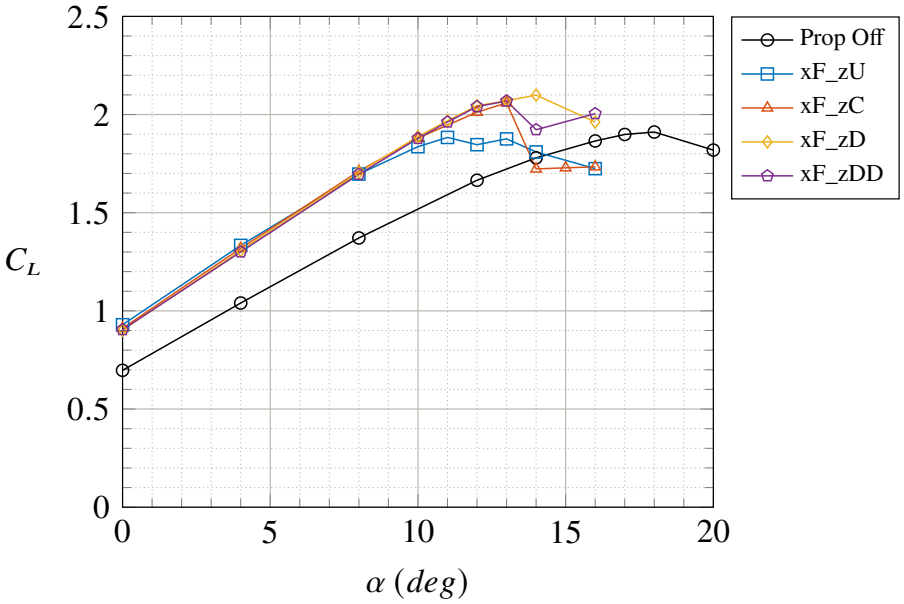

Figure 3.103: Wing lift curves by varying the Z-Position of DEP propellers with xF fixed - $\delta_f = 15°$ - $V_\infty = 20\ m/s$ - $Re_\infty = 5.48 \cdot 10^5$ - $RPM_{DEP} = 7000$ (In-Board Up) - STAR-CCM+

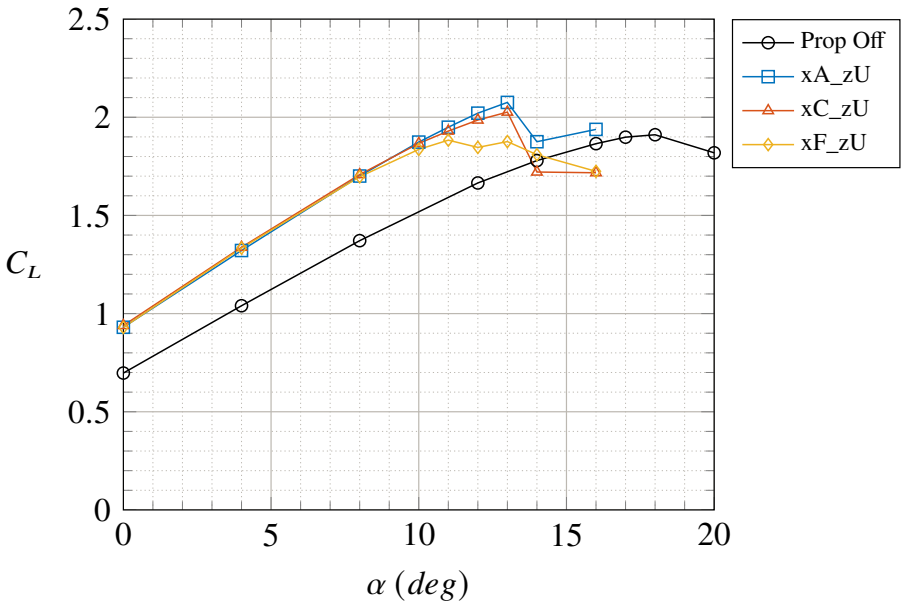

Figure 3.104: Wing lift curves by varying the X-Position of DEP propellers with zU fixed - $\delta_f = 15°$ - $V_\infty = 20\ m/s$ - $Re_\infty = 5.48 \cdot 10^5$ - $RPM_{DEP} = 7000$ (In-Board Up) - STAR-CCM+

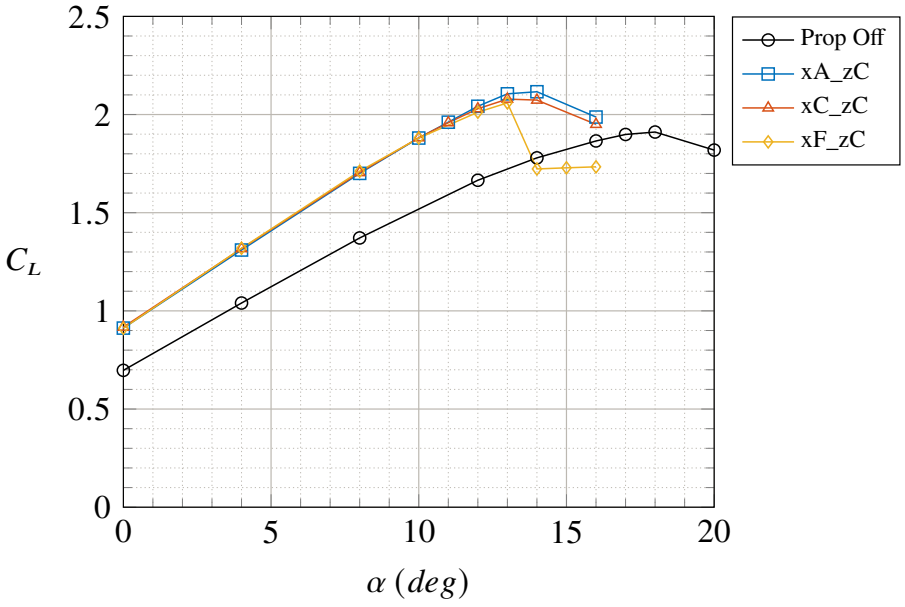

Figure 3.105: Wing lift curves by varying the X-Position of DEP propellers with zC fixed - $\delta_f = 15°$ - $V_\infty = 20\ m/s$ - $Re_\infty = 5.48 \cdot 10^5$ - $RPM_{DEP} = 7000$ (In-Board Up) - STAR-CCM+

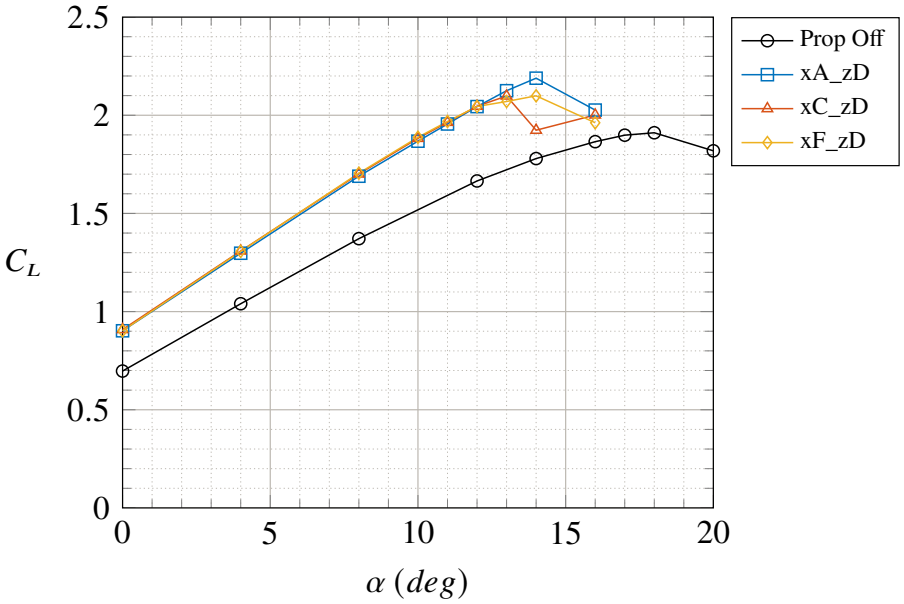

Figure 3.106: Wing lift curves by varying the X-Position of DEP propellers with zD fixed - $\delta_f = 15°$ - $V_\infty = 20\ m/s$ - $Re_\infty = 5.48 \cdot 10^5$ - $RPM_{DEP} = 7000$ (In-Board Up) - STAR-CCM+

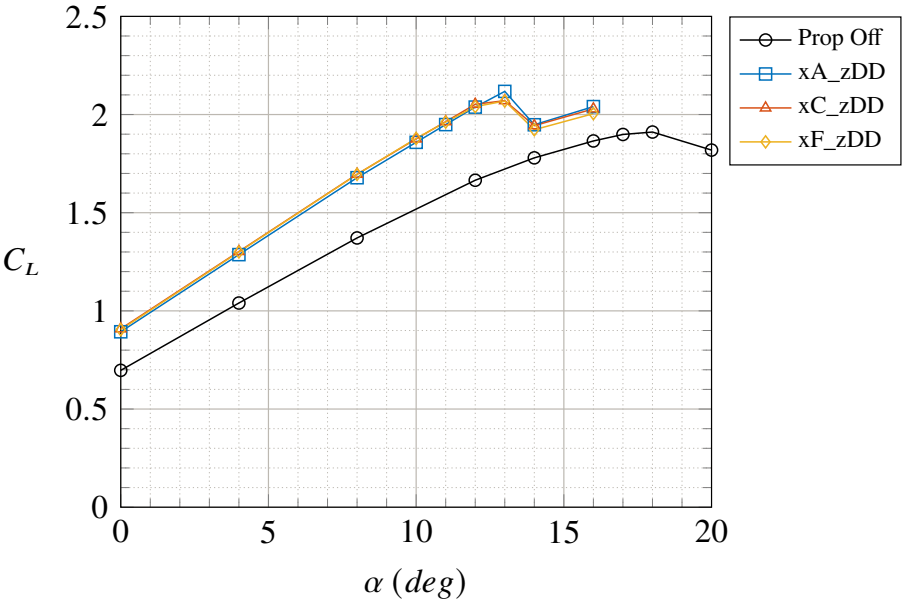

Figure 3.107: Wing lift curves by varying the X-Position of DEP propellers with zDD fixed - $\delta_f = 15°$ - $V_\infty = 20\ m/s$ - $Re_\infty = 5.48 \cdot 10^5$ - $RPM_{DEP} = 7000$ (In-Board Up) - STAR-CCM+

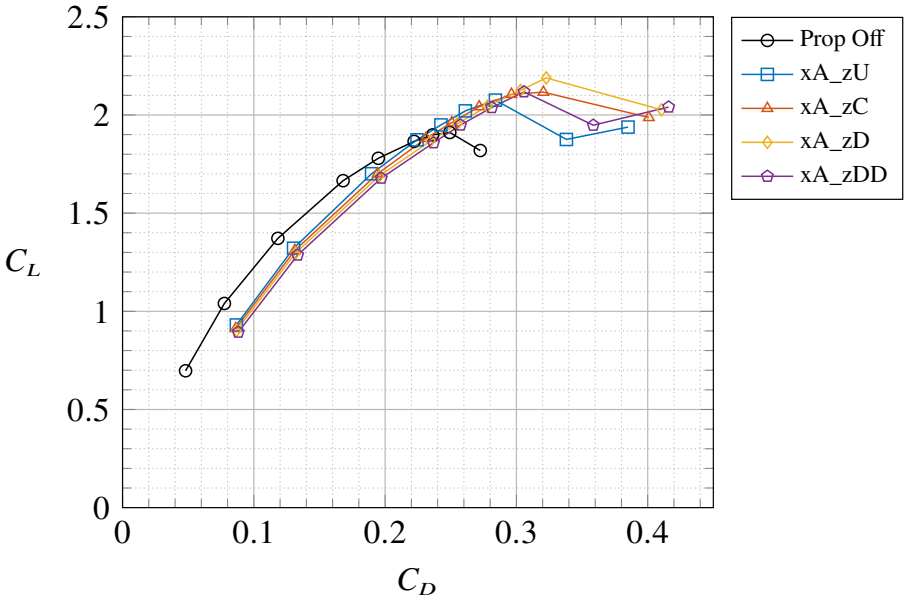

Figure 3.108: Wing drag polars by varying the Z-Position of DEP propellers with xA fixed - $\delta_f = 15°$ - $V_\infty = 20\ m/s$ - $Re_\infty = 5.48 \cdot 10^5$ - $RPM_{DEP} = 7000$ (In-Board Up) - STAR-CCM+

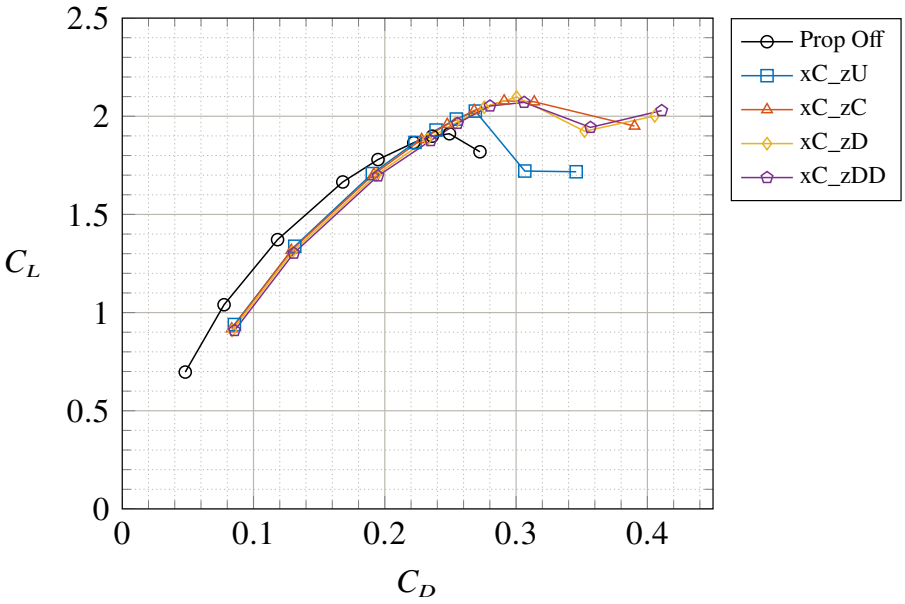

Figure 3.109: Wing drag polars by varying the Z-Position of DEP propellers with xC fixed - $\delta_f = 15°$ - $V_\infty = 20\ m/s$ - $Re_\infty = 5.48 \cdot 10^5$ - $RPM_{DEP} = 7000$ (In-Board Up) - STAR-CCM+

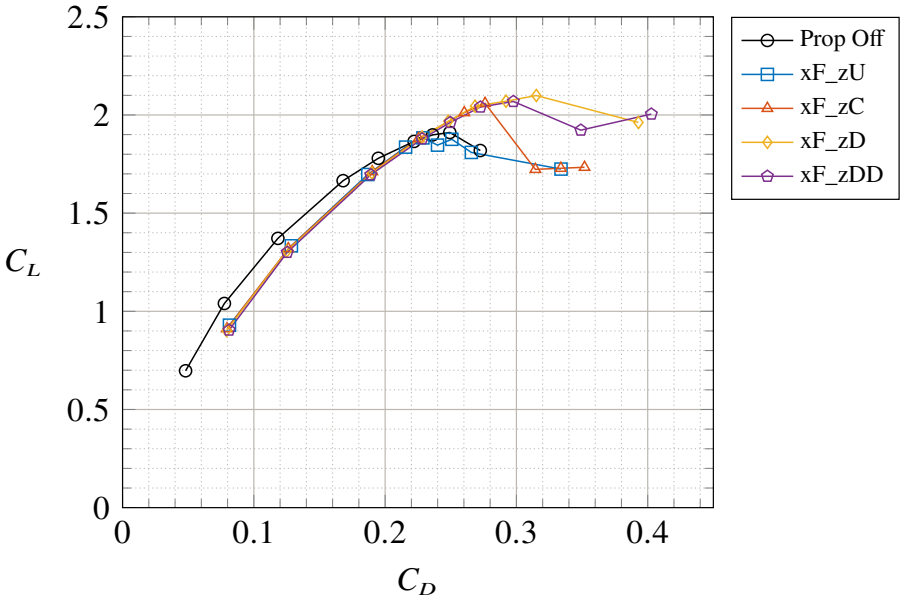

Figure 3.110: Wing drag polars by varying the Z-Position of DEP propellers with xF fixed - $\delta_f = 15°$ - $V_\infty = 20\ m/s$ - $Re_\infty = 5.48 \cdot 10^5$ - $RPM_{DEP} = 7000$ (In-Board Up) - STAR-CCM+

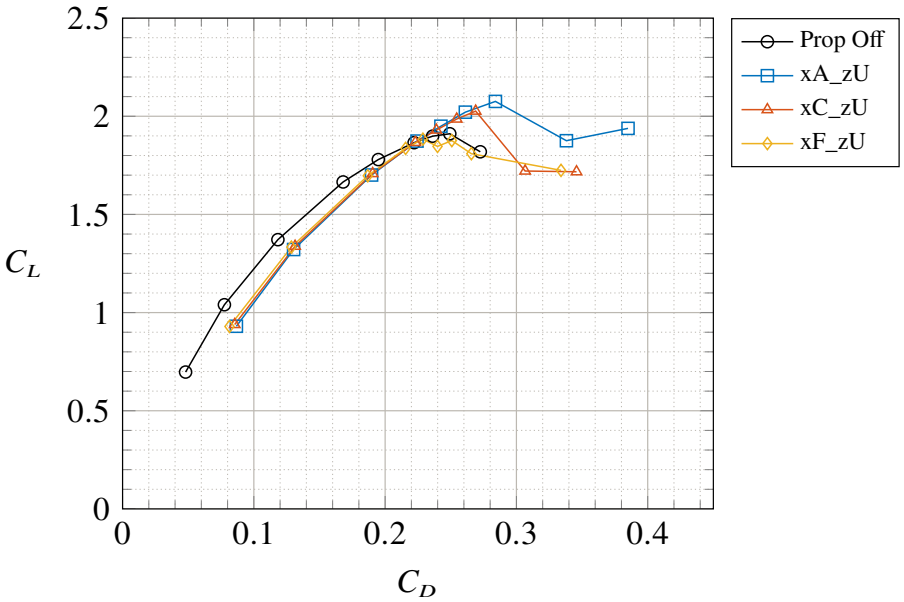

Figure 3.111: Wing drag polars by varying the X-Position of DEP propellers with zU fixed - $\delta_f = 15°$ - $V_\infty = 20\ m/s$ - $Re_\infty = 5.48 \cdot 10^5$ - $RPM_{DEP} = 7000$ (In-Board Up) - STAR-CCM+

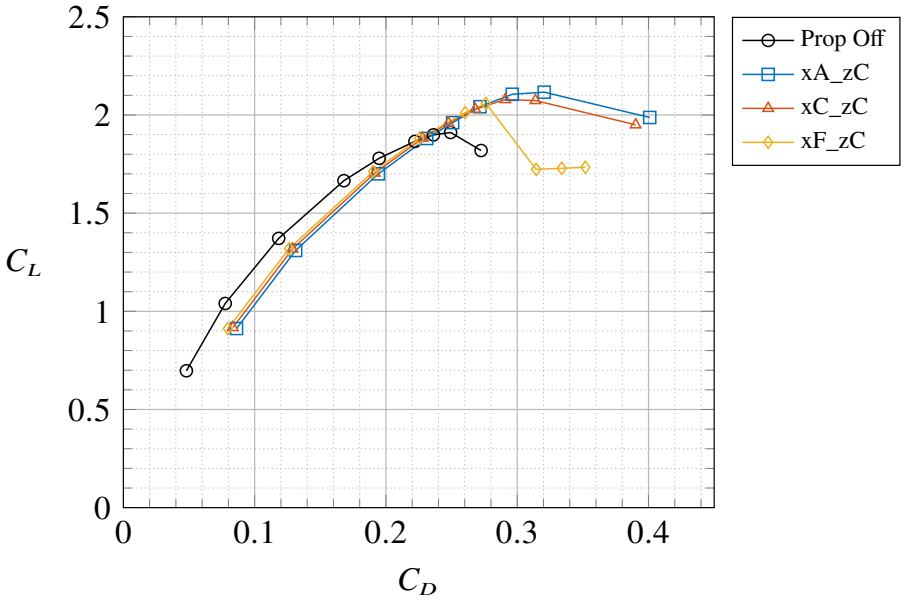

Figure 3.112: Wing drag polars by varying the X-Position of DEP propellers with zC fixed - $\delta_f = 15°$ - $V_\infty = 20\ m/s$ - $Re_\infty = 5.48 \cdot 10^5$ - $RPM_{DEP} = 7000$ (In-Board Up) - STAR-CCM+

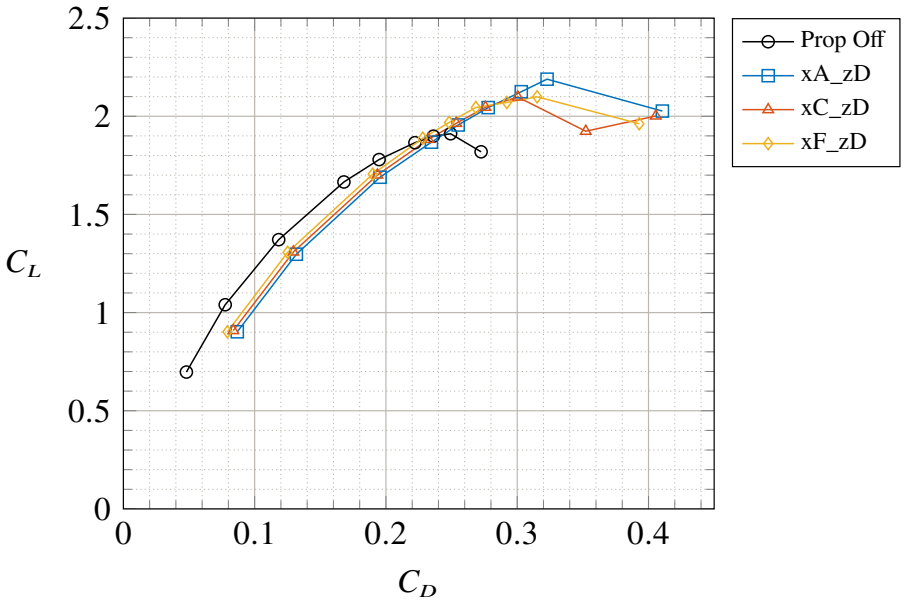

Figure 3.113: Wing drag polars by varying the X-Position of DEP propellers with zD fixed - $\delta_f = 15°$ - $V_\infty = 20\ m/s$ - $Re_\infty = 5.48 \cdot 10^5$ - $RPM_{DEP} = 7000$ (In-Board Up) - STAR-CCM+

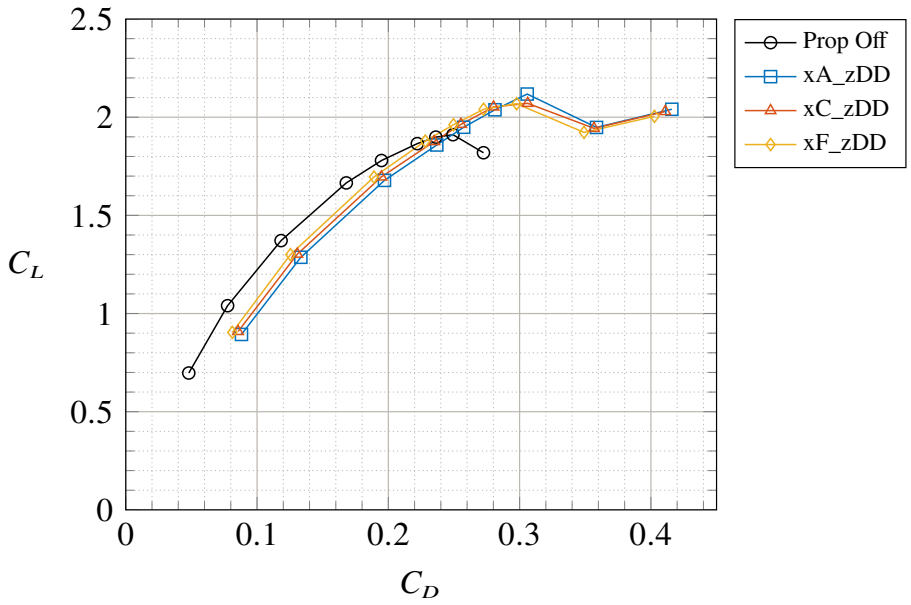

Figure 3.114: Wing drag polars by varying the X-Position of DEP propellers with zDD fixed - $\delta_f = 15°$ - $V_\infty = 20\ m/s$ - $Re_\infty = 5.48 \cdot 10^5$ - $RPM_{DEP} = 7000$ (In-Board Up) - STAR-CCM+

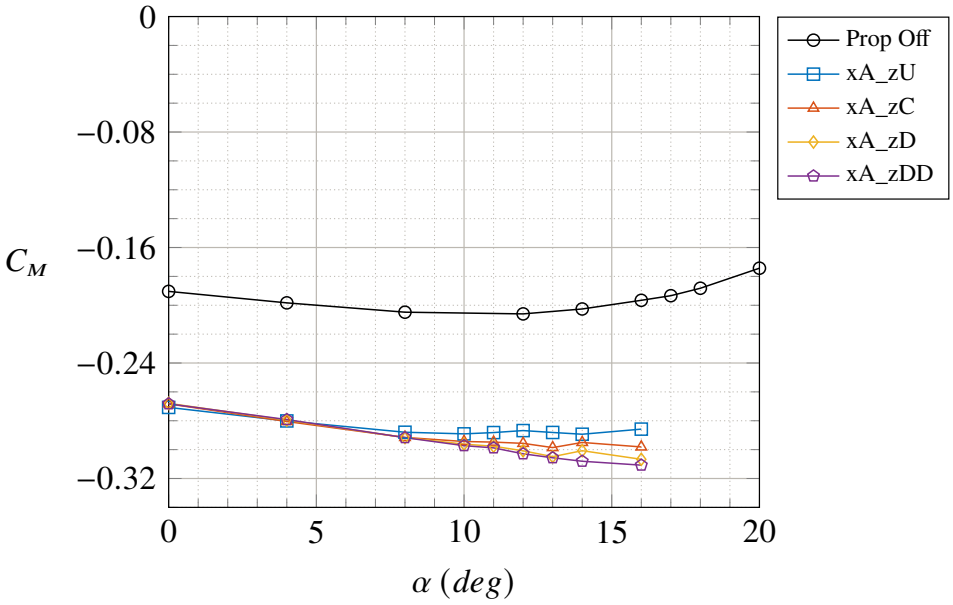

Figure 3.115: Wing pitching moment coefficient by varying the Z-Position of DEP propellers with xA fixed - $\delta_f = 15°$ - $V_\infty = 20\ m/s$ - $Re_\infty = 5.48 \cdot 10^5$ - $RPM_{DEP} = 7000$ (In-Board Up) - STAR-CCM+

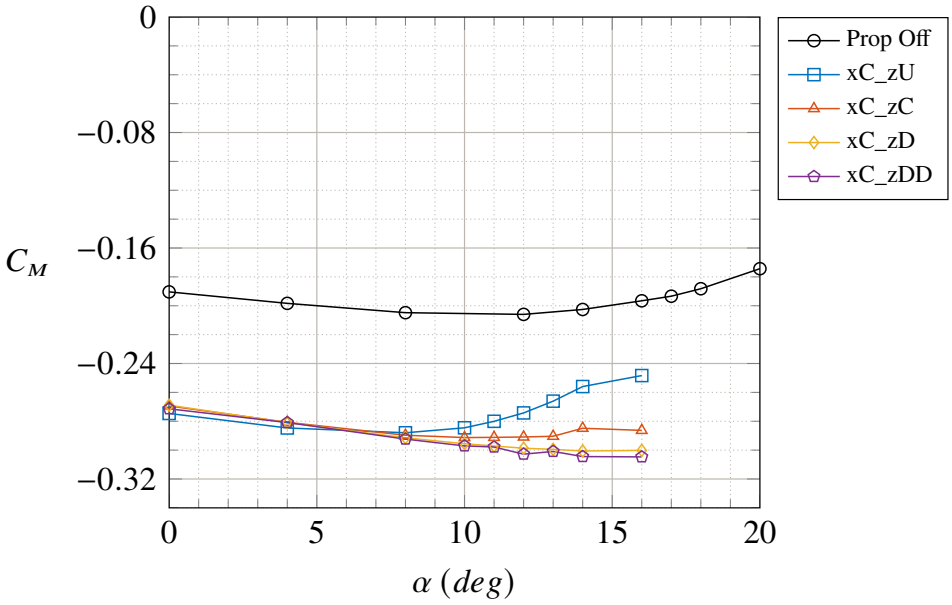

Figure 3.116: Wing pitching moment coefficient by varying the Z-Position of DEP propellers with xC fixed - $\delta_f = 15°$ - $V_\infty = 20\ m/s$ - $Re_\infty = 5.48 \cdot 10^5$ - $RPM_{DEP} = 7000$ (In-Board Up) - STAR-CCM+

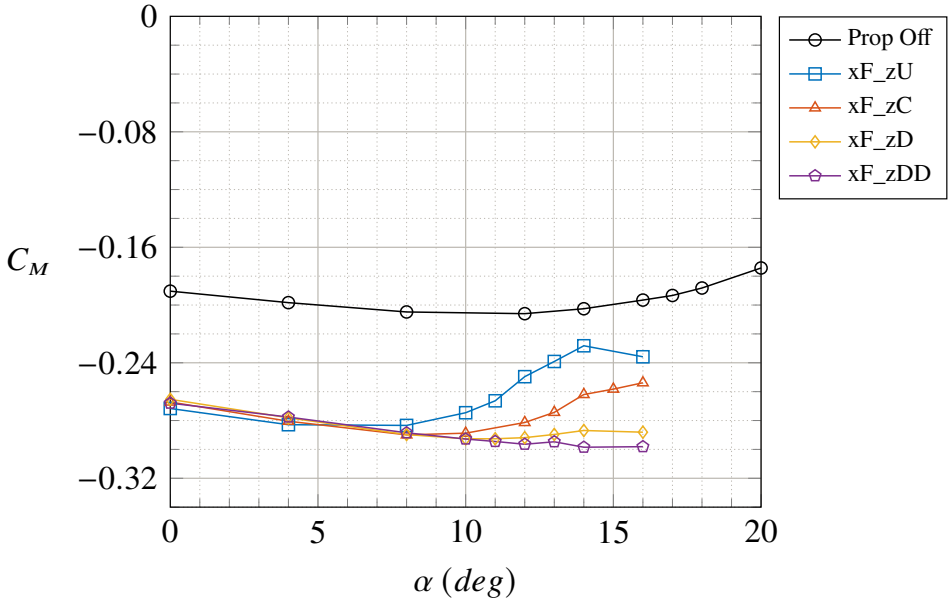

Figure 3.117: Wing pitching moment coefficient by varying the Z-Position of DEP propellers with xF fixed - $\delta_f = 15°$ - $V_\infty = 20\ m/s$ - $Re_\infty = 5.48 \cdot 10^5$ - $RPM_{DEP} = 7000$ (In-Board Up) - STAR-CCM+

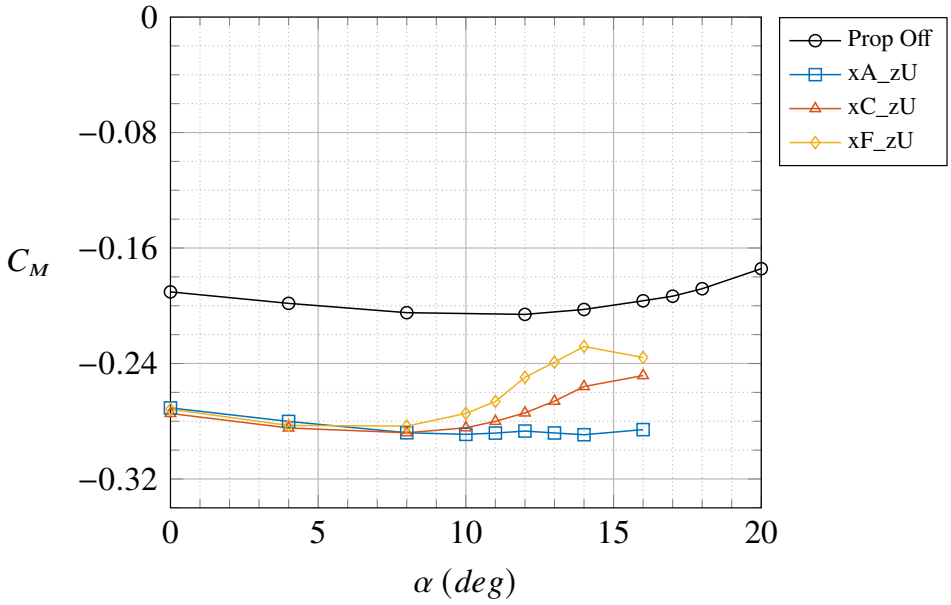

Figure 3.118: Wing pitching moment coefficient by varying the X-Position of DEP propellers with zU fixed - $\delta_f = 15°$ - $V_\infty = 20\ m/s$ - $Re_\infty = 5.48 \cdot 10^5$ - $RPM_{DEP} = 7000$ (In-Board Up) - STAR-CCM+

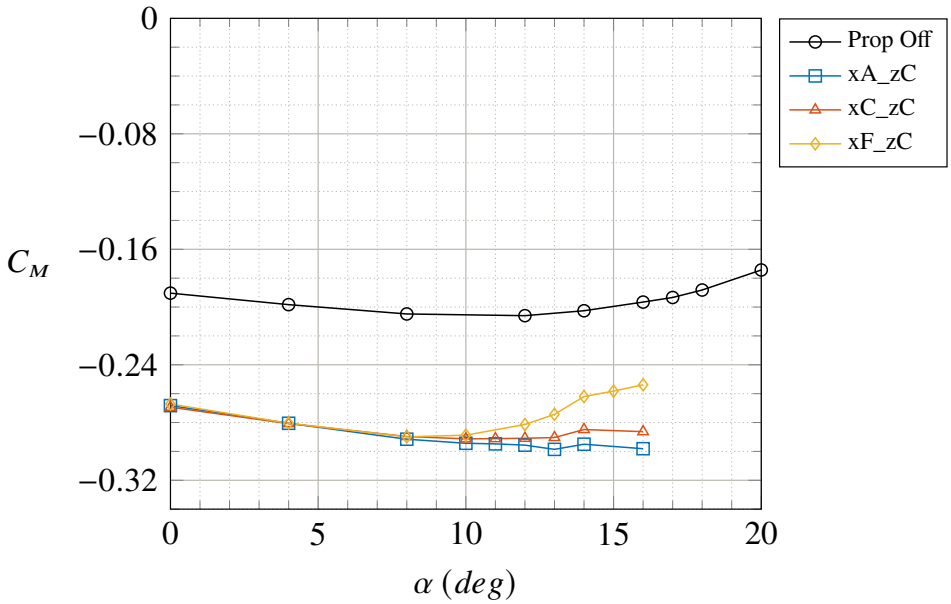

Figure 3.119: Wing pitching moment coefficient by varying the X-Position of DEP propellers with zC fixed - $\delta_f = 15°$ - $V_\infty = 20\ m/s$ - $Re_\infty = 5.48 \cdot 10^5$ - $RPM_{DEP} = 7000$ (In-Board Up) - STAR-CCM+

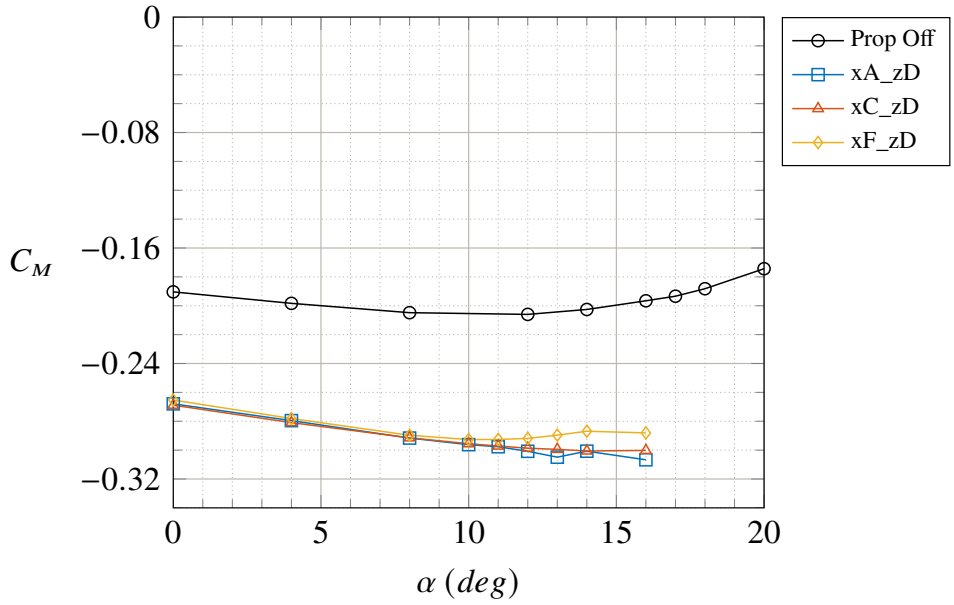

Figure 3.120: Wing pitching moment coefficient by varying the X-Position of DEP propellers with zD fixed - $\delta_f = 15°$ - $V_\infty = 20\ m/s$ - $Re_\infty = 5.48 \cdot 10^5$ - $RPM_{DEP} = 7000$ (In-Board Up) - STAR-CCM+

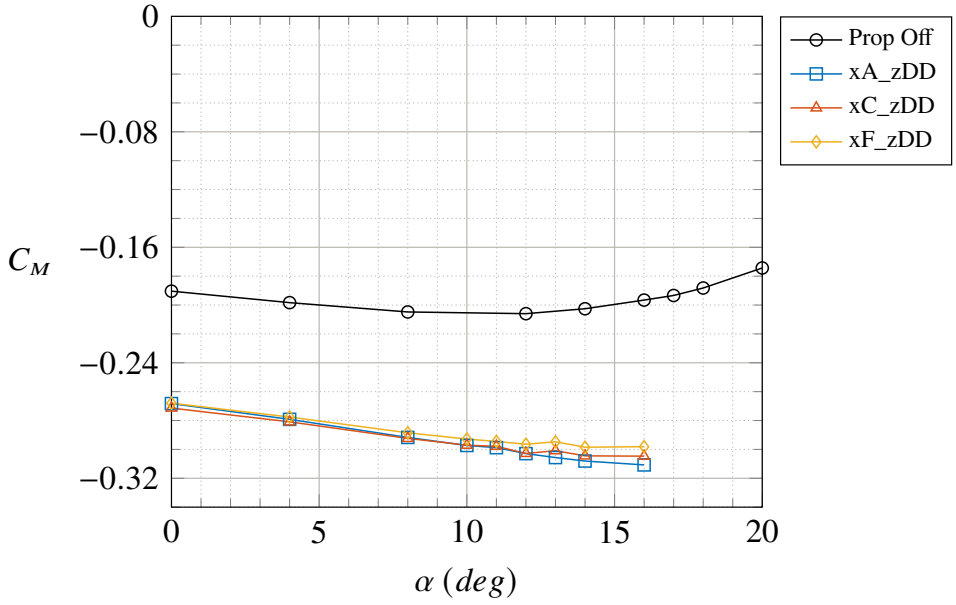

Figure 3.121: Wing pitching moment coefficient by varying the X-Position of DEP propellers with zDD fixed - $\delta_f = 15°$ - $V_\infty = 20\ m/s$ - $Re_\infty = 5.48 \cdot 10^5$ - $RPM_{DEP} = 7000$ (In-Board Up) - STAR-CCM+

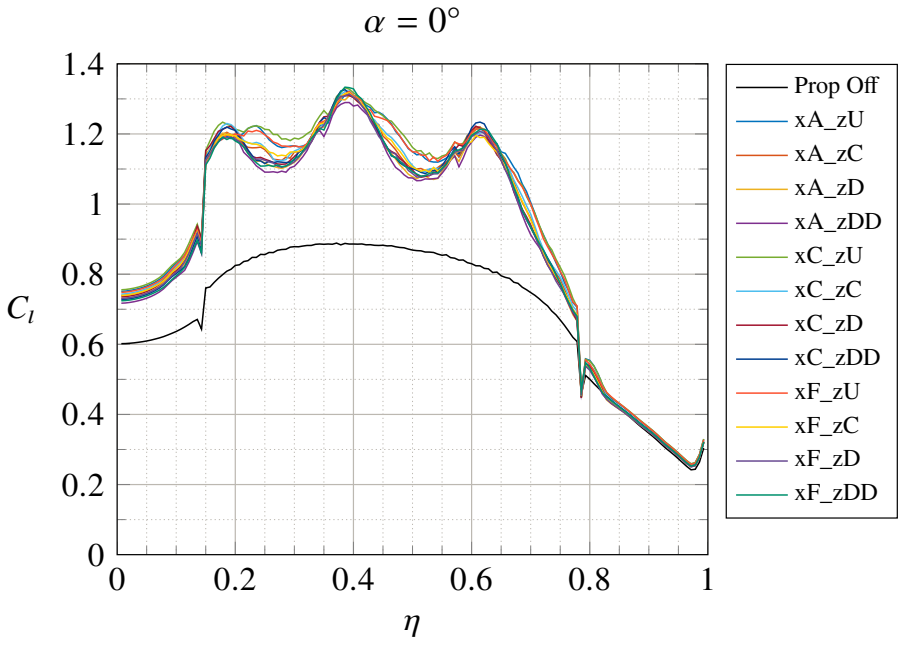

Figure 3.122: Wing load distribution by varying the position of DEP propellers - $\delta_f = 15°$ - $V_\infty = 20\ m/s$ - $Re_\infty = 5.48 \cdot 10^5$ - $RPM_{DEP} = 7000$ (In-Board Up) - STAR-CCM+

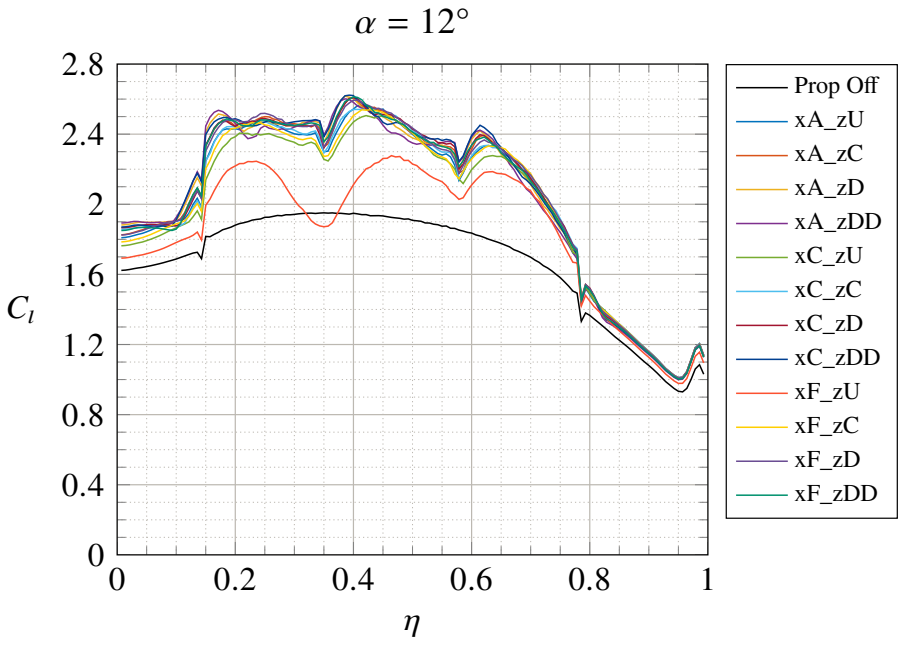

Figure 3.123: Wing load distribution by varying the position of DEP propellers - $\delta_f = 15°$ - $V_\infty = 20\ m/s$ - $Re_\infty = 5.48 \cdot 10^5$ - $RPM_{DEP} = 7000$ (In-Board Up) - STAR-CCM+

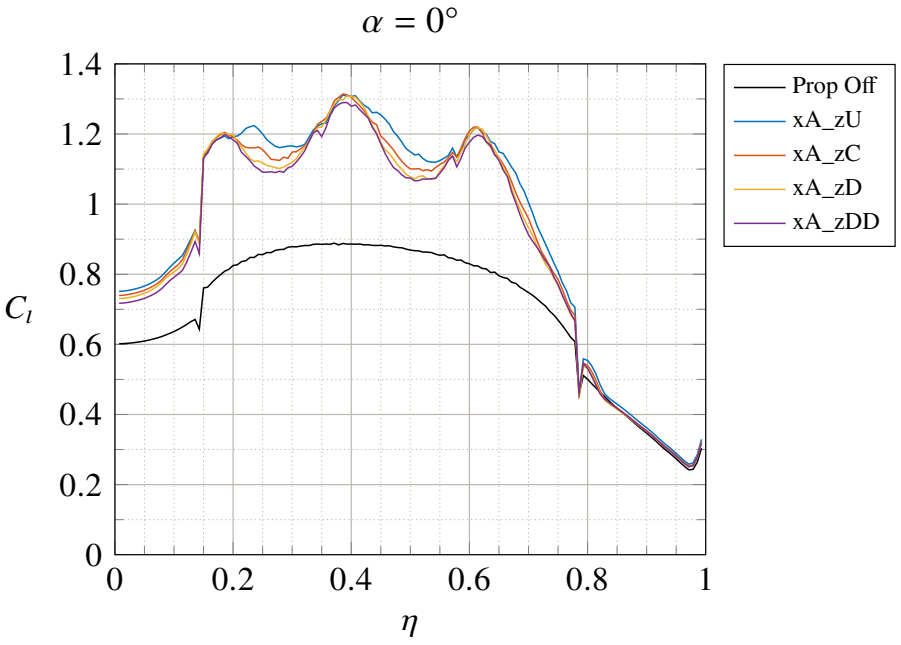

Figure 3.124: Wing load distribution by varying the Z-Position of DEP propellers with xA fixed - $\delta_f = 15°$ - $V_\infty = 20\ m/s$ - $Re_\infty = 5.48 \cdot 10^5$ - $RPM_{DEP} = 7000$ (In-Board Up) - STAR-CCM+

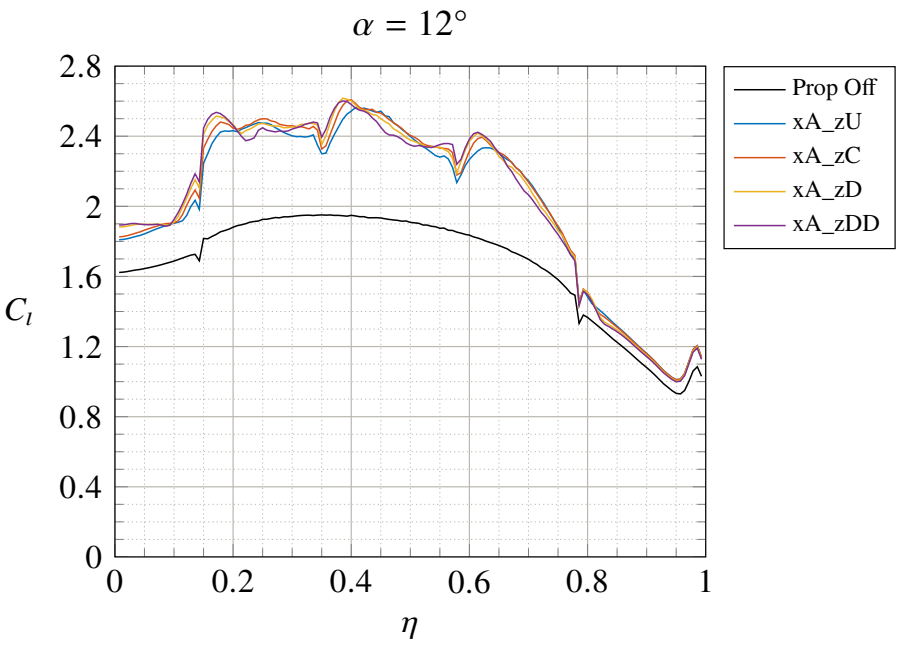

Figure 3.125: Wing load distribution by varying the Z-Position of DEP propellers with xA fixed - $\delta_f = 15°$ - $V_\infty = 20\ m/s$ - $Re_\infty = 5.48 \cdot 10^5$ - $RPM_{DEP} = 7000$ (In-Board Up) - STAR-CCM+

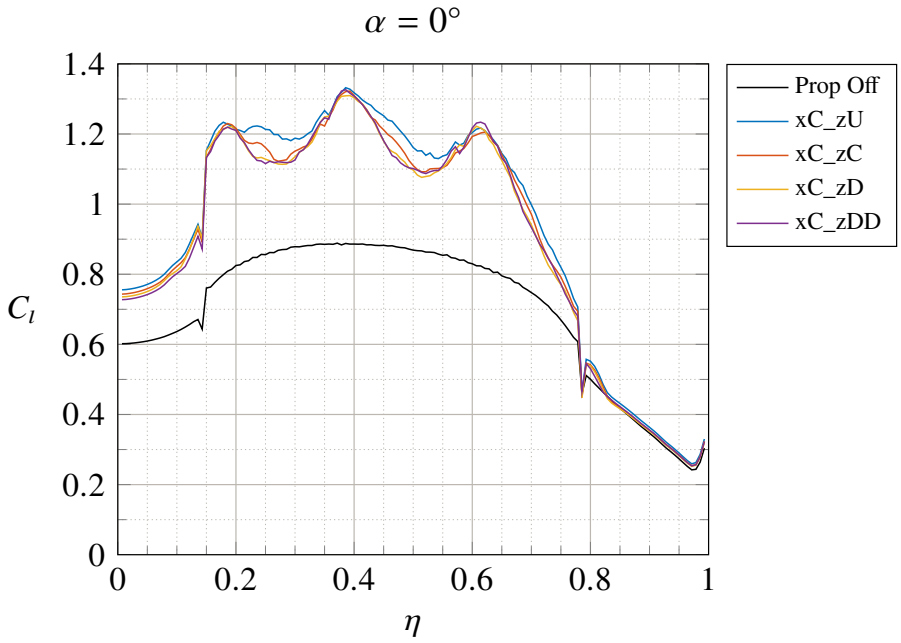

Figure 3.126: Wing load distribution by varying the Z-Position of DEP propellers with xC fixed - $\delta_f = 15°$ - $V_\infty = 20\ m/s$ - $Re_\infty = 5.48 \cdot 10^5$ - $RPM_{DEP} = 7000$ (In-Board Up) - STAR-CCM+

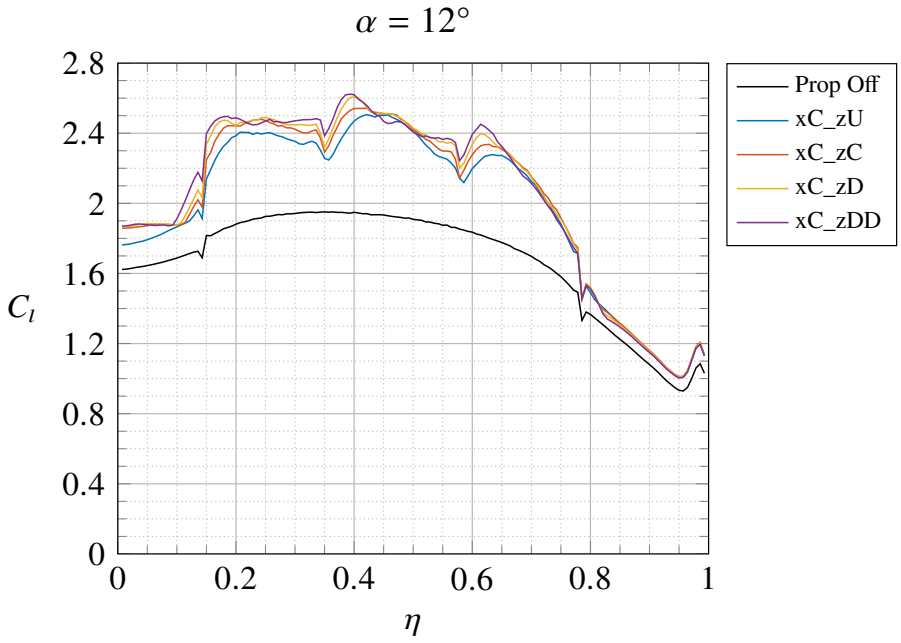

Figure 3.127: Wing load distribution by varying the Z-Position of DEP propellers with xC fixed - $\delta_f = 15°$ - $V_\infty = 20\ m/s$ - $Re_\infty = 5.48 \cdot 10^5$ - $RPM_{DEP} = 7000$ (In-Board Up) - STAR-CCM+

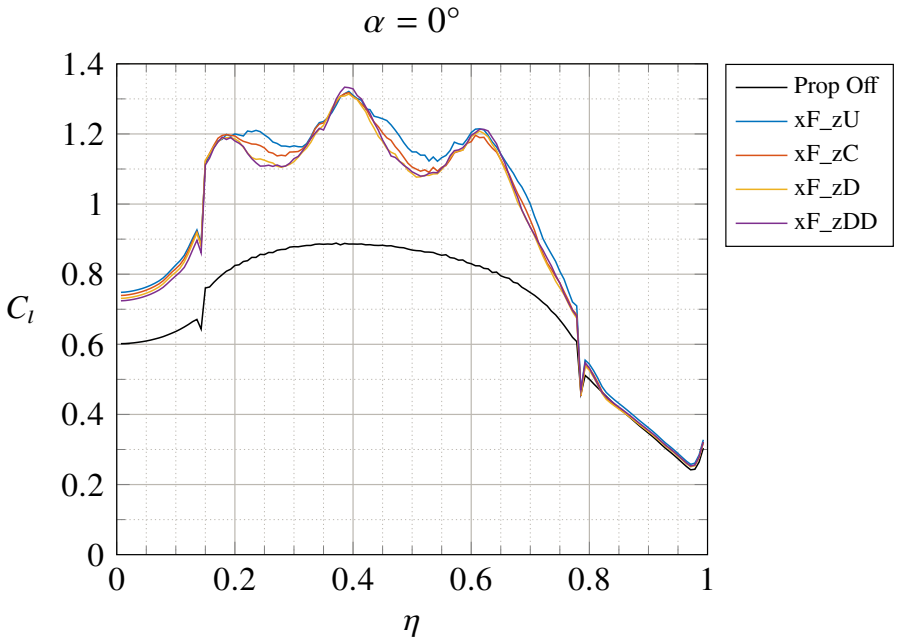

Figure 3.128: Wing load distribution by varying the Z-Position of DEP propellers with xF fixed - $\delta_f = 15°$ - $V_\infty = 20\ m/s$ - $Re_\infty = 5.48 \cdot 10^5$ - $RPM_{DEP} = 7000$ (In-Board Up) - STAR-CCM+

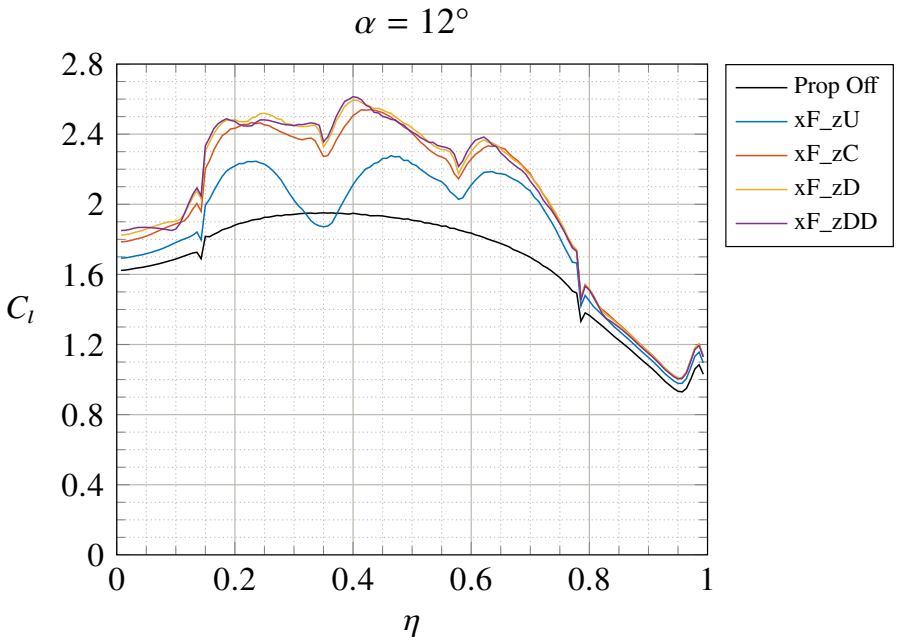

Figure 3.129: Wing load distribution by varying the Z-Position of DEP propellers with xF fixed - $\delta_f = 15°$ - $V_\infty = 20\ m/s$ - $Re_\infty = 5.48 \cdot 10^5$ - $RPM_{DEP} = 7000$ (In-Board Up) - STAR-CCM+

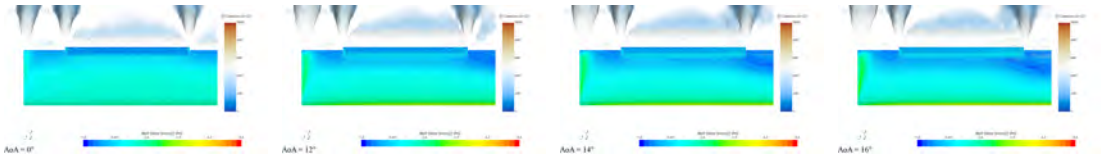

(a) $\alpha = 0°$ - Prop Off **(b)** $\alpha = 12°$ - Prop Off **(c)** $\alpha = 14°$ - Prop Off **(d)** $\alpha = 16°$ - Prop Off

Figure 3.130: Contours of the X-Component of wall shear stress and Q-Criterion isosurfaces for the prop off condition - $\delta_f = 15°$ - $V_\infty = 20\ m/s$ - $Re_\infty = 5.48 \cdot 10^5$ - STAR-CCM+

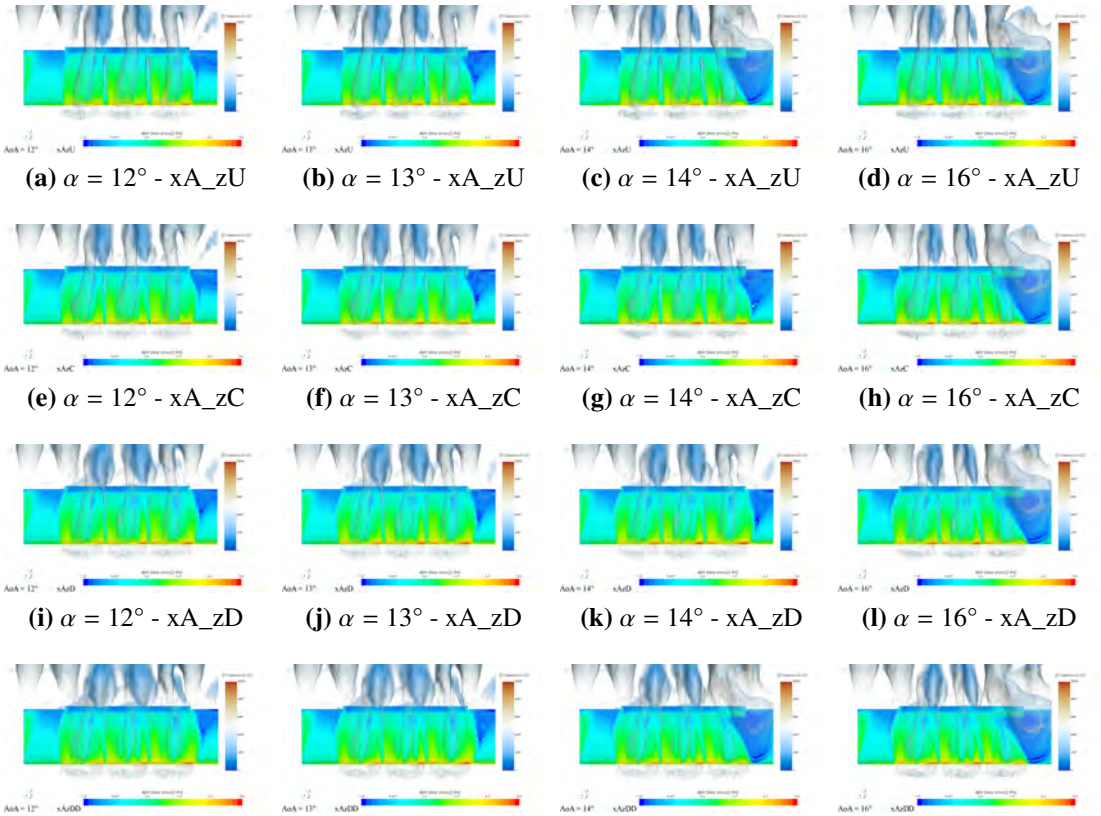

(a) $\alpha = 12°$ - xA_zU **(b)** $\alpha = 13°$ - xA_zU **(c)** $\alpha = 14°$ - xA_zU **(d)** $\alpha = 16°$ - xA_zU

(e) $\alpha = 12°$ - xA_zC **(f)** $\alpha = 13°$ - xA_zC **(g)** $\alpha = 14°$ - xA_zC **(h)** $\alpha = 16°$ - xA_zC

(i) $\alpha = 12°$ - xA_zD **(j)** $\alpha = 13°$ - xA_zD **(k)** $\alpha = 14°$ - xA_zD **(l)** $\alpha = 16°$ - xA_zD

(m) $\alpha = 12°$ - xA_zDD **(n)** $\alpha = 13°$ - xA_zDD **(o)** $\alpha = 14°$ - xA_zDD **(p)** $\alpha = 16°$ - xA_zDD

Figure 3.131: Contours of the X-Component of wall shear stress and Q-Criterion isosurfaces for xA position fixed and varying the Z-Position of DEP propellers - $\delta_f = 15°$ - $V_\infty = 20\ m/s$ - $Re_\infty = 5.48 \cdot 10^5$ - $RPM_{DEP} = 7000$ (In-Board Up) - STAR-CCM+

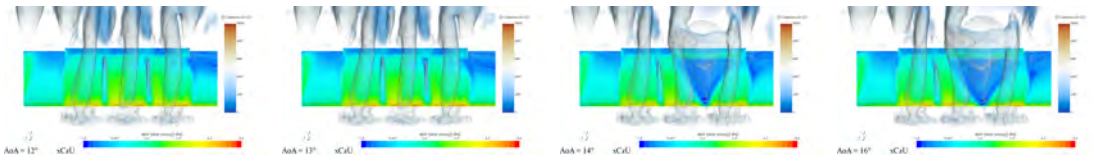

(a) α = 12° - xC_zU **(b)** α = 13° - xC_zU **(c)** α = 14° - xC_zU **(d)** α = 16° - xC_zU

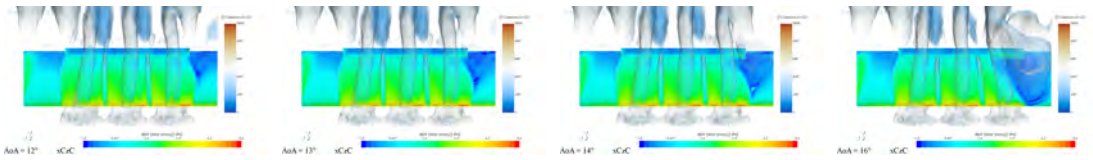

(e) α = 12° - xC_zC **(f)** α = 13° - xC_zC **(g)** α = 14° - xC_zC **(h)** α = 16° - xC_zC

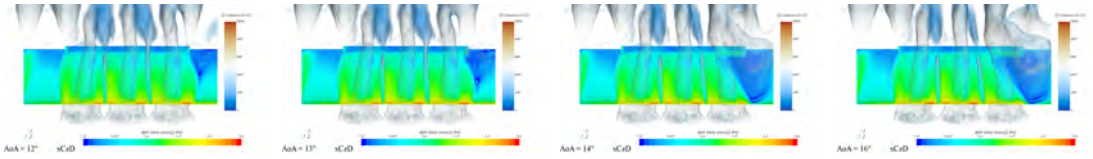

(i) α = 12° - xC_zD **(j)** α = 13° - xC_zD **(k)** α = 14° - xC_zD **(l)** α = 16° - xC_zD

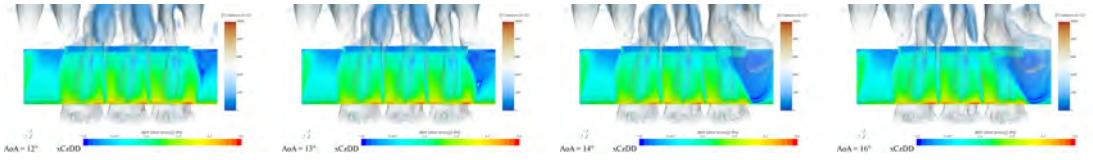

(m) α = 12° - xC_zDD **(n)** α = 13° - xC_zDD **(o)** α = 14° - xC_zDD **(p)** α = 16° - xC_zDD

Figure 3.132: Contours of the X-Component of wall shear stress and Q-Criterion isosurfaces for xC position fixed and varying the Z-Position of DEP propellers - δ_f = 15° - V_∞ = 20 m/s - $Re_\infty = 5.48 \cdot 10^5$ - RPM_{DEP} = 7000 (In-Board Up) - STAR-CCM+

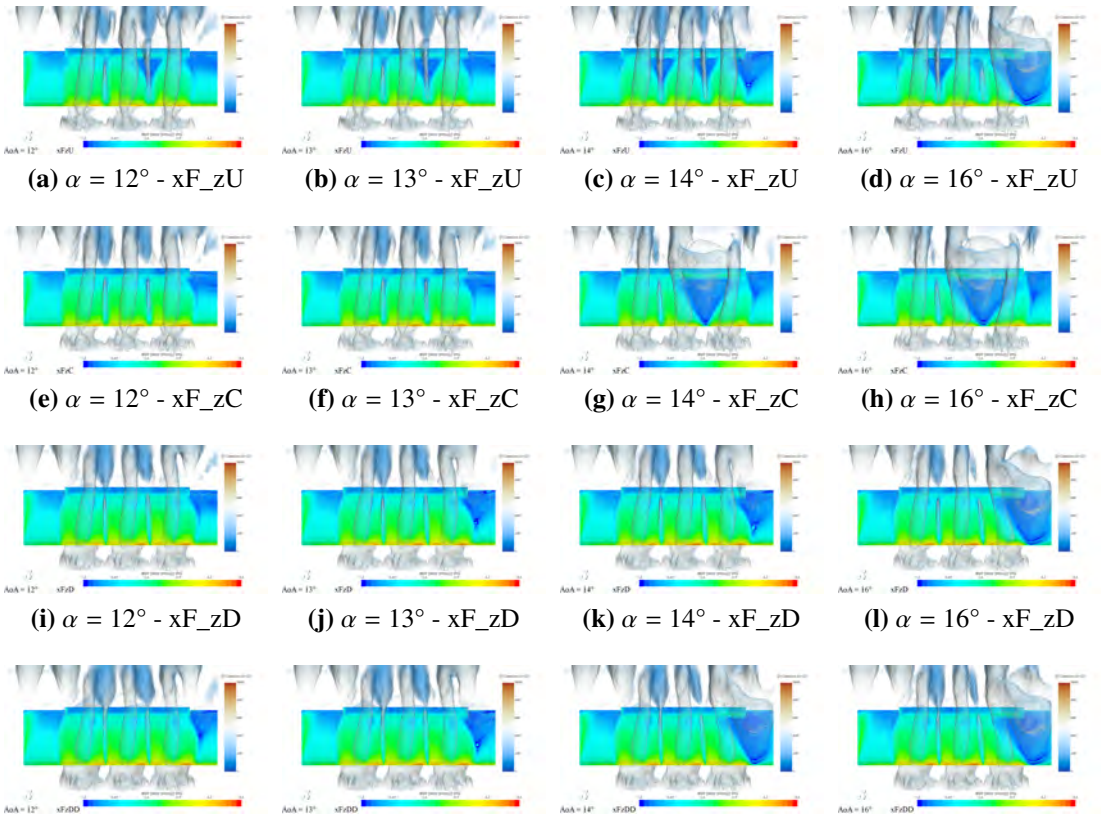

(a) α = 12° - xF_zU **(b)** α = 13° - xF_zU **(c)** α = 14° - xF_zU **(d)** α = 16° - xF_zU

(e) α = 12° - xF_zC **(f)** α = 13° - xF_zC **(g)** α = 14° - xF_zC **(h)** α = 16° - xF_zC

(i) α = 12° - xF_zD **(j)** α = 13° - xF_zD **(k)** α = 14° - xF_zD **(l)** α = 16° - xF_zD

(m) α = 12° - xF_zDD **(n)** α = 13° - xF_zDD **(o)** α = 14° - xF_zDD **(p)** α = 16° - xF_zDD

Figure 3.133: Contours of the X-Component of wall shear stress and Q-Criterion isosurfaces for xF position fixed and varying the Z-Position of DEP propellers - δ_f = 15° - V_∞ = 20 m/s - $Re_\infty = 5.48 \cdot 10^5$ - RPM_{DEP} = 7000 (In-Board Up) - STAR-CCM+

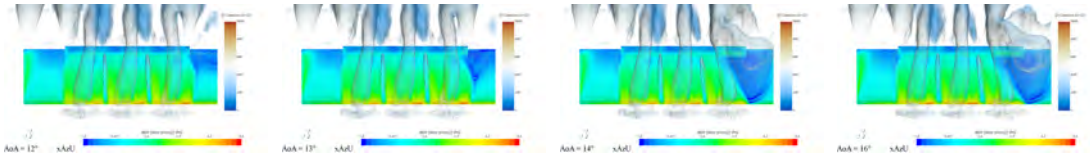

(a) $\alpha = 12°$ - xA_zU **(b)** $\alpha = 13°$ - xA_zU **(c)** $\alpha = 14°$ - xA_zU **(d)** $\alpha = 16°$ - xA_zU

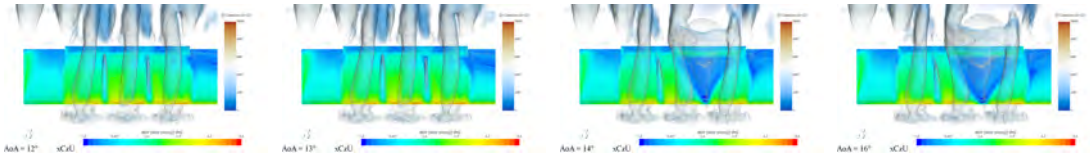

(e) $\alpha = 12°$ - xC_zU **(f)** $\alpha = 13°$ - xC_zU **(g)** $\alpha = 14°$ - xC_zU **(h)** $\alpha = 16°$ - xC_zU

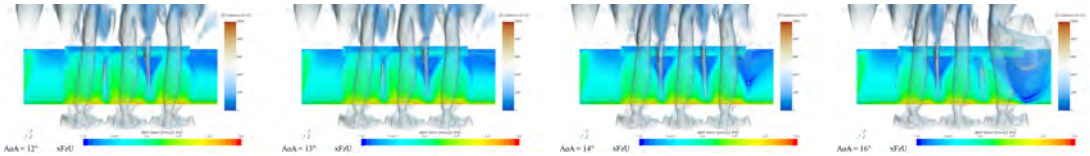

(i) $\alpha = 12°$ - xF_zU **(j)** $\alpha = 13°$ - xF_zU **(k)** $\alpha = 14°$ - xF_zU **(l)** $\alpha = 16°$ - xF_zU

Figure 3.134: Contours of the X-Component of wall shear stress and Q-Criterion isosurfaces for zU position fixed and varying the X-Position of DEP propellers - $\delta_f = 15°$ - $V_\infty = 20\ m/s$ - $Re_\infty = 5.48 \cdot 10^5$ - $RPM_{DEP} = 7000$ (In-Board Up) - STAR-CCM+

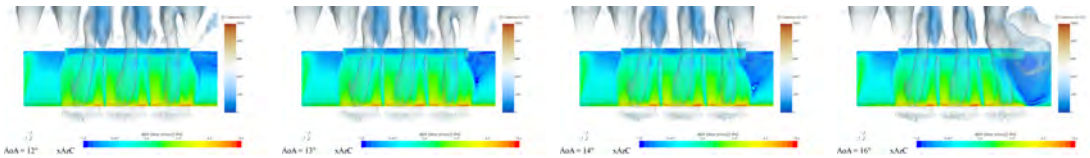

(a) $\alpha = 12°$ - xA_zC **(b)** $\alpha = 13°$ - xA_zC **(c)** $\alpha = 14°$ - xA_zC **(d)** $\alpha = 16°$ - xA_zC

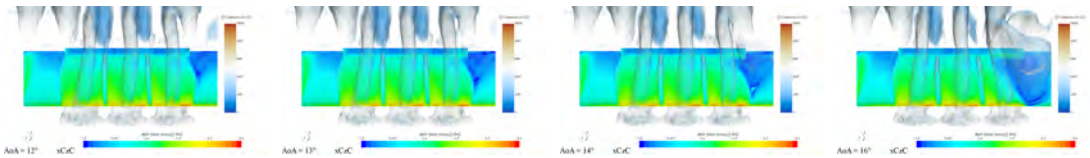

(e) $\alpha = 12°$ - xC_zC **(f)** $\alpha = 13°$ - xC_zC **(g)** $\alpha = 14°$ - xC_zC **(h)** $\alpha = 16°$ - xC_zC

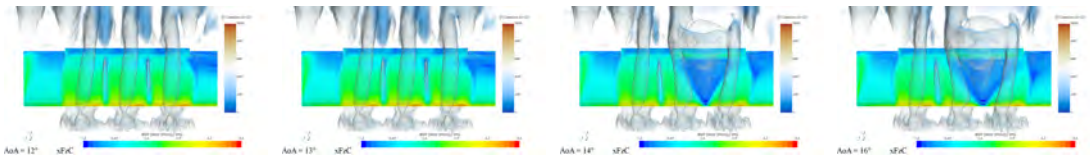

(i) $\alpha = 12°$ - xF_zC **(j)** $\alpha = 13°$ - xF_zC **(k)** $\alpha = 14°$ - xF_zC **(l)** $\alpha = 16°$ - xF_zC

Figure 3.135: Contours of the X-Component of wall shear stress and Q-Criterion isosurfaces for zC position fixed and varying the X-Position of DEP propellers - $\delta_f = 15°$ - $V_\infty = 20\ m/s$ - $Re_\infty = 5.48 \cdot 10^5$ - $RPM_{DEP} = 7000$ (In-Board Up) - STAR-CCM+

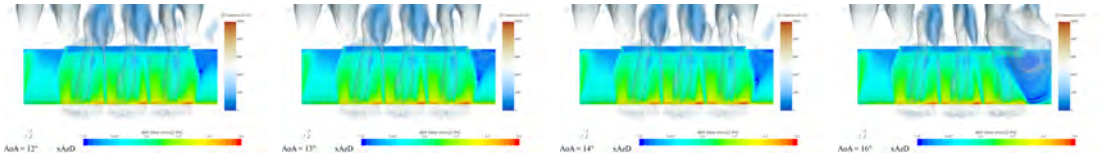

(a) $\alpha = 12°$ - xA_zD **(b)** $\alpha = 13°$ - xA_zD **(c)** $\alpha = 14°$ - xA_zD **(d)** $\alpha = 16°$ - xA_zD

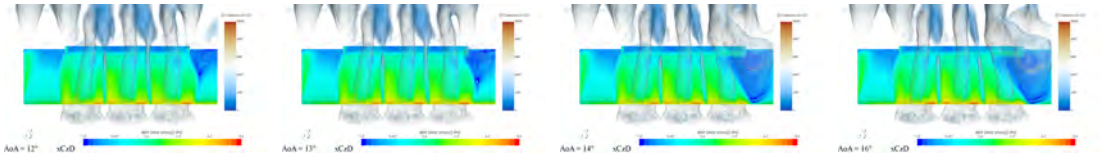

(e) $\alpha = 12°$ - xC_zD **(f)** $\alpha = 13°$ - xC_zD **(g)** $\alpha = 14°$ - xC_zD **(h)** $\alpha = 16°$ - xC_zD

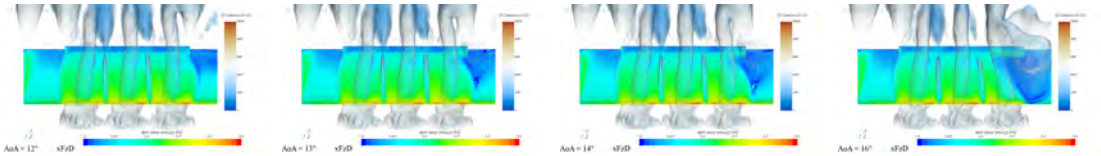

(i) $\alpha = 12°$ - xF_zD **(j)** $\alpha = 13°$ - xF_zD **(k)** $\alpha = 14°$ - xF_zD **(l)** $\alpha = 16°$ - xF_zD

Figure 3.136: Contours of the X-Component of wall shear stress and Q-Criterion isosurfaces for zD position fixed and varying the X-Position of DEP propellers - $\delta_f = 15°$ - $V_\infty = 20\ m/s$ - $Re_\infty = 5.48 \cdot 10^5$ - $RPM_{DEP} = 7000$ (In-Board Up) - STAR-CCM+

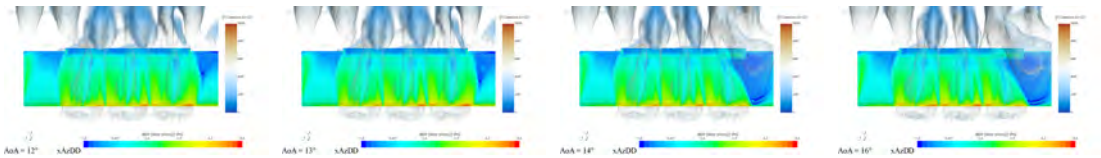

(a) $\alpha = 12°$ - xA_zDD **(b)** $\alpha = 13°$ - xA_zDD **(c)** $\alpha = 14°$ - xA_zDD **(d)** $\alpha = 16°$ - xA_zDD

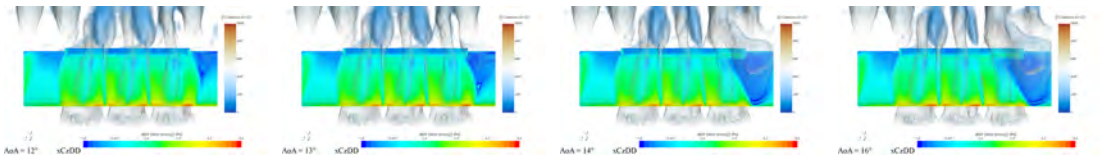

(e) $\alpha = 12°$ - xC_zDD **(f)** $\alpha = 13°$ - xC_zDD **(g)** $\alpha = 14°$ - xC_zDD **(h)** $\alpha = 16°$ - xC_zDD

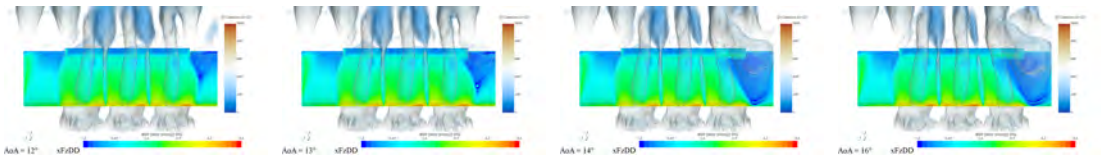

(i) $\alpha = 12°$ - xF_zDD **(j)** $\alpha = 13°$ - xF_zDD **(k)** $\alpha = 14°$ - xF_zDD **(l)** $\alpha = 16°$ - xF_zDD

Figure 3.137: Contours of the X-Component of wall shear stress and Q-Criterion isosurfaces for zDD position fixed and varying the X-Position of DEP propellers - $\delta_f = 15°$ - $V_\infty = 20\ m/s$ - $Re_\infty = 5.48 \cdot 10^5$ - $RPM_{DEP} = 7000$ (In-Board Up) - STAR-CCM+

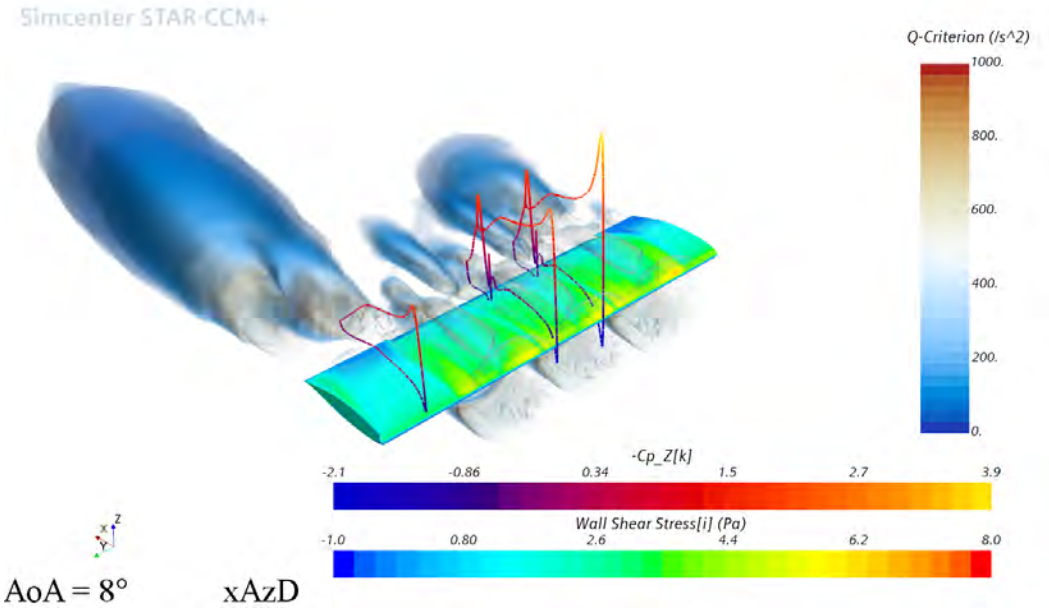

(a) $\alpha = 8°$ - xA_zD

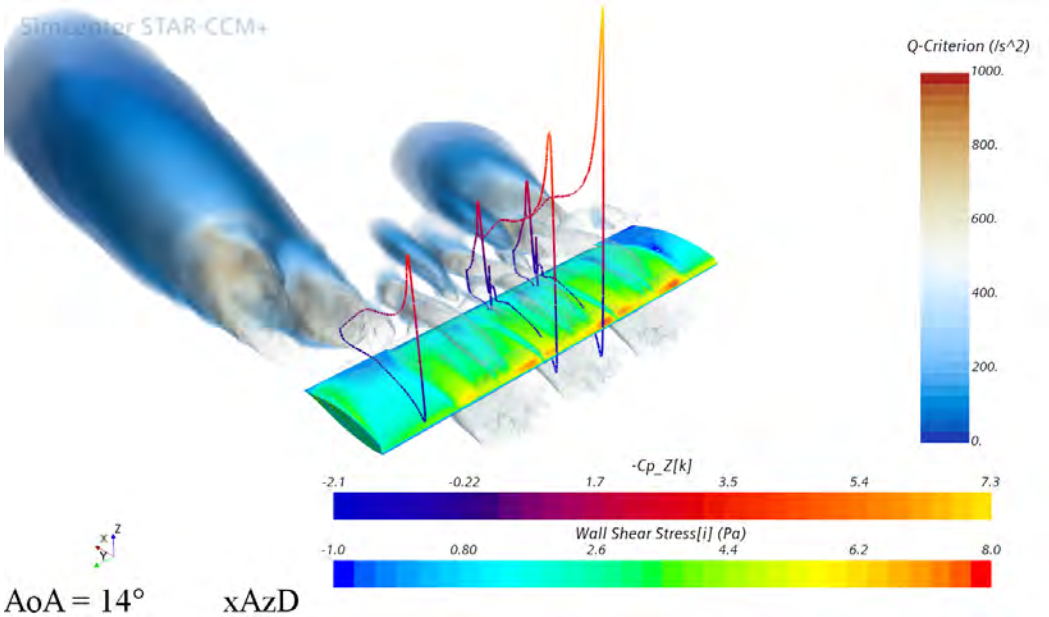

(b) $\alpha = 14°$ - xA_zD

Figure 3.138: 3D view of pressure coefficient distribution on three different sections ($0.65\,m$, $0.75\,m$, $1.25\,m$) - $\delta_f = 15°$ - $V_\infty = 20\ m/s$ - $Re_\infty = 5.48 \cdot 10^5$ - $RPM_{DEP} = 7000$ (In-Board Up) - STAR-CCM+

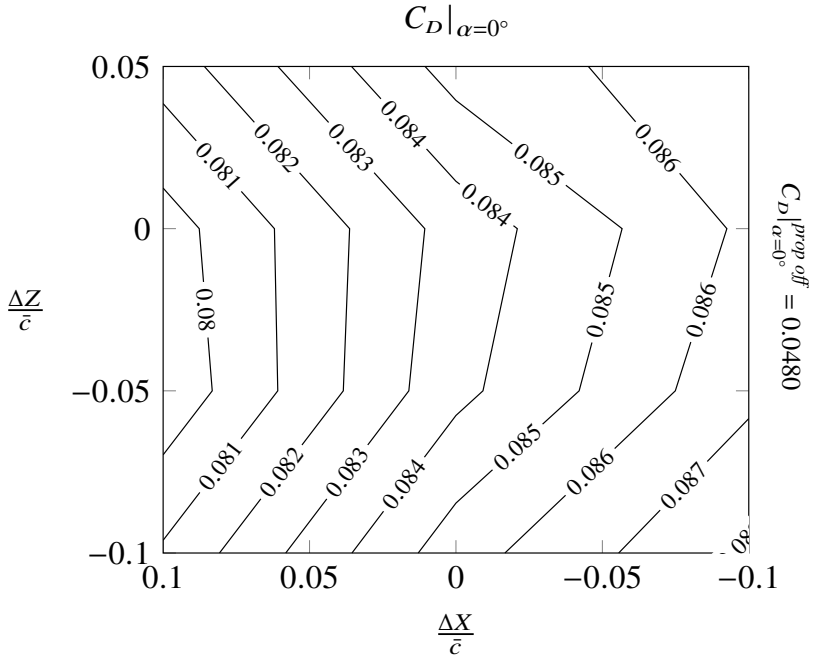

Figure 3.139: Extrapolated values of $C_D|_{\alpha=0^\circ}$ of wing by varying the position of DEP propellers - $\delta_f = 15^\circ$ - $V_\infty = 20\ m/s$ - $Re_\infty = 5.48 \cdot 10^5$ - $RPM_{DEP} = 7000$ (In-Board Up) - STAR-CCM+

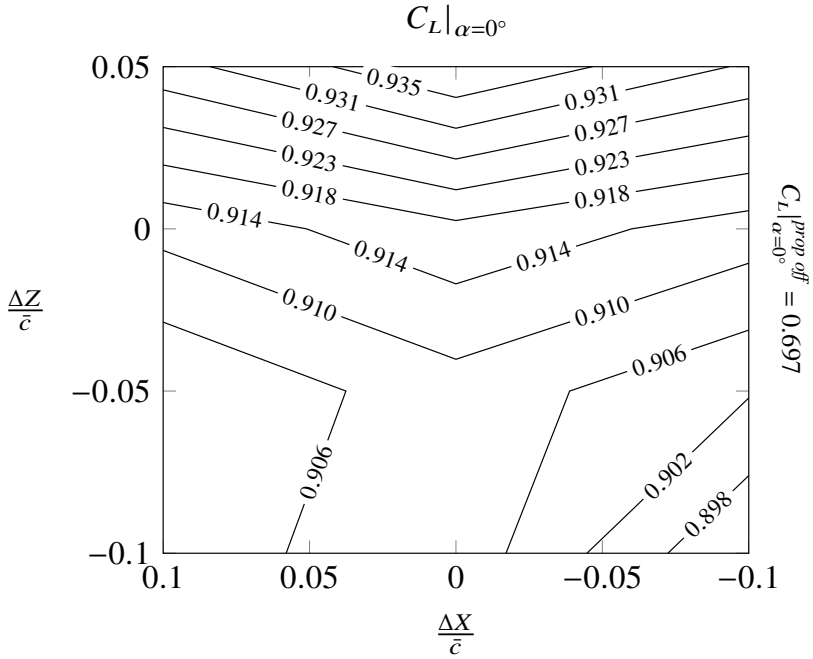

Figure 3.140: Values of $C_L|_{\alpha=0^\circ}$ of wing by varying the position of DEP propellers - $\delta_f = 15^\circ$ - $V_\infty = 20\ m/s$ - $Re_\infty = 5.48 \cdot 10^5$ - $RPM_{DEP} = 7000$ (In-Board Up) - STAR-CCM+

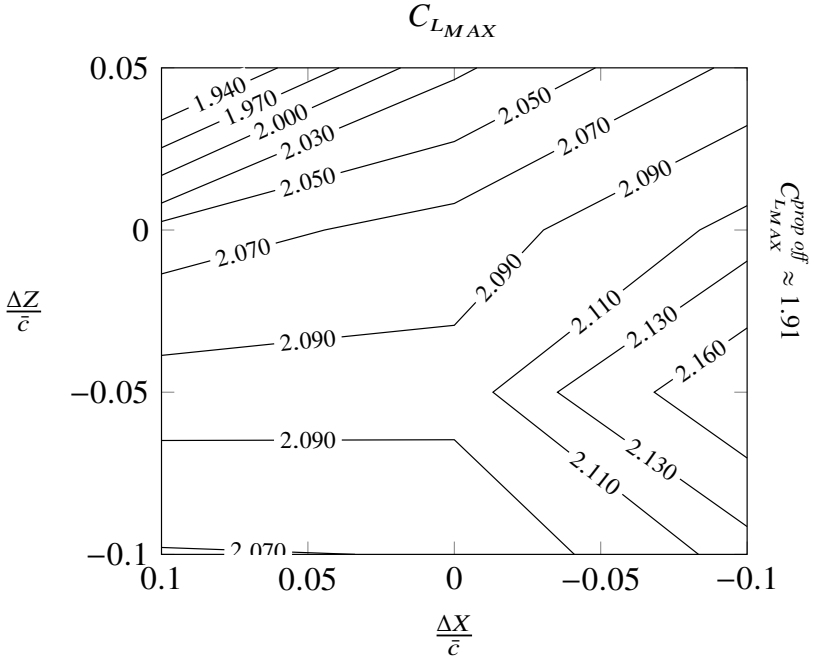

Figure 3.141: Values of $C_{L_{MAX}}$ (corresponding to different angles of attack) of wing by varying the position of DEP propellers - $\delta_f = 15°$ - $V_\infty = 20\ m/s$ - $Re_\infty = 5.48{\cdot}10^5$ - $RPM_{DEP} = 7000$ (In-Board Up) - STAR-CCM+

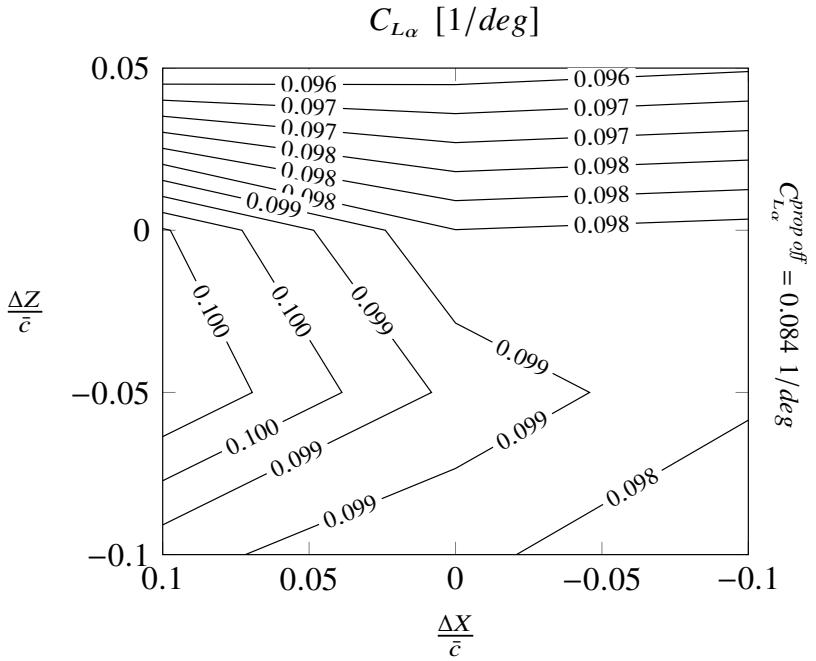

Figure 3.142: Lift curve slope of wing by varying the position of DEP propellers - $\delta_f = 15°$ - $V_\infty = 20\ m/s$ - $Re_\infty = 5.48 \cdot 10^5$ - $RPM_{DEP} = 7000$ (In-Board Up) - STAR-CCM+

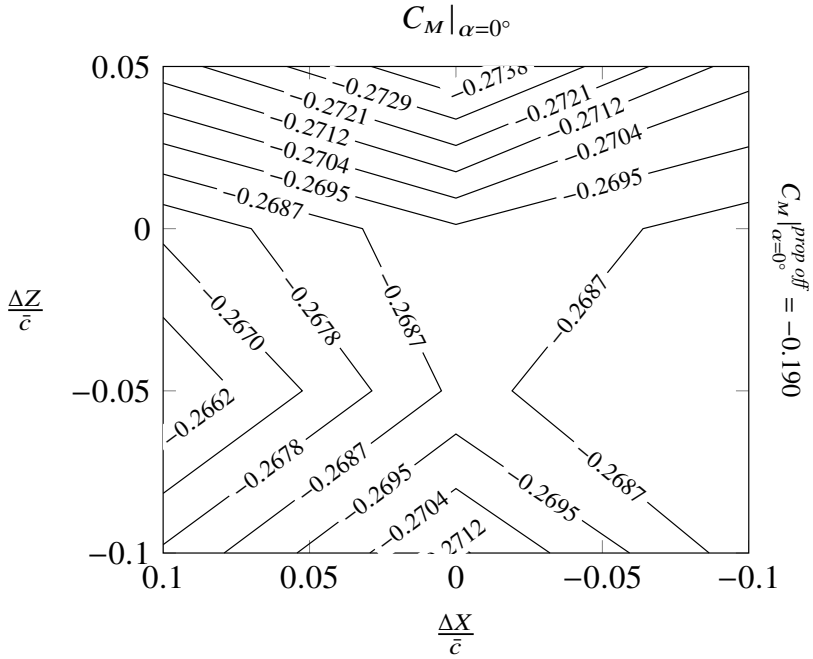

Figure 3.143: Values of $C_M|_{\alpha=0°}$ of wing by varying the position of DEP propellers - $\delta_f = 15°$ - $V_\infty = 20\ m/s$ - $Re_\infty = 5.48 \cdot 10^5$ - $RPM_{DEP} = 7000$ (In-Board Up) - STAR-CCM+

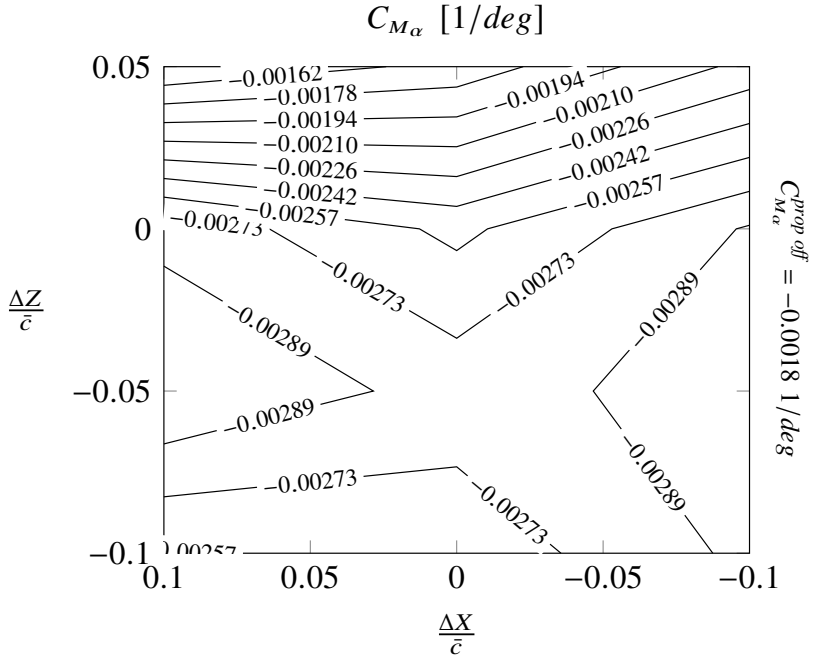

Figure 3.144: Pitching moment curve slope of wing by varying the position of DEP propellers - $\delta_f = 15°$ - $V_\infty = 20\ m/s$ - $Re_\infty = 5.48 \cdot 10^5$ - $RPM_{DEP} = 7000$ (In-Board Up) - STAR-CCM+

3.3.4 DEP effects on flapped configuration (30 deg)

Increasing the flap deflection up to 30 degrees, the xC_zD still corresponds to the highest maximum lift coefficient. However,the lift curves exhibit larger differences at high angles of attack, respect to the two other wing configurations previously analyzed. Fixed the xA and xC positions (Fig. 3.149 and 3.150), moving down the DEP propellers, from the zU to the zD position, a higher maximum lift coefficient can be reached; however, the lift curve related to the zDD position exhibits a stall anticipation, with a lower maximum lift coefficient respect to the zD position. The xF position (fixed) shows that moving the DEP propellers from the zDD to the zU position leads to a stall delay, but to a lower maximum lift coefficient. For each Z-Position fixed, the highest maximum lift coefficient is reached with the xA position.

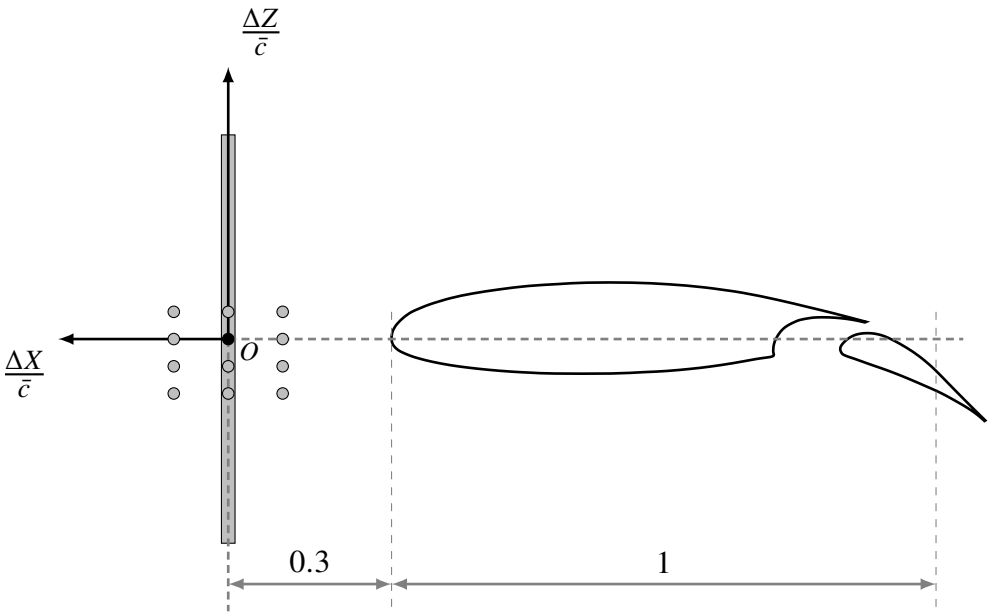

Figure 3.145: Sketch of dimensionless disks positions with respect to the wing leading edge

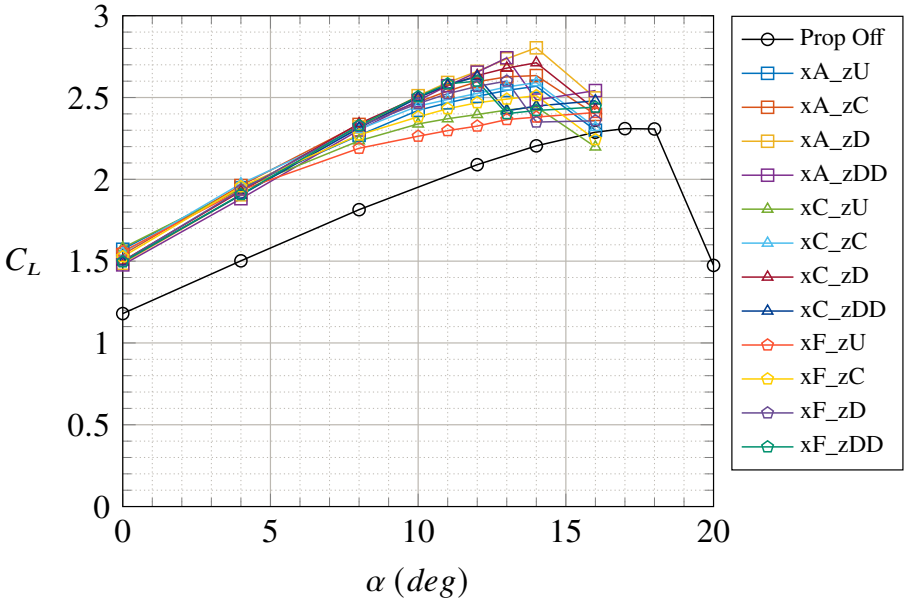

Figure 3.146: Wing lift curves by varying the position of DEP propellers - δ_f = 30° - V_∞ = 20 m/s - $Re_\infty = 5.48 \cdot 10^5$ - RPM_{DEP} = 7000 (In-Board Up) - STAR-CCM+

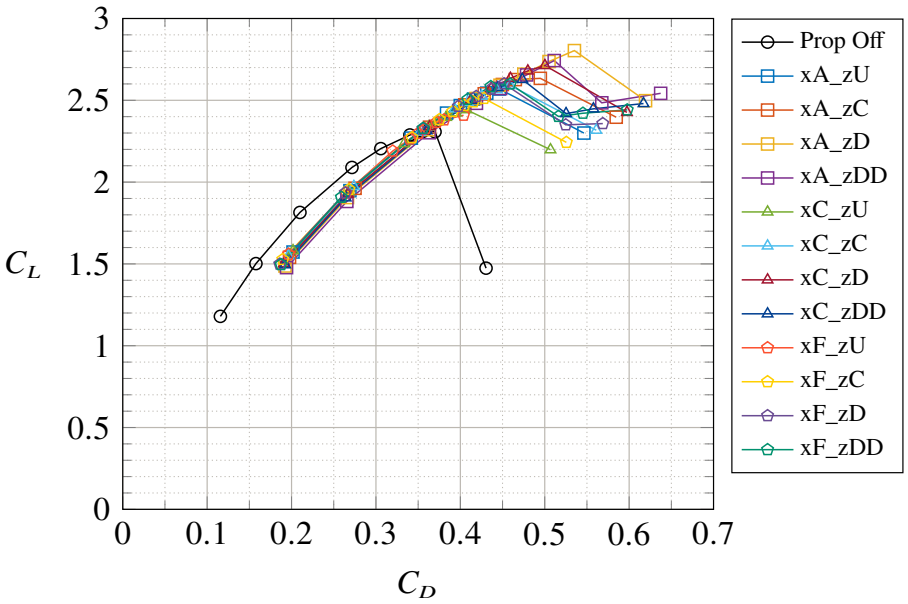

Figure 3.147: Wing drag polars by varying the position of DEP propellers - δ_f = 30° - V_∞ = 20 m/s - $Re_\infty = 5.48 \cdot 10^5$ - RPM_{DEP} = 7000 (In-Board Up) - STAR-CCM+

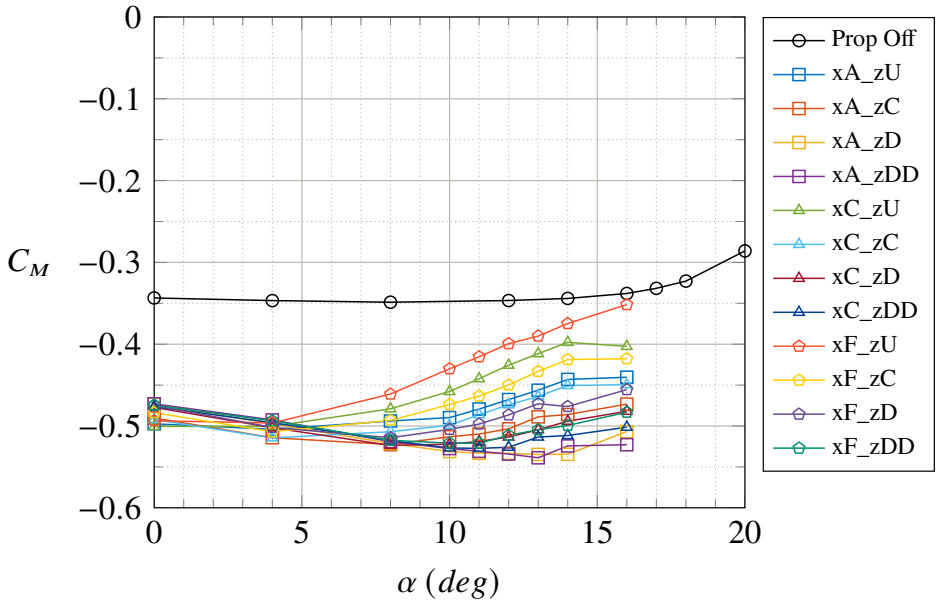

Figure 3.148: Wing pitching moment coefficient by varying the position of DEP propellers - $\delta_f = 30°$ - $V_\infty = 20\ m/s$ - $Re_\infty = 5.48 \cdot 10^5$ - $RPM_{DEP} = 7000$ (In-Board Up) - STAR-CCM+

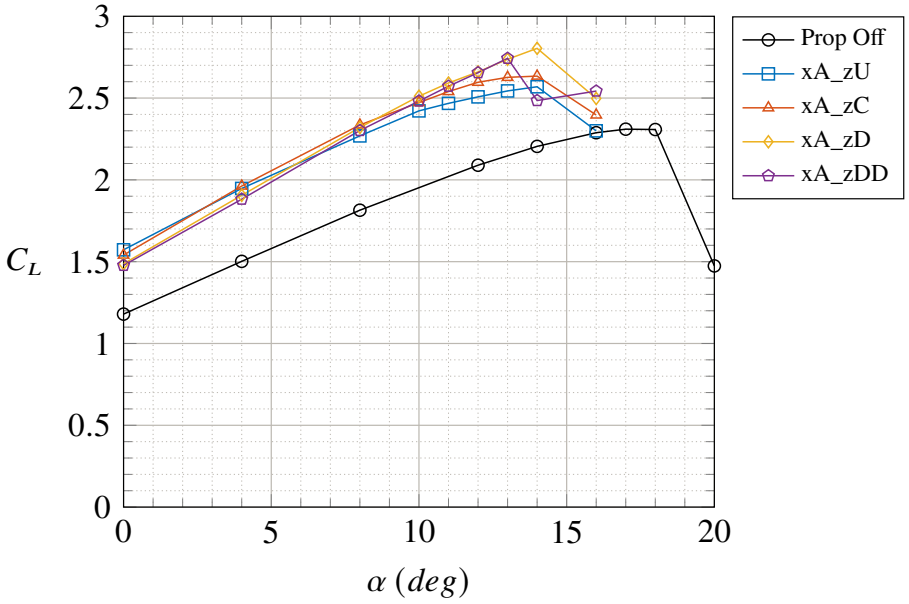

Figure 3.149: Wing lift curves by varying the Z-Position of DEP propellers with xA fixed - $\delta_f = 30°$ - $V_\infty = 20\ m/s$ - $Re_\infty = 5.48 \cdot 10^5$ - $RPM_{DEP} = 7000$ (In-Board Up) - STAR-CCM+

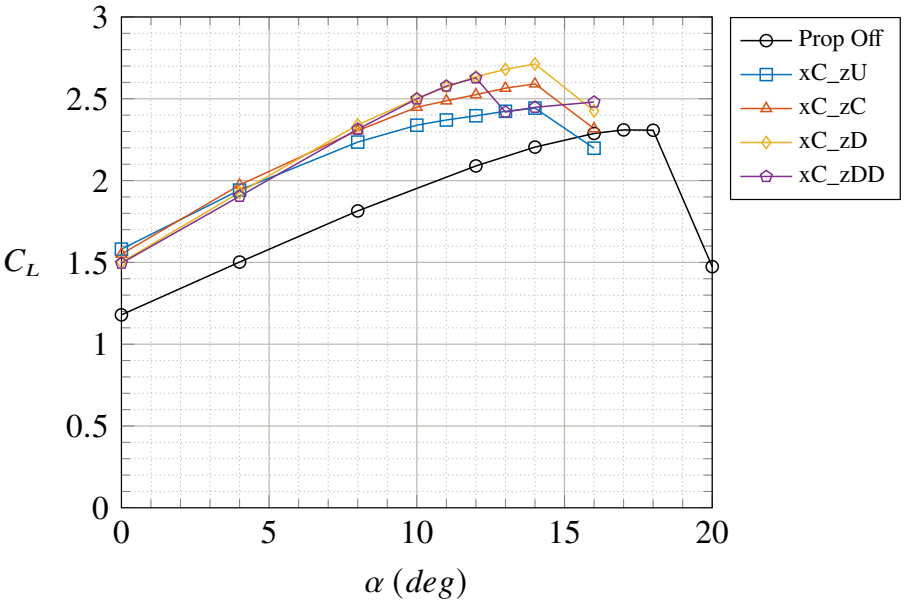

Figure 3.150: Wing lift curves by varying the Z-Position of DEP propellers with xC fixed - $\delta_f = 30°$ - $V_\infty = 20\ m/s$ - $Re_\infty = 5.48 \cdot 10^5$ - $RPM_{DEP} = 7000$ (In-Board Up) - STAR-CCM+

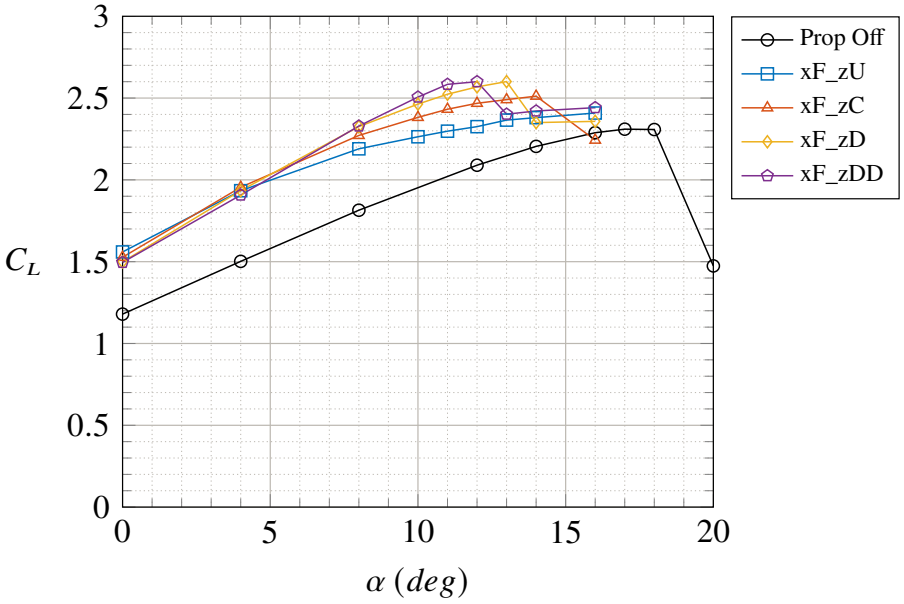

Figure 3.151: Wing lift curves by varying the Z-Position of DEP propellers with xF fixed - $\delta_f = 30°$ - $V_\infty = 20\ m/s$ - $Re_\infty = 5.48 \cdot 10^5$ - $RPM_{DEP} = 7000$ (In-Board Up) - STAR-CCM+

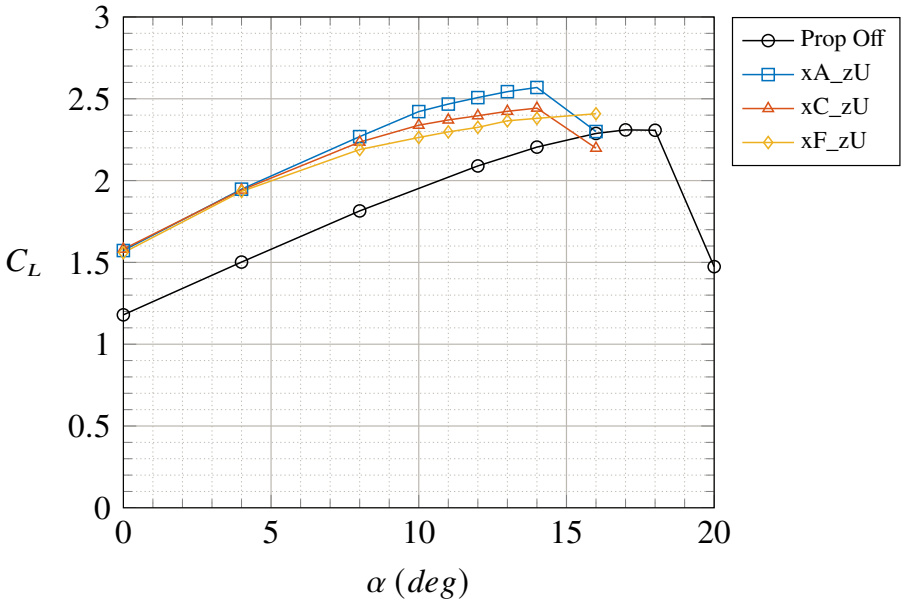

Figure 3.152: Wing lift curves by varying the X-Position of DEP propellers with zU fixed - $\delta_f = 30°$ - $V_\infty = 20\ m/s$ - $Re_\infty = 5.48 \cdot 10^5$ - $RPM_{DEP} = 7000$ (In-Board Up) - STAR-CCM+

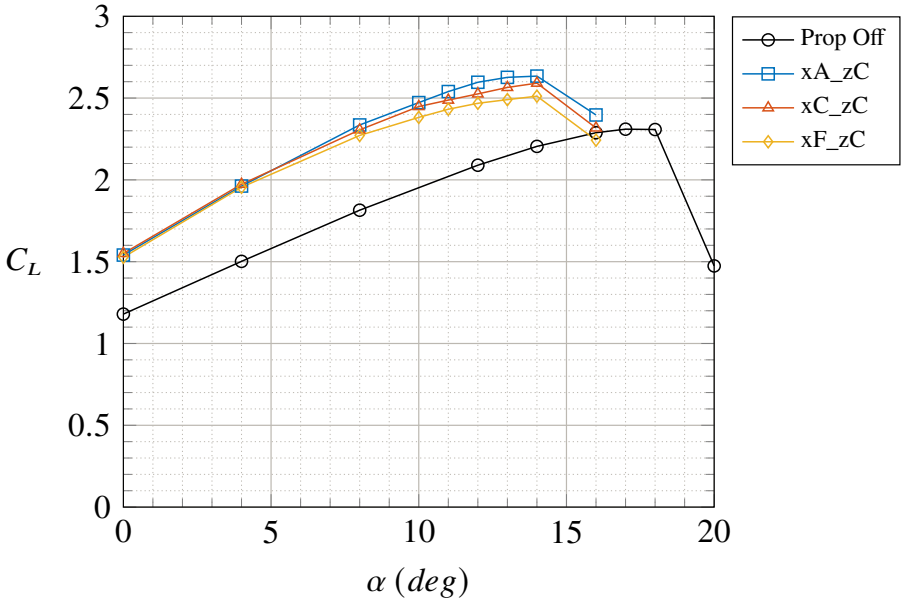

Figure 3.153: Wing lift curves by varying the X-Position of DEP propellers with zC fixed - $\delta_f = 30°$ - $V_\infty = 20\ m/s$ - $Re_\infty = 5.48 \cdot 10^5$ - $RPM_{DEP} = 7000$ (In-Board Up) - STAR-CCM+

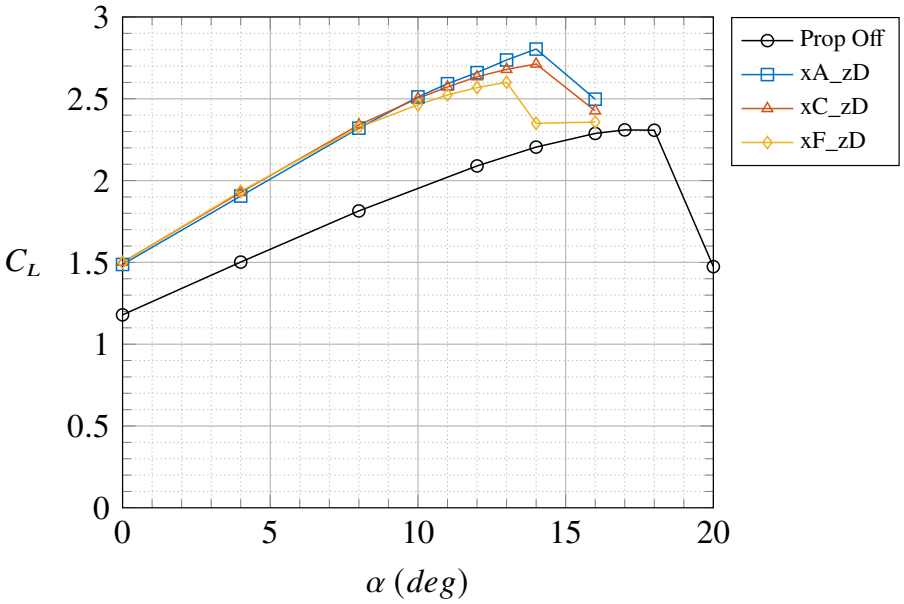

Figure 3.154: Wing lift curves by varying the X-Position of DEP propellers with zD fixed - $\delta_f = 30°$ - $V_\infty = 20\ m/s$ - $Re_\infty = 5.48 \cdot 10^5$ - $RPM_{DEP} = 7000$ (In-Board Up) - STAR-CCM+

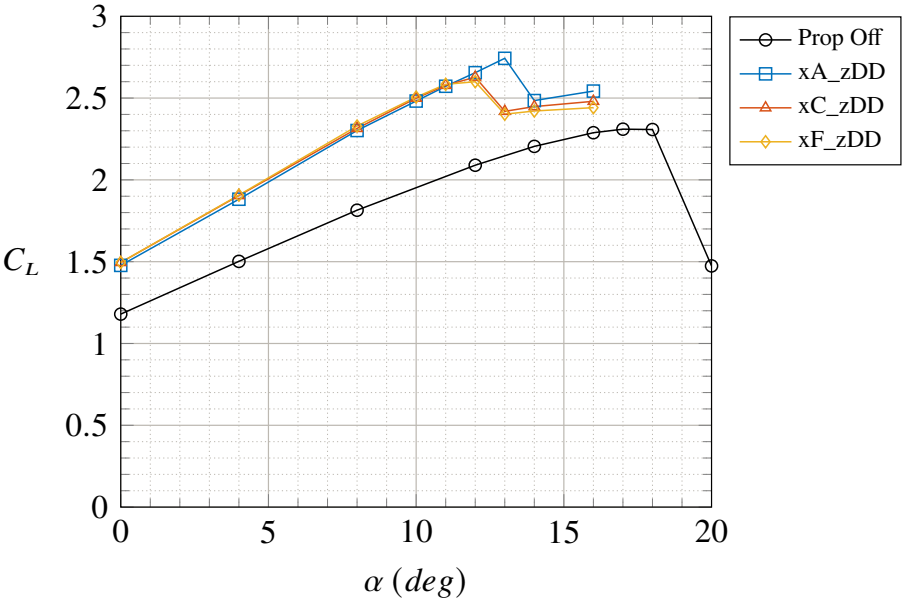

Figure 3.155: Wing lift curves by varying the X-Position of DEP propellers with zDD fixed - $\delta_f = 30°$ - $V_\infty = 20\ m/s$ - $Re_\infty = 5.48 \cdot 10^5$ - $RPM_{DEP} = 7000$ (In-Board Up) - STAR-CCM+

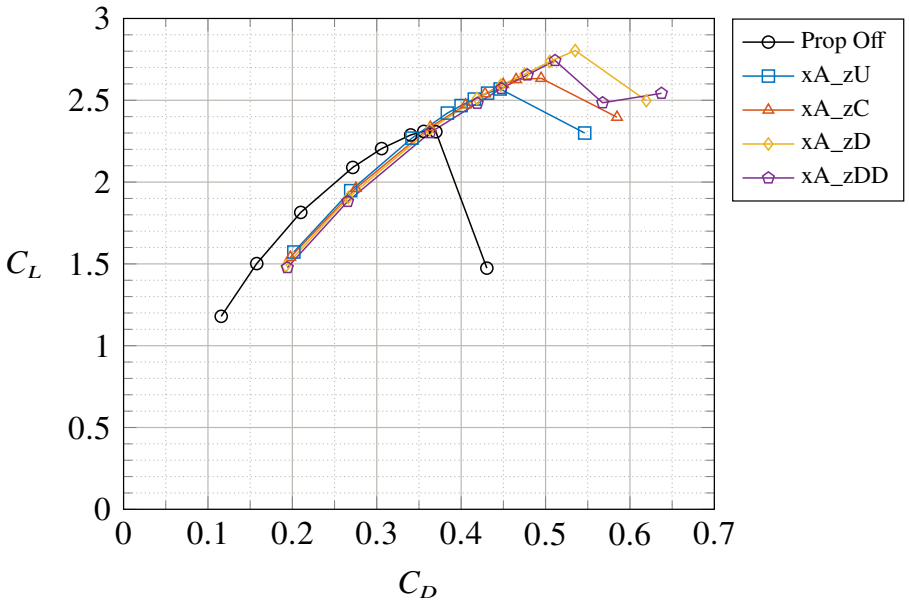

Figure 3.156: Wing drag polars by varying the Z-Position of DEP propellers with xA fixed - $\delta_f = 30°$ - $V_\infty = 20\ m/s$ - $Re_\infty = 5.48 \cdot 10^5$ - $RPM_{DEP} = 7000$ (In-Board Up) - STAR-CCM+

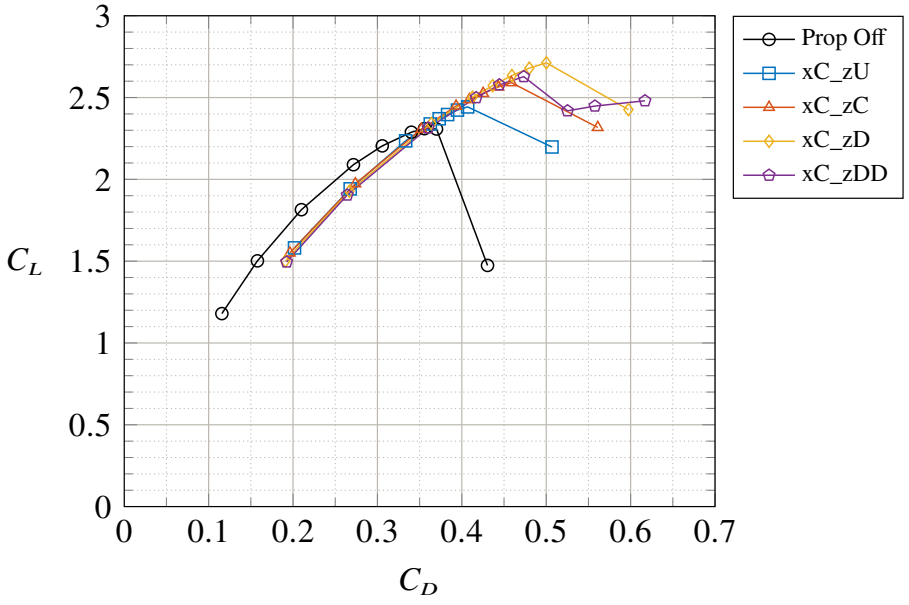

Figure 3.157: Wing drag polars by varying the Z-Position of DEP propellers with xC fixed - $\delta_f = 30°$ - $V_\infty = 20\ m/s$ - $Re_\infty = 5.48 \cdot 10^5$ - $RPM_{DEP} = 7000$ (In-Board Up) - STAR-CCM+

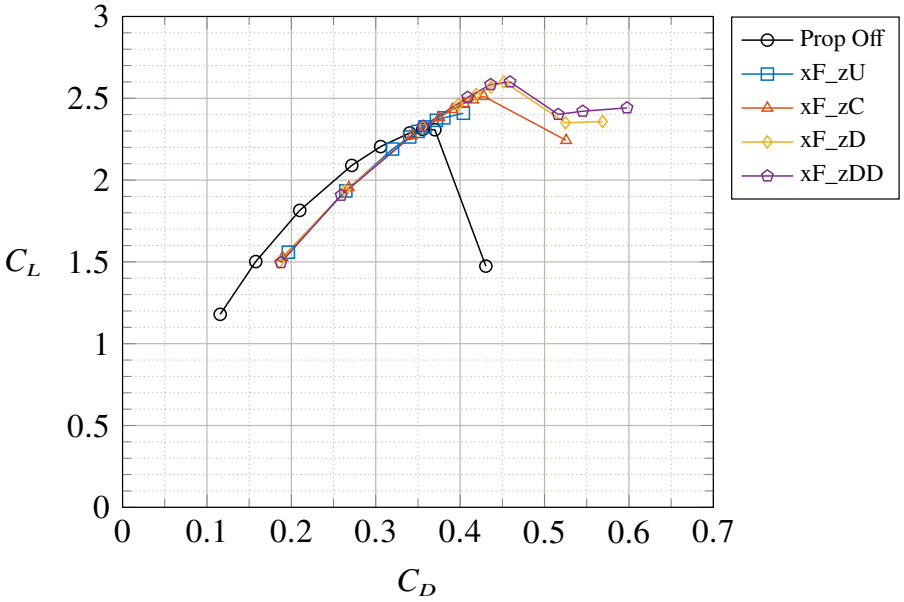

Figure 3.158: Wing drag polars by varying the Z-Position of DEP propellers with xF fixed - $\delta_f = 30°$ - $V_\infty = 20\ m/s$ - $Re_\infty = 5.48 \cdot 10^5$ - $RPM_{DEP} = 7000$ (In-Board Up) - STAR-CCM+

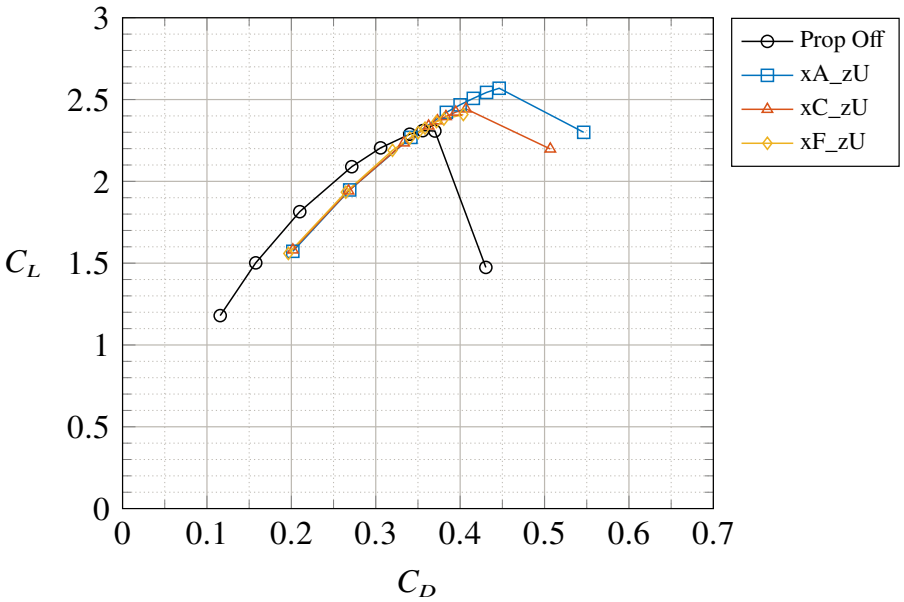

Figure 3.159: Wing drag polars by varying the X-Position of DEP propellers with zU fixed - $\delta_f = 30°$ - $V_\infty = 20\ m/s$ - $Re_\infty = 5.48 \cdot 10^5$ - $RPM_{DEP} = 7000$ (In-Board Up) - STAR-CCM+

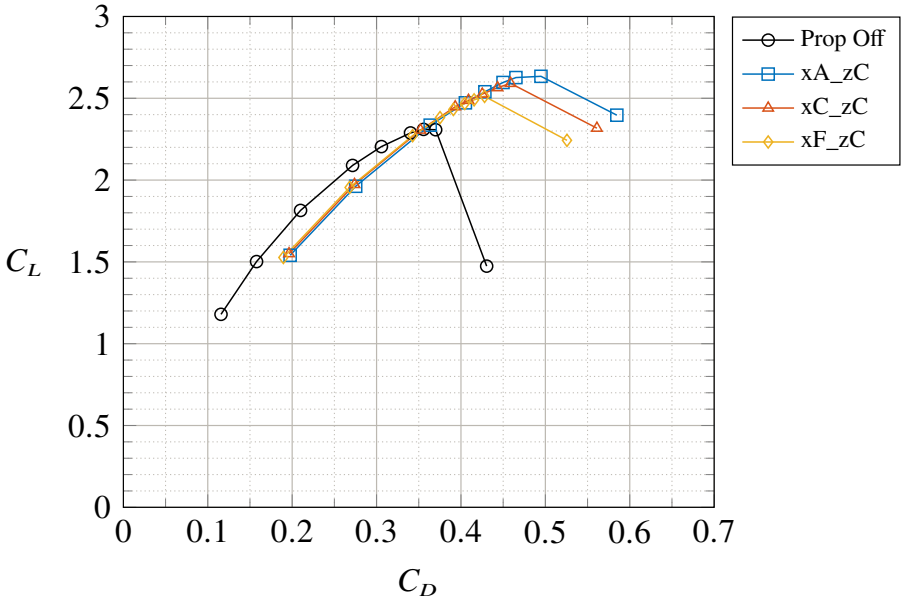

Figure 3.160: Wing drag polars by varying the X-Position of DEP propellers with zC fixed - $\delta_f = 30°$ - $V_\infty = 20\ m/s$ - $Re_\infty = 5.48 \cdot 10^5$ - $RPM_{DEP} = 7000$ (In-Board Up) - STAR-CCM+

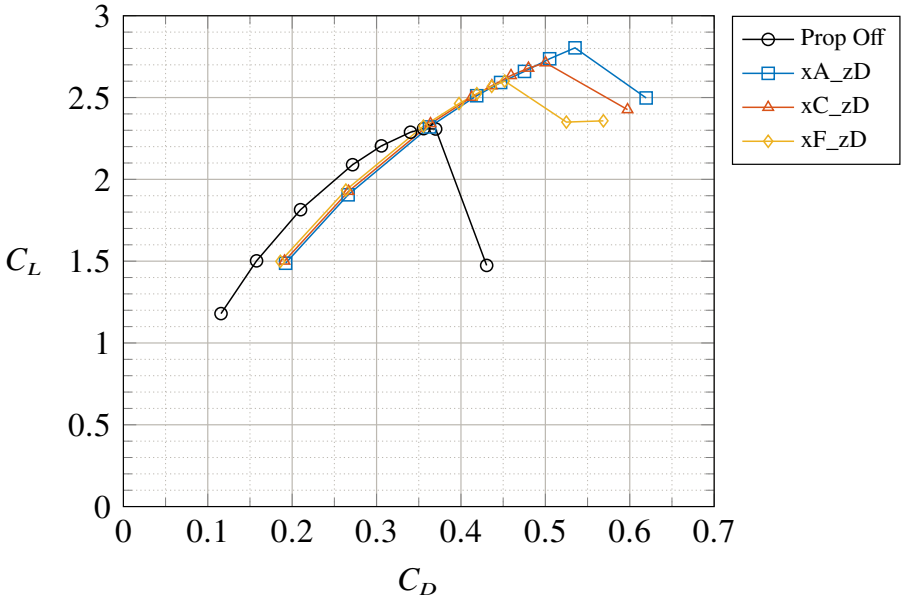

Figure 3.161: Wing drag polars by varying the X-Position of DEP propellers with zD fixed - $\delta_f = 30°$ - $V_\infty = 20\ m/s$ - $Re_\infty = 5.48 \cdot 10^5$ - $RPM_{DEP} = 7000$ (In-Board Up) - STAR-CCM+

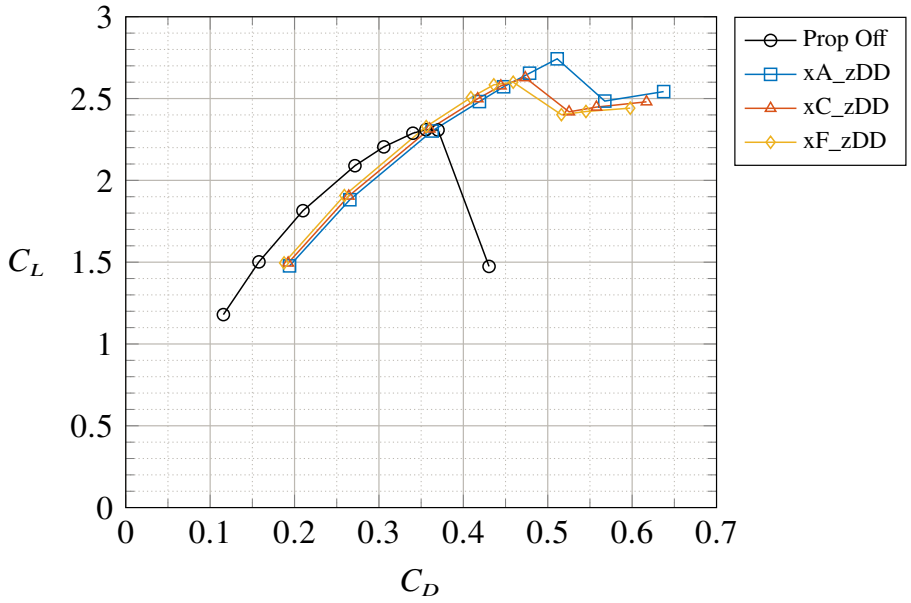

Figure 3.162: Wing drag polars by varying the X-Position of DEP propellers with zDD fixed - $\delta_f = 30°$ - $V_\infty = 20\ m/s$ - $Re_\infty = 5.48 \cdot 10^5$ - $RPM_{DEP} = 7000$ (In-Board Up) - STAR-CCM+

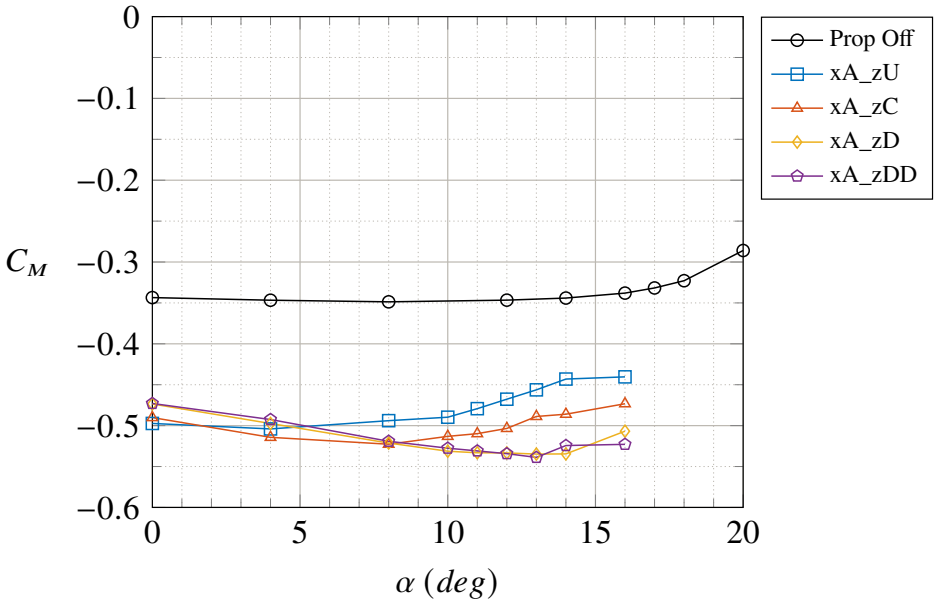

Figure 3.163: Wing pitching moment coefficient by varying the Z-Position of DEP propellers with xA fixed - $\delta_f = 30°$ - $V_\infty = 20\ m/s$ - $Re_\infty = 5.48 \cdot 10^5$ - $RPM_{DEP} = 7000$ (In-Board Up) - STAR-CCM+

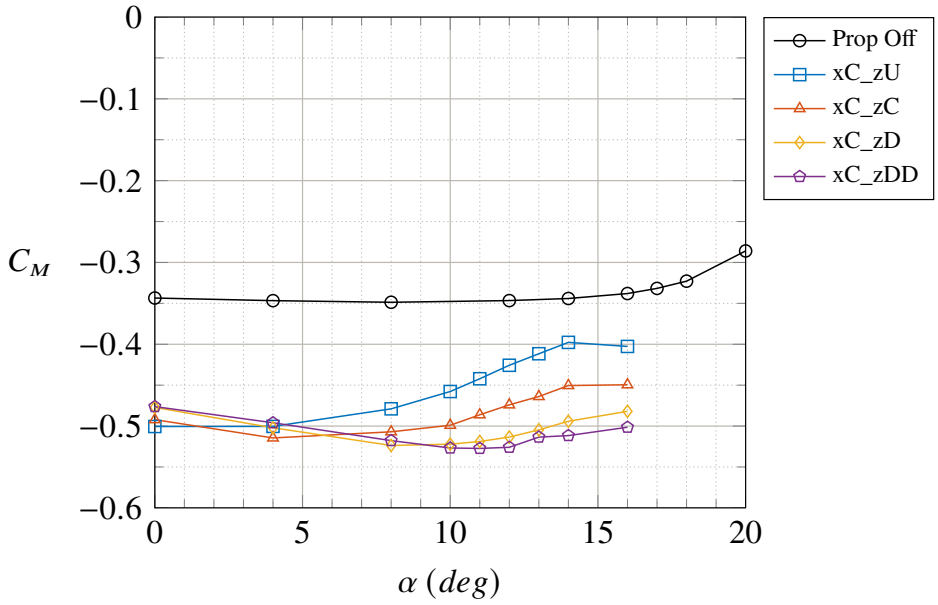

Figure 3.164: Wing pitching moment coefficient by varying the Z-Position of DEP propellers with xC fixed - $\delta_f = 30°$ - $V_\infty = 20\ m/s$ - $Re_\infty = 5.48 \cdot 10^5$ - $RPM_{DEP} = 7000$ (In-Board Up) - STAR-CCM+

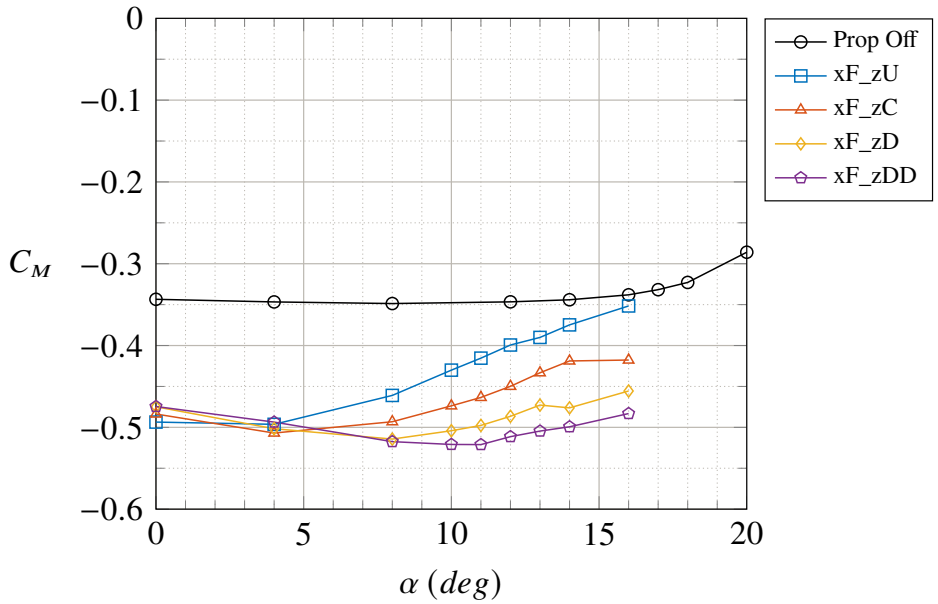

Figure 3.165: Wing pitching moment coefficient by varying the Z-Position of DEP propellers with xF fixed - $\delta_f = 30°$ - $V_\infty = 20\ m/s$ - $Re_\infty = 5.48 \cdot 10^5$ - $RPM_{DEP} = 7000$ (In-Board Up) - STAR-CCM+

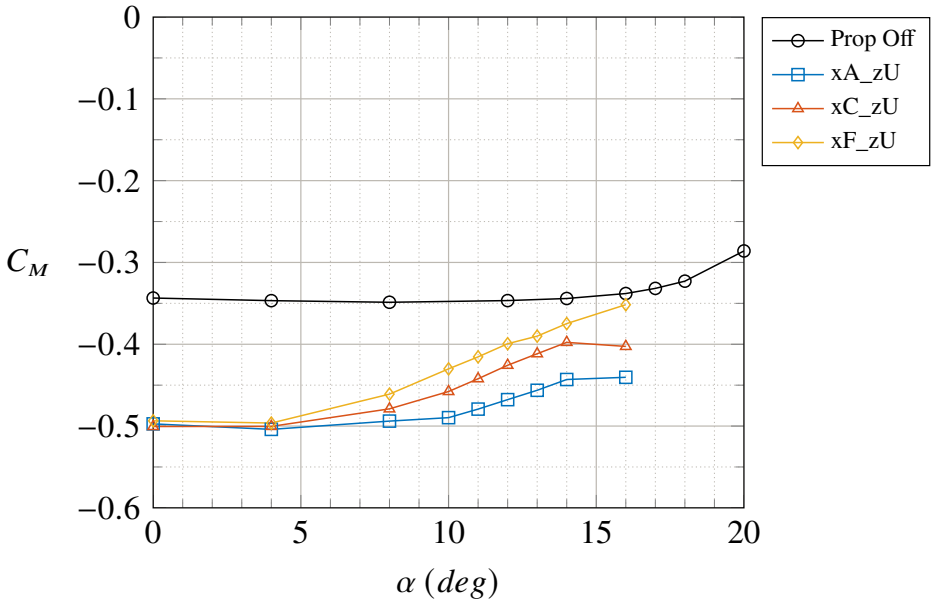

Figure 3.166: Wing pitching moment coefficient by varying the X-Position of DEP propellers with zU fixed - $\delta_f = 30°$ - $V_\infty = 20\ m/s$ - $Re_\infty = 5.48 \cdot 10^5$ - $RPM_{DEP} = 7000$ (In-Board Up) - STAR-CCM+

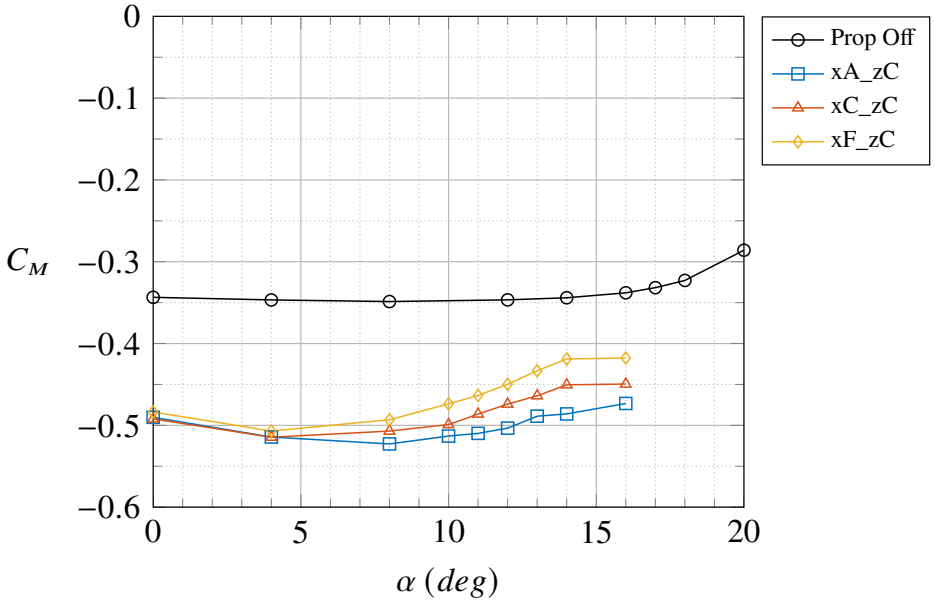

Figure 3.167: Wing pitching moment coefficient by varying the X-Position of DEP propellers with zC fixed - $\delta_f = 30°$ - $V_\infty = 20\ m/s$ - $Re_\infty = 5.48 \cdot 10^5$ - $RPM_{DEP} = 7000$ (In-Board Up) - STAR-CCM+

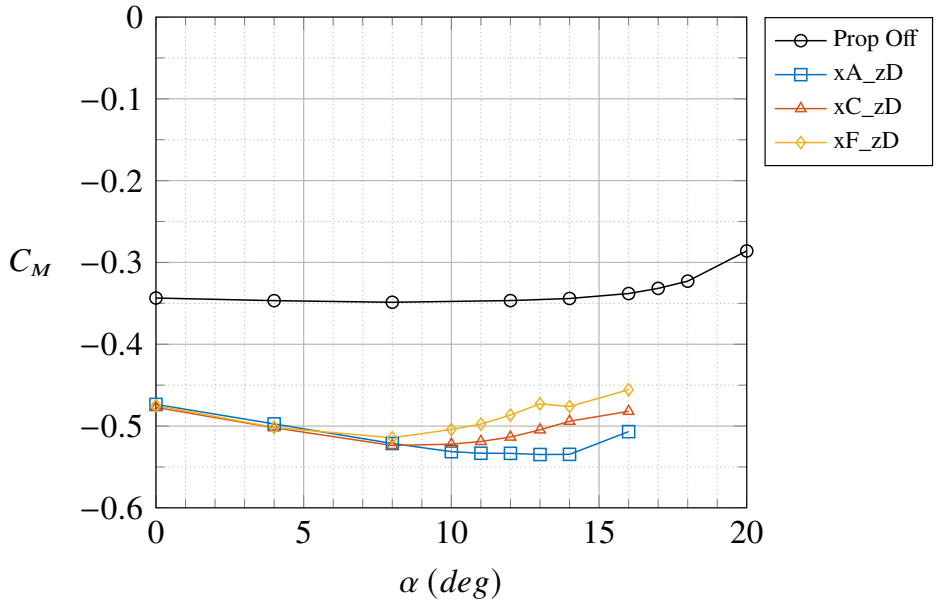

Figure 3.168: Wing pitching moment coefficient by varying the X-Position of DEP propellers with zD fixed - $\delta_f = 30°$ - $V_\infty = 20\ m/s$ - $Re_\infty = 5.48 \cdot 10^5$ - $RPM_{DEP} = 7000$ (In-Board Up) - STAR-CCM+

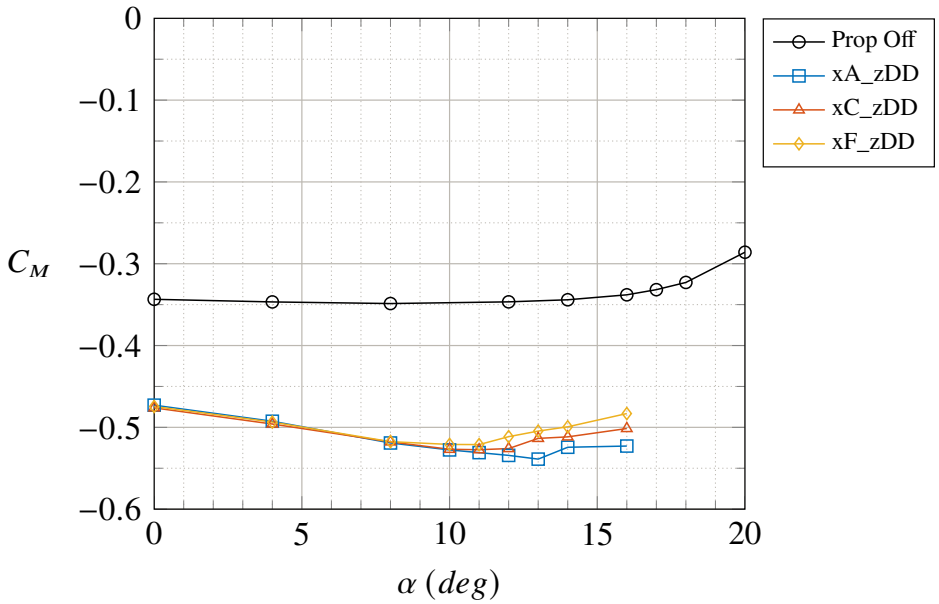

Figure 3.169: Wing pitching moment coefficient by varying the X-Position of DEP propellers with zDD fixed - $\delta_f = 30°$ - $V_\infty = 20\ m/s$ - $Re_\infty = 5.48 \cdot 10^5$ - $RPM_{DEP} = 7000$ (In-Board Up) - STAR-CCM+

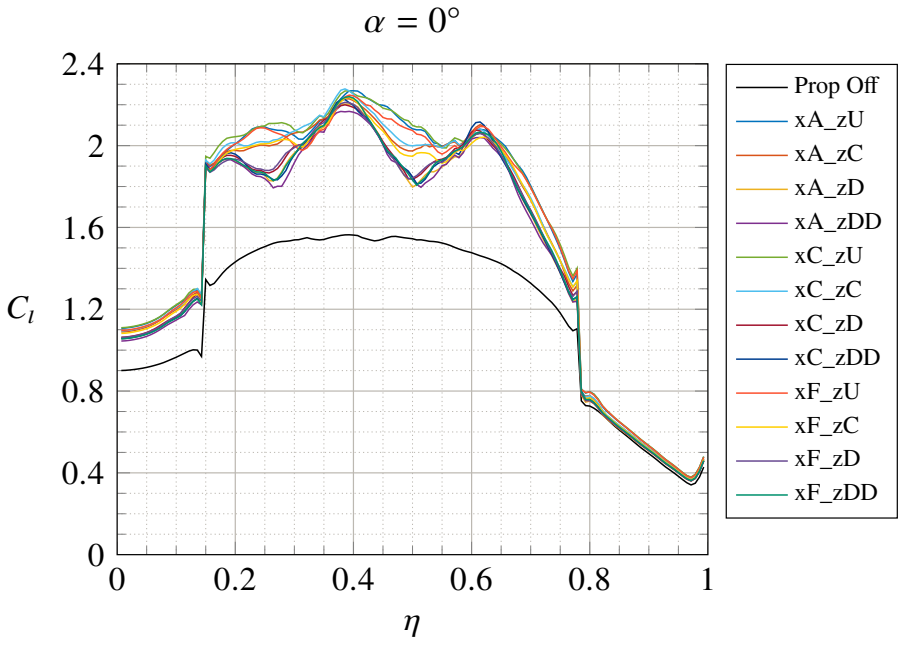

Figure 3.170: Wing load distribution by varying the position of DEP propellers - $\delta_f = 30°$ - $V_\infty = 20\ m/s$ - $Re_\infty = 5.48 \cdot 10^5$ - $RPM_{DEP} = 7000$ (In-Board Up) - STAR-CCM+

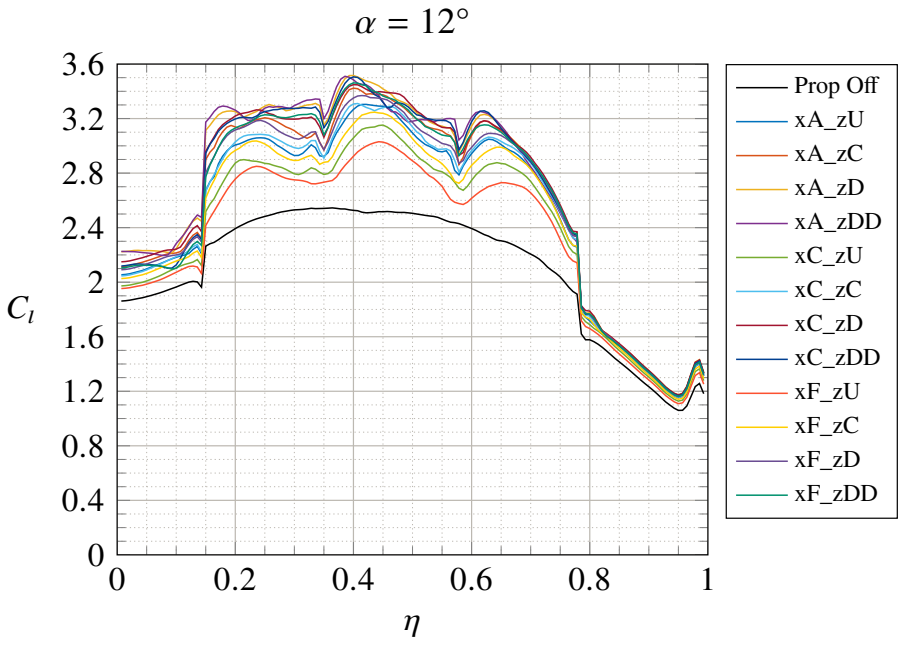

Figure 3.171: Wing load distribution by varying the position of DEP propellers - $\delta_f = 30°$ - $V_\infty = 20\ m/s$ - $Re_\infty = 5.48 \cdot 10^5$ - $RPM_{DEP} = 7000$ (In-Board Up) - STAR-CCM+

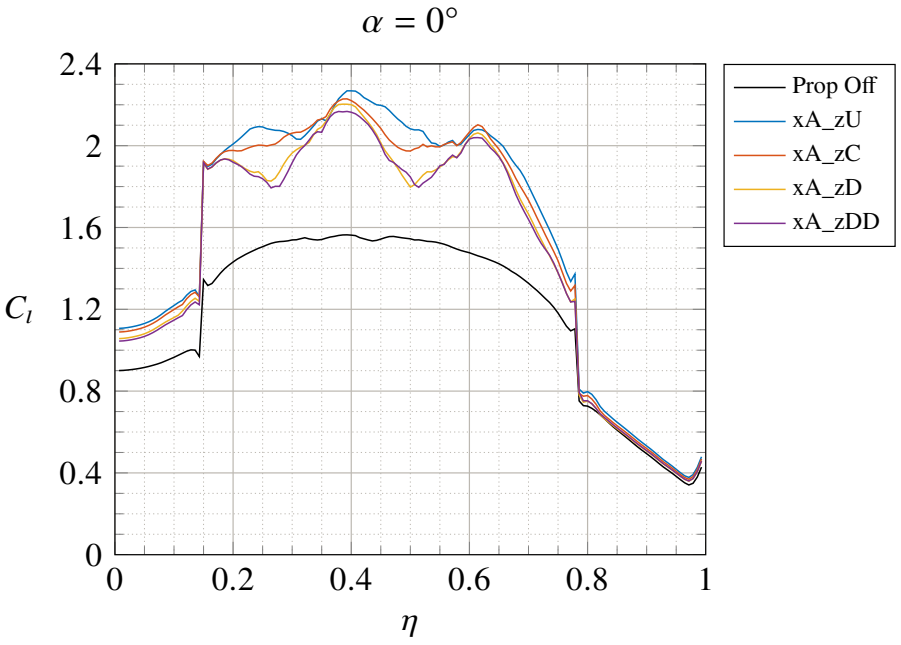

Figure 3.172: Wing load distribution by varying the Z-Position of DEP propellers with xA fixed - $\delta_f = 30°$ - $V_\infty = 20\ m/s$ - $Re_\infty = 5.48 \cdot 10^5$ - $RPM_{DEP} = 7000$ (In-Board Up) - STAR-CCM+

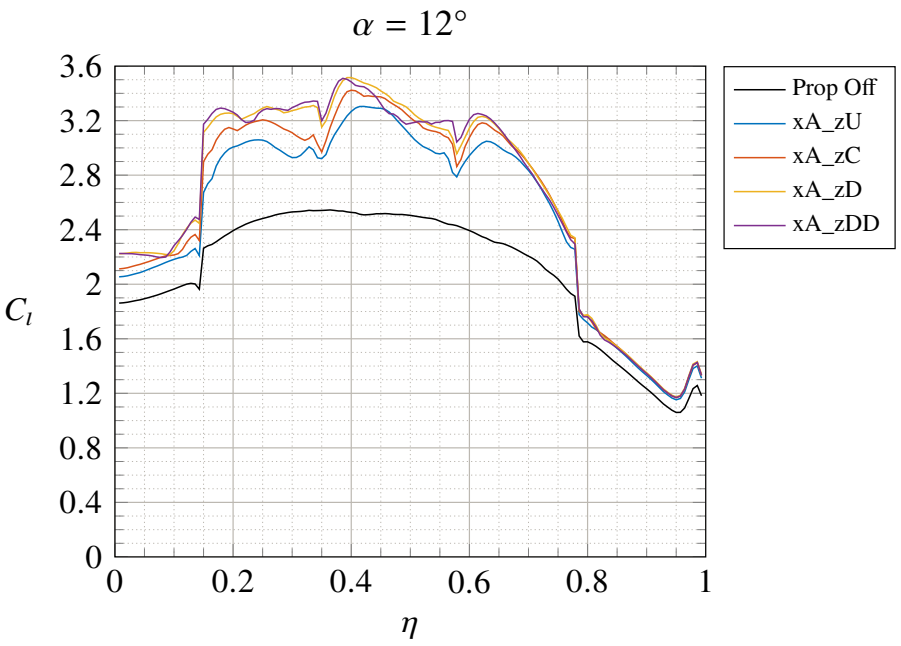

Figure 3.173: Wing load distribution by varying the Z-Position of DEP propellers with xA fixed - $\delta_f = 30°$ - $V_\infty = 20\ m/s$ - $Re_\infty = 5.48 \cdot 10^5$ - $RPM_{DEP} = 7000$ (In-Board Up) - STAR-CCM+

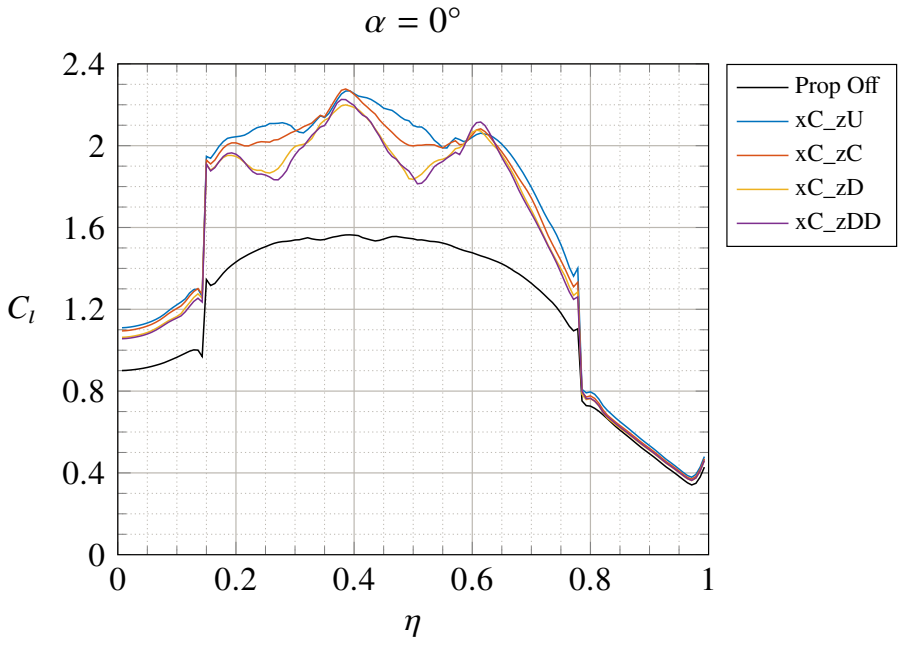

Figure 3.174: Wing load distribution by varying the Z-Position of DEP propellers with xC fixed - $\delta_f = 30°$ - $V_\infty = 20\ m/s$ - $Re_\infty = 5.48 \cdot 10^5$ - $RPM_{DEP} = 7000$ (In-Board Up) - STAR-CCM+

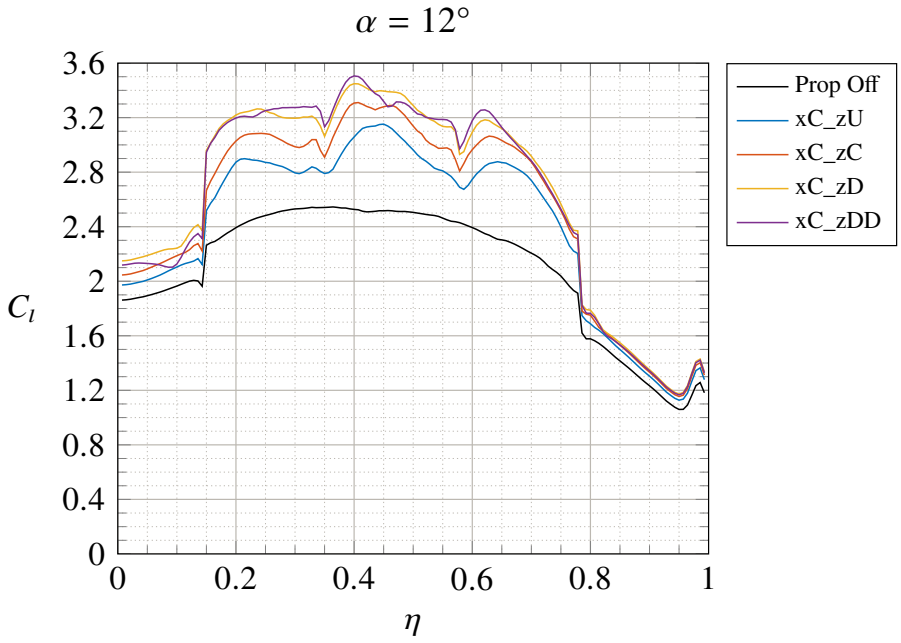

Figure 3.175: Wing load distribution by varying the Z-Position of DEP propellers with xC fixed - $\delta_f = 30°$ - $V_\infty = 20\ m/s$ - $Re_\infty = 5.48 \cdot 10^5$ - $RPM_{DEP} = 7000$ (In-Board Up) - STAR-CCM+

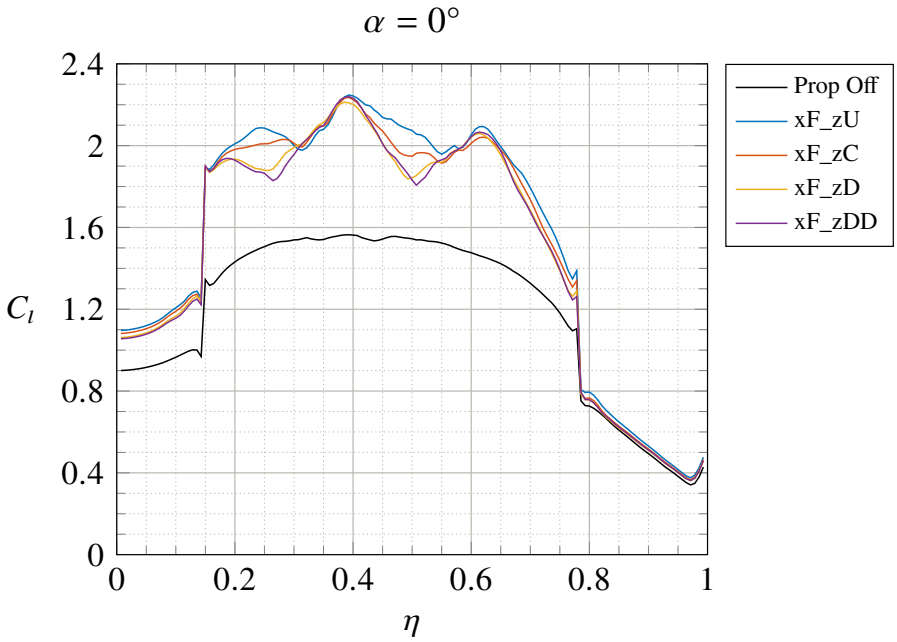

Figure 3.176: Wing load distribution by varying the Z-Position of DEP propellers with xF fixed - $\delta_f = 30°$ - $V_\infty = 20\ m/s$ - $Re_\infty = 5.48 \cdot 10^5$ - $RPM_{DEP} = 7000$ (In-Board Up) - STAR-CCM+

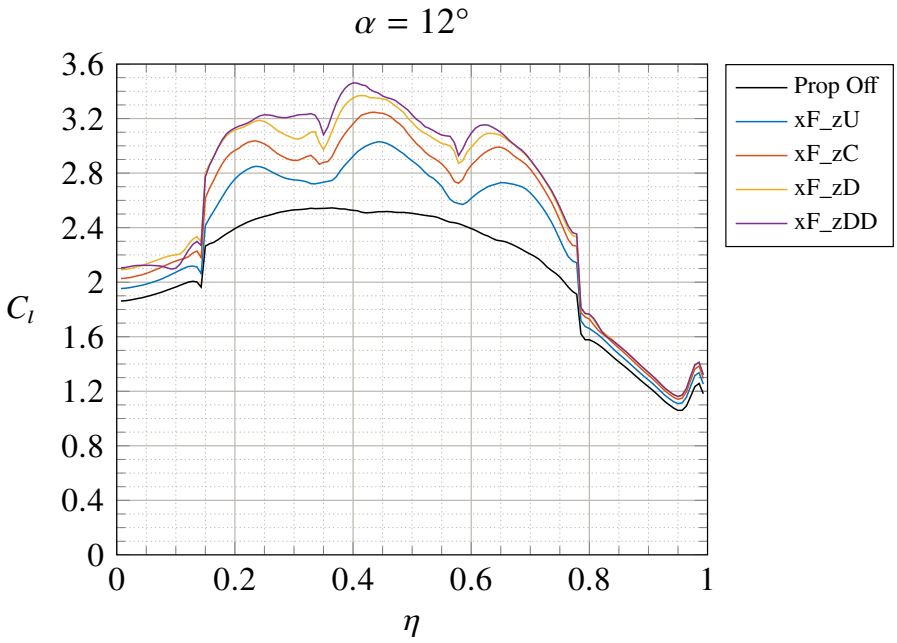

Figure 3.177: Wing load distribution by varying the Z-Position of DEP propellers with xF fixed - $\delta_f = 30°$ - $V_\infty = 20\ m/s$ - $Re_\infty = 5.48 \cdot 10^5$ - $RPM_{DEP} = 7000$ (In-Board Up) - STAR-CCM+

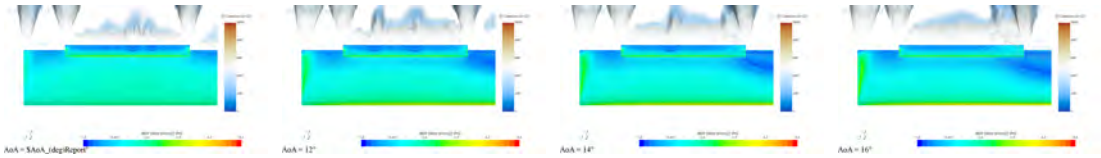

(a) $\alpha = 0°$ - Prop Off **(b)** $\alpha = 12°$ - Prop Off **(c)** $\alpha = 14°$ - Prop Off **(d)** $\alpha = 16°$ - Prop Off

Figure 3.178: Contours of the X-Component of wall shear stress and Q-Criterion isosurfaces for the prop off condition - $\delta_f = 30°$ - $V_\infty = 20\ m/s$ - $Re_\infty = 5.48 \cdot 10^5$ - STAR-CCM+

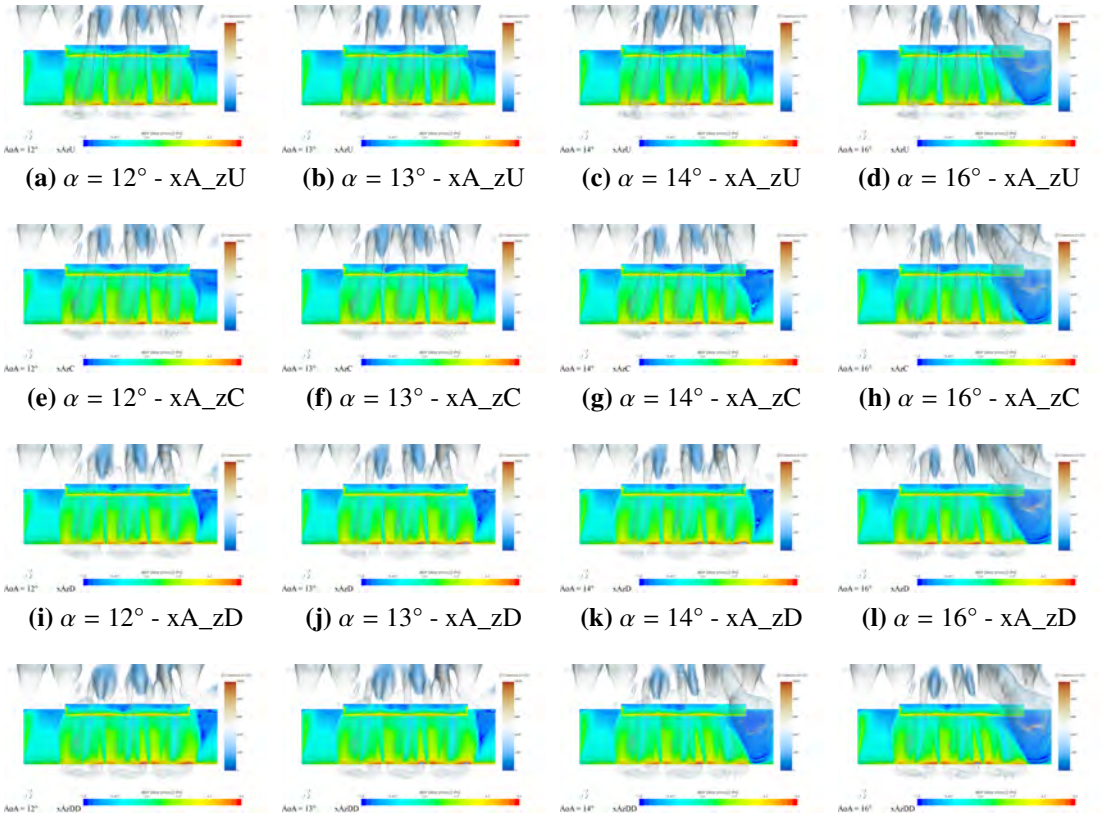

(a) $\alpha = 12°$ - xA_zU **(b)** $\alpha = 13°$ - xA_zU **(c)** $\alpha = 14°$ - xA_zU **(d)** $\alpha = 16°$ - xA_zU

(e) $\alpha = 12°$ - xA_zC **(f)** $\alpha = 13°$ - xA_zC **(g)** $\alpha = 14°$ - xA_zC **(h)** $\alpha = 16°$ - xA_zC

(i) $\alpha = 12°$ - xA_zD **(j)** $\alpha = 13°$ - xA_zD **(k)** $\alpha = 14°$ - xA_zD **(l)** $\alpha = 16°$ - xA_zD

(m) $\alpha = 12°$ - xA_zDD **(n)** $\alpha = 13°$ - xA_zDD **(o)** $\alpha = 14°$ - xA_zDD **(p)** $\alpha = 16°$ - xA_zDD

Figure 3.179: Contours of the X-Component of wall shear stress and Q-Criterion isosurfaces for xA position fixed and varying the Z-Position of DEP propellers - $\delta_f = 30°$ - $V_\infty = 20\ m/s$ - $Re_\infty = 5.48 \cdot 10^5$ - $RPM_{DEP} = 7000$ (In-Board Up) - STAR-CCM+

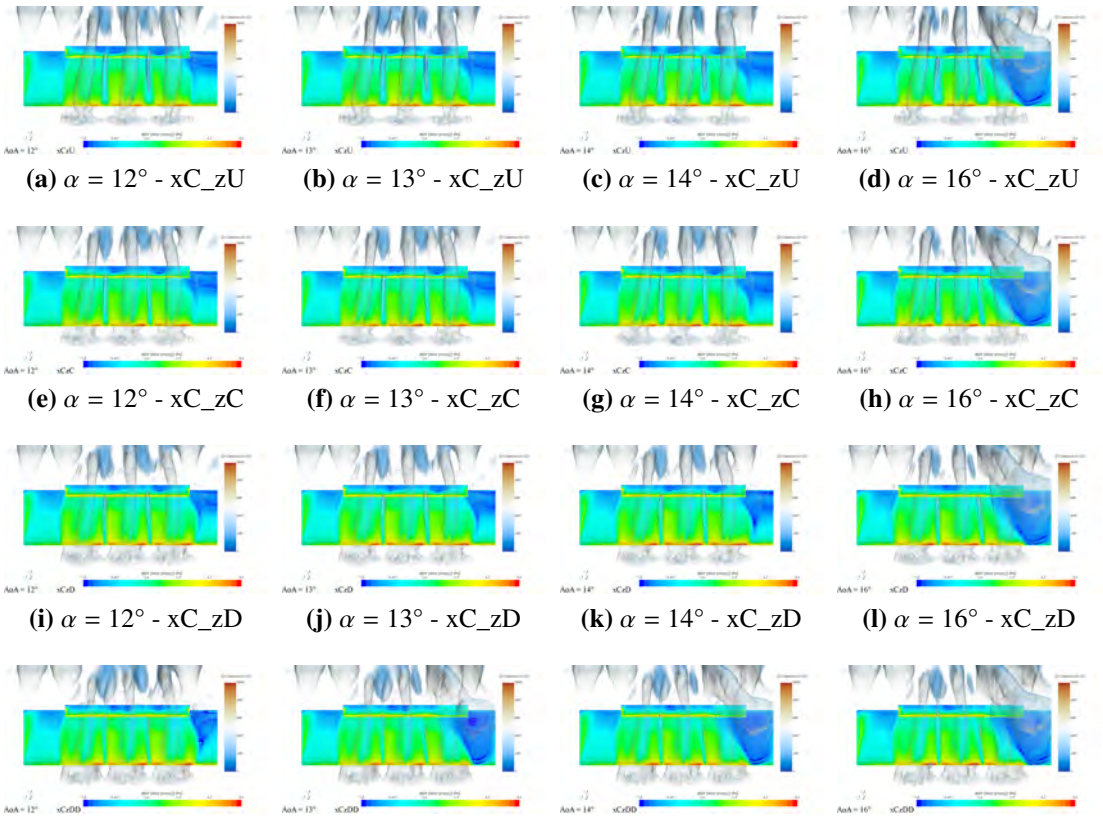

(a) α = 12° - xC_zU **(b)** α = 13° - xC_zU **(c)** α = 14° - xC_zU **(d)** α = 16° - xC_zU

(e) α = 12° - xC_zC **(f)** α = 13° - xC_zC **(g)** α = 14° - xC_zC **(h)** α = 16° - xC_zC

(i) α = 12° - xC_zD **(j)** α = 13° - xC_zD **(k)** α = 14° - xC_zD **(l)** α = 16° - xC_zD

(m) α = 12° - xC_zDD **(n)** α = 13° - xC_zDD **(o)** α = 14° - xC_zDD **(p)** α = 16° - xC_zDD

Figure 3.180: Contours of the X-Component of wall shear stress and Q-Criterion isosurfaces for xC position fixed and varying the Z-Position of DEP propellers - δ_f = 30° - V_∞ = 20 m/s - $Re_\infty = 5.48 \cdot 10^5$ - RPM_{DEP} = 7000 (In-Board Up) - STAR-CCM+

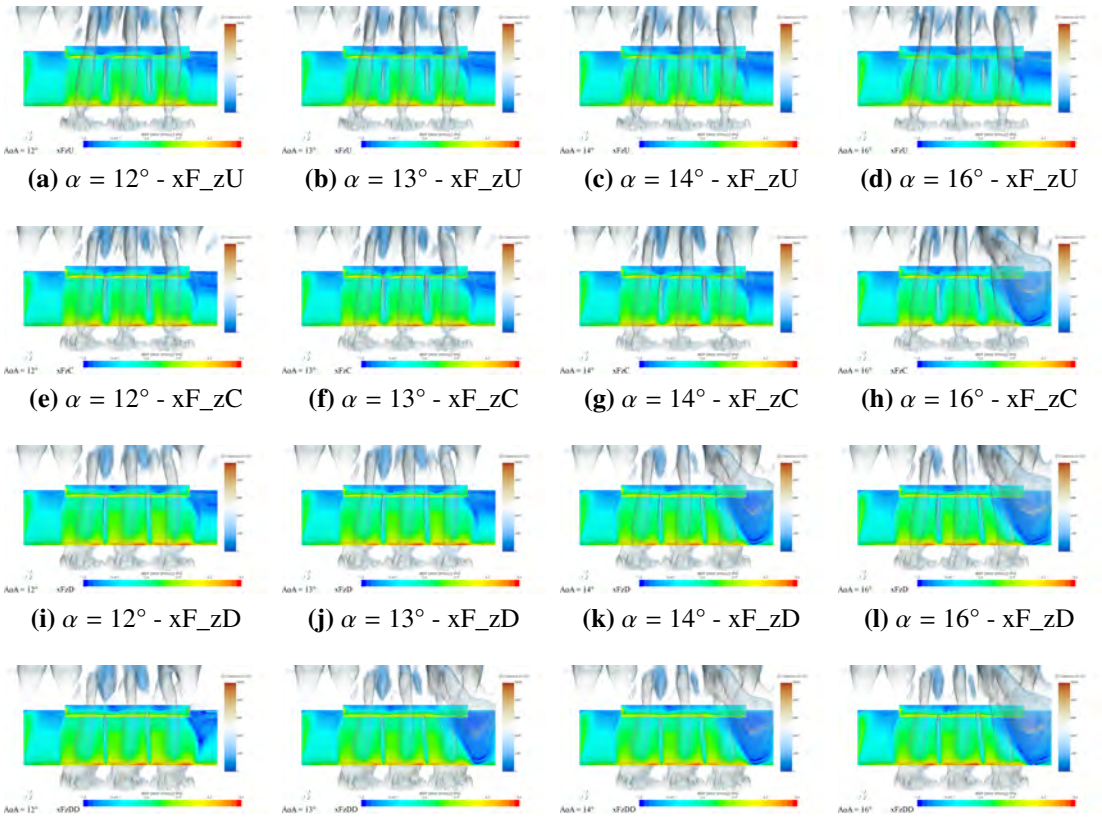

(a) α = 12° - xF_zU **(b)** α = 13° - xF_zU **(c)** α = 14° - xF_zU **(d)** α = 16° - xF_zU

(e) α = 12° - xF_zC **(f)** α = 13° - xF_zC **(g)** α = 14° - xF_zC **(h)** α = 16° - xF_zC

(i) α = 12° - xF_zD **(j)** α = 13° - xF_zD **(k)** α = 14° - xF_zD **(l)** α = 16° - xF_zD

(m) α = 12° - xF_zDD **(n)** α = 13° - xF_zDD **(o)** α = 14° - xF_zDD **(p)** α = 16° - xF_zDD

Figure 3.181: Contours of the X-Component of wall shear stress and Q-Criterion isosurfaces for xF position fixed and varying the Z-Position of DEP propellers - δ_f = 30° - V_∞ = 20 m/s - $Re_\infty = 5.48 \cdot 10^5$ - RPM_{DEP} = 7000 (In-Board Up) - STAR-CCM+

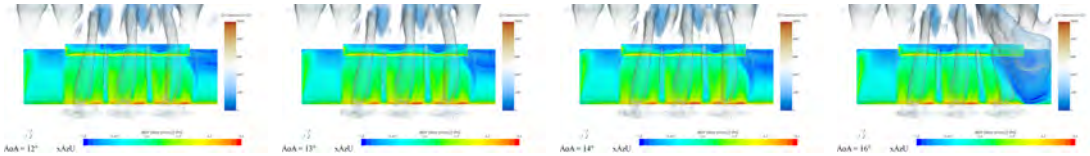

(a) $\alpha = 12°$ - xA_zU **(b)** $\alpha = 13°$ - xA_zU **(c)** $\alpha = 14°$ - xA_zU **(d)** $\alpha = 16°$ - xA_zU

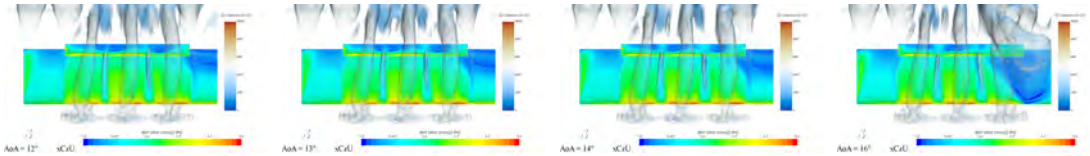

(e) $\alpha = 12°$ - xC_zU **(f)** $\alpha = 13°$ - xC_zU **(g)** $\alpha = 14°$ - xC_zU **(h)** $\alpha = 16°$ - xC_zU

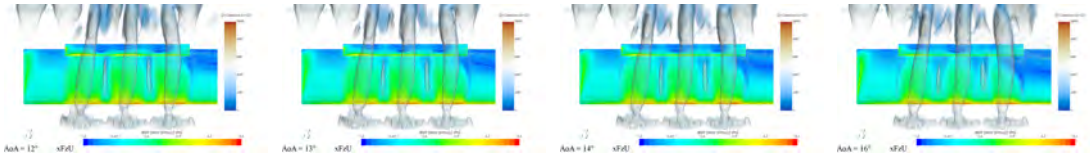

(i) $\alpha = 12°$ - xF_zU **(j)** $\alpha = 13°$ - xF_zU **(k)** $\alpha = 14°$ - xF_zU **(l)** $\alpha = 16°$ - xF_zU

Figure 3.182: Contours of the X-Component of wall shear stress and Q-Criterion isosurfaces for zU position fixed and varying the X-Position of DEP propellers - $\delta_f = 30°$ - $V_\infty = 20\ m/s$ - $Re_\infty = 5.48 \cdot 10^5$ - $RPM_{DEP} = 7000$ (In-Board Up) - STAR-CCM+

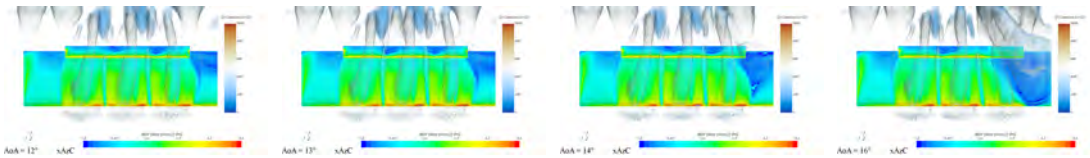

(a) $\alpha = 12°$ - xA_zC **(b)** $\alpha = 13°$ - xA_zC **(c)** $\alpha = 14°$ - xA_zC **(d)** $\alpha = 16°$ - xA_zC

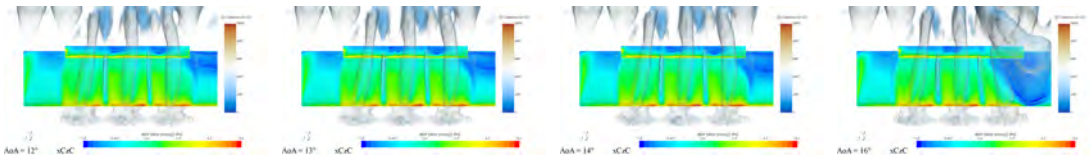

(e) $\alpha = 12°$ - xC_zC **(f)** $\alpha = 13°$ - xC_zC **(g)** $\alpha = 14°$ - xC_zC **(h)** $\alpha = 16°$ - xC_zC

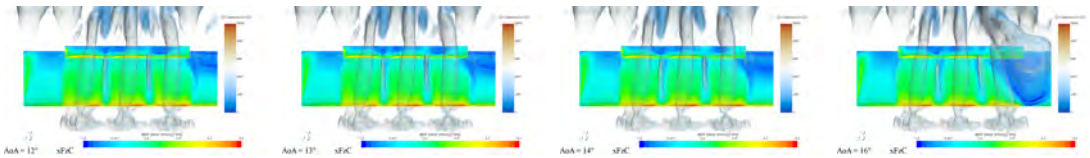

(i) $\alpha = 12°$ - xF_zC **(j)** $\alpha = 13°$ - xF_zC **(k)** $\alpha = 14°$ - xF_zC **(l)** $\alpha = 16°$ - xF_zC

Figure 3.183: Contours of the X-Component of wall shear stress and Q-Criterion isosurfaces for zC position fixed and varying the X-Position of DEP propellers - $\delta_f = 30°$ - $V_\infty = 20\ m/s$ - $Re_\infty = 5.48 \cdot 10^5$ - $RPM_{DEP} = 7000$ (In-Board Up) - STAR-CCM+

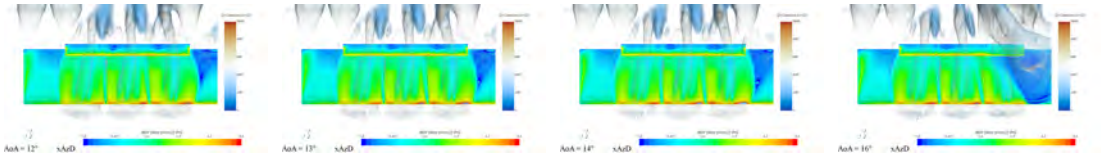

(a) $\alpha = 12°$ - xA_zD **(b)** $\alpha = 13°$ - xA_zD **(c)** $\alpha = 14°$ - xA_zD **(d)** $\alpha = 16°$ - xA_zD

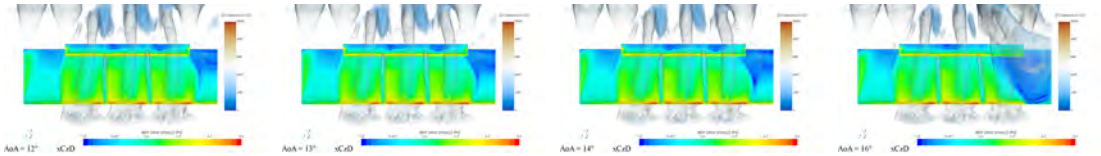

(e) $\alpha = 12°$ - xC_zD **(f)** $\alpha = 13°$ - xC_zD **(g)** $\alpha = 14°$ - xC_zD **(h)** $\alpha = 16°$ - xC_zD

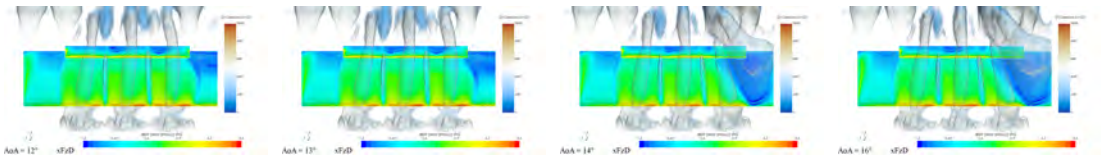

(i) $\alpha = 12°$ - xF_zD **(j)** $\alpha = 13°$ - xF_zD **(k)** $\alpha = 14°$ - xF_zD **(l)** $\alpha = 16°$ - xF_zD

Figure 3.184: Contours of the X-Component of wall shear stress and Q-Criterion isosurfaces for zD position fixed and varying the X-Position of DEP propellers - $\delta_f = 30°$ - $V_\infty = 20\ m/s$ - $Re_\infty = 5.48 \cdot 10^5$ - $RPM_{DEP} = 7000$ (In-Board Up) - STAR-CCM+

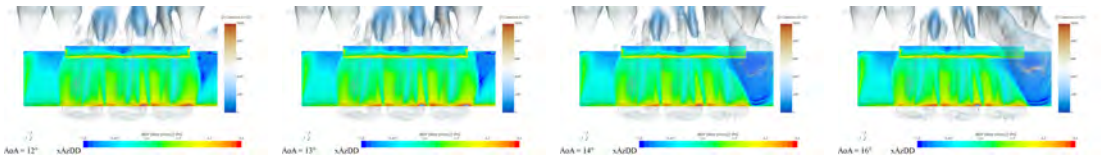

(a) $\alpha = 12°$ - xA_zDD **(b)** $\alpha = 13°$ - xA_zDD **(c)** $\alpha = 14°$ - xA_zDD **(d)** $\alpha = 16°$ - xA_zDD

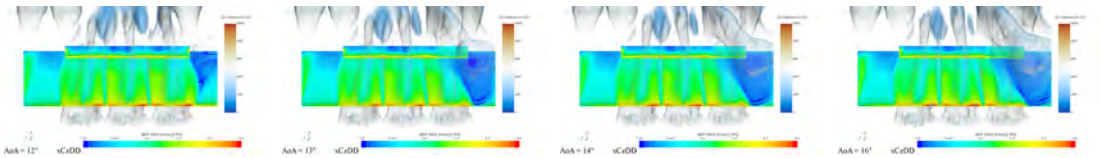

(e) $\alpha = 12°$ - xC_zDD **(f)** $\alpha = 13°$ - xC_zDD **(g)** $\alpha = 14°$ - xC_zDD **(h)** $\alpha = 16°$ - xC_zDD

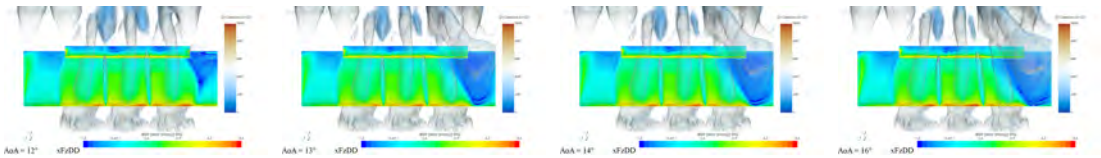

(i) $\alpha = 12°$ - xF_zDD **(j)** $\alpha = 13°$ - xF_zDD **(k)** $\alpha = 14°$ - xF_zDD **(l)** $\alpha = 16°$ - xF_zDD

Figure 3.185: Contours of the X-Component of wall shear stress and Q-Criterion isosurfaces for zDD position fixed and varying the X-Position of DEP propellers - $\delta_f = 30°$ - $V_\infty = 20\ m/s$ - $Re_\infty = 5.48 \cdot 10^5$ - $RPM_{DEP} = 7000$ (In-Board Up) - STAR-CCM+

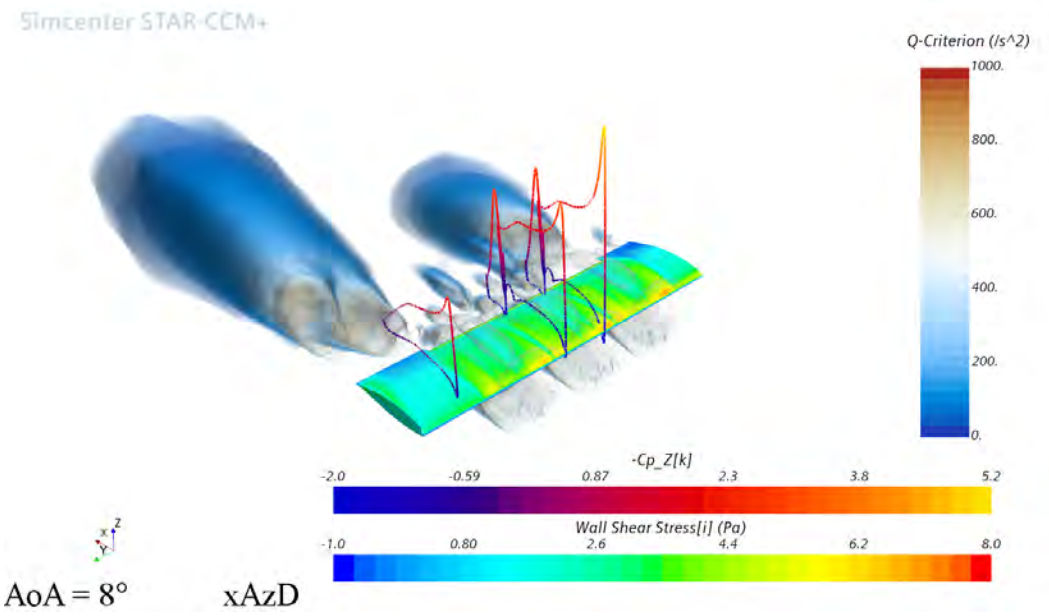

(a) $\alpha = 8°$ - xA_zD

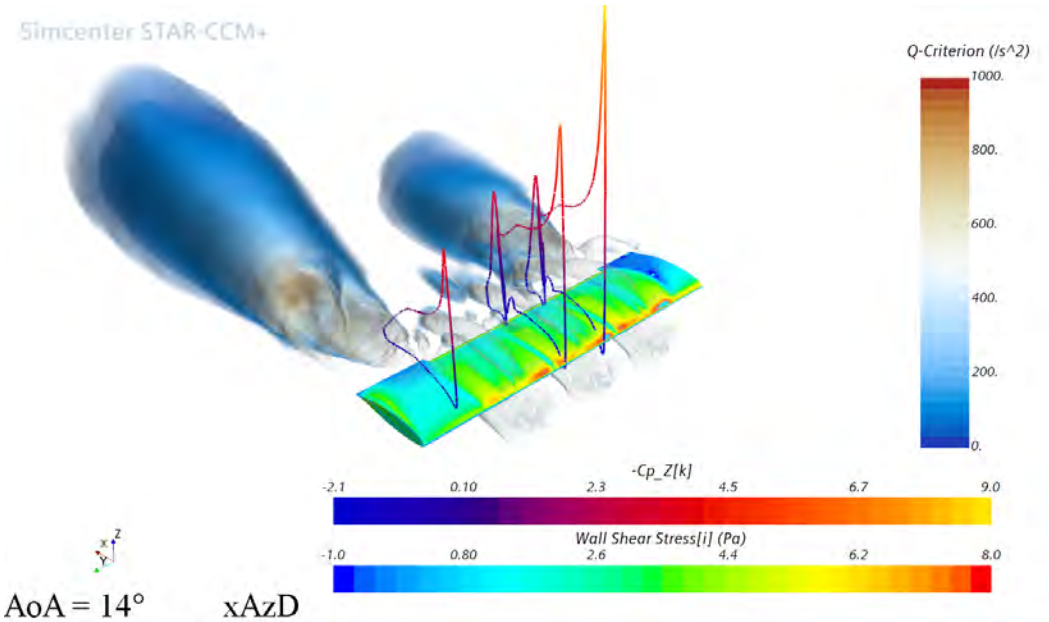

(b) $\alpha = 14°$ - xA_zD

Figure 3.186: 3D view of pressure coefficient distribution on three different sections (0.65 m, 0.75 m, 1.25 m) - $\delta_f = 30°$ - $V_\infty = 20\ m/s$ - $Re_\infty = 5.48 \cdot 10^5$ - $RPM_{DEP} = 7000$ (In-Board Up) - STAR-CCM+

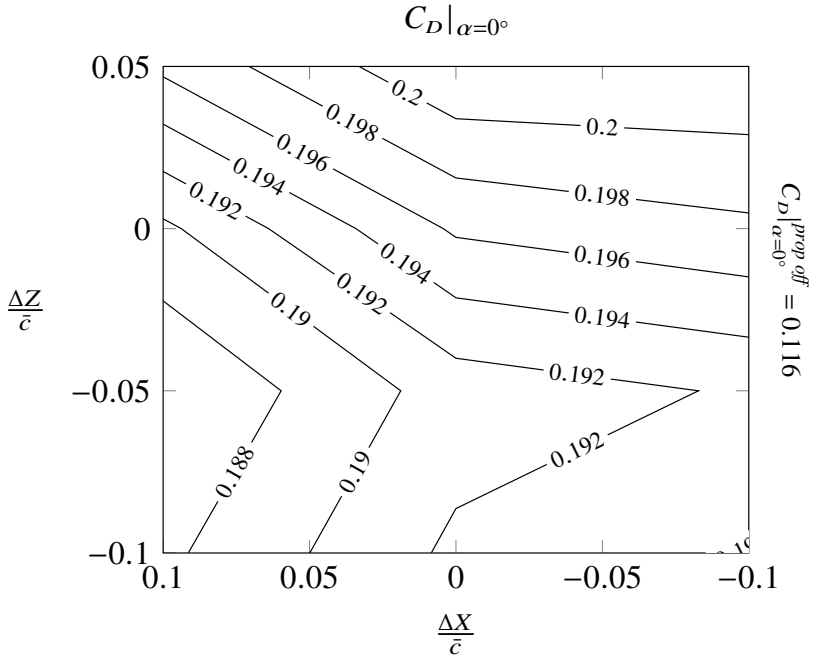

Figure 3.187: Values of $C_D|_{\alpha=0°}$ of wing by varying the position of DEP propellers - $\delta_f = 30°$ - $V_\infty = 20\ m/s$ - $Re_\infty = 5.48 \cdot 10^5$ - $RPM_{DEP} = 7000$ (In-Board Up) - STAR-CCM+

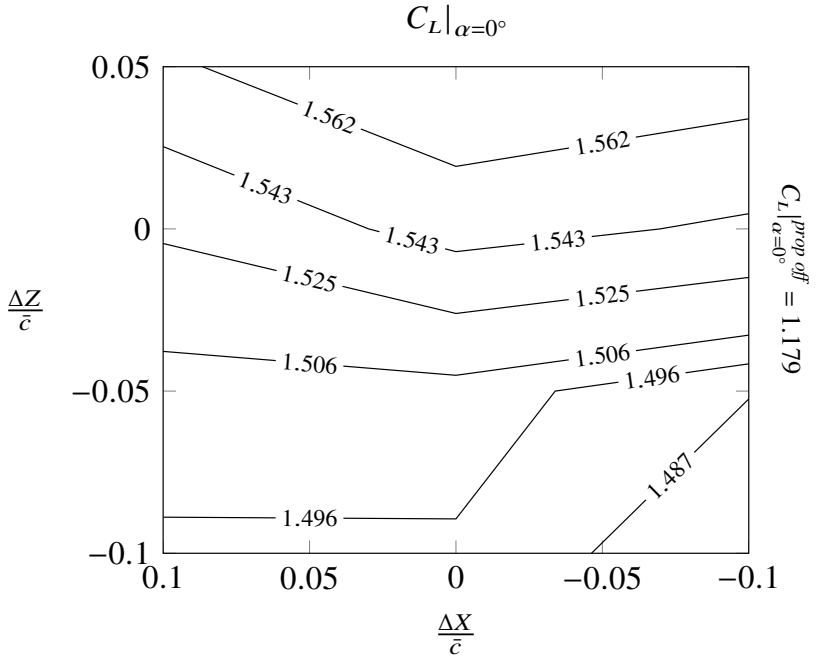

Figure 3.188: Values of $C_L|_{\alpha=0°}$ of wing by varying the position of DEP propellers - $\delta_f = 30°$ - $V_\infty = 20\ m/s$ - $Re_\infty = 5.48 \cdot 10^5$ - $RPM_{DEP} = 7000$ (In-Board Up) - STAR-CCM+

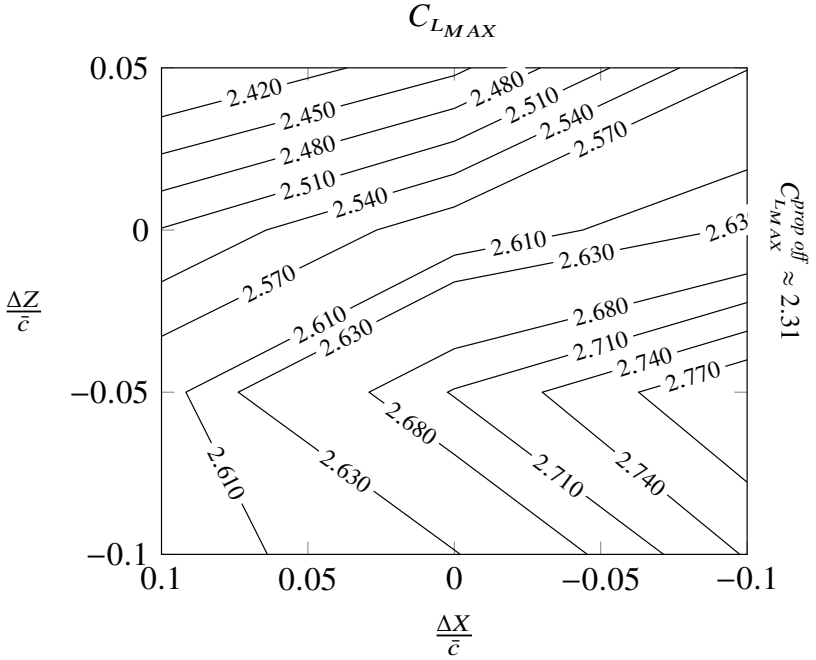

Figure 3.189: Values of $C_{L_{MAX}}$ (corresponding to different angles of attack) of wing by varying the position of DEP propellers - $\delta_f = 30°$ - $V_\infty = 20\ m/s$ - $Re_\infty = 5.48{\cdot}10^5$ - $RPM_{DEP} = 7000$ (In-Board Up) - STAR-CCM+

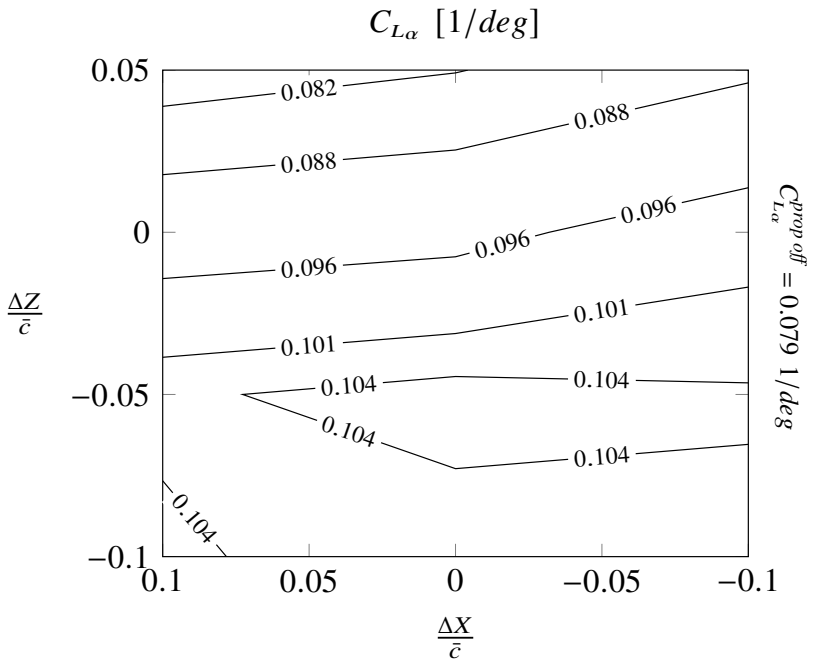

Figure 3.190: Lift curve slope of wing by varying the position of DEP propellers - $\delta_f = 30°$ - $V_\infty = 20\ m/s$ - $Re_\infty = 5.48 \cdot 10^5$ - $RPM_{DEP} = 7000$ (In-Board Up) - STAR-CCM+

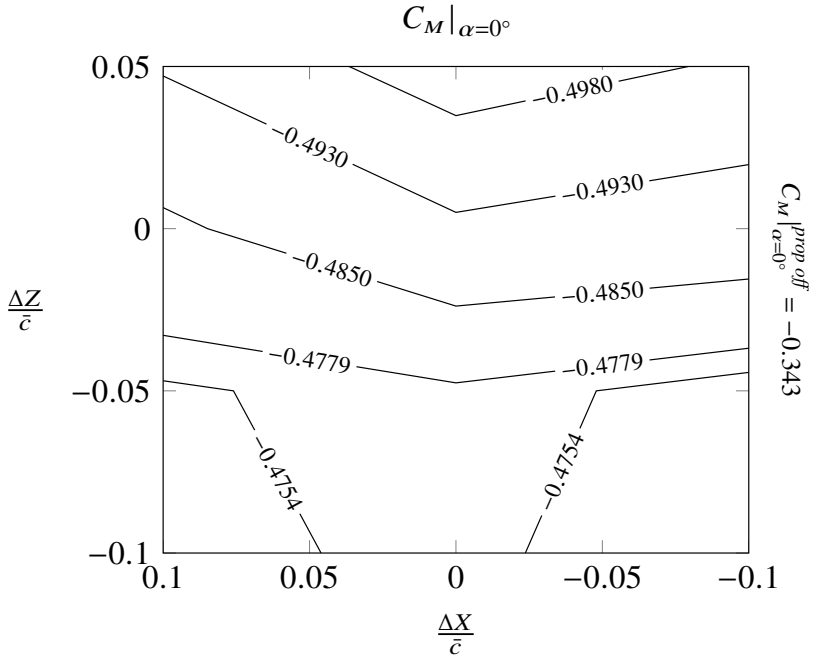

Figure 3.191: Values of $C_M|_{\alpha=0°}$ of wing by varying the position of DEP propellers - $\delta_f = 30°$ - $V_\infty = 20\ m/s$ - $Re_\infty = 5.48 \cdot 10^5$ - $RPM_{DEP} = 7000$ (In-Board Up) - STAR-CCM+

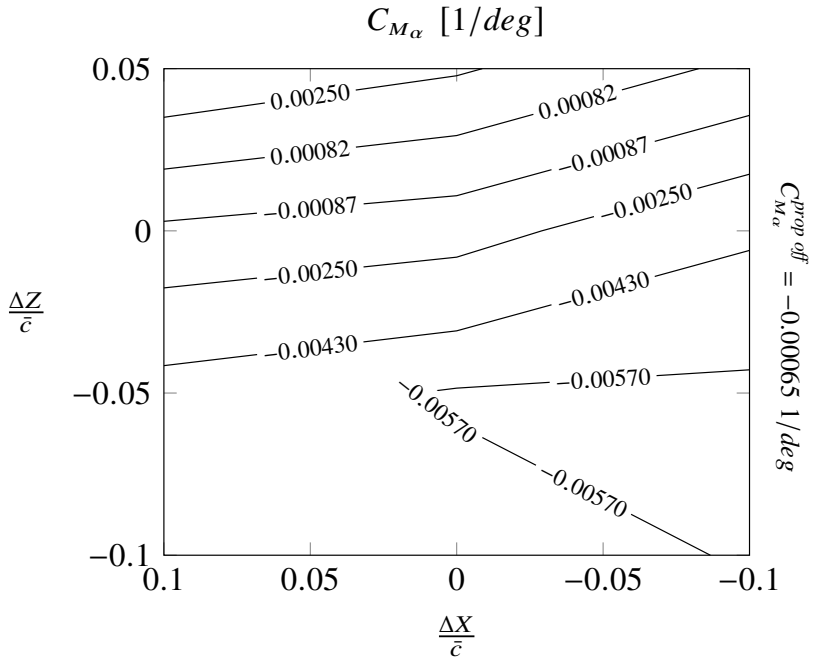

Figure 3.192: Pitching moment curve slope of wing by varying the position of DEP propellers - $\delta_f = 30°$ - $V_\infty = 20\ m/s$ - $Re_\infty = 5.48 \cdot 10^5$ - $RPM_{DEP} = 7000$ (In-Board Up) - STAR-CCM+

3.3.5 Tip propeller effects

In this section, the effect of the tip-mounted propeller (introduced at the beginning of this chapter) is analyzed. The propeller is located at 1.4 m (the wing tip) and 20% of wing chord ahead of the wing leading edge, aligned with the tip chord. Fig. 3.194 represents the wing aerodynamic performance in clean configuration with only tip propeller enabled, compared to the prop off condition. As expected, there is a reduction of the drag coefficient (at the same C_L) generated by the counter-rotating propeller respect to the wing-tip vortices. The reduction of induced drag is quantified by the induced drag factor, e_w, which changes from a prop off value of $e_w^{\text{prop off}} = 0.85$ to a value $e_w^{\text{tip on}} = 1.1$, even higher than 1. The same consideration can be done for the flapped configurations, Fig. 3.198 and 3.202. From the lift curves in the figures, it is clear that in this case the tip-mounted propeller also generates a little increase in lift coefficient. Due to the relative low-value of wing aspect-ratio, the influence of the tip propeller (the percentage of the wetted area influenced by the propeller slipstream is about 14% of the semispan) is propagated until the wing root section, changing the wing-loading as highlighted in Fig. 3.196 and 3.197.

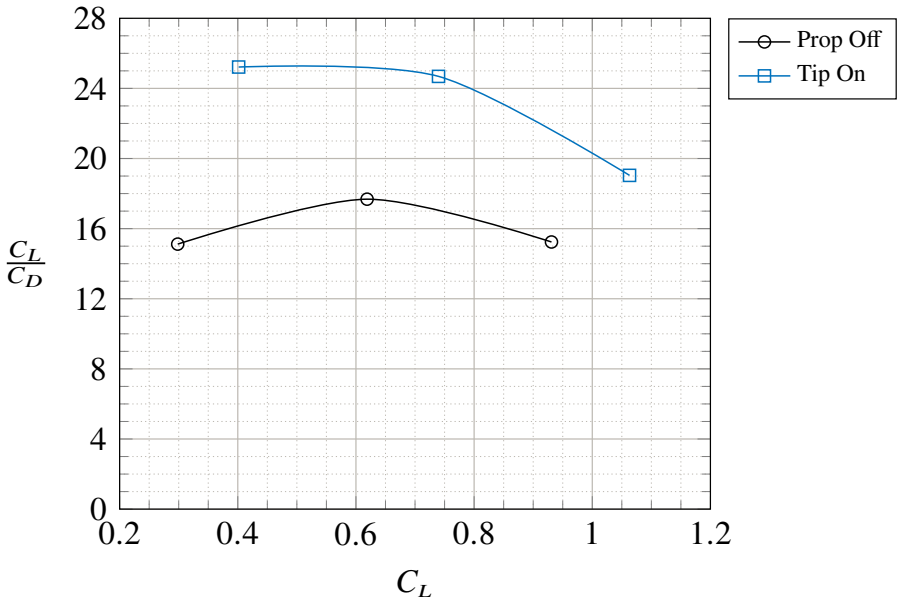

Figure 3.193: Wing efficiency with tip propeller enabled - No flap - $V_\infty = 20\ m/s$ - $Re_\infty = 5.48 \cdot 10^5$ - $RPM_{TIP} = 2000$ (In-Board Up) - STAR-CCM+

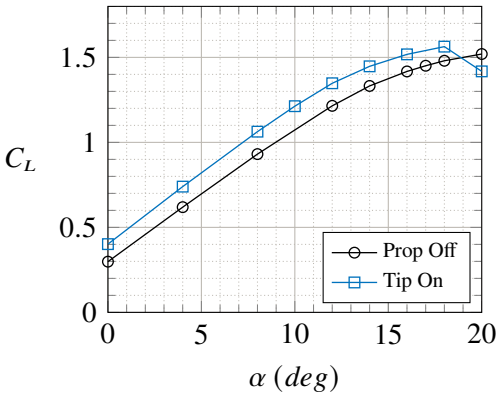

(a) Lift coefficient

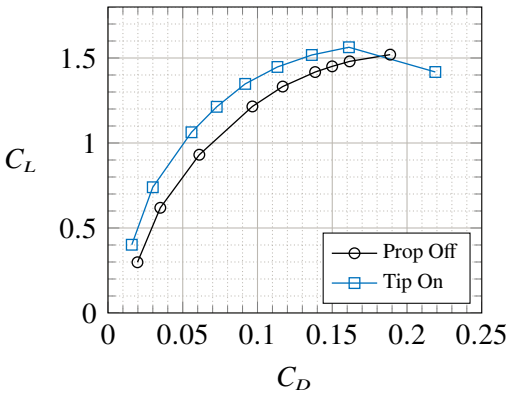

(b) Drag polar

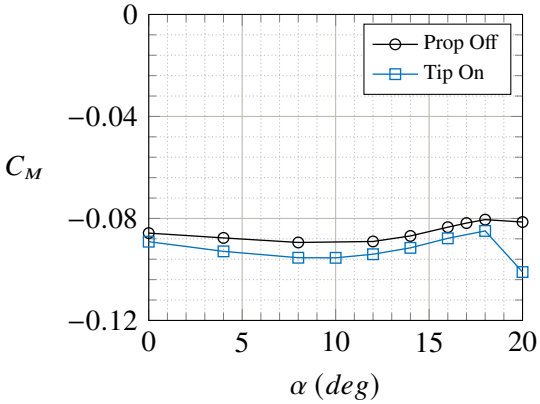

(c) Pitching moment coefficient

Figure 3.194: Wing aerodynamic performance with only tip propeller enabled - No flap - $V_\infty = 20\ m/s$ - $Re_\infty = 5.48 \cdot 10^5$ - $RPM_{TIP} = 2000$ (In-Board Up) - STAR-CCM+

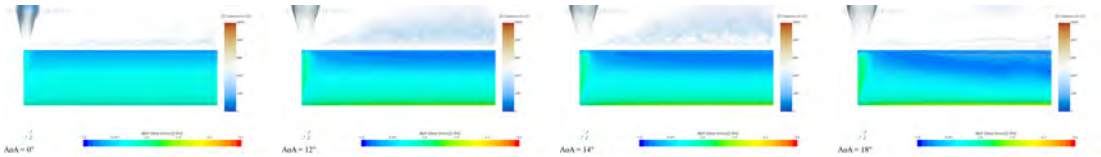

(a) $\alpha = 0°$ - Prop Off **(b)** $\alpha = 12°$ - Prop Off **(c)** $\alpha = 14°$ - Prop Off **(d)** $\alpha = 18°$ - Prop Off

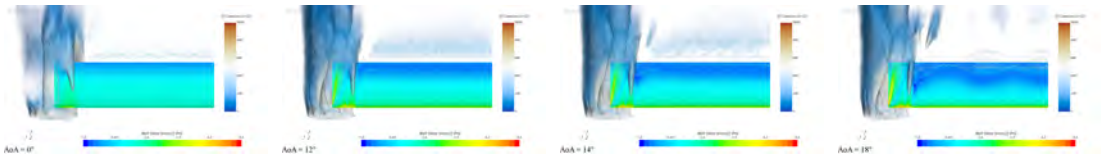

(e) $\alpha = 0°$ - Tip On **(f)** $\alpha = 12°$ - Tip On **(g)** $\alpha = 14°$ - Tip On **(h)** $\alpha = 18°$ - Tip On

Figure 3.195: Contours of the X-Component of wall shear stress and Q-Criterion isosurfaces - No flap - $V_\infty = 20\ m/s$ - $Re_\infty = 5.48 \cdot 10^5$ - $RPM_{TIP} = 2000$ (In-Board Up) - STAR-CCM+

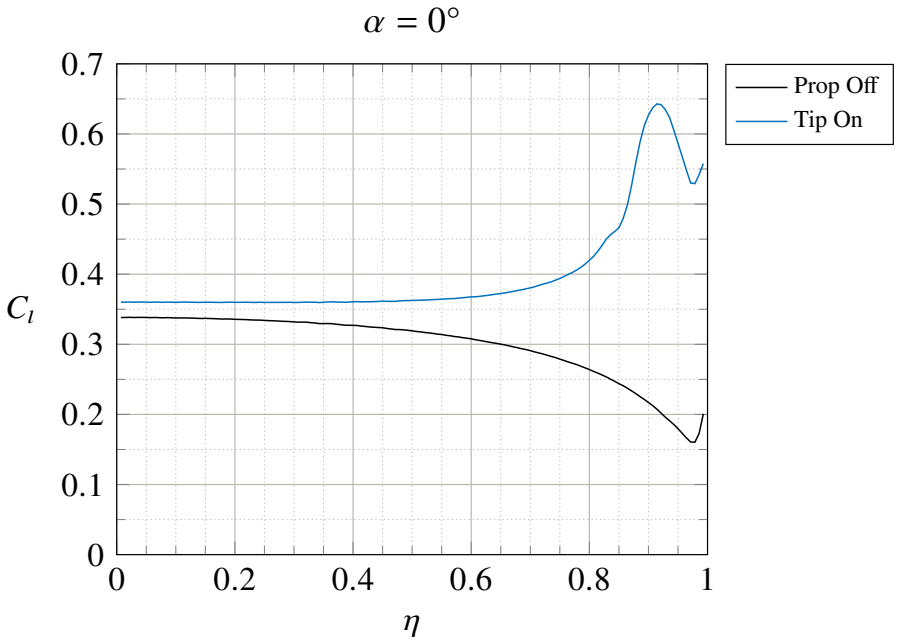

Figure 3.196: Wing load distribution with the tip propeller enabled - No flap - $V_\infty = 20\ m/s$ - $Re_\infty = 5.48 \cdot 10^5$ - $RPM_{TIP} = 2000$ (In-Board Up) - STAR-CCM+

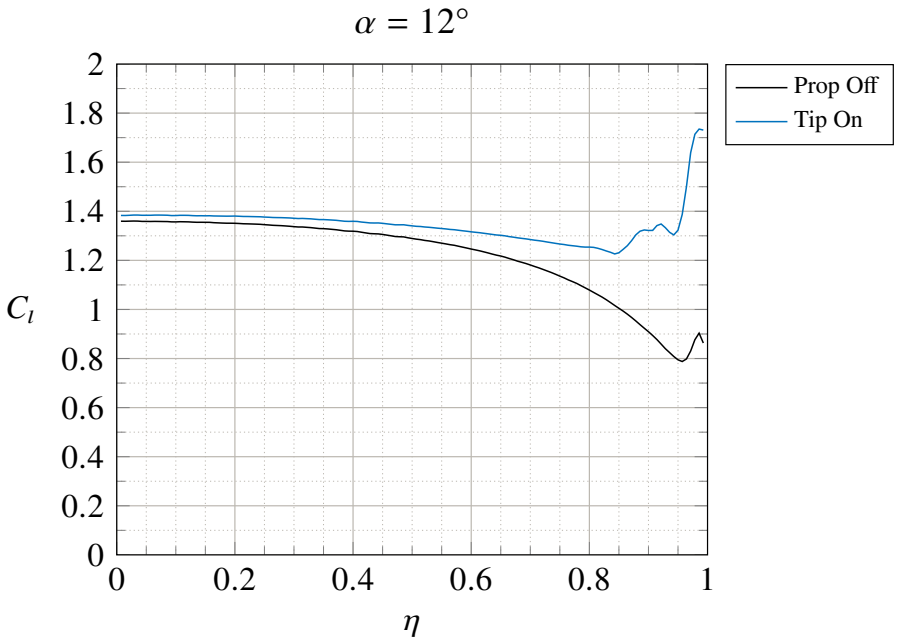

Figure 3.197: Wing load distribution with the tip propeller enabled - No flap - $V_\infty = 20\ m/s$ - $Re_\infty = 5.48 \cdot 10^5$ - $RPM_{TIP} = 2000$ (In-Board Up) - STAR-CCM+

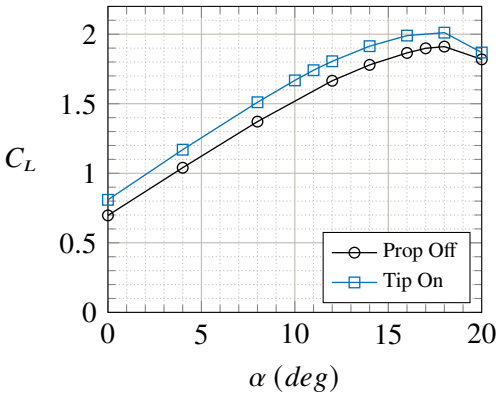

(a) Lift coefficient

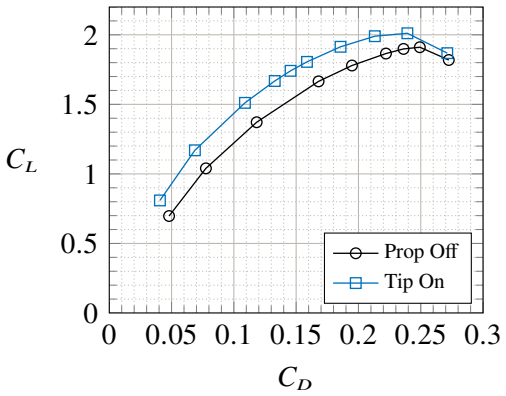

(b) Drag polar

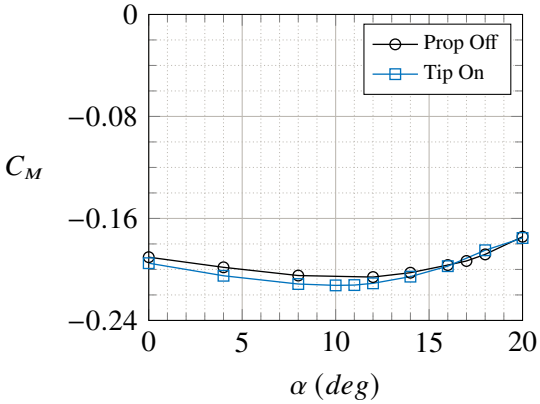

(c) Pitching moment coefficient

Figure 3.198: Wing aerodynamic performance with only tip propeller enabled - $\delta_f = 15°$ - $V_\infty = 20\ m/s$ - $Re_\infty = 5.48 \cdot 10^5$ - $RPM_{TIP} = 2000$ (In-Board Up) - STAR-CCM+

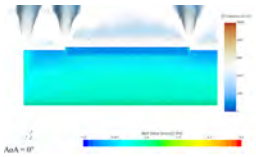

(a) $\alpha = 0°$ - Prop Off

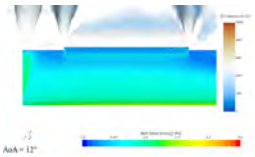

(b) $\alpha = 12°$ - Prop Off

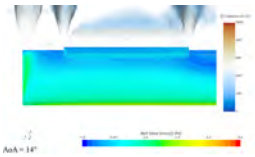

(c) $\alpha = 14°$ - Prop Off

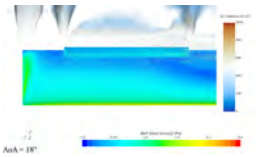

(d) $\alpha = 18°$ - Prop Off

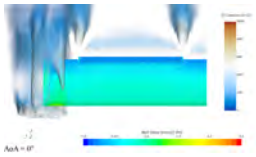

(e) $\alpha = 0°$ - Tip On

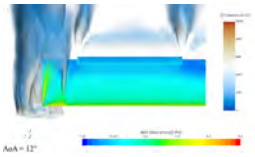

(f) $\alpha = 12°$ - Tip On

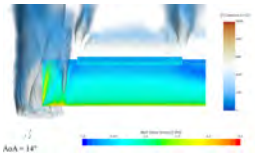

(g) $\alpha = 14°$ - Tip On

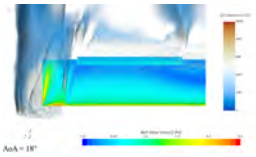

(h) $\alpha = 18°$ - Tip On

Figure 3.199: Contours of the X-Component of wall shear stress and Q-Criterion isosurfaces - $\delta_f = 15°$ - $V_\infty = 20\ m/s$ - $Re_\infty = 5.48 \cdot 10^5$ - $RPM_{TIP} = 2000$ (In-Board Up) - STAR-CCM+

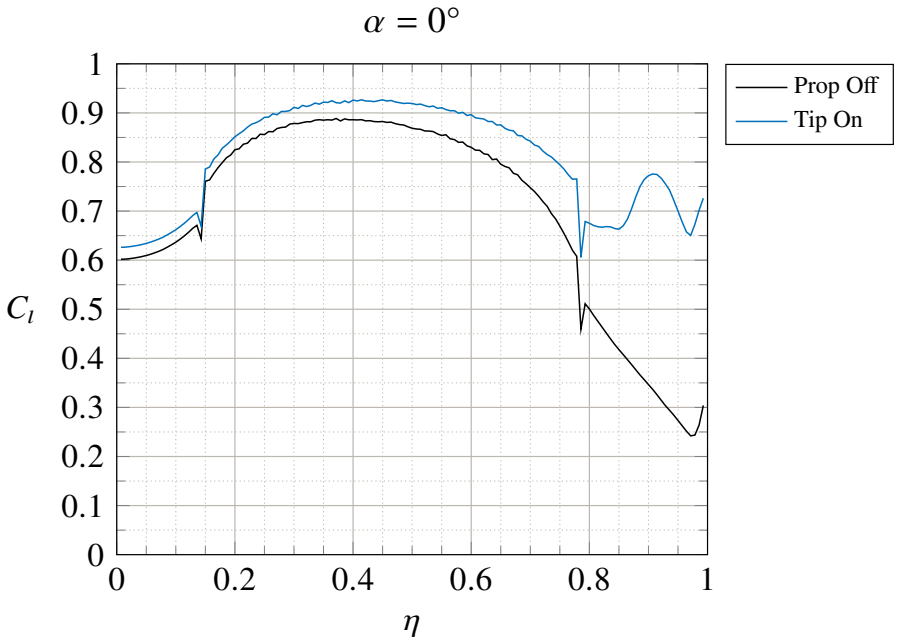

Figure 3.200: Wing load distribution with the tip propeller enabled - $\delta_f = 15°$ - $V_\infty = 20\ m/s$ - $Re_\infty = 5.48 \cdot 10^5$ - $RPM_{TIP} = 2000$ (In-Board Up) - STAR-CCM+

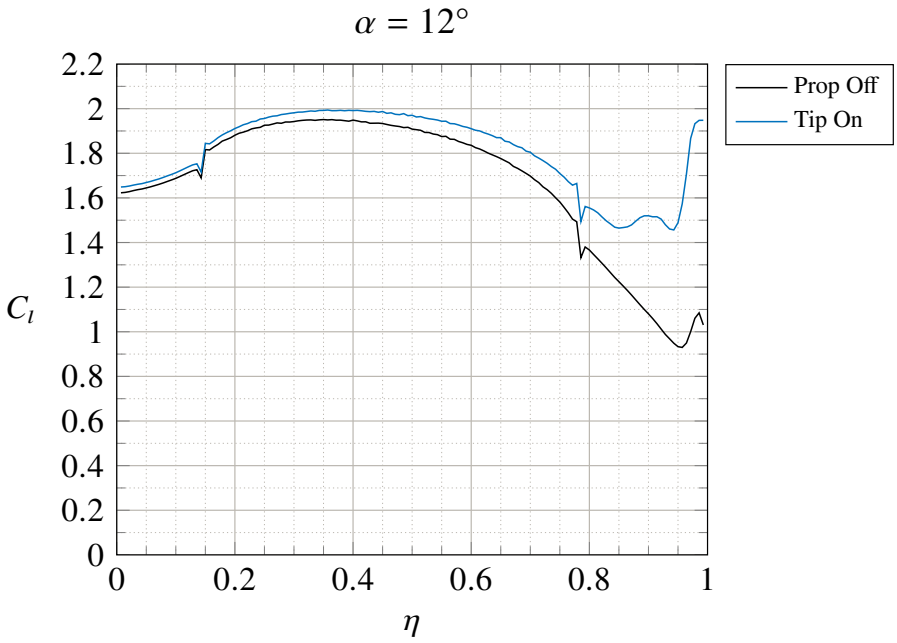

Figure 3.201: Wing load distribution with the tip propeller enabled - $\delta_f = 15°$ - $V_\infty = 20\ m/s$ - $Re_\infty = 5.48 \cdot 10^5$ - $RPM_{TIP} = 2000$ (In-Board Up) - STAR-CCM+

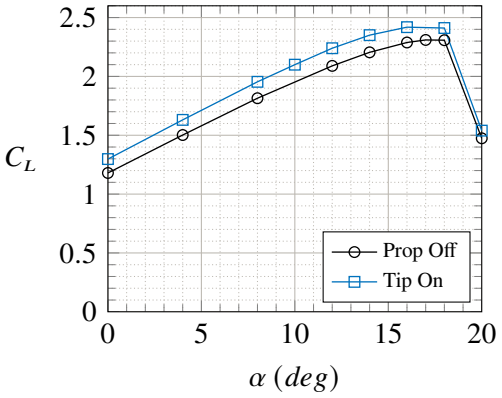

(a) Lift coefficient

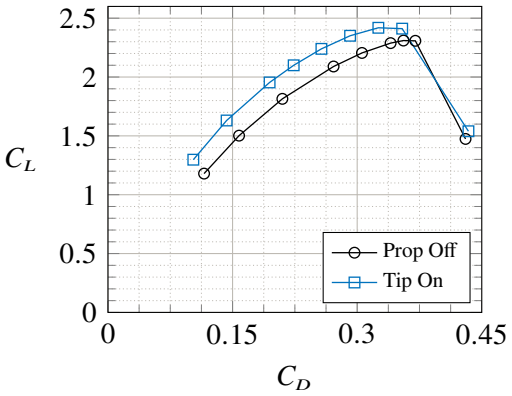

(b) Drag polar

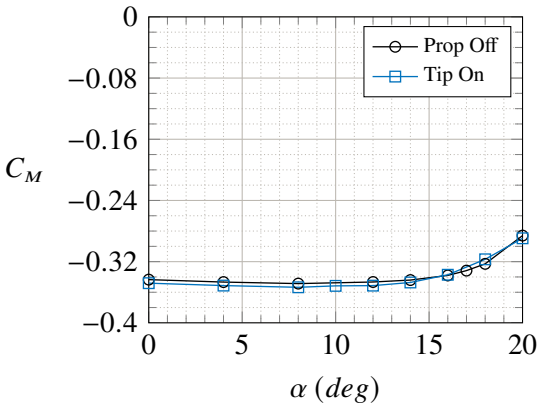

(c) Pitching moment coefficient

Figure 3.202: Wing aerodynamic performance with only tip propeller enabled - $\delta_f = 30°$ - $V_\infty = 20\ m/s$ - $Re_\infty = 5.48 \cdot 10^5$ - $RPM_{TIP} = 2000$ (In-Board Up) - STAR-CCM+

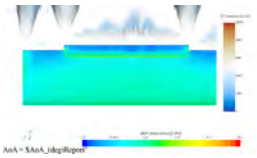

(a) $\alpha = 0°$ - Prop Off

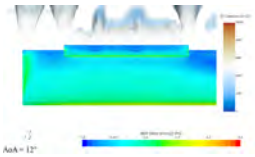

(b) $\alpha = 12°$ - Prop Off

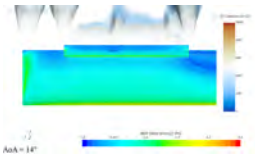

(c) $\alpha = 14°$ - Prop Off

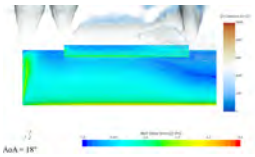

(d) $\alpha = 18°$ - Prop Off

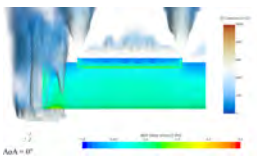

(e) $\alpha = 0°$ - Tip On

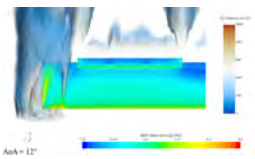

(f) $\alpha = 12°$ - Tip On

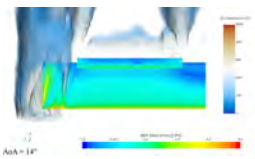

(g) $\alpha = 14°$ - Tip On

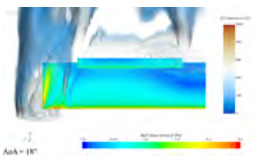

(h) $\alpha = 18°$ - Tip On

Figure 3.203: Contours of the X-Component of wall shear stress and Q-Criterion isosurfaces - $\delta_f = 30°$ - $V_\infty = 20\ m/s$ - $Re_\infty = 5.48 \cdot 10^5$ - $RPM_{TIP} = 2000$ (In-Board Up) - STAR-CCM+

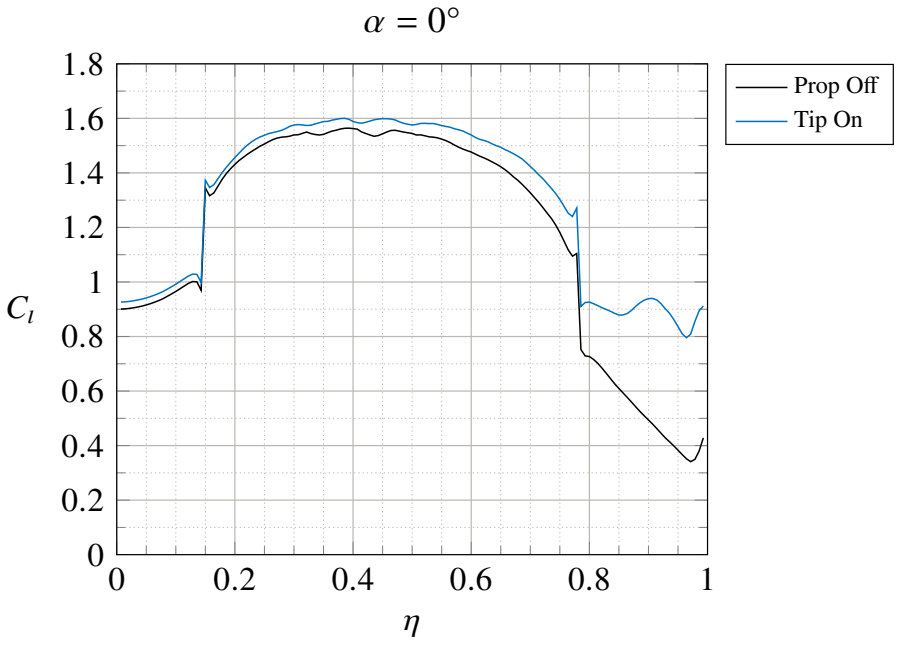

Figure 3.204: Wing load distribution with the tip propeller enabled - $\delta_f = 30°$ - $V_\infty = 20\ m/s$ - $Re_\infty = 5.48 \cdot 10^5$ - $RPM_{TIP} = 2000$ (In-Board Up) - STAR-CCM+

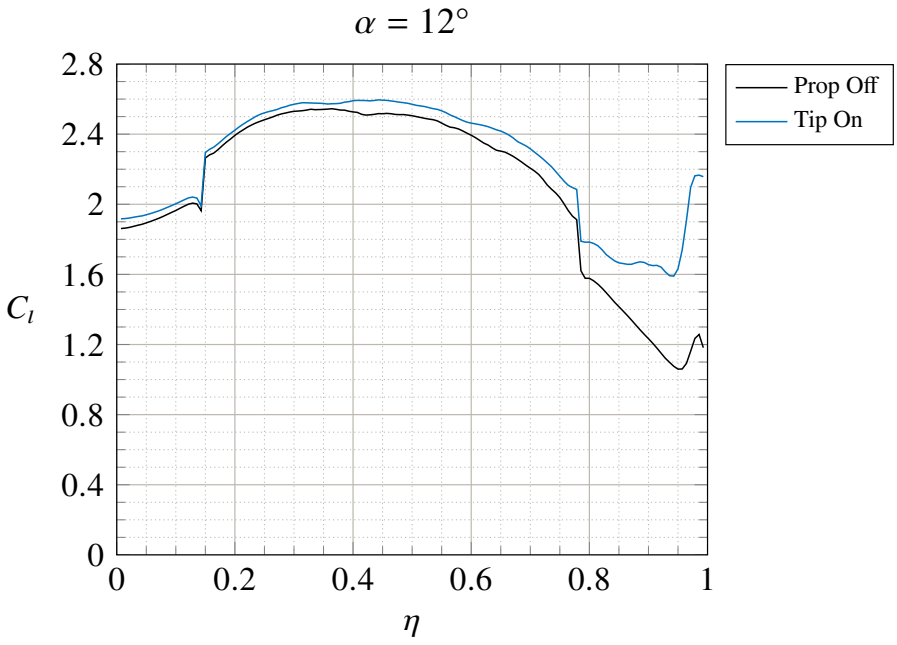

Figure 3.205: Wing load distribution with the tip propeller enabled - $\delta_f = 30°$ - $V_\infty = 20\ m/s$ - $Re_\infty = 5.48 \cdot 10^5$ - $RPM_{TIP} = 2000$ (In-Board Up) - STAR-CCM+

Chapter 4

Conclusions

The results presented in the previous chapter have shown that for the wing in clean configuration the better behaviour at stall is reached when the DEP propellers are mounted in the xA_zC position. Regarding the flapped configurations, the xA_zD position seems to be the better choice. Fig. 4.2, 4.3 and 4.4 represents the aerodynamic coefficients for these positions which corresponds to the better behaviour at stall for each configuration. It is possible to see that, fixed an angle of attack, the increment of the generic aerodynamic coefficient respect to the prop off condition becomes larger. From the results of the analyses, an indicative value of the highest difference of maximum lift coefficient between DEP on and prop off condition, for each configuration, can be calculated (referring to the DEP positions mentioned above). These values are collected in Tab. 4.1. Fig. 4.2 also contains the results of the vortex lattice method with VSPAERO. For the clean wing the method is in good agreement with the CFD results, at least in the linear zone of the lift curve, both in prop off and in dep on condition, with a slight underestimation of the slope. Regarding the flapped configurations, the differences between the two methods are more evident. However, in terms of ΔC_L between prop off and dep on conditions, the method gives good results.

Regarding the clean wing, from Fig. 3.49 it is clear that there is no benefit, for this type of wing, from flying with DEP propellers enabled, because there is a breakdown of the maximum efficiency. Indeed, there is a loss of efficiency of about 4 in the better case, corresponding to the DEP propellers position xF_zU, which is, by the way, the worst position from the point of view of stall. Another effect of the DEP propellers is to shift the point of maximum efficiency to higher lift coefficient (a possible lift coefficient in cruise could be around 0.8, instead of a value of 0.6 corresponding to the prop off

condition).

On the other hand, the flapped configurations can take more advantage from the presence of DEP propellers, of course. Assuming that a flap deflection of 15 degrees corresponds to a takeoff condition, at best the maximum lift coefficient can be augmented of about 0.28 (see Tab. 4.1), which means a reduction of takeoff distance and takeoff speed, with the possibility to reduce the wing area and the maximum takeoff weight. However, there is also an increase in drag coefficient which in takeoff condition is detrimental.

A flap deflection of 30 degrees can be considered a landing condition, for which a $\Delta C_{L_{MAX}}$ of 0.49 can be reached. This lift augmentation is beneficial for landing performance, but it is generated by the DEP propellers blowing, so there is a certain amount of thrust which is undesired on landing. Nevertheless, the high increase in drag coefficient generated by the DEP propellers is in this case well accepted. Concerning

	$\Delta C_{L_{MAX}}$
Clean (xA_zC)	0.05
$\delta_f = 15°$ (xA_zD)	0.28
$\delta_f = 30°$ (xA_zD)	0.49

Table 4.1: Indicative values of the maximum $\Delta C_{L_{MAX}}$ achievable for each configuration

the tip-mounted propellers, as said before the aerodynamic effects are beneficial because the wing efficiency is increased. However, in case of a twin-engine aircraft for example, the vertical tail design could be very challenging, due to the One Engine Inoperative (OEI) condition which become very critical in such a case. A possible way to deal with this problem is to consider the utilisation of DEP propellers to balance the yawing moment introduced by an engine failure.

Furthermore, other consideration from the structural point of view must be made. If the presence of an array of propellers distributed spanwise have the effect to reduce the bending moment in flight (considering in case of DEP also electric motors, power sources, transmission lines, etc.), conversely some aeroelastic problems could arise.

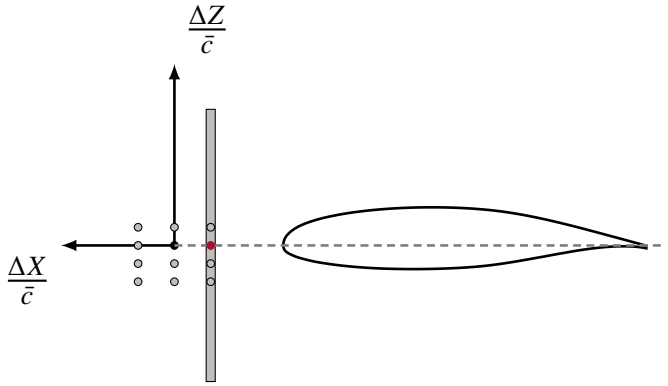

(a) Clean - xA_zC

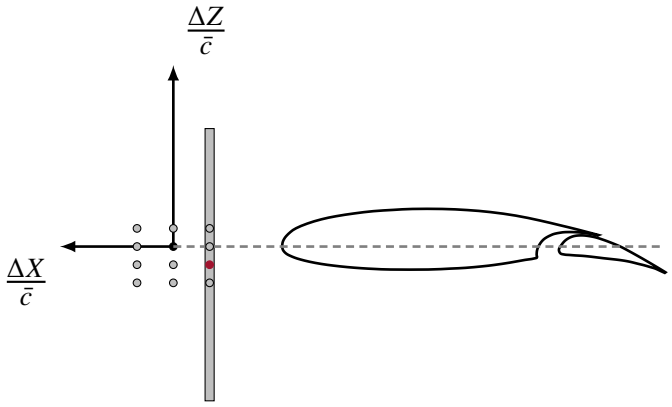

(b) $\delta_f = 15°$ - xA_zD

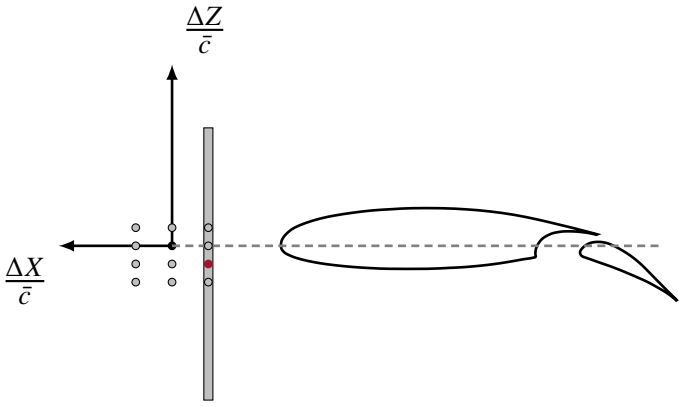

(c) $\delta_f = 30°$ - xA_zD

Figure 4.1: DEP propellers position which leads to the highest maximum lift coefficient for each wing configuration

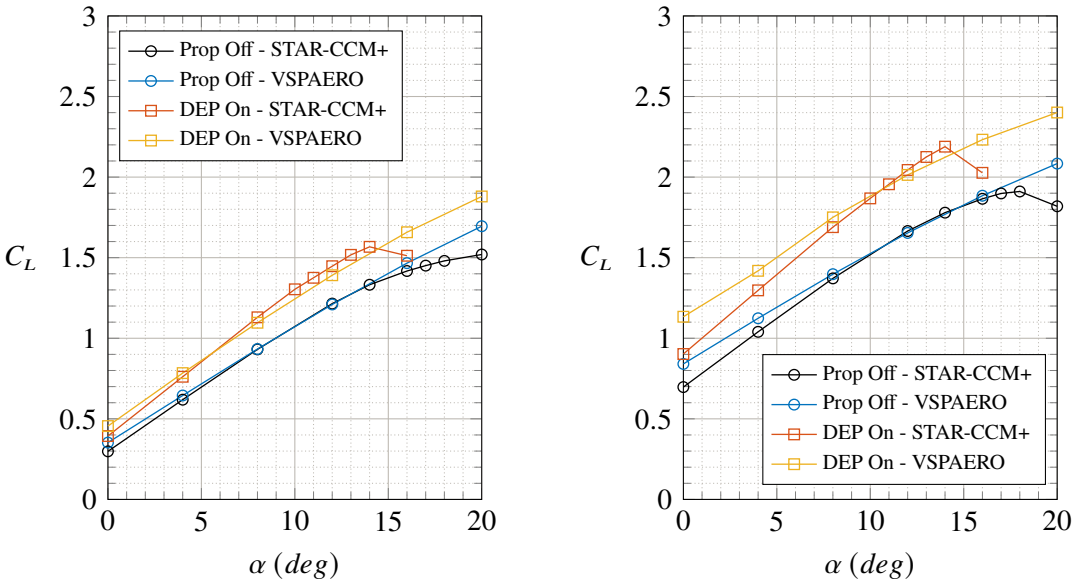

(a) Clean - xA_zC

(b) $\delta_f = 15°$ - xA_zD

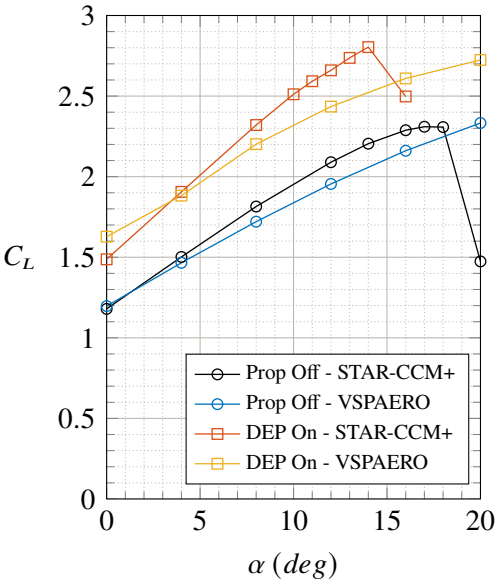

(c) $\delta_f = 30°$ - xA_zD

Figure 4.2: Wing lift curves for the "better" positions (related to stall) of DEP propellers for different wing configurations - $V_\infty = 20\ m/s$ - $Re_\infty = 5.48 \cdot 10^5$ - $RPM_{DEP} = 7000$ (In-Board Up)

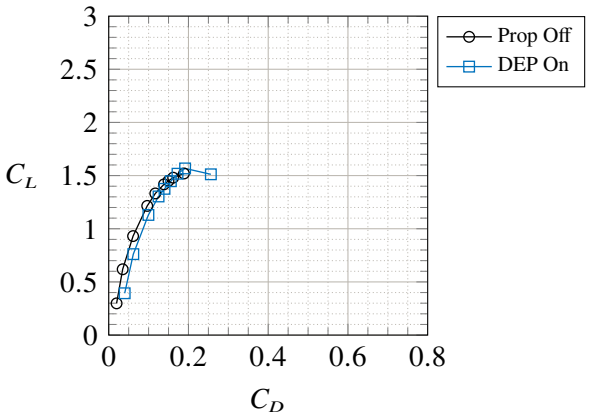

(a) Clean - xA_zC

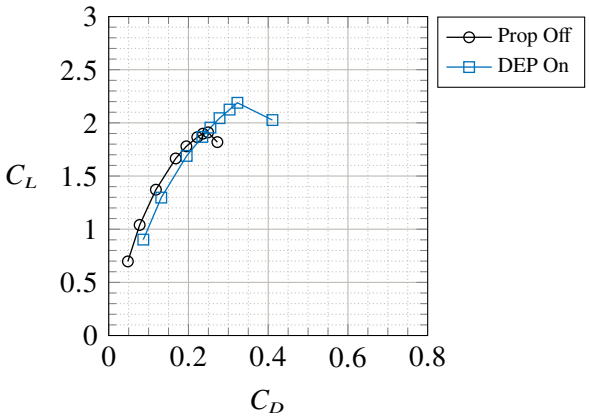

(b) δ_f = 15° - xA_zD

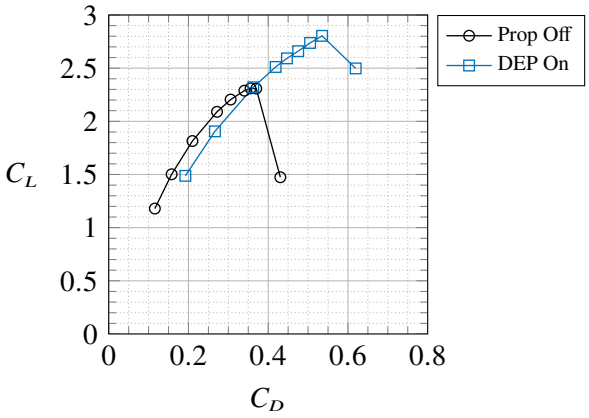

(c) δ_f = 30° - xA_zD

Figure 4.3: Drag polars for the "better" positions (related to stall) of DEP propellers for different wing configurations - V_∞ = 20 m/s - Re_∞ = 5.48 · 10^5 - RPM_{DEP} = 7000 (In-Board Up) - STAR-CCM+

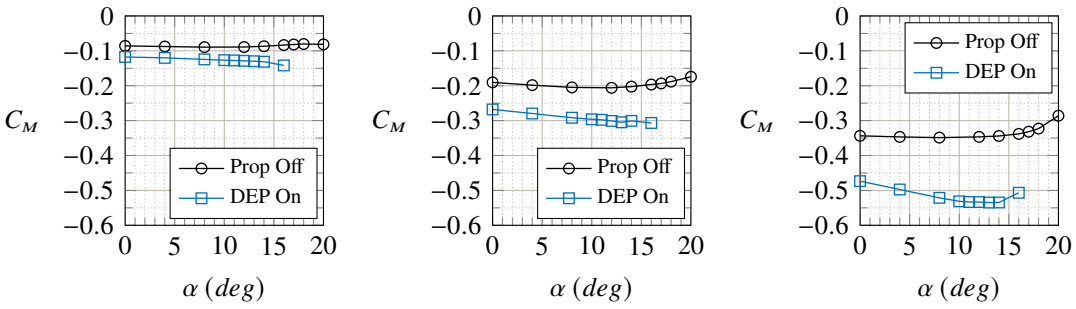

(a) Clean - xA_zC **(b)** $\delta_f = 15°$ - xA_zD **(c)** $\delta_f = 30°$ - xA_zD

Figure 4.4: Pitching moment coefficient for the "better" positions (related to stall) of DEP propellers for different wing configurations - $V_\infty = 20\ m/s$ - $Re_\infty = 5.48 \cdot 10^5$ - $RPM_{DEP} = 7000$ (In-Board Up) - STAR-CCM+

References

[1] Hyun D. Kim, Aaron T. Perry, and Phillip J. Ansell. "A Review of Distributed Electric Propulsion Concepts for Air Vehicle Technology". In: *2018 AIAA/IEEE Electric Aircraft Technologies Symposium*. DOI: 10.2514/6.2018-4998. eprint: https://arc.aiaa.org/doi/pdf/10.2514/6.2018-4998. URL: https://arc.aiaa.org/doi/abs/10.2514/6.2018-4998.

[2] Hyun Kim, Jeff Berton, and Scott Jones. "Low Noise Cruise Efficient Short Take-Off and Landing Transport Vehicle Study". In: Sept. 2006. ISBN: 978-1-62410-043-7. DOI: 10.2514/6.2006-7738.

[3] J. Felder et al. "Turboelectric Distributed Propulsion in a Hybrid Wing Body Aircraft". In: 2011.

[4] Geoffrey Hill et al. "Integration of Propulsion-Airframe-Aeroacoustic Technologies and Design Concepts for a Quiet Blended-Wing-Body Transport". In: *AIAA 4th Aviation Technology, Integration and Operations (ATIO) Forum*. DOI: 10.2514/6.2004-6403. eprint: https://arc.aiaa.org/doi/pdf/10.2514/6.2004-6403. URL: https://arc.aiaa.org/doi/abs/10.2514/6.2004-6403.

[5] Joseph D. Kummer and Thong Q. Dang. "High-Lift Propulsive Airfoil with Integrated Crossflow Fan". In: *Journal of Aircraft* 43.4 (2006), pp. 1059–1068. DOI: 10.2514/1.17610. eprint: https://doi.org/10.2514/1.17610. URL: https://doi.org/10.2514/1.17610.

[6] Joseph A. Schetz et al. "Propulsion and aerodynamic performance evaluation of jet-wing distributed propulsion". In: *Aerospace Science and Technology* 14.1 (2010), pp. 1–10. ISSN: 1270-9638. DOI: https://doi.org/10.1016/j.

ast.2009.06.010. URL: http://www.sciencedirect.com/science/article/pii/S1270963809000480.

[7] Andy Ko, J. Schetz, and William Mason. "Assessment of the Potential Advantages of Distributed Propulsion for Aircraft". In: (Jan. 2003).

[8] H. Kim. "Distributed Propulsion Vehicles". In: 2010.

[9] M. D. Patterson. "Conceptual Design of High-Lift Propeller Systems for Small Electric Aircraft". In: 2016.

[10] Alex Stoll. "Comparison of CFD and Experimental Results of the LEAPTech Distributed Electric Propulsion Blown Wing". In: June 2015. DOI: 10.2514/6.2015-3188.

[11] Karen A. Deere et al. "Computational Analysis of Powered Lift Augmentation for the LEAPTech Distributed Electric Propulsion Wing". In: *35th AIAA Applied Aerodynamics Conference*. DOI: 10.2514/6.2017-3921. eprint: https://arc.aiaa.org/doi/pdf/10.2514/6.2017-3921. URL: https://arc.aiaa.org/doi/abs/10.2514/6.2017-3921.

[12] Nicholas K. Borer et al. "Design and Performance of the NASA SCEPTOR Distributed Electric Propulsion Flight Demonstrator". In: *16th AIAA Aviation Technology, Integration, and Operations Conference*. DOI: 10.2514/6.2016-3920. eprint: https://arc.aiaa.org/doi/pdf/10.2514/6.2016-3920. URL: https://arc.aiaa.org/doi/abs/10.2514/6.2016-3920.

[13] Pierluigi Della Vecchia et al. "Numerical analysis of propeller effects on wing aerodynamic: tip mounted and distributed propulsion". In: *Transportation Research Procedia* 29 (2018). Aerospace Europe CEAS 2017 Conference, pp. 106–115. ISSN: 2352-1465. DOI: https://doi.org/10.1016/j.trpro.2018.02.010. URL: http://www.sciencedirect.com/science/article/pii/S2352146518300140.

[14] Danilo Ciliberti and Pierluigi Della Vecchia et al. *D5.1 Enabling Technologies*. ELectric Innovative Commuter Aircraft, 2020.

[15] Melvin H. Snyder and Glen W. Zumwalt. "Effects of wingtip-mounted propellers on wing lift and induced drag." In: *Journal of Aircraft* 6.5 (1969), pp. 392–397. DOI: 10.2514/3.44076. eprint: https://doi.org/10.2514/3.44076. URL: https://doi.org/10.2514/3.44076.

[16] James C. Patterson, Glynn R. Bartlett, and United States. *Evaluation of installed performance of a wing-tip-mounted pusher turboprop on a semispan wing*. NASA Techincal Paper 2739, 1987.

[17] Tomas Sinnige et al. "Wingtip-Mounted Propellers: Aerodynamic Analysis of Interaction Effects and Comparison with Conventional Layout". In: *Journal of Aircraft* 56.1 (2019), pp. 295–312. DOI: 10.2514/1.C034978. eprint: https://doi.org/10.2514/1.C034978. URL: https://doi.org/10.2514/1.C034978.

[18] Renato Tognaccini. *Lezioni di Aerodinamica dell'Ala Rotante*. URL: http://wpage.unina.it/rtogna/ar2019.pdf. Last visited on 2021/02/21. Università degli Studi di Napoli "Federico II", 2019.

[19] Fred E. Weick. *Full-Scale Wind-Tunnel Tests With a Series of Propellers of Different Diameters on a Single Fuselage*. Tech. rep. NACA TR-339, 1931.

[20] Sydney Goldstein. "On the Vortex Theory of Screw Propellers". In: *Proceedings of the Royal Society of London. Series A, Containing Papers of a Mathematical and Physical Character* 123.792 (1929), pp. 440–465. ISSN: 09501207. URL: http://www.jstor.org/stable/95206.

[21] F. Chow et al. "Numerical investigations of an airfoil in a nonuniform stream". In: *Journal of Aircraft* 7 (1970), pp. 531–537.

[22] L. Veldhuis. "Propeller Wing Aerodynamic Interference". In: 2005.

[23] Carlo de NICOLA. *Appunti per un corso di AERODINAMICA DEGLI AEROMOBILI*. Università degli Studi di Napoli "Federico II", 2018.

[24] "Simcenter STAR-CCM+ 2020.2 User Guide". In: 2020.

[25] Jeffrey K. Viken et al. "Design of the Cruise and Flap Airfoil for the X-57 Maxwell Distributed Electric Propulsion Aircraft". In: *35th AIAA Applied Aerodynamics Conference*. DOI: 10.2514/6.2017-3922. eprint: https://arc.aiaa.org/doi/pdf/10.2514/6.2017-3922. URL: https://arc.aiaa.org/doi/abs/10.2514/6.2017-3922.

[26] *Journal of Fluids Engineering Editorial Policy Statement on the Control of Numerical Accuracy*. https://journaltool.asme.org/templates/jfenumaccuracy.pdf.

[27] Leonard E. Schwer. *IS YOUR MESH REFINED ENOUGH? Estimating Discretization Error using GCI*. https://www.dynamore.de/de/download/papers/forum08/dokumente/I-I-03.pdf.